

The Thermal and Mechanical Behavior of Faults

by

Matthew Adam d'Alessio

B.S. (Stanford University) 1999

A dissertation submitted in partial satisfaction
of the requirements for the degree of

Doctor of Philosophy

in

Geology

in the

GRADUATE DIVISION

of the

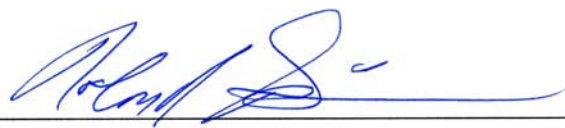
UNIVERSITY OF CALIFORNIA, BERKELEY

Committee in charge:

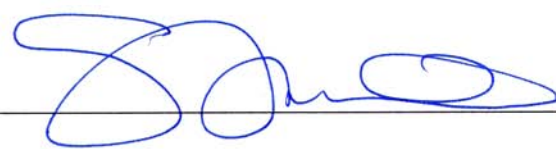
Professor Roland Bürgmann, Chair
Professor Douglas Dreger
Professor Stephen Mahin

Fall 2004

The dissertation of Matthew Adam d'Alessio is approved.


Chair _____ Date 08/30/2004


_____ Date 08/30/2004


_____ Date 08/30/2004

University of California, Berkeley

Fall 2004

The Thermal and Mechanical Behavior of Faults

Copyright © 2004

by

Matthew Adam d'Alessio

Abstract

The Thermal and Mechanical Behavior of Faults

by

Matthew Adam d'Alessio

Doctor of Philosophy in Geology

University of California, Berkeley

Professor Roland Bürgmann, Chair

Fault behavior is controlled to a large degree by the geometry and frictional properties of faults. Using a combination of field observations and modeling of fault systems throughout California, I discuss these different factors affecting the thermal and mechanical behavior of faults.

Field observations of strike slip faults in the central Sierra Nevada, California, combined with a mechanical analysis of fault interaction, show that a cluster of small faults flanking the tip of a large fault zone will tend to diffuse the stress concentration near the fault zone tip, thus inhibiting its ability to link and grow.

Observations of surface deformation allow us to determine the geometry and kinematics of faults in the San Francisco Bay Area. I present a new compilation of over 200 horizontal surface velocities collected using Global Positioning System observations from 1993-2003. I interpret this velocity field using a 3-D block model to determine the relative contributions of block offset, elastic strain accumulation, and shallow aseismic creep.

Large earthquakes generate frictional heat, and the magnitude of heating is related the frictional strength of the fault. I present apatite fission-track (AFT) analyses of samples from the San Gabriel fault zone in southern California. There is no evidence of a localized thermal anomaly, indicating that either there has never been an earthquake with > 4 m of slip at this locality or the average apparent coefficient of friction is < 0.4 .

The San Andreas Fault Observatory at Depth Pilot Hole traverses the upper 2 km of a site 1.8 km west of the San Andreas fault (SAF) near Parkfield, California. To evaluate the burial and exhumation history of the site in relation to the kinematics and mechanics of the SAF, I present AFT and (U-Th)/He analyses from Pilot Hole samples. There has been < 1.5 km of total vertical motion adjacent to the SAF since ~ 60 Ma.

Numerical models show that faults with heterogeneous frictional asperities produce heat flow patterns that are asymmetric across the fault as well as along-strike. This asymmetry has implications for conclusions about fault strength drawn from existing heat flow measurements.

Contents

Contents	i
List of Figures	v
List of Tables	viii
Acknowledgements	ix
1 Introduction	1
1.1 The Earthquake Cycle	1
1.2 Key Concept: Fault Geometry	4
1.3 Key Concept: Frictionally Generated Heat	7
1.4 Relationships and Feedbacks	8
2 Fault terminations and barriers to fault growth	9
2.1 ABSTRACT	9
2.2 Introduction	9
2.3 Geologic setting	13
2.4 Fault system	14
2.5 Mechanical analysis	17
2.5.1 Reduced shear stress concentration	19
2.5.2 Fracture energy	19
2.5.3 Effects of mechanical interaction on secondary fractures	21
2.5.4 Slip profile near the fault tip	21
2.6 Discussion	23

2.6.1	Role of a nearby lithologic boundary	23
2.6.2	Cluster of small faults	25
2.6.3	Scale dependence	25
2.6.4	Implications for fluid flow and erosion	26
2.6.5	Crack-tip shielding	26
2.7	Conclusions	27
3	Slicing up the San Francisco Bay Area:	
	Block kinematics and fault slip rates from GPS-derived surface velocities	28
3.1	ABSTRACT	28
3.2	Introduction	29
3.3	GPS Data and Processing	30
3.3.1	Data Collection	30
3.3.2	GPS Processing	30
3.3.3	No Outlier Exclusion	31
3.4	Block Modeling Methodology	33
3.4.1	Dislocation modeling	33
3.4.2	Block Modeling	34
3.4.3	Inclusion of Global Data	35
3.4.4	Fault Geometry	35
3.4.5	Surface Creep	41
3.5	Results	42
3.5.1	Global Plate Motion	45
3.5.2	Sierra Nevada / Great Valley Block	47
3.5.3	Poles of Rotation of Bay Area Blocks	48
3.5.4	Slip Rates on Bay Area Faults	48
3.5.5	Shallow Creep	52
3.6	Discussion	54
3.6.1	Comparing the Models	54
3.6.2	Dipping faults	57
3.6.3	Convergence in the Coast Range	59
3.6.4	Implications for fault system development	64

3.6.5	Fault Connections	65
3.6.6	Locking Depth	68
3.6.7	Comparison With Long Term Slip Rates	71
3.7	Conclusions	72
4	No frictional heat along the San Gabriel fault, California: Evidence from fission-track thermochronology	80
4.1	ABSTRACT	80
4.2	Introduction	81
4.2.1	Frictional Heating	81
4.2.2	Thermochronology and Frictional Heat	82
4.3	San Gabriel Fault Zone	83
4.3.1	Site Description	83
4.3.2	Samples	85
4.4	Fission-track Results and Analysis	85
4.5	Constraining Fault Strength	88
4.6	Conclusions	89
5	Constraining the exhumation and burial history of the SAFOD Pilot Hole with apatite fission track and (U-Th)/He thermochronometry	93
5.1	ABSTRACT	93
5.2	Introduction	94
5.3	SAFOD setting	94
5.4	Samples and Thermochronometry Results	94
5.5	Apatite Fission Track Length Analysis and Thermal Model	96
5.6	Interpretation	97
5.7	Conclusions	99
5.8	Appendix: Fission Track Analysis Procedure	99
6	Frictional heterogeneity and heat flow	104
6.1	ABSTRACT	104
6.2	Introduction	104
6.3	Existing formulations of frictional heat	106
6.3.1	Rupture Process	106

6.3.2	Transport of Frictional Heat	107
6.4	Heat Flow Distribution about a finite fault	107
6.5	Lateral Transport	110
6.5.1	Method	111
6.5.2	A Single Asperity	111
6.5.3	Dependence on Slip Rate	112
6.5.4	Multiple Asperities and the Infinite Limit	114
6.5.5	Frictional Asperities and Interpretations of Heat Flow	115
6.6	The Creeping San Andreas Fault	116
6.7	Comparisons with Observations	119
6.7.1	Comparing Predictions to Observations	119
6.8	Conclusions	123
6.9	Appendix	125
6.9.1	Point Source	125
6.9.2	Rectangular Source	126

Bibliography

128

List of Figures

1.1	Thermal and mechanical behavior of faults concept map	2
1.2	Stages of the earthquake cycle	3
1.3	Geometry of the Pear Lake fault system compared to the San Andreas fault System	6
2.1	Cartoon showing two mechanisms for fault growth	11
2.2	Photos of fault terminations	12
2.3	Location and generalized geology of the Trail Fork fault system	13
2.4	Map of the west end of the Trail Fork fault system	15
2.5	Cumulative left-lateral offset of marker dikes	16
2.6	Normalized fault-parallel shear stress concentrations near model fault system tips	18
2.7	Relative fracture energy as a function of overlap distance	20
2.8	Normalized differential stress versus normalized least compressive stress	22
2.9	Comparison between slip profiles obtained from field measurements of offset dikes and from modeling results	24
3.1	The BÄVÜ data set: Map of the San Francisco Bay Area with GPS Velocities from 1994-2003 relative to station LUTZ	32
3.2	Western hemisphere GPS velocities from BÄVÜ in ITRF2000-NNR reference frame	36
3.3	California GPS velocities from BÄVÜ in a stable North America reference frame	37
3.4	Map of model geometry	38
3.5	Map of GPS velocities near the Hayward fault	42
3.6	GPS velocities from data and Preferred model	43
3.7	Difference between observed GPS velocities and model calculations for three different model scenarios	44
3.8	Map showing calculated poles of rotation for blocks in the Bay Area	49
3.9	Depth of seismicity (D_{95}) for the Bay Area	51

3.10	Surface creep rate on the Hayward fault – observations and block model results . . .	53
3.11	Residual velocity and best-fit slip rates for three different model geometries . . .	55
3.12	Residual velocity for multiple model variations	56
3.13	Profiles of GPS velocities along profiles perpendicular to the San Andreas fault system	60
3.14	Effect of profile orientation on fault-perpendicular profiles	61
3.15	Map view of small-circle orientation of PA-NA and PA-SNGV relative motion . .	63
3.16	Orientation of faults compared to orientation of PA-SNGV relative motion over geologic time	66
3.17	Model misfit v. locking depth for the preferred geometry	69
4.1	Typical temperature vs. time histories calculated for different distances away from a fault	82
4.2	Location of samples along San Gabriel fault in southern California	84
4.3	Apatite fission-track age as a function of distance from San Gabriel fault	86
4.4	Fission-track length distributions for select samples	86
4.5	Forward modeling of thermal history of samples 8b-2 and 8f-2	87
4.6	Constraints on maximum value of apparent coefficient of friction	88
5.1	Simplified tectonic map of central California with Salinian granitic bodies and geologic map for the SAFOD site near Parkfield	95
5.2	Apatite fission track and (U-Th)/He ages plotted with respect to depth and temperature for the SAFOD Pilot Hole	96
5.3	Modeled thermal histories for samples CU4800 and CU5100	98
6.1	Predicted surface heat flow for a single, vertical, rectangular fault patch of various sizes	109
6.2	Temporal Evolution of heat flow on a finite fault patch	110
6.3	Comparison between 2-D and 3-D models	111
6.4	Heat flow distribution for a single moving asperity	113
6.5	Heat flow distribution for for a single asperity at different slip rates.	114
6.6	Heat flow distribution for multiple asperities	115
6.7	Location map and heat flow near the creeping section of the San Andreas fault .	117
6.8	Different models for how the length and position of the creeping section could have evolved over time	118

6.9	Creeping section heat flow distribution for various models	120
6.10	Creeping section heat flow models as a function of distance along strike	121
6.11	Comparison of heat flow observations and models	124

List of Tables

1.1	Thesis chapters in relation to the concept map of Fig. 1.1.	8
3.1	Global GPS stations included in modeling of stable North America and Pacific plates.	31
3.2	Definition of model geometry	39
3.3	Model name abbreviation key	40
3.4	Misfit statistics for different models. Note that TwoPlate excludes all data within 100 km of the plate boundary.	46
3.5	Vectors representing axes of relative rotation from various studies.	74
3.5	(continued) Vectors representing axes of relative rotation from various studies . .	75
3.6	Predicted velocity at the Farallon Islands in a stable North America reference frame	76
3.7	Comparison of strike-slip rates for geologic estimates and this study	77
3.8	Tensile slip rates	78
3.9	Shallow strike-slip creep rates	79
4.1	Apatite Fission Track Analyses - San Gabriel Fault	90
4.2	Measured track lengths for all samples	92
5.1	SAFOD Pilot Hole Summary of Observations	100
5.2	Apatite Fission Track Analyses - SAFOD Pilot Hole	101
5.3	Fission Track Length Analysis Details	102
5.4	Summary of thermal histories determined for the SAFOD Pilot Hole	103
6.1	Variable values for reference model	108
6.2	Variables and meanings	127

Acknowledgements

Lo alecha ham'lacha ligmor, V'lo atah ven chorin l'hibateil mi-menah.

It is not for you to complete the work, but neither are you free to desist from it.

– *Pirkei Avot 2:21*

(The Book of Principles from the Mishnah, a third century Jewish text)

This dissertation is not a completed work. Like most science, it probably raises more questions that it answers. It is a progress report on my own work and on the work of so many scientists before me, and represents my best effort to make a contribution to the scientific community. In that sense, it serves as a microcosm for the broader goals that I strive to achieve in my my life. While the individual chapters give proper acknowledgment to the scientific advances that I build upon, this section is my chance to share my gratitude for the contributions people have made to this dissertation work and my broader life up to this point. Rarely is one give the opportunity to reflect on the people that have made these contributions, so I intend to take full advantage of the moment.

I begin by thanking some of the people around me that provided essential logistical support for my time in graduate school. The talented and professional staff of the Berkeley Seismological Laboratory always ran a tight ship where things got done efficiently, and more importantly, they got them done right. Eleanor Blair and Myriam Cotton always had a smile for me when we passed in the halls, they always were understanding when I made mistakes that caused them more work, and they always made sure that I got paid. I want to particularly thank Christina Jordan for her ever-friendly smile as she took over 150 pounds of rock from me to be shipped across the country just two weeks before Christmas. I hope the folks at FEDEX were equally cheerful! Charley Paff, Doug Neuhauser, and Pete Lombard always managed to keep the computers running. I can't even count the number of times they were on campus overnight, working behind the scenes during a hacker invasion or disk crisis. Lind Gee and Rick McKenzie helped direct the BSL's outreach efforts, bringing in a constant stream of youngsters to re-energize me about earthquake science. There's nothing quite like having 20 fourth graders jumping up and down trying to make an earthquake to make you realize how exciting earth science really is. Mark Murray provided outstanding technical support as I struggled through GPS processing. I thank Barbara Romanowicz and the BSL students and staff members for creating a friendly and close knit community that welcomed me and answered my steady flow of naive questions about seismology. Staff at the Berkeley Geochronology Center, including Paul Renne and Warren Sharp, provided valuable feedback during the early stages of my career as a budding thermochronologist. Future conversations with Ken Farley and Danny Stockli, and Lisa Gilley furthered these efforts. Early conversations with Art Lachenbruch, Colin Williams, and Tom Hanks at the U.S. Geological Survey helped advance my appreciation of the richness of the fault strength problem. My dissertation committee members Douglas Dreger and Stephen Mahin provided valuable comments on this dissertation. Professor David Pollard, my undergraduate advisor, helped me in the right direction as I began my journey into the world of earth science.

I thank my advisor, Roland Bürgmann, for providing me the motivation, guidance and resources to do exciting science. When I first arrived at Berkeley, Roland handed me three separate, fully-funded proposals in which I could become involved. They were projects that included extensive field work in California, Nepal, and beyond. He said he was willing to be flexible to allow me to tailor them to fit my interests. After a few weeks of reading and preliminary work in a few different directions, I took him up on the latter half of his offer, and chose option *four*. We worked together to come up with a new idea to explore the interesting and exciting topic of frictionally generated heat along faults. The physics of friction and heat flow are so simple and fundamental that an introductory background in physics gave me all of the tools I needed to explore them. But at the same time, when these concepts were applied to the real Earth, they became so rich and so complex that they represented the keys to understanding earthquakes. Roland made sure I had the resources to explore this new project idea, he helped me obtain funding, and he seemed as excited as I was to explore this new aspect of fault science. His enthusiasm along with his total support of me as a young scientist resulted in the last three chapters of this thesis and the basis for my upcoming postdoctoral research. And, I should note that work from one of the original three proposals he gave me comprises Chapter 3 of this dissertation, so I didn't completely neglect his original ideas! Roland has been patient during times when I didn't seem focused, encouraging when I was struggling with new problems, and a role model as he achieved an impressive balance between a rich scientific research program and a growing family.

As part of my early exploration on my frictional heat project, I went into the field in the San Gabriel mountains to view some excellent examples of exhumed fault systems. Roland had recently seen a presentation by Ann Blythe describing the thermal history of the region. So, off I headed down to southern California in a rented pickup truck to see the faults and meet with Dr. Blythe. I met with Ann at a coffee shop near her house and told her about some of the ideas Roland and I had about using fission track thermochronology to look at frictional heat. She was interested and encouraging. She then asked, "who is doing your fission track work?" I replied that we hadn't gotten that far. What followed was one of the fundamental turning points in my doctoral work. Ann offered to run five samples for us for free. Excited about the prospect, I drove off into the mountains to collect samples. The next few days were filled with adventure, including 1) getting my truck stuck and walking to a nearby back-country fire station, only to have a U.S. Forest Service "Hot Shot Team" come to bail me out; 2) taking a wrong turn and accidentally climbing 5000 vertical feet on a single-lane dirt road, only to turn around and go right back down again; 3) realizing that the dashed line on a field guide was meant to indicate the arbitrary path the author used to travel through the dense shrubs down a steep ravine, and was not an established, marked, or maintained trail; 4) hiking too close to a hawk's nest while in that ravine, only to be chased by the mother hawk who shrieked and dive bombed me as I fled in terror; 5) while fleeing from the talons of the diving hawk, reaching the top of a dry waterfall with a 10 meter drop-off, and then deciding to use the previously mentioned field guide as a mechanism to protect my behind as I slid down the rock face; and finally, 6) collecting some really interesting samples that form the basis for Chapter 4 of this dissertation. Ann's generous offer of 5 free samples became 10, ten became 30, and 30 became 60. Somewhere along the way, we started writing collaborative proposals so that we could both get paid. Ann's cheerful attitude along with her careful and meticulous work made our collaboration a true joy. For example, faced with an impending deadline, Ann managed

to move into a new house, take care of her 4-year old, and work with Roland and I to write a paper in four days flat without seeming the slightest bit flustered. I am very proud of the way that we all worked together on that paper to present a clear and interesting story. The work, presented in Chapter 5 of this dissertation, was a true collaborative effort and is so much better than any one of us could have created alone.

Another collaboration that led to amazing field excursions involved a Stephen Martel as a mentor and field partner. Steve taught me how to be a good field geologist, a good modeler, and a good thinker. We spent many an evening hiding inside the confines of his tent to avoid the killer mosquitos at Bear Creek, chatting about everything from life plans to world events and politics. We faced constant battles with hail, snow, marmots, and the inevitable setting of the sun. Steve taught me that this job is not just about the geology. It's about the people, the place, and the experience. I consider Steve a great colleague and friend, and I am happy that we had the opportunity to work together. Chapter 1 is representative of the work we did together in some of the most spectacular landscapes on the planet – in what Steve referred to as “God’s country.” If you’ve ever been to the John Muir Wilderness, you know what he means.

I am so happy that some of my best friends from high school continue to be there for me. These include Ori Neidich, Steve Flores, Sam Schaevitz, Chip Dietrich, Adam Sager, and Josh Klein. My good friends from college, Rob Baesman, Nicholas Solter, Alex Osipovich, Judy Liebman, and Brad Daniels, Melissa Mills, and the Geo Buddies, were never more than a phone call away when I needed support or encouragement. When I arrived at McCone Hall as a new Ph.D. student, I was instantly introduced to a wonderful community of graduate students in our department. Among these were my office-mates Kanani Lee and Helge Gonnerman, my former apartment-mate Sofia Akber (who is responsible for Loraine coming into my life), and the entering class of fellow first years. My research group has always been a vibrant combination of people, including fellow students David Schmidt, Ingrid Johanson, Dennis Templeton, and Edwin “Trey” Apel and postdocs Frederique Rolandone, Andy Freed, George Hilley, and Evelyn Price. Group lunch, an amazing spirit of helping one another, fun excursions in the field, and valuable feedback on active research were just part of what made our group a cohesive and wonderful team. In addition to my friends within our department, a number of new friends emerged from my time at Berkeley, including Michael Wood-Vasey, Alysia Marino, Elaine Musgrave, Dave Petterson, Dan Enemark, Abby Fuller, Julie Morphee, David Gibson, Morgan Ames, and Whit Myers. We managed to dance on Wednesday nights, take hikes on Valentine’s Day, relax at dinner parties, commiserate about the challenges of graduate school, or just talk until late into the evening about the meaning of life itself.

Home is where the heart is, and my home has always been a loving place. To begin with, I would like to thank, in alphabetical order, Airplane Bear, Big Black Bear, Black Bear, Brown Bear, Lily Bear, Paddles Bear, Seal Bear, and Turtle Bear for their constant cuteness and unconditional love. Mrs. Hummingbird and her two newborns visited me frequently at the window outside my desk at home, and the Cooper’s Hawk family provided hours of fascination as they built their own home outside my office window. Together, they helped make Cottage truly feel like home while I was in graduate school.

My family goes back five generations in California on both sides, so having a loving and supportive family around has always been an important part of my life. I know that a wonderful

combination of aunts, uncles, cousins, and my new family-in-law are all cheering for me as I submit this dissertation, and I thank them for that.

My parents always wanted me to be a doctor. While they might have preferred it if I had been the type of doctor where I fixed people rather than crushed rocks, they supported me at every step by telling me to do whatever makes me happiest. One could argue that my love of Geology is actually very much their own fault (no pun intended). My love of science began early on as my mother volunteered at my preschool teaching science classes (often involving fruit and other treats). As I got a bit older, she went back to school to pursue her own degree in science. In addition to tackling the horrors of chemistry class, she managed to study flash cards with her own fascinating sketches of marine invertebrates while making dinner each night. As a family, we took hikes, went camping, and even had a few very memorable backpacking trips. I have to say I've come a long way from carrying a tiny little backpack with my "blankey" and asking "are we there yet?" every ten minutes. Now, I relish the fact that I get paid to go backpacking in the beautiful outdoors that they taught me to appreciate. My parents also instilled an essential value that I have tried to maintain throughout my education – 'always remember to give back.' They never explicitly said that phrase to me, but it is immediately apparent when you look at their actions. My mother founded a grass-roots organization to protect our local creek system. My father has always been generous with his time and energy, and his most recent step is truly amazing. He left his high-powered business job to work at a non-profit organization devoted to helping troubled, at-risk children get a second (or third) chance. His decision to put his talents to work for people that really need help makes me very proud. I thank both my parents for believing in me, and constantly giving me something to believe in.

It wasn't too long ago that my brother was a rebellious teenager and we were at each other's throats. Though it wasn't until recently that Brad and I became good friends ourselves, he has always shown me the value of friendship. He is generous and always there for his friends. Growing up and seeing this has served as an inspiration to me. Another great thing that I have learned from my brother is persistence. He never gives up, and sticks with things that he knows are right. This drive has allowed him to follow his dreams, even if the dream takes him far from his friends and far from home. That takes a lot of courage, and I thank him for demonstrating it. His persistence served as a model for me as I battled with this dissertation over the last few years.

I was also lucky enough to grow up near my grandparents, each of whom made an impact on my life. My Grandma Vicky was confined to a wheelchair after contracting polio when my father was young. Despite the challenges that life gave her, I always remember her as cheerful and loving. I remember how much she loved swimming with her grandchildren, and how she taught us to play cards. I remember that she liked to write stories, which inspired me to try writing a few on an old typewriter when I was young – a skill that became very important as I did a whole lot of typing to create this dissertation. I am also thankful that my Aunt Barbara, who reminds me so much of my grandmother, inherited every ounce of Grandma Vicky's capacity to love and continues where my grandmother left off. My Grandpa 'D' ('D' for d'Alessio) believed in education. He was always very direct about telling us what was important, and getting an education was a vital part of it. Writing this dissertation is in part a tribute to him and all he taught us. I remember visiting the library at U.C. Berkeley when I was in high school, about

two years after Grandpa died. I thought that it would be fun to search for how many entries the library had under the name “d’Alessio.” I didn’t expect to find much, so I was completely astonished to find my grandfather’s name listed among them. My grandpa, who I really admired and really missed, was alive in the institutional memory of the University by way of his Masters thesis from 1934. In a sense, he had been written into the Book of Life for all eternity. I hope my thesis will be shelved right next to his work on, “State regulation of insurance rates: a study of rate supervision of fire and casualty insurance in the United States.” Encountering his thesis several years ago is certainly the reason that these acknowledgments are so lengthy as I leave behind my own record for future discovery. My other grandfather, Grandpa ‘A’ (‘A’ for Arthur) was also very enthusiastic about learning. I remember he knew pieces of seven or more different languages. I have fond memories of him listening to tapes of Jazz, some of it dating back to the time that he swept my grandmother off her feet and they put a wedding together in 9 days before he shipped out to sea again in the Pacific campaign of WWII. He was an attorney and worked for a time on cases with prisoners at San Quentin, a place that I taught Geology and Math as a volunteer during graduate school. Grandpa was diagnosed with cancer when I was young, but he fought it for over a decade – outliving even the most optimistic predictions. He eventually went into estate law, and I remember him saying that he wanted to outlive his clients so that he could do what they had asked him to do. He was working up until the night he died. Like each of my grandparents, Grandpa A taught me to value life and to have the courage to fight for it. However, what I remember most about Grandpa A was his pictures. I loved it when he got out the slide projector and showed me pictures from his and Grandma’s world travels to Israel, Egypt, Greece, and Scandinavia. I not only inherited Grandpa’s camera and slide projector, but I also inherited his love for capturing these moments on film and sharing them with others. His camera and his appreciation of the beauty around him have served me well for photographing geology throughout my graduate school career. Last, but not least, I would like to thank my Grandma Lenee. Grandma was the only grandparent around to meet Loraine and to be present at our wedding. While I have lots of memories of her from when I was young – baking lace cookies, running around her apartment – a lot of what I will remember of her has to do with her last few months. Grandma waited until after my wedding to have a crucial operation. The recovery took several months, and it was hard for her to get back on her feet. Loraine and I visited her every weekend during that time, and it provided an opportunity for us all to share some very tough times. A lot of the time Grandma was too tired to talk, so sometimes I just talked to her while she listened and sometimes we just sat there together. I think Grandma was afraid, but she was a fighter. She was facing some very big issues about life and death, and one time she started crying while I was there with her. I wanted to tell her something that would make her feel better. When struggling for the right words or idea to help her get through, I realized something that has become very important for me to know. I realized that it is O.K. to be afraid. I told her about the first time I went into the field alone, and how I got chased by an angry mother hawk. I told her that I was afraid during that whole experience, but it was alright to feel that way sometimes. Knowing that it is alright to be afraid has enabled me to try things that I never would have dared to attempt. The other thing I told her that day was that after the whole ordeal with the hawk and sliding down the dry waterfall, I got an ice cream cone, and that made everything seem instantly better. She smiled for the first time in days. I went and got us ice cream which we ate together, savoring the cool treat. Which brings me to the most important lesson that Grandma taught me. More than anybody

else I have ever met, Grandma knew how to appreciate things. I remember sitting beside her on a bench overlooking Pinecrest Lake. My feet were too short to reach the ground, so they just dangled there on a summer day. While many people read, swam, hiked, or fished, Grandma could just sit there, soaking in the beauty. From her, I learned that the highest form of prayer and the key to happiness itself is to appreciate what you have and all that is around you. This is a message that I hope will continue to guide my life on each new journey to come.

The last person that I would like to thank is the most recent addition to my family, my unbelievably wonderful wife, Loraine Lundquist. I met Loraine on a camping trip within 3 weeks of arriving at Berkeley for graduate school. We got lost together on a hiking trip up Reverse Peak in Long Valley, and the rest, as they say, is history. In the words of Louis Armstrong, I am so happy that I met and married my “Sweet Loraine.” In our ketubah, the Jewish marriage contract, Loraine and I promised to support one another through difficult times. I am thankful for her love and support. Graduate school hasn’t always been easy for either one of us, and I am so happy that we have had one another throughout the process. Loraine has done everything from helping me derive equations to reminding me that the end is in sight. We also promised to celebrate life’s joy together, and we do that constantly. We celebrate a well-cooked meal by clinking our forks together. We celebrate the end of a week by having a relaxing Friday evening together. We celebrated one year of wedded bliss with a trip to Hawaii and a second year with a trip to Yellowstone (with travel funds provided in part by my field work and her conference travel, respectively). Having now made it through wedding planning and a dissertation, I am convinced that our honeymoon will never end.

Curriculum Vitæ

Matthew Adam d'Alessio

Education

1999	Stanford University B.S., Geological and Environmental Sciences
2004	University of California Berkeley Ph.D., Geology

Biographical Sketch

Born August 4, 1977, Marin County, California

Matt grew up in the Bay Area, and was home alone during the 1989 Loma Prieta Earthquake reading his middle school earth science textbook. Though he was traumatized at the time, he quickly forgot about earth science until his sophomore year in college when his introductory Geology class at Stanford University was the first class that required him to go to the beach. He majored in Geological and Environmental Sciences with a focus on Engineering Geology and Hydrogeology. He became involved in undergraduate research mapping faults with GPS, and eventually went on to graduate school at U.C. Berkeley, where he has spent the past 5 years working on his Ph.D. in Geology. He is interested in a broad range of problems in the science of earthquake faults, including the effects of fault geometry on fault behavior, frictional heat generation along faults, and surface deformation related to the earthquake cycle. Other earth science highlights include working as an intern for Geomatrix Consultants doing geologic hazard assessment for major civic projects, appearing in a PBS special on earthquakes, and teaching mathematics and earth science to inmates at San Quentin State Prison. He is also the third generation in his family to receive a degree from both Stanford and U.C. Berkeley. He also became the third generation to marry a U.C. Berkeley graduate when he married Loraine Louise Lundquist on July 20, 2002.

Chapter 1

Introduction

In its simplest definition, a fault is a fracture separating two blocks of crust that slide past one another. With sliding comes friction. The combination of this simple picture with the mechanical properties of the fault and surrounding crustal blocks provides a strong base for exploring factors that control the behavior of faults. In one sense, faults live and die by their frictional properties. Friction determines how and when a fault slips, how faults interact with each other, and influences fault geometry. Frictional strength affects heat production, deformation, and stresses in the rocks around faults. If our goal is to determine when, where, and how much a fault will slip, we need to know what factors control that behavior. To first order, friction helps answer all these questions. The simplest earthquake prediction is that a fault will slip when tectonic stresses exceed the frictional strength of the “weakest patch” of fault. To produce a more specific description of earthquake behavior, we need to quantify the rate of stress accumulation, the frictional strength of faults, and other factors that may influence these quantities. In this dissertation, I focus on understanding the role of fault geometry, kinematics, and frictional properties in controlling the thermal and mechanical behavior of faults. Several of these properties and processes are interdependent, with complex feedbacks (Fig. 1.1). Different chapters of this thesis explore different parts of this system. Chapters 2 and 3 focus on the kinematic and mechanical aspects of fault behavior, while the last three chapters emphasize the inter-relationship between fault friction, fault slip, and frictional heat generation. In this chapter, I describe the conceptual framework that ties these chapters together, but I leave most of the historical background and details to the individual chapters.

1.1 The Earthquake Cycle

A simple illustration of a fault and its behavior over time (Fig 1.2) forms the framework for much of my analysis. This illustration shows three stages of what is known as the “earthquake cycle” [see Chapter 5 of *Scholz, 2002*]. Figure 1.2a shows a fault and crustal blocks at the

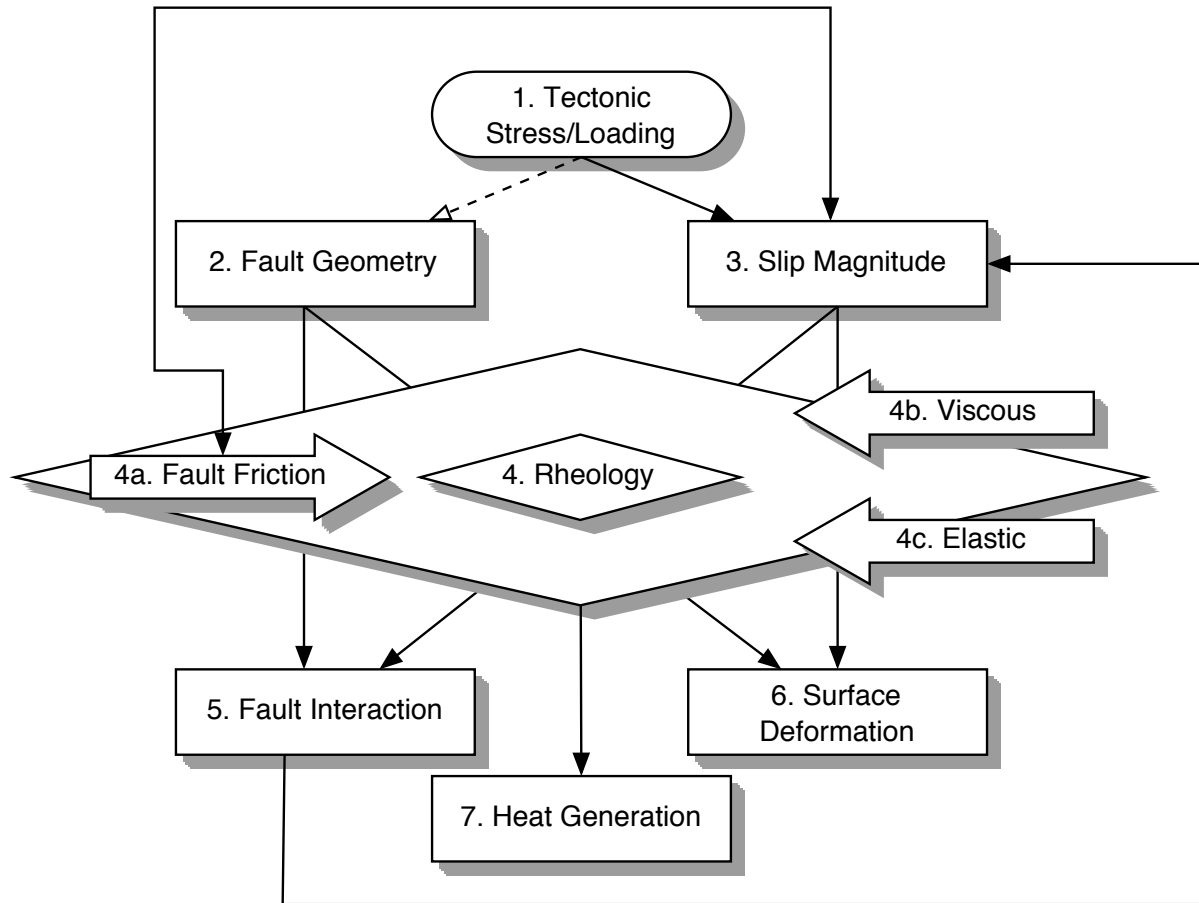


Figure 1.1. The thermal and mechanical behavior of faults is complex, with a number of interconnected properties and processes controlling fault behavior. Numbers are for reference in Table 1.1.

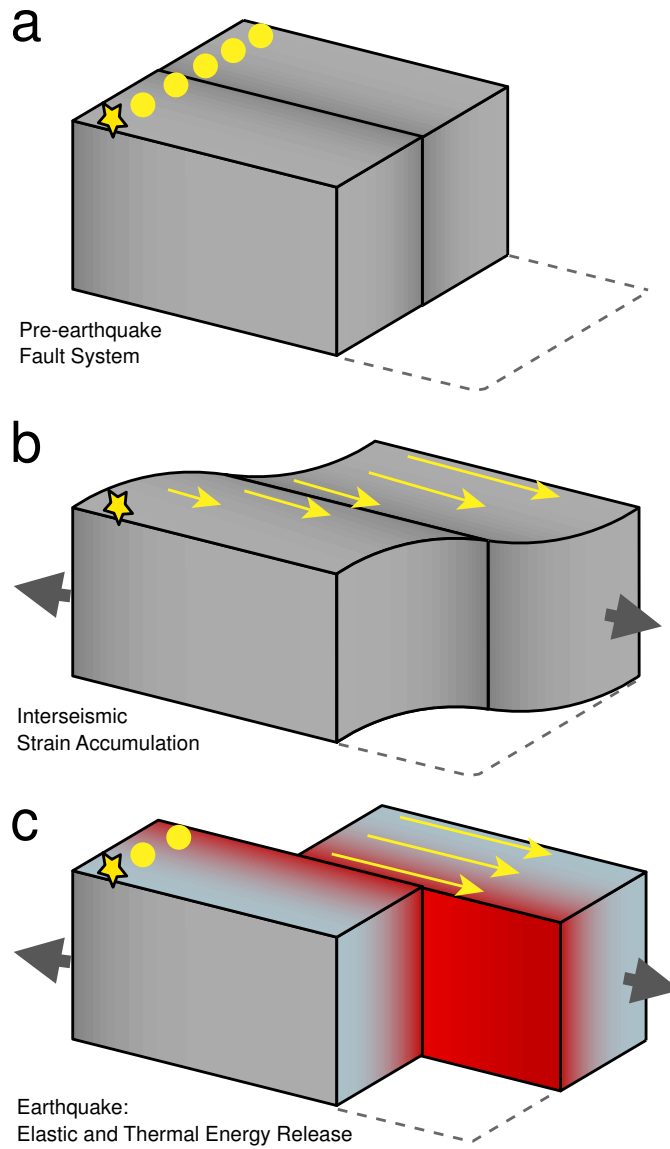


Figure 1.2. Stages of the earthquake cycle. a) Initial fault geometry before any large earthquakes; b) application of tectonic forces and elastic strain accumulation; c) earthquake slip causing the release of elastic energy, which is then converted into primarily thermal energy.

beginning stage of the cycle. Before any earthquakes have occurred on this fault, the crustal blocks are in thermal equilibrium with the mantle and atmosphere, and gravity exerts the only force in the system.

With the application of tectonic forces (Fig. 1.2b), the system begins to deform. Because stress on the fault plane is lower than the frictional strength of the fault, the fault remains locked near the surface and deformation must be accommodated in the surrounding blocks. While there are several conceptual models of how strain is accommodated that include viscous flow and permanent deformation that have variable properties in the surrounding blocks, in this dissertation I focus entirely on blocks that behave purely elastically and are homogeneous throughout. This is an oversimplification and a limitation of the analysis, but is a necessary step to investigate the effect of a few individual variables. The time period during which elastic strain accumulates is referred to as the “interseismic” period and can last from years to millennia.

Eventually, the stress exceeds the static frictional strength of the fault and the fault slips in an earthquake (Fig. 1.2c). The amount of fault slip is a function of the amount of elastic strain in the surrounding blocks. The movement of the blocks releases the elastic strain, which is converted to mechanical and thermal energy by breaking apart rock fragments, producing seismic waves, and generating frictional heat. For faults that have a component of vertical displacement, additional work is done against gravity to raise one side of the fault up, but in this dissertation I focus almost entirely on strike-slip faults where motion primarily horizontal.

Kanamori and Brodsky [2001] refer to earthquakes as primarily “thermal events” because the majority of earthquake energy is believed to be converted into frictional heat. This observation is supported by both laboratory [*Lockner and Okubo*, 1983] and seismic observations [*McGarr*, 1999]. Despite this distribution of energy, few investigators have explored the thermal behavior of faults compared to the more commonly studied seismic waves. Because frictionally generated heat is a very direct way to investigate the frictional properties of faults, I focus entirely on the thermal energy sink.

After the fault has relieved elastic strain, the earthquake cycle begins again. Through repeated slip events, blocks can be displaced hundreds of kilometers by active faults. This overall picture of the earthquake cycle is overly simplistic. In the following sections, I describe how the chapters of this dissertation address more realistic fault behavior at different stages of this cycle.

1.2 Key Concept: Fault Geometry

Figure 1.2a shows two blocks of rock separated by a fault plane. This geometry is highly idealized, and natural faults can have substantially more complicated shapes in all three dimensions. Faults have curves, bends, steps, branches, and other discontinuities. These features allow continuous networks of faults or “fault systems” to form with complicated geometries.

While fault geometry and geometric complexity of fault systems enter into all of the chapters, I explore them most directly in the Chapters 2 and 3. In **Chapter 2**, I focus on the

questions of where, how, and why faults terminate. This chapter, based on my published work in *d'Alessio and Martel* [2004b], is a collaborative project with Stephen Martel at the University of Hawaii. It emphasizes the important role that fault interaction plays in controlling fault behavior. The ability of faults to interact depends strongly on their geometry. I present a field example of the termination of an ancient and inactive fault in the Sierra Nevada mountains of California. This fault was once several kilometers below the surface while it was active, but has since been exhumed via uplift and erosion. A thorough examination of exhumed faults provides a glimpse into faults at all scales from aerial photos to thin sections, a range that is simply not possible for active faults at seismogenic depths. Interpretation of exhumed fault behavior requires inferences about the conditions at the time of faulting, but exhumed faults can be powerful analogs to today's active faults. For example, Fig. 1.3 shows the geometry of an exhumed fault in the Sierra Nevada compared with the geometry of the San Andreas fault system (after *d'Alessio and Martel* [2004a]). Many of the geometric relationships from the active fault system are also present in this exhumed fault. For the field example in Chapter 2, I use a 2-D elastic model to show that the observed slip magnitude on dozens of small faults near the termination of a large fault system is controlled by their geometry relative to the larger structure, and that interaction between all these features could have caused the fault to stop growing and terminate.

Like fault terminations, another important geometric feature of faults is the connections between them. Physical connection of adjacent faults as well as stress transfer through an elastic medium allow faults to interact and affects the magnitude and distribution of slip [*Bürgmann et al.*, 1994b] and the ability for faults to rupture in a large earthquake [*Harris and Day*, 1999]. Part of the goal of **Chapter 3** is to evaluate the possible connections between faults in the San Francisco Bay Area. Unlike the field example from the previous chapter, it is not possible to directly quantify the amount of slip on individual faults in the system at depth. Instead, I collected and compiled a data set of surface deformation observations derived from the Global Positioning System (GPS). This data set represents the most detailed picture of crustal deformation in the Bay Area ever achieved and includes the velocities of over 200 stations in the Bay Area during 1993-2003, a time of relatively constant strain accumulation and no large earthquakes. In the idealized conceptual model of faulting in Fig. 1.2b, these data are represented by the arrows along the surface showing a deformation gradient across the fault. I use a 3-D kinematic "block" model calculate the long-term deep slip rates of Bay Area faults from the pattern of surface deformation related to elastic strain accumulation. These slip rates can provide input for seismic hazard analysis [e.g., *Working Group on Northern California Earthquake Probabilities*, 2003]. The modeling technique also allows me to test the hypotheses about the way some Bay Area faults are connected – these connections are hotly debated and have important implications about the distribution of slip (and thus seismic hazard) in the region. In Chapter 3, I demonstrate the importance of knowing the geometry of an active fault as well as challenges in defining that geometry, and how that geometry originated.

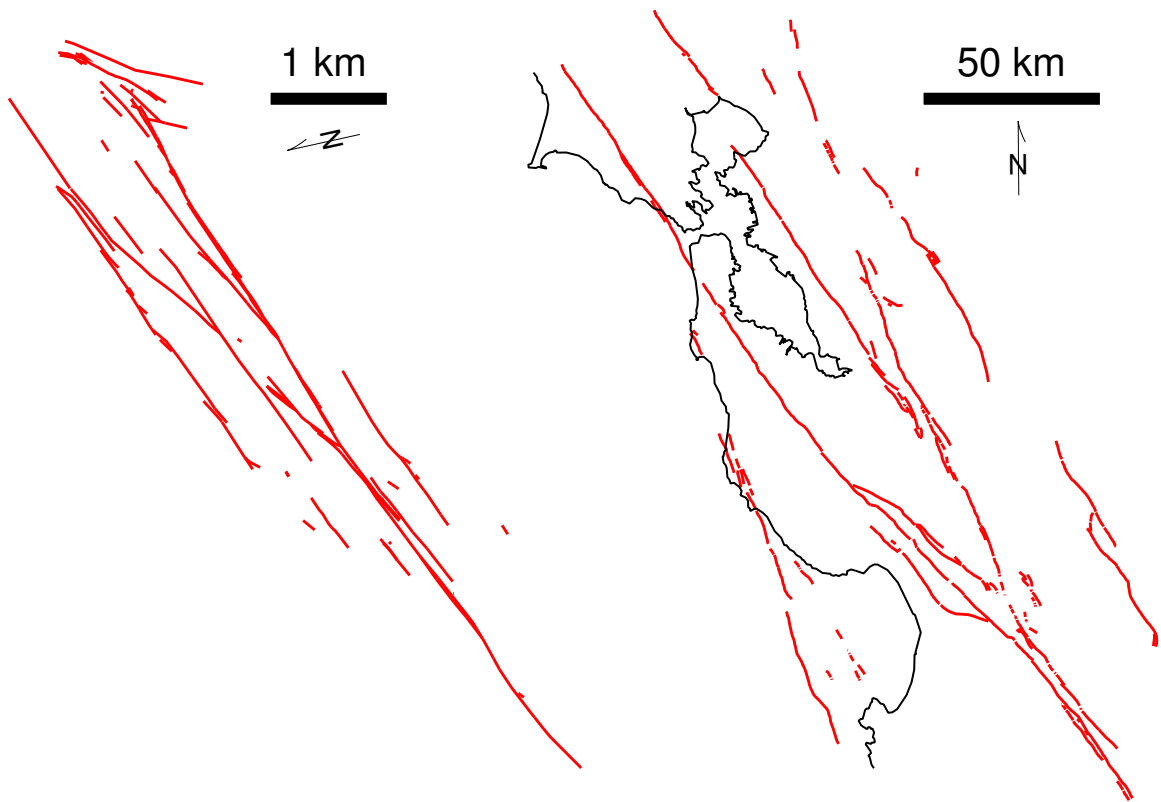


Figure 1.3. Geometry of a fault in the Sierra Nevada mountains compared with geometry of the San Andreas fault system in the Bay Area. The Pear Lake fault system (left) is a 7 km long left-lateral strike-slip fault in jointed granitic rock. After *d'Alessio and Martel* [2004a].

1.3 Key Concept:

Frictionally Generated Heat

Despite the crucial role of fault friction in controlling fault behavior, there is a fundamental debate about the strength of natural faults. According to studies using a variety of techniques, natural faults appear to be nearly an order of magnitude weaker than faults simulated in the laboratory. A debate has raged for three decades over the validity of the measurements of the frictional strength of natural faults versus the possible mechanisms that might cause the apparent discrepancy. The introductions to Chapters 4 and 6 describe the specifics of this debate in more detail. In Chapters 4-6, we focus on frictional heat with the aim of providing independent constraints on the strength of natural faults, with the goal of resolving this debate.

Frictional heat is generated during each individual earthquake, and the amount of heat is directly related to the amount of slip in the earthquake and the frictional stress resisting motion. While a number of theoretical papers have been written estimating the amount of heat that should be generated in individual earthquake events, very few measurements have ever been made because of the complete lack of thermal observations along active fault zones at depths within the seismogenic zone. In **Chapter 4**, I present a new technique for quantifying the amount of frictional heat along exhumed fault zones using thermochronology. This chapter is based on my published work in *d'Alessio et al.* [2003], a collaborative project with Ann Blythe at the University of Southern California. Radiometric dating techniques have long been used to determine the timing of different cooling events (such as the age of a pluton intrusion or the timing of exhumation related to a mountain-building episode), but I use the same techniques to quantify localized heating along an ancient and abandoned trace of the San Gabriel fault in southern California. The constraint described in Chapter 4 is one of the most direct estimates of the frictional strength of a natural fault ever determined.

There is currently an effort underway to collect a suite of measurements from seismogenic depths along the active San Andreas fault at Parkfield, California. The San Andreas Observatory at Depth (SAFOD) will provide the first thermal measurements from an active fault at depths of up to 4 km. These measurements, along with additional contributions from thermochronology like we describe in the previous chapter, will provide us unprecedented detail into frictional heat generation along an active fault. Drilling is underway during 2004-2005. In **Chapter 5**, I present essential measurements on the long-term thermal history of the area derived from samples collected in the 2.1 km deep SAFOD Pilot Hole drilled in 2002. This work is based on further collaboration with Ann Blythe reported in our publication *Blythe et al.* [2004]. My modeling of thermochronologic data from the Pilot Hole constrains the baseline thermal history of the region, allowing future observations to be collected in the fault crossing boreholes to be interpreted in a rich geologic context.

One of the key concerns about any single constraint on the frictional strength of faults like those described in Chapters 4 and 5 is that they represent point-measurements along a fault that is likely to have a complex, heterogeneous frictional strength distribution. In **Chapter 6**, I explore the theoretical implications of frictional strength heterogeneity. Most previous descriptions of frictional heating at all scales assume that faults extend infinitely along strike and have homogeneous frictional strength along this entire extent. These models are used to

infer the strength of faults from thermal observations. I show that the predicted heat flow distribution from faults with heterogeneous friction is very different than the heat flow for homogeneous faults. I then present the theoretical predictions for an example of a known frictional heterogeneity along the creeping section of the San Andreas fault near Parkfield, California (near the SAFOD drill site) and compare these to existing thermal observations.

1.4 Relationships and Feedbacks

I show one representation of the complex interrelationship between different properties controlling fault behavior in Fig. 1.1. Table 1.1 shows how each of chapter of the thesis relates to this concept map.

Table 1.1. Thesis chapters in relation to the concept map of Fig. 1.1.

Chapter	Concepts	Topic
2	1-2-4c-5-3	Interaction between faults forms a barrier to fault growth
3	1-2,3-4c-6	Strain accumulation in the San Francisco Bay Area
4	1-3-4a-7	Localized heat generation along the San Gabriel fault
5	1-3-4-6,7	The long-term thermal evolution of the Salinian Block at Parkfield, CA
6	1-3-4a-7	Effect of frictional heterogeneity on surface heat flow

Chapter 2

Fault terminations and barriers to fault growth

2.1 ABSTRACT

Field observations of strike slip faults in jointed granitic rocks of the central Sierra Nevada, California, combined with a mechanical analysis of fault interaction, provide insight into how fault terminations vary with scale. We document here a strike-slip fault system 2-3 km long. Clustered about the west end of the fault system are several dozen faults that parallel the three main fault zones in the system. We interpret this cluster of small faults as a barrier that inhibited growth of fault zones in the fault system. A two-dimensional mechanical analysis shows that a cluster of small faults flanking the tip of a large fault zone will tend to diffuse the stress concentration near the fault zone tip – an analogous effect in engineering is known as crack-tip shielding. Near-tip stress concentrations promote fault growth, and processes that decrease these stress concentrations inhibit fault growth. As faults lengthen and grow, they interact with features at greater distances and over a broader area, so the potential for tip shielding effects will increase as fault length increases. This effect can account for why the mechanisms and character of fault terminations would tend to vary as a function of scale.

2.2 Introduction

Although recent studies at various scales address how faults nucleate and grow, few have addressed the equally fundamental issue of how faults terminate. These issues are all important if we are to better understand the faulting process, for fault growth and fault termination are

inextricably intertwined; the mechanisms by which faults grow will determine what factors can cause them to terminate.

Geologists recognize two main ways that faults grow in brittle crystalline rock: (1) propagation by shear fracture of the host rock (Fig. 2.1A); and (2) linkage of fault segments that originate as planes of preexisting weaknesses (Fig. 2.1B). In the first mechanism, faults grow by the development of a “process zone” where microfractures forming near the fault tip eventually coalesce into a through-going fault [e.g., *Cowie and Scholz*, 1992; *Anders and Wiltschko*, 1994; *Scholz et al.*, 1993]. The microfractures form as a result of the fault-tip stress concentration, which must be high enough to fracture the rock for the fault to propagate. This stress concentration migrates with the fault tip and fractures formed to the side of the fault tip are left behind as the tip propagates [e.g., *Vermilye and Scholz*, 1998], resulting in a fault flanked by a wake of smaller fractures. Where weak preexisting structures such as joints or bedding planes exist, faults can form and grow by exploiting them (the second mechanism). As slip nucleates on a preexisting structure, stress concentrations in the host rock can remain low until the region of slip reaches the termination of the structure [*Martel and Pollard*, 1989]. High stress concentrations confined to the fault tip commonly result in fracturing localized near the fault tip rather than everywhere along the fault. The fractures allow a fault to grow by linking with neighboring faults fracture [*Segall and Pollard*, 1983]. A fault growing by segment linkage would likely terminate either where no nearby segments exist to link to, or where it reaches a heterogeneity or structure that inhibits linkage. This paper addresses both growth mechanisms but focuses primarily on a field example of faults growing by segment linkage.

Fracturing near the ends of faults is common and is a widespread process for linking faults. Fault-end fractures are particularly well documented for small faults, faults with traces no longer than several tens of meters [e.g., *Moore*, 1963; *Segall and Pollard*, 1980, 1983; *Granier*, 1985]. At these terminations, high near-tip stresses commonly result in the creation of opening-mode fractures oriented at 15°- 35° angles oblique to the fault that are termed “tail cracks” (e.g., Fig. 2.2A). Tail cracks are reproduced in laboratory experiments where a plate with a precut fracture is sheared [*Brace and Bombalakis*, 1963], and their orientation can be predicted by continuum mechanics theory (Martel, 1997). Simple scaling arguments indicate that the length of tail cracks should be proportional to fault length and fault slip, provided that the region of non-elastic deformation near the end of a fault is small relative to the fault length (Pollard and Segall, 1987). Tail cracks commonly are observed at the ends of small faults (Fig. 2.2A) and at linkages between small faults, but the ends of longer faults (Fig. 2.2B, 2C) appear to be zones of significantly more complex deformation [e.g., *Bayasgalan et al.*, 1999; *Storti et al.*, 2001; *Pachell and Evans*, 2002]. Scale thus appears to affect deformation near the ends of faults, but we know of no physical explanations or analyses in the geologic literature that explain this scale dependence.

We focus on the nature of features near the ends of large faults and the role of these features in fault termination. We document the termination of a strike-slip fault system in jointed granitic rock where slip is shared among dozens of nearly parallel strike-slip faults clustered around the fault system tip. We then present a mechanical analysis that shows how preexisting structures could diminish and diffuse the stress concentration near a fault end, potentially forming a barrier to fault growth. To our knowledge, this kind of phenomenon, known in the fracture mechanics literature as “crack-tip shielding”, has not been applied to a discussion of

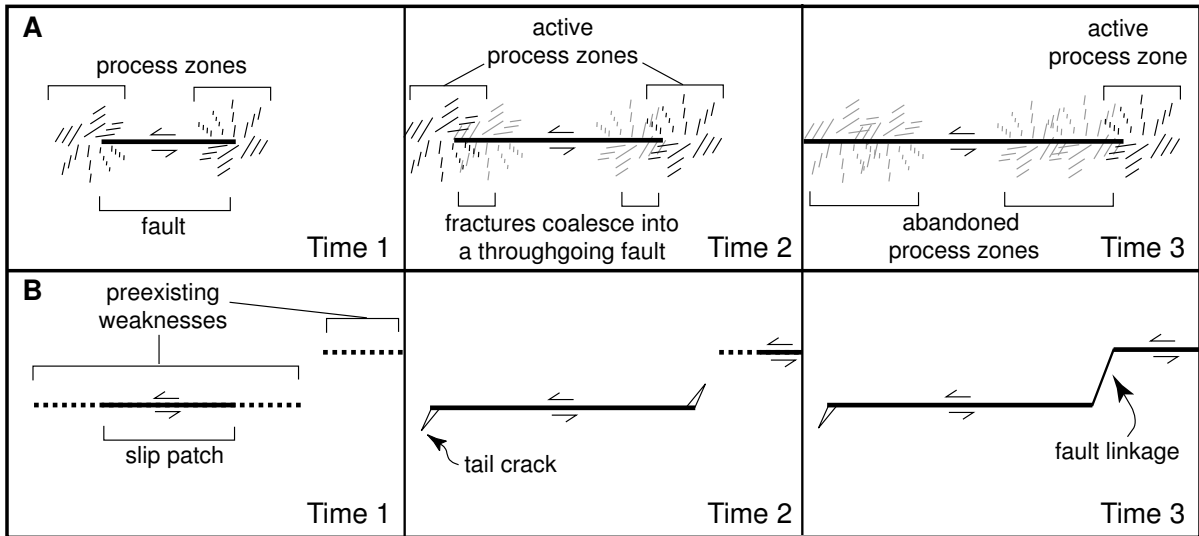


Figure 2.1. Cartoon showing two mechanisms for fault growth: (A) through a “process zone” (after Vermilye and Scholz, 1998); and (B) by segment linkage of preexisting weaknesses (after Segall and Pollard, 1983). Note that microfracturing within the process zone is not drawn to scale. In A-1, high stress concentrations near the fault tip induce microfracturing in what is termed the “process zone.” In A-2, the microfractures have coalesced into a throughgoing fault segment and a new process zone forms near the new tip of the fault. In A-3, the fault continues to grow, leaving behind a wake of fractures extending along the length of the fault. In the lower set of panels, a patch of a preexisting structure begins to slip in B-1. Stresses at the patch tip are lower than in the process zone scenario because the weakness that the patch grows along cannot support high shear stresses. In B-2, the slip patch extends to the end of the physical weakness generating high near-tip stresses in the host rock that lead to the formation of “tail cracks.” A nearby slip patch is also growing (upper right of this panel). In B3, the fault system grows by the linkage of neighboring fault segments. Fracturing only occurs at the ends of the fault system and at segment boundaries at this stage.

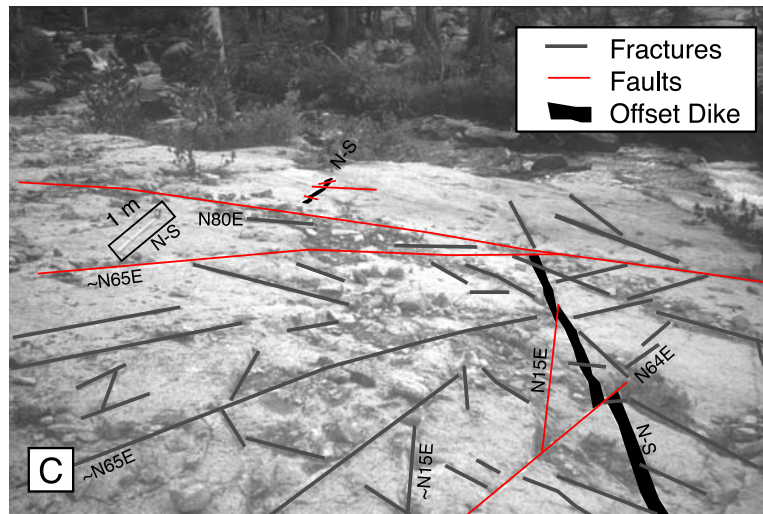
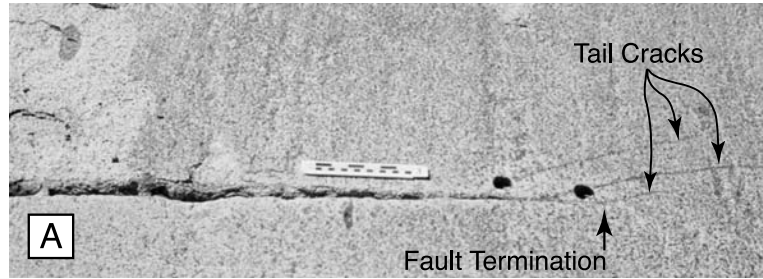


Figure 2.2. (A) Opening mode fractures near the ends of a small left-lateral fault. Scale is 15 cm long. The dark circles near the fault termination are where core samples were drilled. (B) View towards $S15^{\circ}W$ showing secondary fractures near the end of a left-lateral fault system nearly 3 km long (near location F on Fig. 2.4). The rectangle in the upper left outlines a tape measure oriented north-south and extended to a length of 1 m. (C) Same as 2B, but with interpretive lines to highlight the locations of fractures. Selected fracture orientations are labeled.

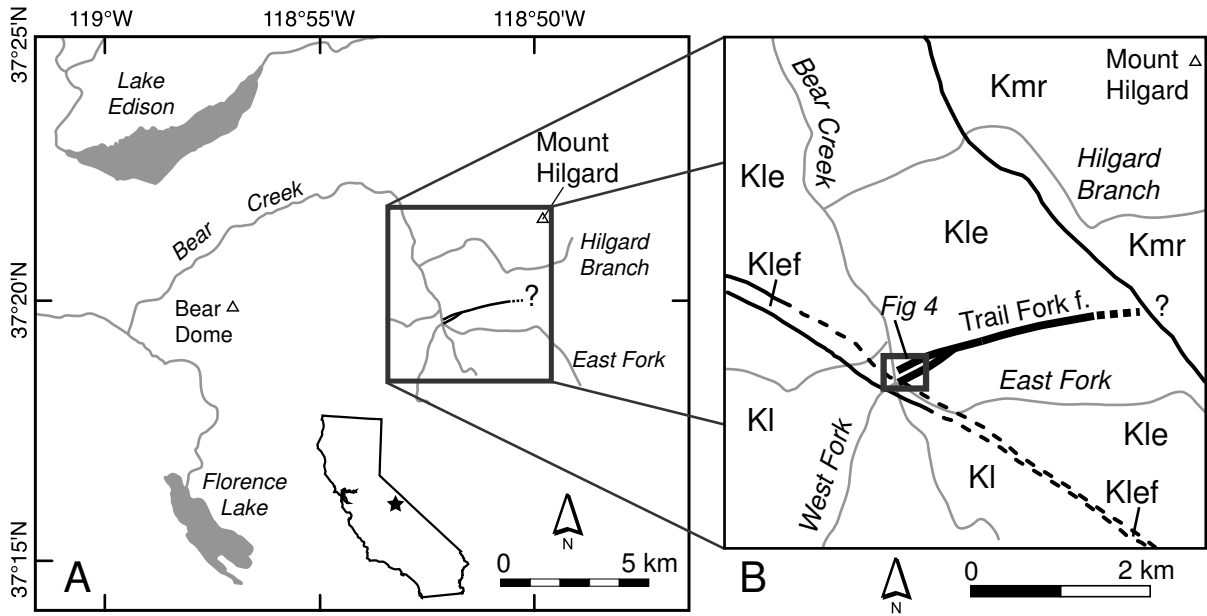


Figure 2.3. (A) Location of the Trail Fork fault system in the Mount Abbott Quadrangle, California. (B) Generalized geology in the vicinity of the study area after *Lockwood and Lydon* [1975]. From oldest to youngest: Kl, medium-grained Lamarck Granodiorite; Klef, fine-grained facies of Lake Edison Granodiorite; Kle, fine- to medium-grained Lake Edison Granodiorite; Kmr, medium-grained Quartz Monzonite of Mono Recess. Grey box indicates location of detailed mapping shown in Fig. 2.4. Heavy lines denote contacts; they are dashed where the location is approximate.

fault terminations. The influence of this shielding mechanism is likely to vary with scale and could explain, at least in part, the observed scale-dependent variation in fault end structure.

2.3 Geologic setting

The area of our study is located along Bear Creek in the central Sierra Nevada of California (Fig. 2.3). The late Cretaceous granodiorite host plutons contain prominent joints and faults that strike east-northeast and generally dip more steeply than 80° [*Lockwood and Lydon*, 1975]. The joint spacing is fairly heterogeneous and ranges from only a few centimeters to more than ten meters, while joint trace length is typically no longer than several tens of meters. Field relationships, mineralogic evidence, geochronologic data, and thermo-elastic modeling results collectively indicate that the joints formed during pluton cooling and prior to faulting [*Segall and Pollard*, 1983; *Bergbauer and Martel*, 1999]. The age of pluton emplacement is ~ 90 Ma [*Bergbauer and Martel*, 1999] and faulting within the pluton occurred between 79 and 85 Ma [*Segall et al.*, 1990].

Segall and Pollard [1983] show that the small faults formed by slip along the preexisting regional joints, citing observations that the faults and joints 1) are parallel; 2) have similar trace lengths; and 3) have similar mineral assemblages, except that the assemblages in the faults are deformed mylonitically, whereas those in the joints are undeformed. They find no evidence that these faults grew as shear fractures, but they do show how small faults link to form longer fault systems. *Martel et al.* [1988] and *Martel* [1990] present additional evidence indicating that fault zones in the Mount Abbot quadrangle as long as several kilometers also exploited preexisting joints and grew by linkage.

2.4 Fault system

We focus here on a fault system near the Trail Fork outcrop of *Segall and Pollard* [1983]. This fault system extends from the East Fork of Bear Creek, cuts across the Trail Fork outcrop of *Segall and Pollard* [1983], and loses its topographic definition about 2.7 km east of Bear Creek (Fig. 2.3). The maximum left-lateral offset measured across this system is 46 meters. The fault system ends within the Lake Edison Granodiorite less than 100 meters from the older Lamarck Granodiorite. The Trail Fork fault system contains two styles of faults: “small faults” and larger “fault zones” [*Martel et al.*, 1988]. Small faults are individual reactivated joints that accommodate as much as a few meters of slip each. They appear as discrete fractures no more than a few centimeters thick that are filled by chlorite, epidote, and quartz. Fault zones at Trail Fork are bounded by two parallel faults spaced 0.25 - 3 m apart with highly fractured and hydrothermally altered rock in between. The fault zones accommodate tens of meters of slip and appear as prominent topographic troughs where the altered and fractured material has preferentially eroded. Both the small faults and the fault zones in the study area strike east-northeast, dip at nearly 90° , and have slickenlines within 10° of horizontal; they essentially parallel each other and regional joints.

Figure 2.4 shows small faults, fault zones, and offset dikes near the west end of the Trail Fork fault system. The figure also shows the locations of five traverses, marked by brackets, used to quantify offset across the faults. Figure 2.5 shows the cumulative left-lateral offset along these traverses with the positions of offsets projected onto lines trending $S25^\circ E$ (approximately perpendicular to fault zone strike). Along Traverse 1, about 300 meters from the west end of the southernmost fault zone, slip is concentrated in three well defined fault zones. Along Traverse 2, two hundred meters closer to the end, slip is shared evenly among several parallel fault zones. Along Traverse 3, the topographic expression of the two southernmost fault zones is weak, and slip is shared among more than two dozen nearly parallel small faults. Near Location C, these faults are spaced less than one meter apart; this is the smallest average fault spacing along our five traverses. Traverse 4 contains a gap in the data owing to the local absence of markers for measuring slip; this gap is marked by a dashed line in Fig. 2.5. For Traverse 5, beyond the west ends of the fault zones, the cumulative offset is only about one third that along Traverse 1 and is accommodated entirely by small faults. Figures 2.4 and 2.5 thus show that near the ends of the three fault zones the slip across them decreases and becomes shared with the small faults.

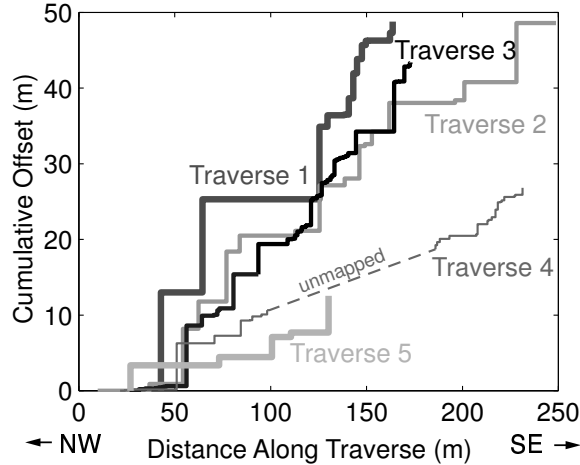


Figure 2.5. Cumulative left-lateral offset of marker dikes across the entire fault system of Figure 2.4. The locations of the fault offsets are as projected onto traverses trending $S25^{\circ}E$ (perpendicular to the fault system); see Fig. 2.4. Each step represents an offset marker, and the height of the step corresponds to the amount of offset. Along Traverse 1, slip is concentrated in three fault zones, each with more than ten meters of offset. Along Traverse 3, near the end of the fault zones, the offset is shared rather evenly among dozens of small faults.

Where outcrops provide the most complete and continuous exposures (southeast of Location C and near Location F on Fig. 2.4), we observe abundant secondary fractures associated with the termination of the fault system (Fig. 2.2B, 2C). These fractures have traces with maximum lengths of several meters and exhibit a broad range of strike orientations. They dip steeply and are not sheeting fractures with a shallow dip. Only a small percentage of them intersect the nearest fault zone in the plane of the outcrop. They typically accommodate no lateral offset – most are joints, though a few of the fractures have slipped 1-2 cm in a sense consistent with left-lateral slip on the fault system. These fractures of diverse strikes probably are not the remnants of a process zone because we observe them only near the terminations of fault zones rather than along their entire extent, as would be expected for the wake of fractures in a process zone (Fig. 2.1A). Although at least some of these fractures are mineralized, we have not attempted to characterize the mineral fillings. Based upon the unusual clustering of fractures near the fault system end, their absence far from the fault end, and the slip observed on some of them, we infer that the cluster as a whole is related to the fault system end. This observed distribution of secondary fractures is quite different from the localized tail cracks that form with preferred orientations at the ends of small faults (Fig. 2.2A).

The field evidence strongly indicates that the numerous parallel small faults near the tip of the southern Trail Fork fault zone did not form in a process zone associated with a propagating fault tip, but rather formed by slip along joints that predate faulting. Like the fractures of diverse orientation, the concentration of parallel small faults near the fault zone tip is not observed far from the end. In the following analysis, we therefore treat the small faults near

Location C as having originated from joints that predate faulting, in the same manner as other small faults nearby [Segall and Pollard, 1983; Martel et al., 1988].

2.5 Mechanical analysis

What effect do the small faults near the end of the fault system have on the development of the large fault zone in the system? Could a cluster of small faults form a “barrier” to fault zone growth? To address these questions, gain insight into the mechanical interaction of the small faults and the large fault zone, and to better understand the observed fracture pattern in map view we conducted two-dimensional plane strain mechanical analyses using the boundary element method [Crouch and Starfield, 1983]. Here we present the results of the analyses and assess the implications for fault propagation and secondary fracture growth. The boundary element method works by dividing the faults lengthwise into small elements and then determining how much each element has to slip in order to satisfy specified boundary conditions. The method yields both the slip on the elements and the stresses in the surrounding material.

Analyses of two fault system geometries illustrate how small faults can interact with a larger fault zone. Case A involves a single fault zone with a trace length of 2 km (top panel of Fig. 2.6). Case B involves an identical fault zone, but with six parallel small faults at one end. At the west end of the Trail Fork fault system, individual small fault traces are tens of meters long but cluster around the southernmost fault zone over a distance > 120 m along strike (from B to D on Fig. 2.4). We evaluate a range of possible lengths for the small faults from 50 m to 200 m. In Fig. 2.6B, we show one model scenario with a cluster of small faults that are 100 m long; the geometry mimics the conditions at Trail Fork but does not account for the precise number or geometry of the many faults of Fig. 2.4. We later discuss how variations on this geometry affect the system.

For the boundary conditions, all the faults are modeled as frictionless to obtain the maximum possible fault interaction, and their walls are required to remain in contact. The frictionless faults modeled here are not sensitive to changes in the normal traction on them, and these changes are small anyway given the geometry of the fault arrangement. The far field stress is considered to be uniform and one of pure shear, with the maximum shear stress far from the fault (τ^∞) acting parallel to the fault (Fig. 2.6, inset in lower panels). We consider compression as positive, with σ_1 being the most compressive horizontal stress and σ_3 being the least compressive horizontal stress. We treat the host rock as a homogeneous, isotropic, linear elastic solid. Our boundary elements are typically 0.5 - 2 m long, allowing detailed examination of near-tip stresses and slip gradients. These assumptions as a whole allow us to focus on the relative differences between several model scenarios with different fault geometries in order to evaluate how fault interaction alters slip and near-fault stress fields. Our results, therefore, highlight the differences between the models and may be applied to a wide range of natural faulting environments.

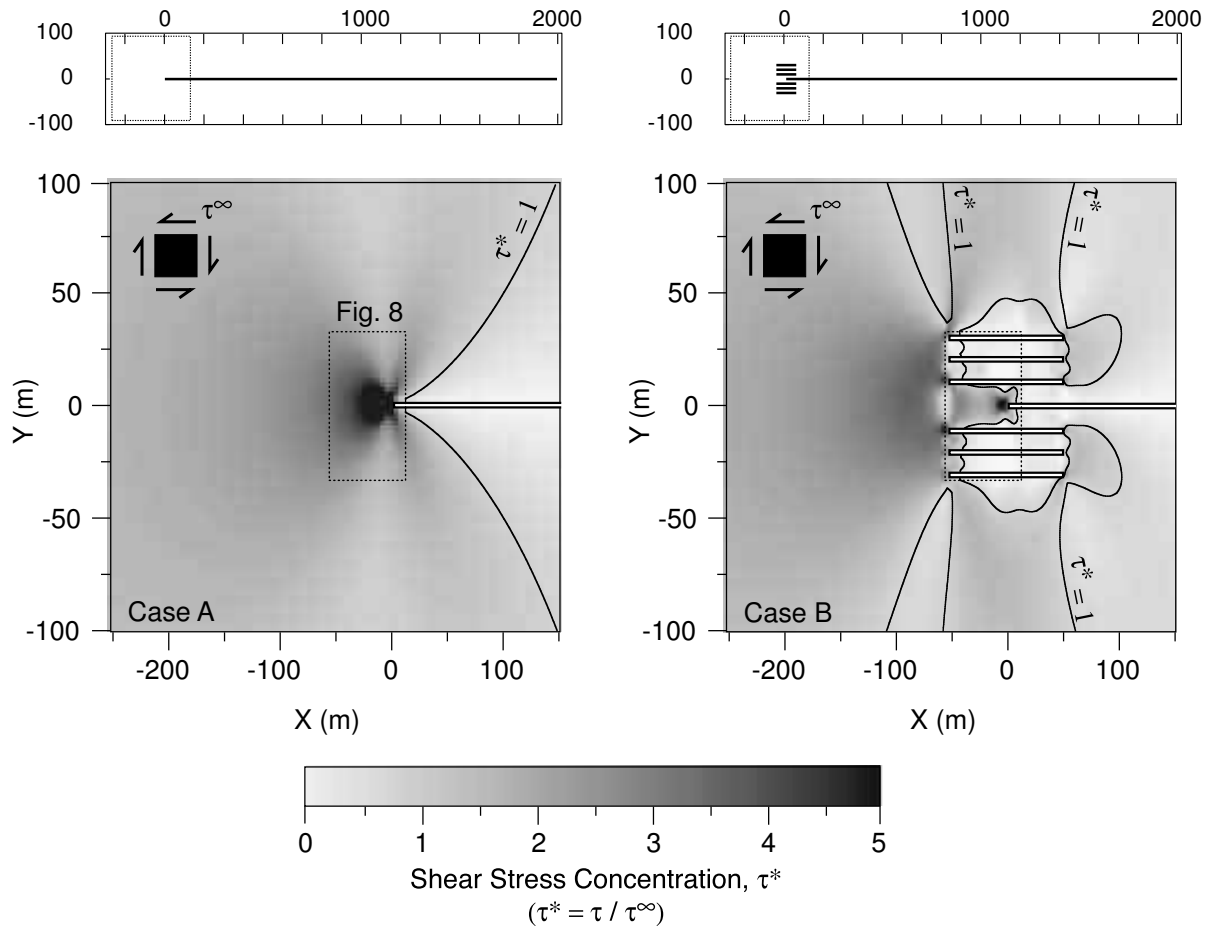


Figure 2.6. Normalized fault-parallel shear stress concentrations near the tip of an isolated frictionless model fault zone (Case A), and a fault zone with a cluster of smaller faults flanking one end (Case B). The top row of panels shows the geometries over the entire extent of the model fault systems. The dotted boxes near the left-hand end of the fault zone outlines the areas shown in the lower panel. The lower panels illustrate the fault-parallel shear stress relative to the far-field value. Contours are for $\tau^*=1$. Diagram inset into lower panels shows the applied stress state with τ^∞ parallel to the faults. The cluster of small faults in Case B diffuses the stress concentration at the tip of the long fault zone.

2.5.1 Reduced shear stress concentration

The large panels of Fig. 2.6 show the fault-parallel shear stress near the tip of the fault zone as normalized by the remote shear stress ($\tau^* = \tau/\tau^\infty$). Both cases show a stress concentration near the tip of the fault zone, but the concentration is much less in Case B and than in Case A. In Case A, roughly 85% of the area shows a fault-parallel shear stress exceeding the far-field level (i.e., $\tau^* > 1$). In Case B, for only about 65% of the area is $\tau^* > 1$. Higher stress concentrations are diffused even more; the area where $\tau^* > 4$ (i.e., the round, dark area at the tip of the 2-km-long fault zone) is one ninth the size in Case B than in Case A. Figure 2.6 shows that the mechanical interaction of the faults decreases the shear stress near the tip of the fault zone, which diminishes the tendency for it to grow in plane as a shear fracture.

2.5.2 Fracture energy

The mechanical energy available to advance the fault zone tip an incremental amount (G) also is lower in Case B than for the isolated fault zone in Case A. The fracture energy, G , is related to the magnitude of the near-tip stress concentration [Lawn and Wilshaw, 1975] and likewise is a measure of a faults ability to grow. For two faults with identical boundary element distributions (the case here) the calculated ratio of G for the two faults is approximately equal to the square of the ratio of slip at the fault-tip elements [Willemse and Pollard, 1994]. In our analysis, boundary elements near the tip of the longest fault zone are 0.03% of the total fault length. In Fig. 2.7, we show how G changes (relative to G for an isolated fault zone of equal length) as a function of the amount of overlap between the fault zone and the small faults. We consider three lengths of small faults: 50m, 100m, and 200m. As the fault zone tip approaches the cluster (overlap < 0), G increases, reaching a maximum shortly before the fault zone and small faults overlap. So for underlapped faults, growth of the fault zone is encouraged. As the fault zone tip extends into the small fault cluster (overlap > 0), G plummets, reaching a minimum where the fault zone tip is near the center of the cluster. Pollard and Aydin [1988] show that an analogous effect occurs for opening mode fractures. The maximum reduction of G is substantial, ranging from about 36% for the 50m-long faults to about 88% for the 200m-long faults. The cluster thus robs the fault zone tip of the energy needed for it to propagate and can act as a barrier to fault zone growth. This “barrier effect” continues even after the fault zone tip extends through the cluster. The three different curves in Fig. 2.7 show that the barrier effect reduces the ability of the fault zone to propagate as a shear fracture for a wide range of small fault lengths and overlap distances.

The precise fault-tip stress field will vary for different fault geometries, but nearby small flanking faults generally yield reductions in shear stress concentrations at the fault zone tip. An analogous effect known in engineering as “crack-tip shielding” [e.g., Weertman, 1996, , p. 164] results in an increased resistance to fracture propagation. For a fault, an increased resistance to slip will influence its slip profile [e.g., Cowie and Scholz, 1992] and should retard secondary fracturing near its ends [Martel, 1997], thus diminishing its ability to physically link with neighboring faults. Crack-tip shielding thus can inhibit fault growth, no matter whether the growth would occur by linkage mechanisms or by propagation as a shear fracture.

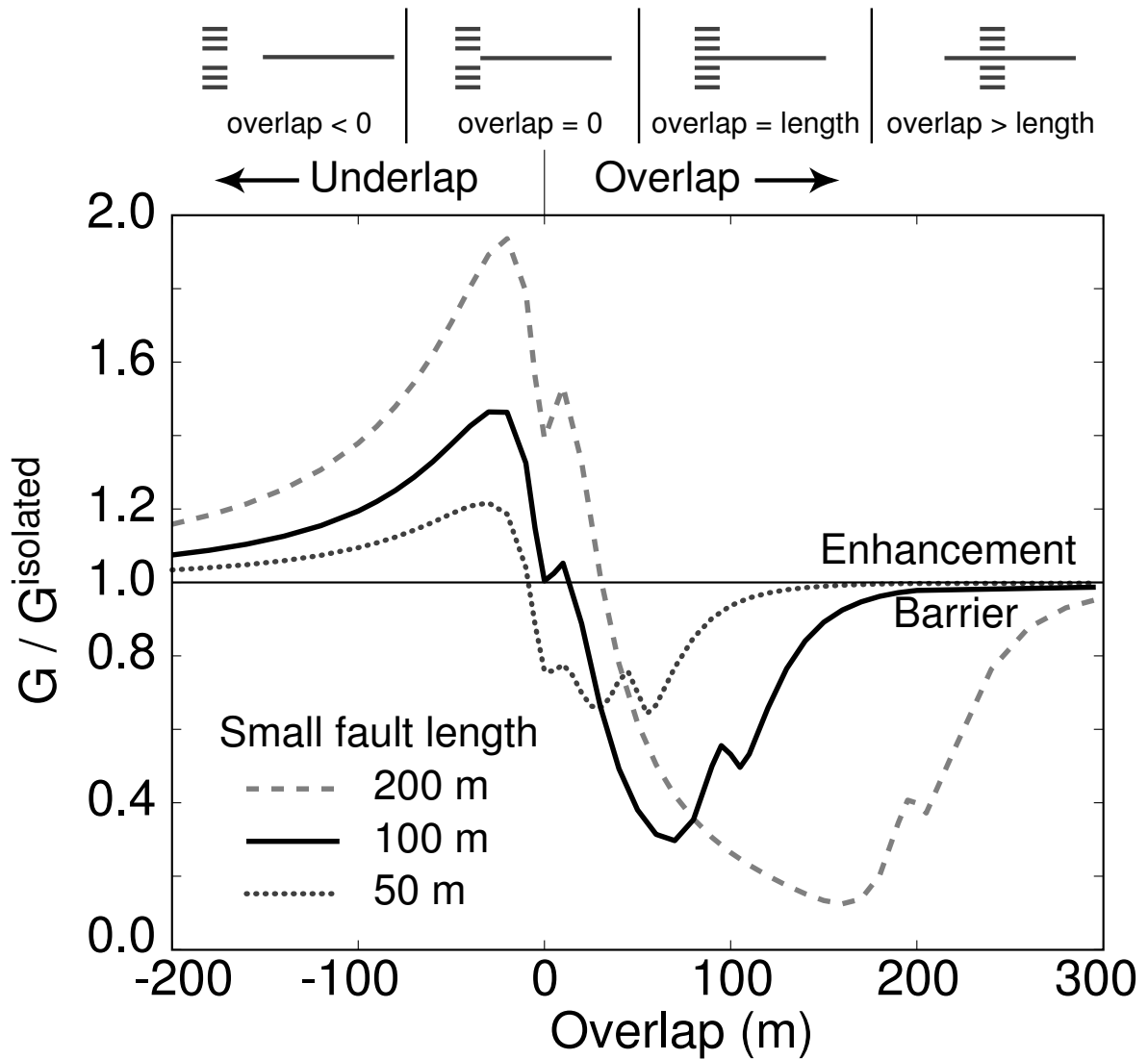


Figure 2.7. Relative fracture energy for a large frictionless fault zone 2 km long near a cluster of small faults as a function of along-strike overlap. The fracture energy (G) is shown relative to the fracture energy of an isolated frictionless fault zone ($G^{isolated}$) of identical length, as in Case A of Fig. 2.6. The curves correspond to small faults with different lengths (50, 100, and 200 m, or $\sim 2.5\%$, $\sim 5\%$, and $\sim 10\%$ of the fault zone length). Values greater than 1 indicate enhanced growth potential relative to an isolated fault zone of the same length, while values below 1 indicate a reduced growth potential (i.e., the cluster acts as a barrier to fault growth). Schematic at top shows relation between fault zone and small fault cluster for different overlap distances (not to scale). Jumps in the fracture energy occur where the main fault zone tip is abreast the tips of adjacent small faults (see the central two panels at top of the figure).

2.5.3 Effects of mechanical interaction on secondary fractures

As support to our hypothesis that crack-tip shielding altered the stress field near the tip of the Trail Fork fault system, our model results show that the shielding effect produces a near-tip stress field that can also account for the broad range of fracture orientations observed near the end of the fault system (Fig. 2.4, Location F). Secondary fractures at the tip of a small fault typically have a distinct preferred orientation (e.g., Fig. 2.2A), while secondary fractures at the end of the Trail Fork fault zone display a wide range of orientations (Fig. 2.2B). We find that mechanical interaction among the small faults and the fault zones could inhibit the opening of fractures with preferred orientations near the end of the Trail Fork fault system. Opening mode fractures only form where the effective least compressive stress is tensile (negative in our sign convention), and they grow along a surface perpendicular to the least compressive stress. Where the ambient differential stress is zero (i.e., the maximum compressive stress σ_1 is identical to the least compressive stress σ_3), the orientations of the principal stresses are not uniquely determined, and fractures that open will not have a systematic orientation [e.g., *Olson and Pollard*, 1989]. In contrast, fractures opening under high differential stresses will have a preferred orientation parallel to the maximum compressive stress. A plot of differential stress ($\sigma_1^* - \sigma_3^*$) versus least compressive stress (σ_3^*) thus will indicate whether fractures tend to form with a strongly preferred orientation, unsystematic orientations, or not at all [*Sibson*, 2000]. The superscript star indicates that we normalize each of these stress components by the magnitude of the applied far-field shear stress, τ^∞ . In Fig. 2.8, we plot these normalized stresses for every point in a regularly spaced grid that spans the region near the tip of the longest faults in our models. This area (indicated by the dotted box in the lower panel of Fig. 2.6) corresponds to the region where we observe highly varied orientations of secondary fractures in the field (Fig. 2.4). Conditions favoring the opening of new fractures with a preferred orientation lie in the upper left portion of this figure. Case B has a lower peak differential stress, a greater clustering of points near a differential stress of zero, and more points where σ_3^* is compressive and fracture opening tends to be inhibited. Fractures would be less likely to open and would be less likely to show a strong preferred orientation in Case B than in Case A. The more compressive values of σ_3^* in Case B mean that fractures that do open will also tend to be shorter than in Case A. We conclude that fault interaction like that of Case B tends to retard the opening of long secondary fractures with a preferred orientation as compared to Case A.

2.5.4 Slip profile near the fault tip

Figure 2.9 shows the slip profile for the Trail Fork fault system compared with the combined slip of all the model faults in Case B. In both the data and the model, a local maximum in fault slip occurs near the center of the cluster of small faults (Location C in Fig. 2.4). The difference between the magnitude of the local maximum in the data and model probably stems largely from the simplified geometry of our model. We model only six small faults in Case B, but the Trail Fork fault zone is flanked by over two dozen small faults. The local minimum in slip corresponds to the eastern end of the small faults in both the data and model (Location B in Fig. 2.4). The model slip distribution therefore captures the first order features observed

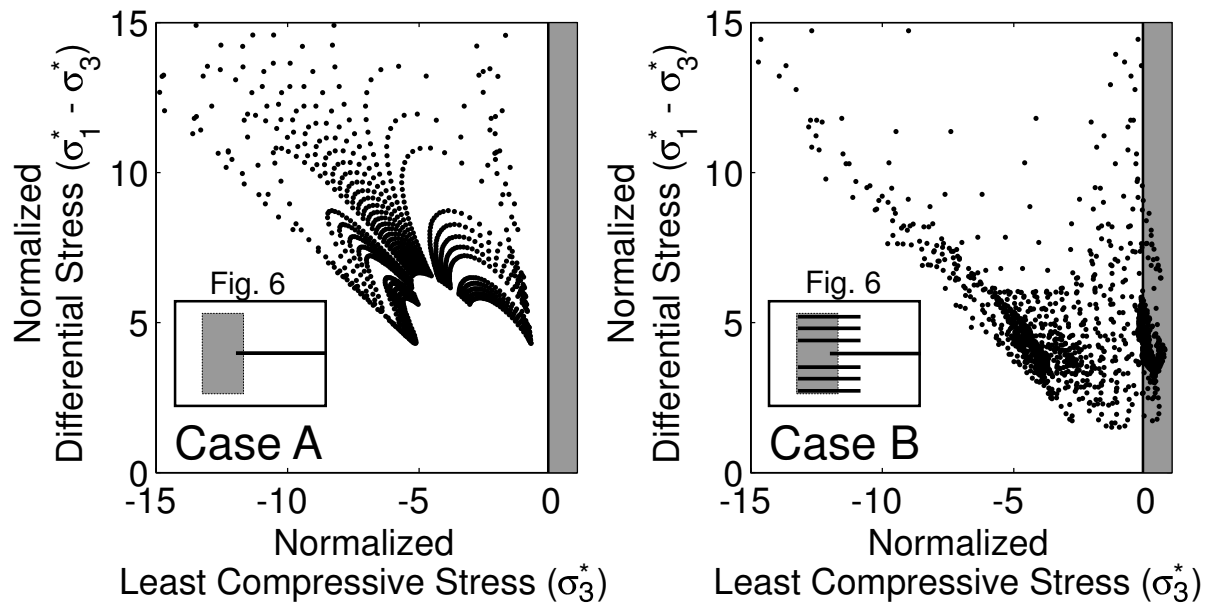


Figure 2.8. Normalized differential stress versus normalized least compressive stress for each grid point in the near-tip region of our boundary element model. The superscript stars in the axes labels indicates that stress components are normalized by the remote shear stress (τ^∞). The inset figures show a schematic reproduction of Fig. 2.6 with the region considered for this figure indicated by the shaded box. Tension is negative and the shaded region on the right side of the plot indicates compressive stresses. Points plotting in the upper left are most likely to be associated with opening mode fractures with a strongly preferred orientation. Case A (left), with the isolated fault zone, is more likely to produce such fractures than Case B. The systematic pattern of the plot for Case A results from the simple geometry of an isolated fault. The presence of the small faults generally reduces the differential stress and makes the least compressive stress more compressive near the tip of the large fault zone.

at the Trail Fork fault system. Lengthening the faults in the model or increasing their number would cause the model results to match the observations even better.

2.6 Discussion

The Trail Fork fault system terminates in a cluster of abundant small faults where the slip profile and character of secondary fractures is qualitatively consistent with our model results. We suggest that the small faults impeded the fault system from linking and growing by sharply diminishing the mechanical energy available for fracture at the fault tip (G) compared to an isolated fault. If G drops below the threshold fracture energy for faults to grow (G_{crit}), then the small faults will form an effective barrier to fault growth. The absolute value of G is a function of the regional stresses, fault strength, and elastic properties of the rock at the time of faulting, and none of these are reliably constrained for the conditions of faulting at Trail Fork. Nonetheless, the relative reductions in G shown in our results are substantial (as much as 88% reduction) and suggest that a cluster of small faults near the end of a longer fault zone can have a profound impact on its ability to grow.

A fault system growing by segment linkage will end if there are no fault segments beyond its tip available for linking, but there are abundant structures beyond the west end of the Trail Fork fault system that could have been exploited (Traverse 5, Fig. 2.4). These structures are individual slipped joints that accommodate centimeters to tens of centimeters of left-lateral offset, an order of magnitude less slip than the nearby fault system. The fault system was unable to grow by linking to these nearby structures, and we infer that crack-tip shielding is a substantial part of the reason why.

2.6.1 Role of a nearby lithologic boundary

The Trail Fork site is located within the Lake Edison Granodiorite but lies less than 100 meters east of the contact with the older Lamarck Granodiorite. The evidence at hand indicates that the Trail Fork fault system probably was not substantially affected by the Lamarck Granodiorite. First, the Trail Fork fault system lies within the younger pluton, and hence could not have been truncated by the older one. Second, field observations show that numerous joints, faults, and photolineaments parallel to the Trail Fork fault system occur in both plutons and cut across the contact between the plutons near the Trail Fork site [e.g., *Lockwood and Lydon, 1975; Bergbauer and Martel, 1999; Pachell and Evans, 2002*]. Although *Bürgmann et al. [1994b]* show that contrasts in rock stiffness along a fault can affect slip, we have no direct evidence of a substantial rigidity contrast between the two similar granodiorite bodies at the time of faulting. Pronounced differences in rigidity arising from temperature differences between the plutons appear unlikely because both plutons cooled through the closure temperature of ^{40}Ar in biotite contemporaneously (about $330 \pm 50^\circ\text{C}$ at ~ 80 Ma; *Bergbauer and Martel [1999]*), indicating that the two plutons were at about the same temperature during faulting. The contact shows no evidence of being free to slip in the manner of many sedimentary contacts, so we do not expect that the contact itself to play a significant mechanical role in fault termination.

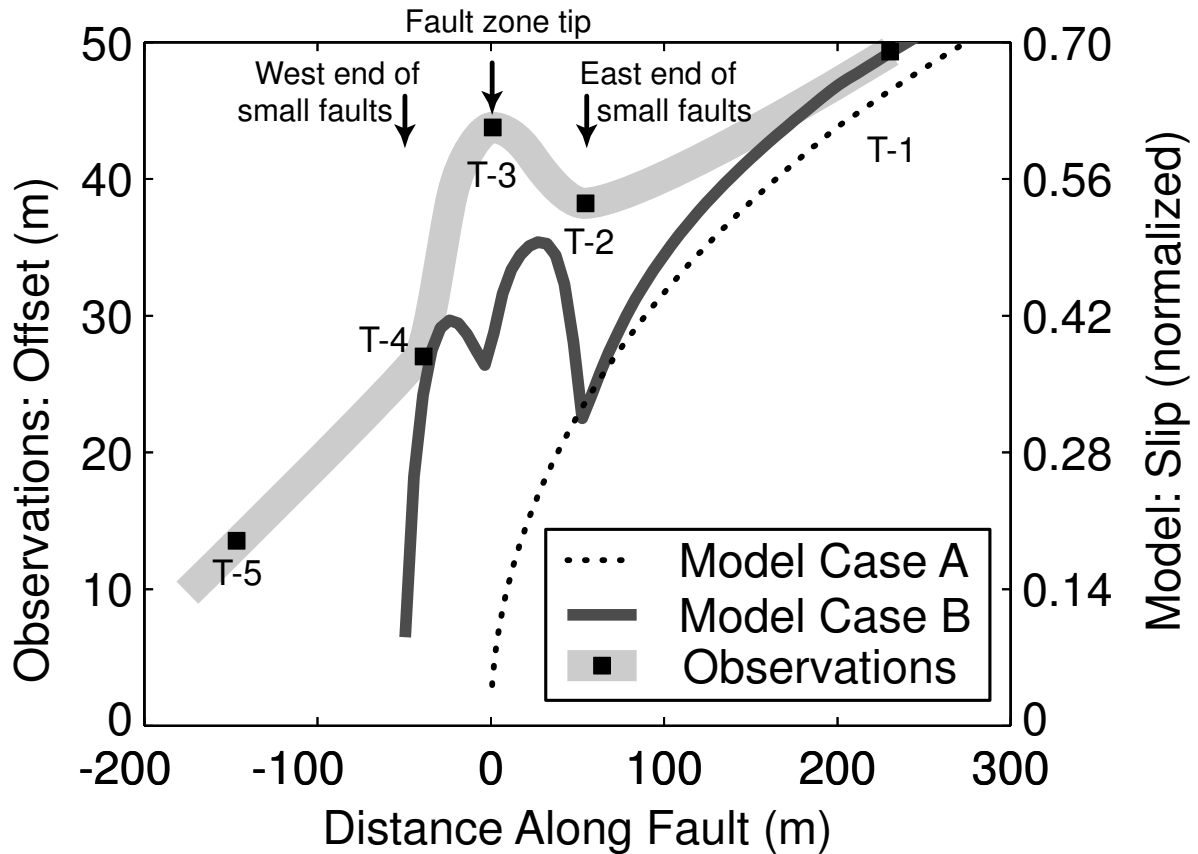


Figure 2.9. Comparison between slip profiles obtained from field measurements of offset dikes and from modeling results. For the observations, we sum offsets from the fault zones and adjacent small faults along each of the transects, indicated by the squares labeled T-1 through T-5 (T for Traverse). The observations are connected by a smooth cubic spline interpolation as the thickest light-colored curve. Slip along faults south of Location F in Fig. 2.4 is not included in the calculation due to a lack of markers for measuring offsets. For the model results, we sum slip on all faults from model Case B of Fig. 2.6 and normalize them by the maximum slip of the long fault zone. Zero distance corresponds to point C in Fig. 2.4 for the observations and the tip of the long fault zone in the models (as in Fig. 2.6). We plot the data and model together, scaling the models so that the Case B curve passes through the easternmost data point T-1. Because of this arbitrary scaling, the comparison is schematic. The double-maximum in the model is a result of near-tip effects from the termination of the fault zone at zero distance. Note the correspondence in both the observations and the model results of the local peak in slip where the cluster of ~ 100 m long small faults is centered, and the local minimum in slip at the east end of most of the small faults.

For these reasons we conclude that the proximity to the contact between the plutons probably was not a substantial mechanical barrier to fault growth.

2.6.2 Cluster of small faults

At Trail Fork, the cluster of small faults originated as a cluster of closely spaced joints with an average spacing less than a meter. Joint spacing is relatively heterogeneous in the Bear Creek region but a spacing as large as several meters is fairly common [e.g., *Segall and Pollard, 1983; Martel et al., 1988*]. The clustering of fractures spaced less than a meter apart, as at Trail Fork, is rare in this area. The Trail Fork small faults are associated spatially with dikes that predate both fault slip and jointing; this association occurs at other nearby outcrops as well [*Segall and Pollard, 1983; Martel et al., 1988*]. These relationships raise the prospect that dikes served as preferential nucleation sites for closely spaced fractures that subsequently inhibited fault growth. An alternative is that the abundance of joints is related to the nearby pluton contact; this raises the possibility that the pluton contact indirectly acted as a barrier because of the presence of the preexisting joints.

2.6.3 Scale dependence

Deformation near the end of the Trail Fork fault system differs sharply from deformation near the ends of many nearby small faults tens of meters long. Small faults several meters long commonly display a few oblique opening-mode tail cracks several decimeters long within a meter of the end of the fault trace (Fig. 2.2A). If these fault-end features were scaled up to a fault zone a few kilometers long, then oblique tail cracks a few hundred meters long should exist within a few hundred meters of the fault system termination. We observe no such features at Trail Fork. Instead, we document areas of closely spaced opening-mode fractures with a wide distribution of strikes and with lengths less than 1% of the total length of the fault system (Fig. 2.2C).

The fixed spacing of preexisting weaknesses may explain the different termination styles of small and large faults. The distance over which a fault can interact with nearby structures depends on the dimensions of the fault, and as a fault lengthens it will be able to interact with features at a greater distance. The spacing of preexisting weaknesses is fixed, however, so features that are “distant” when a fault is small become “closer” (relative to the fault length) as it grows. Thus, longer faults have more opportunity to interact with the limited population of preexisting planes of weaknesses than would a smaller fault. Our modeling shows that interaction with weaknesses near the fault tip can impede the ability of a fault to link and grow, and can affect the size and distribution of secondary fractures near the fault tip. We suggest that as faults become larger they increasingly will tend to end in a broad, ill-defined distribution of smaller faults and unsystematically oriented secondary fractures because of the shielding effect induced by preexisting weaknesses. The fracture energy of a fault increases with fault length [e.g., *Lawn and Wilshaw, 1975*], so longer faults need more substantial barriers to stop their growth than shorter faults, other factors being equal. Previous workers have found that mechanical barriers like lithologic contrasts are effective when faults are small but

are overcome as faults grow longer [e.g., *Wilkins and Gross, 2002*]. The effectiveness of a crack-tip shield barrier, however, can grow as a fault grows because larger faults can interact with more structures over a broader area. If shielding structures are closely spaced and extend over a broad area, the increase in interaction can be more important than the increase in G caused by the faults lengthening. We therefore expect that crack-tip shielding will continue to be important as faults grow to great lengths and might not be overcome like barriers resulting from scale-independent mechanical discontinuities such as lithologic boundaries.

2.6.4 Implications for fluid flow and erosion

Secondary fractures with a consistent and predictable orientation at the end of a small strike-slip fault provide preferentially oriented conduits for fluid flow while the secondary fractures at the ends of larger faults seem to show considerable variation in their orientation. The diversity of fracture orientations will tend to yield a more connected fracture network provided that the fractures are long enough to intersect each other and the fault. At Trail Fork the secondary fractures are sufficiently short that the fracture network is not well connected everywhere within the plane of the outcrop, but the fractures still might be well connected in three dimensions, and the fractures are better connected than those at the ends of small faults. We suggest that the hydraulic connectivity of fractures at the ends of faults will tend to increase with fault size. Other factors being equal, this will tend to make for greater hydraulic conductivity as well. A broad area of secondary fractures of diverse orientations near the ends of large strike slip faults would also create sites particularly susceptible to erosion. This could explain why glacially carved lakes occur at the ends of many of the larger faults in the jointed granitic rock of the Sierra Nevada [e.g., *Moore, 1963; Lockwood and Lydon, 1975; Moore, 1978; Moore and Sisson, 1987*].

2.6.5 Crack-tip shielding

Linear elastic fracture mechanics predicts that a fault with uniform driving stress would have an infinitely large stress concentration and an infinite slope of the slip profile at its tips, conditions which are impossible in nature [e.g., *Martel, 1997*]. The most popular theoretical explanation for how the stress concentration is diffused by inelastic deformation near the tips of faults in nature involves a region of high cohesive strength or frictional heterogeneity along the fault near its tip. This region commonly is referred to as a “cohesive end zone” (CEZ). The CEZ produces tapered slip profiles near fault ends. For faults growing by a process-zone, the CEZ is a direct result of the process zone immature portions of the fault that have just formed by the linkage of process zone fractures have higher friction than more mature sections of the fault that are “smoothed out” as slip accumulates [*Cowie and Scholz, 1992*]. Tapered slip profiles also have been observed in fault systems growing by segment linkage [see *Schultz, 1999*], but the physical mechanism causing the CEZ for these faults is not well understood. *Gupta and Scholz [2000]* use numerical models to show that fault interaction can lead to tapered slip profiles in stepovers between en-echelon normal faults. Our model results indicate that fault interaction resulting in crack-tip shielding is a physical mechanism for producing a CEZ effect in faults

growing by either segment linkage or shear fracture. Crack-tip shielding effectively reduces the near-tip stress concentration because slip on the flanking faults distributes the strain energy of the system over a broader area—slip on the flanking faults can account for the inelastic deformation attributed to a theoretical CEZ. Both our model results and observations of the slip profile at Trail Fork show a tapering of slip near the end of the fault system as predicted by CEZ theory. We attribute this gradient to crack-tip shielding due to fault interaction.

The extent to which mechanical interaction causes natural faults to terminate depends on the abundance of preexisting structures that could serve as crack-tip shields. A tip shielding process need not require preexisting fault-parallel joints. Parallel bedding planes could similarly inhibit growth of bedding-plane faults in sedimentary rocks [e.g., *Roering et al., 1997*]. *Pollard and Segall* [1987] invoke a tip shielding phenomenon in their discussion of dike propagation where shielding is provided by process zone fractures (i.e., by fractures generated by the dike propagation process itself). Perhaps faults growing via a process zone could even be shielded by slip along the fractures they generate near their tips, resulting in the termination of faults by the very mechanism that allows them to grow.

For dynamic earthquake rupture, a process analogous to segment linkage is important in allowing earthquake ruptures to propagate great distances. Dynamic simulations have shown that ruptures can terminate if the distance between fault segments is sufficiently great [*Harris and Day, 1999*] consistent with the results for stepovers in the static models [*Aydin and Schulz, 1990*]. If the crack-tip shielding we argue for in the static case of fault growth has an analog in dynamic rupture growth, perhaps slip on sub-parallel faults or activation of fractures within the fault damage zone could help arrest earthquake rupture. For example, *King* [1986] suggests that slip on fractures generated in the damage zone around fault bends could form a “relaxation barrier” that redistributes stress, essentially acting as a crack tip-shield. Slip along fractures within the damage zones of seismogenic faults is well documented in both exhumed faults [e.g., *Chester and Logan, 1987; Little, 1995*] and for the aftershocks of large earthquakes [*Liu et al., 2003*]. If some portion of the total slip on these fractures is contemporaneous with earthquake rupture, a shielding effect would contribute to rupture termination.

2.7 Conclusions

The west end of the Trail Fork fault system is paralleled by numerous closely spaced small faults and marked by joints of many orientations. The ends of fault zones in the system are not sharply defined, in contrast to small faults, and slip is shared relatively evenly with the flanking small faults. Mechanical analyses indicate that slip on the clustered small faults 1) diffuses the shear stress concentration at the end of the larger fault zones; and 2) redistributes stress such that fractures near fault zone tips will be less likely to form, and be less likely to form at a preferred orientation. These effects reduce a fault's ability to grow as a shear fracture, impede physical linkage, and therefore could cause faults to terminate regardless of the specific mechanism of fault growth. Because faults interact with different features on different length scales, and because the length scale of a fault increases during fault growth, the processes of fault termination, and hence fault growth, seems almost certain to depend on scale.

Chapter 3

Slicing up the San Francisco Bay

Area:

Block kinematics and fault slip rates from GPS-derived surface velocities

3.1 ABSTRACT

Observations of surface deformation allow us to determine the kinematics of faults in the San Francisco Bay Area. We present the Bay Area Velocity Unification (BÄVÜ, “Bay-View”), a new compilation of over 200 horizontal surface velocities computed from campaign-style and continuous Global Positioning System (GPS) observations from 1993-2003. We interpret this interseismic velocity field using a 3-D block model to determine the relative contributions of block motion, elastic strain accumulation, and shallow aseismic creep. The total relative motion between the Pacific plate and the rigid Sierra Nevada/Great Valley (SNGV) microplate is $37.9 \pm 0.6 \text{ mm} \cdot \text{yr}^{-1}$ directed towards $N30.4^\circ W \pm 0.8^\circ$ at the latitude of San Francisco ($\pm 2\sigma$). Fault slip rates from our preferred model are generally in agreement with geologic estimates. The strike-slip rate on the San Gregorio fault of $2.4 \pm 0.5 \text{ mm} \cdot \text{yr}^{-1}$ is constrained by global stations from throughout the Pacific plate as well as local Bay Area stations. We find notable slip on two faults that have not been previously discussed in great detail, both indicative of substantial slip east of the central Bay Area: the West Napa fault ($4.0 \pm 3.0 \text{ mm} \cdot \text{yr}^{-1}$) and a fault or zone of faulting along the eastern margin of the Coast Range ($5.4 \pm 1.0 \text{ mm} \cdot \text{yr}^{-1}$). We

find that the Mount Diablo thrust system allows slip to transfer from the Greenville fault to the Concord/Green Valley fault system, and accommodates $3.9 \pm 0.5 \text{ mm} \cdot \text{yr}^{-1}$ of reverse-slip as well as $4.2 \pm 0.5 \text{ mm} \cdot \text{yr}^{-1}$ of right-lateral strike-slip. Geodetic data permit slip on the northern Calaveras to step either west or east, with our preferred model including slip being partitioned between both the West Napa and Concord/Green Valley fault systems. We resolve $< 3 \text{ mm} \cdot \text{yr}^{-1}$ of convergence perpendicular to the mapped strike of faults along the eastern margin of the Coast Range, but this is balanced by almost equal amounts of extension west of the Bay in our models such that the total convergence across the Bay Area is negligible. The poles of rotation for blocks within the Bay Area are located between the North America-Pacific and North America-SNGV poles, with a progression from west to east. The orientation of present-day relative plate motion cannot explain the strike of most Bay Area faults, but fault strike does loosely correlate with inferred plate motions at the time each fault initiated.

3.2 Introduction

The San Francisco Bay Area hosts a complex plate boundary fault system with large, seismogenic faults that pose a significant hazard to the local urban population. Faults in the Bay Area are predominantly locked at the surface while steady plate-boundary motion continues to deform the surrounding crust. Monitoring this surface deformation allows us to determine block offset and strain accumulation along the faults. Geodetic monitoring of faults in the Bay Area has been a major effort of the scientific community since Reid first formulated the elastic rebound theory [Reid, 1910]. The development of modern survey techniques such as the Global Positioning System (GPS) allows enhanced measurement precision. A number of studies have reported the results of GPS deformation fields and their estimates of the slip distribution on Bay Area faults [Savage *et al.*, 1998; Freymueller *et al.*, 1999; Savage *et al.*, 1999; Murray and Segall, 2001; Prescott *et al.*, 2001]. Studies have also used combinations of GPS and terrestrial geodetic measurements to determine distribution of aseismic creep at depth on the Hayward [Bürgmann *et al.*, 2000; Simpson *et al.*, 2001; Malservisi *et al.*, 2003; Schmidt *et al.*, 2004] and Calaveras [Manaker *et al.*, 2003] faults. While most of these studies assume that deformation occurs at a constant rate over the period of observation, a few geodetic studies focus on transient deformation. Such transients include coseismic offset in the 1868 Hayward fault earthquake [Yu and Segall, 1996], the 1906 San Andreas fault earthquake [Thatcher *et al.*, 1997], and the 1989 Loma Prieta earthquake near the San Andreas fault [Arnadottir and Segall, 1994, 1996]. Postseismic deformation has been described for the 1906 earthquake [Thatcher, 1975; Kenner and Segall, 2000] and for transient effects of the 1989 earthquake near the San Andreas [Bürgmann *et al.*, 1997] and Hayward [Lienkaemper *et al.*, 1997, 2001] faults. Through all these efforts, we have begun to understand the detailed slip distribution of Bay Area faults. Each new study brings higher precision data and more sophisticated modeling techniques employing fewer simplifying assumptions.

We present a compilation of GPS measurements for the Bay Area showing the interseismic velocity field from 1993-2003. We then interpret these velocities using a three-dimensional block model that considers the motion of regional crustal blocks and elastic strain accumulation about block-bounding faults. This modeling effort relaxes many simplifying assumptions used

in previous studies regarding fault geometry, spherical earth effects and also allows for fault perpendicular motion. We evaluate deformation at a range of scales including global tectonics, Bay Area wide deformation, and the details of fault geometry and connections on the scale of kilometers.

3.3 GPS Data and Processing

3.3.1 Data Collection

The Bay Area Velocity Unification (BĀVŪ, pronounced “Bay-View”) includes campaign GPS data collected by six different institutions (U.C. Berkeley; U.S.G.S.; Stanford; U.C. Davis; U. Alaska, Fairbanks; CalTrans) over a decade from 1993 - 2003. Transient deformation from the 1989 Loma Prieta Earthquake decayed to near zero by 1993 [*Segall et al.*, 2000], so this time period should capture relatively steady interseismic strain accumulation.

At U. C. Berkeley we occupy each benchmark in our campaign GPS networks yearly. UNAVCO archives all of our raw data online (<http://archive.unavco.org>). When possible, we collect data for at least two continuous 24-hour sessions, with some occupations spanning as long as seven days. However, much of the study area is in urban or suburban settings, making it impossible to leave GPS equipment unattended. These concerns limit the occupation time to the logistical limits of the human operator. For these sites, occupations may be as short as 6 hours or as long as 12 hours, depending upon the time it takes to travel to the site and the efficiency of the operator. We frequently repeat surveys of these sites for a total of two observations during each year. Other agencies contributing data to the BĀVŪ dataset generally follow the same guidelines and provide at least 6 hours of data per site per day, however a substantial portion of the CalTrans data is limited to 3 hours or less.

3.3.2 GPS Processing

We process campaign GPS data using the GAMIT/GLOBK software package developed at the Massachusetts Institute of Technology [*King and Bock*, 2002; *Herring*, 2002], which uses double-difference phase observations to determine baseline distances and orientations between ground-based GPS receivers. Along with campaign data, we include five global stations from the International GPS Service (IGS) network and four to six nearby continuous stations from the BARD network in our processing runs.

We combine daily ambiguity-fixed, loosely constrained solutions using the Kalman filter approach implemented by GLOBK [*Herring*, 2002]. We include data processed locally as well as solutions for the full IGS and BARD networks processed by and obtained from SOPAC at the Scripps Oceanographic Institute of U.C. San Diego. Using the Kalman filter, we combine all daily solutions to generate an average solution for each month, giving each observation equal weight. We then estimate the average linear velocity of each station in the network from these monthly files. We fix the final positions and velocities of the IGS stations into the ITRF2000

Table 3.1. Global GPS stations included in modeling of stable North America and Pacific plates.

Pacific (6)	CHAT KOKB KWJ1 MKEA TAHI THTI
North America (26)	ALGO AMC2 AOML BARN BRMU CHUR DUBO FAIR FLIN GODE KELY MDO1 MIA3 NLIB NRC1 PIE1 PRDS RCM5 RCM6 SCH2 STJO THU1 USNO WES2 WHIT YELL

No Net Rotation global reference frame [Altamimi *et al.*, 2002] using the GLORG stabilization routine, allowing for rotation and translation of the network. The stations we use to define the reference frame are listed in Table 3.1. We scale the errors following the method used by the Southern California Earthquake Center’s Crustal Motion Map version 3.0 team [SCEC CMM 3.0; Robert W. King, pers. comm., 2003]. We add white noise to the formal uncertainties of all stations with a magnitude of $2 \text{ mm} \cdot \text{yr}^{-1}$ for the horizontal components and $5 \text{ mm} \cdot \text{yr}^{-1}$ for the vertical component. To account for “benchmark wobble,” we add Markov process noise to the solutions with a magnitude of $1 \text{ mm} \cdot \text{yr}^{-\frac{1}{2}}$. We also include select velocities from SCEC CMM 3.0 [Shen *et al.*, 2003] in the Parkfield area to provide better coverage in central California.

We show the $\bar{\text{B}}\bar{\text{A}}\bar{\text{V}}\bar{\text{U}}$ GPS data for the Bay Area in Fig. 3.1 (also Table ES1*). We prefer to visualize velocities in a local reference frame centered around station LUTZ (a BARD continuous site on the Bay Block, roughly at the $\bar{\text{B}}\bar{\text{A}}\bar{\text{V}}\bar{\text{U}}$ network centroid). It accentuates the gradient in deformation across the Bay Area and allows easy visual identification of the differences between stations. We subtract LUTZ’s ITRF2000 velocity from all stations and propagate the correlations in uncertainty to get the error ellipses.

3.3.3 No Outlier Exclusion

We include velocities for all stations that have at least four total observations spanning at least three years. At no point during the data processing or modeling do we exclude data that appear to be “outliers” based on initial assumptions about plate boundary motion or model misfit. This ensures that the data truly dictate the model results, and that scatter in the data is treated formally.

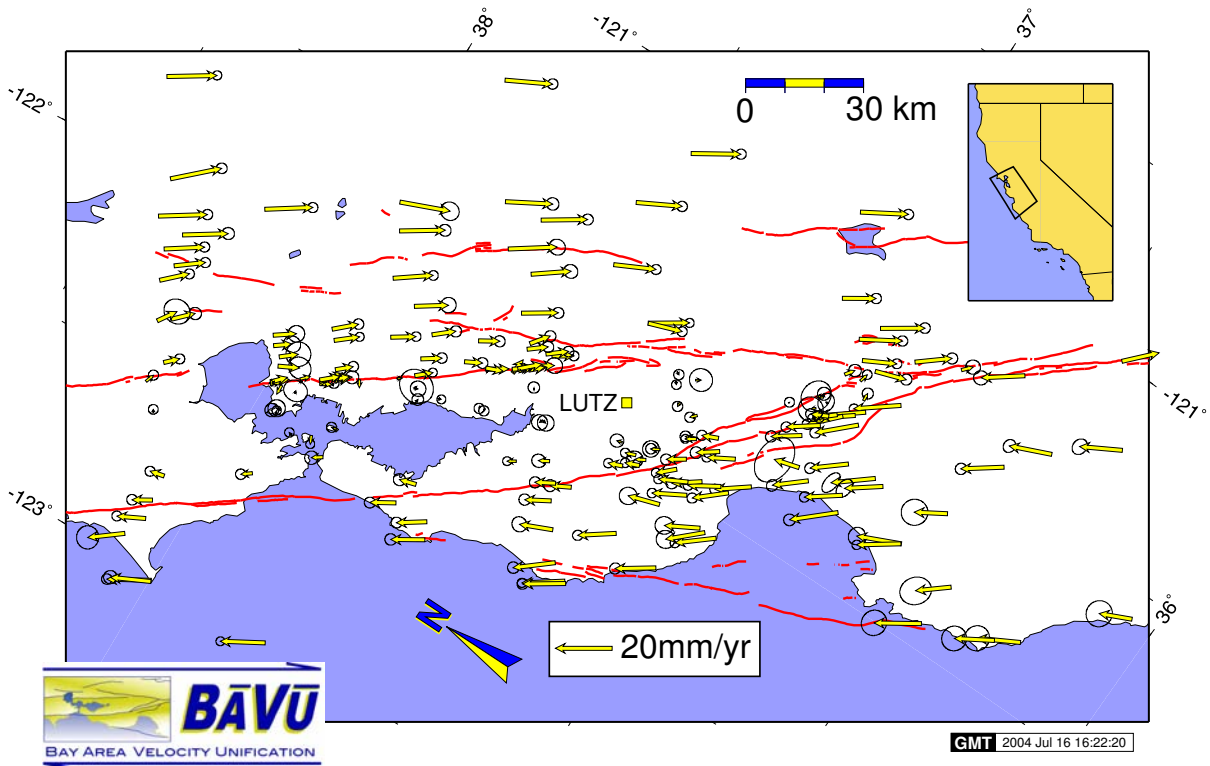


Figure 3.1. The BAVU data set. Map of the San Francisco Bay Area with GPS Velocities from 1994-2003 relative to station LUTZ in the Bay Block. The map projection is about the Pacific Plate–Sierra Nevada/Great Valley (PA-SNGV) pole of rotation, so velocities along a small circle path predicted from the rotation axis of the PA-SNGV block rotation show up as horizontal vectors.

3.4 Block Modeling Methodology

In order to calculate slip along faults at depth from observed surface deformation, we must employ interpretive models. In the following sections, we discuss the physical processes that are represented in our numerical model, including block offset, elastic strain accumulation, and shallow interseismic creep.

3.4.1 Dislocation modeling

The San Andreas fault system forms the boundary between the Pacific (PA) plate and the Sierra Nevada/Great Valley block (SNGV). Far from the fault, plate tectonic motions continue at a relatively constant rate. In the Bay Area, faults are presently locked near the surface, causing the entire region to deform elastically under the influence of this far-field plate motion. One parallel way of representing this system is to imagine that the fault itself is locked near the surface, but continues to slip at depth. *Okada* [1985] presents a useful formulation of the mathematics of this relationship for finite fault segments (“dislocations”) in an isotropic, homogeneous, linearly elastic half space. An essential assumption in dislocation modeling is that we can represent the steady long-term motion between two blocks of crust as deep slip on a discrete elastic dislocation at the boundary between the blocks. While there are a variety of other approaches to the problem, *Gilbert et al.* [1994] support this assumption with the observation that strain accumulation axes are parallel to local fault strikes rather than far-field plate motion. Models also show that geodetic data can be treated in this manner because they are insensitive to the details of the processes driving plate tectonics [*Savage*, 1990, 2000]. We therefore treat the terms “long-term” slip rate and “deep” slip rate for a fault as synonyms. While fault slip rates can be influenced by local stress perturbations from earthquakes or change over geologic time, we make the simplifying assumption that these rates are constant during the decade spanned by the BÄVÜ data set.

Okada’s equations define the relationship between slip on a given fault segment and surface displacement at each station. The equations can be used to calculate a Green’s function for the inverse problem to solve for the slip rate most consistent with the data when fault geometry is assumed. To uniquely define the Green’s function, one must specify the depth at which the fault transitions from the locked behavior near the surface to the deep, continuously slipping dislocation representing the boundary condition of long-term plate motion. The transition could reflect thermally controlled onset of plastic flow [*Sibson*, 1982] or the transition from stable to unstable frictional sliding [*Tse and Rice*, 1986; *Blanpied et al.*, 1995]. Below the transition, rocks can actively deform by plastic creep. For geodetic modeling, this transition is often called the “locking depth” (LD). Dislocation models usually solve for a uniform slip rate at all depths below LD, but the transition in reality may occur gradually over a wider zone. To account for the fact that a fault may not be completely locked at all depths above the transition, additional finite dislocations can be added to an inversion, each with a uniform slip rate covering a patch of the fault surface.

The fault segments in dislocation modeling are mathematically independent of one another and the best statistical fit to the data frequently juxtaposes segments with unrealistically high

slip and very low slip. Since such strong slip heterogeneity would require very high stress concentrations, it is considered physically unreasonable and spatial smoothing is often applied to stabilize the results. The exact smoothing parameters chosen can alter the inferred peak slip and distribution of slip – sometimes changing the character and interpretation of the results [e.g., *Segall and Harris, 1987*].

3.4.2 Block Modeling

Block modeling is an extension of dislocation modeling, but instead of allowing each segment to be independent, we add the additional physical constraint that dislocations form the boundaries of rigid plates, or “blocks” [e.g., *Bennett et al., 1996; Murray and Segall, 2001; McCaffrey, 2002*]. The amount of slip along each dislocation must therefore be consistent with the motion of the entire block, resulting in continuity of slip on adjacent fault segments without a positivity constraint or artificial smoothing. Here we use an extension of the block modeling code by *Meade et al.* [2002, , also has a concise introduction to block modeling] and *Meade and Hager* [2004, , latest formulation of the methodology].

In block modeling, we define blocks on a spherical earth (analogous to plates) bounded by faults. Defining the model geometry therefore requires more information than dislocation modeling because the location of fault connections must be known so that the faults form a continuous boundary around every block (Section 3.4.4). Each block rotates about a “rotation axis” passing through the center of the earth and intersecting the surface at a “pole of rotation” (sometimes referred to as an “Euler pole”, *Cox and Hart* [1986]). The motion of individual points on a block is a result of the rigid rotation of that block plus elastic deformation due to locking of faults at the block boundaries. The motion satisfies:

$$\mathbf{v}(\mathbf{r}_i) = \boldsymbol{\Omega}_i \times \mathbf{r}_i - \sum_{f=1}^{\#Faults} \mathbf{G}_i^f \cdot \mathbf{s}^f \quad (3.1)$$

where \mathbf{r}_i is the position of station i on earth, \mathbf{v} is the predicted velocity, the first term on the right side (cross product term) represents rigid rotation about an axis passing through the center of the earth, and the second term (summation term) represents elastic strain related to fault slip on each segment. $\boldsymbol{\Omega}_i$ is the vector representing the rotation axis for the block on which station i lies. The magnitude of elastic deformation at a point is determined by the Green’s function \mathbf{G} , relating unit slip on fault f to the effect on station i , times the actual magnitude of slip on that fault, \mathbf{s}^f . Our implementation of the block model utilizes what is often referred to as the “backslip” approach to implementing strain accumulation. Essentially, strain accumulation on a fault driven by a deep dislocation that extends from the locking depth to infinite depth is mathematically equivalent to a rigid block offset plus slip on the fault between the surface and the locking depth of opposite slip sense. While this approach avoids implementing dislocations that extend to infinite depths, it assumes that the fault geometry is planar from the surface to infinite depths and causes some limitations to the block geometry that we can implement. As a result, we primarily use vertical fault segments in our model (see Section 3.6.2).

Equation 3.1 includes both $\boldsymbol{\Omega}$ and \mathbf{s} as unknown parameters. However, the slip rate of block bounding faults is a directly determined by the relative rotation of the surrounding blocks. We

can express the magnitude and azimuth of relative motion that must be accommodated along each block boundary as a function of the rotation axes. We resolve this relative motion onto the orientation of the fault that accommodates the motion, and the ratio between strike-slip and dip-slip components is controlled exclusively by the fault orientation ($\mathbf{s} = f(\boldsymbol{\Omega}$, fault strike, fault dip). Because of this relationship, we replace $\mathbf{G}_i^f \cdot \mathbf{s}^f$ in Eq. 3.1 with $\mathbf{J}_i^f \cdot \boldsymbol{\Omega}_i$, where \mathbf{J} is a matrix of partial derivatives relating a unit rotation of each component of $\boldsymbol{\Omega}$ to surface deformation from strain accumulation along block-bounding faults. Thus for each block in the model, there are only three unknown parameters – the three components of $\boldsymbol{\Omega}$. We solve this modified equation in an inverse sense where we know \mathbf{v} and we solve for the $\boldsymbol{\Omega}$ most consistent with these observed velocities.

3.4.3 Inclusion of Global Data

All stations on a given block contribute to the estimated rotation axis. We are therefore able to incorporate data from throughout the Pacific (PA) and North American (NA) plates to determine the total magnitude of relative motion that must be accommodated by Bay Area faults. As long as the assumption that the plates behave rigidly in their interiors is valid, global data far from faults provide valuable constraints. (Strictly speaking, we treat the blocks as purely elastic. Because the blocks are so large, points near the plate interior are virtually unaffected by elastic strain at the block boundaries. Hence, we refer to block interiors as “rigid.”) However, it is not our goal to estimate all global plate motions. Other than the blocks defined within the Bay Area, we only include data and define block boundaries for the PA, NA, and SNGV plates so that we are not biased by uncertainties in the motion of other global plates outside our area of interest. Figure 3.2 shows the distribution of global stations that we use.

Our block geometry includes a boundary between the SNGV and North American plates along the Eastern California Shear Zone (ECSZ) (Fig. 3.3). We exclude sites GOLD and GOL2 from our modeling because they are within the ECSZ and affected by complex local fault geometry that is not within our area of interest [McClusky *et al.*, 2001]. While the SNGV block is thought to behave rigidly [Argus and Gordon, 1991], the Basin and Range between eastern California and the Colorado Plateau is an area of distributed deformation [Thatcher *et al.*, 1999; Bennett *et al.*, 2003]. We do not include data from within the Basin and Range, so we are insensitive to the details of how deformation is distributed across it. Our ECSZ boundary is therefore a proxy for the total deformation in the Basin and Range between the SNGV and stable North America.

3.4.4 Fault Geometry

The geometry of faults, particularly in the presence of branching faults, can have a dramatic effect on the distribution of slip between them [e.g., d’Alessio and Martel, 2004a]. With block-modeling, we face a difficult challenge in defining the precise fault geometry, especially at fault branches and other connections which are not well defined in the Bay Area. Recent geologic and geomorphic mapping efforts throughout the Bay Area, and especially in the northern East Bay



Figure 3.2. Observed global GPS velocities shown in ITRF2000 No Net Rotation (NNR) reference frame. Figure shows only stations included in modeling, but BÄVÜ includes additional global stations from reference frame stabilization. We transform the data into a stable North America reference frame for modeling.

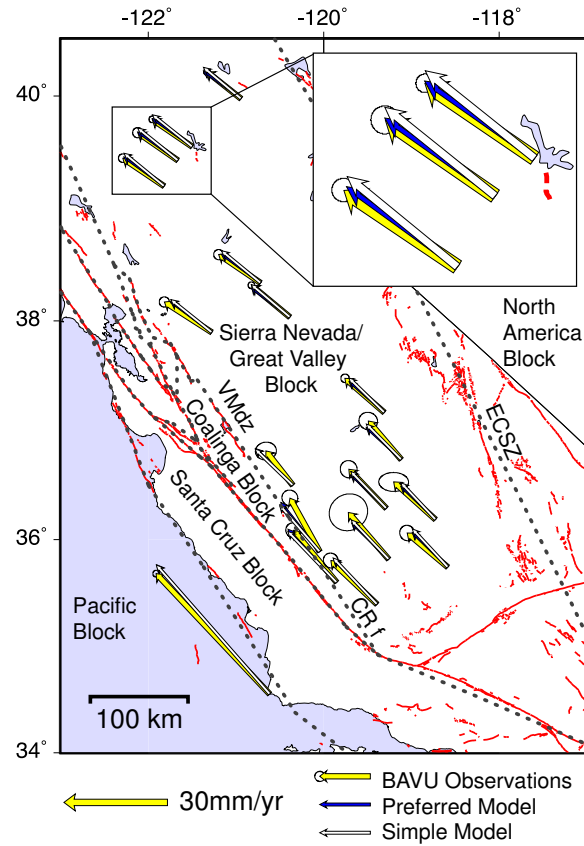


Figure 3.3. GPS observations within California, shown in a reference frame with stable north America (wide vectors with error ellipses) compared with model results (narrow vectors). Dark sinuous lines are Holocene active faults. Dotted grey lines show a representative model geometry from our Complex model that includes all segments. We label select blocks and faults outside the Bay Area. VMdz = Valley Margin deformation zone; ECSZ = Eastern California Shear Zone. The inset shows an enlargement of the area where the two models differ most in the northern section of the figure. Our Preferred model with a Valley Margin deformation zone (darker vectors) fit the data better than models that exclude this fault (Simple model, white vectors).

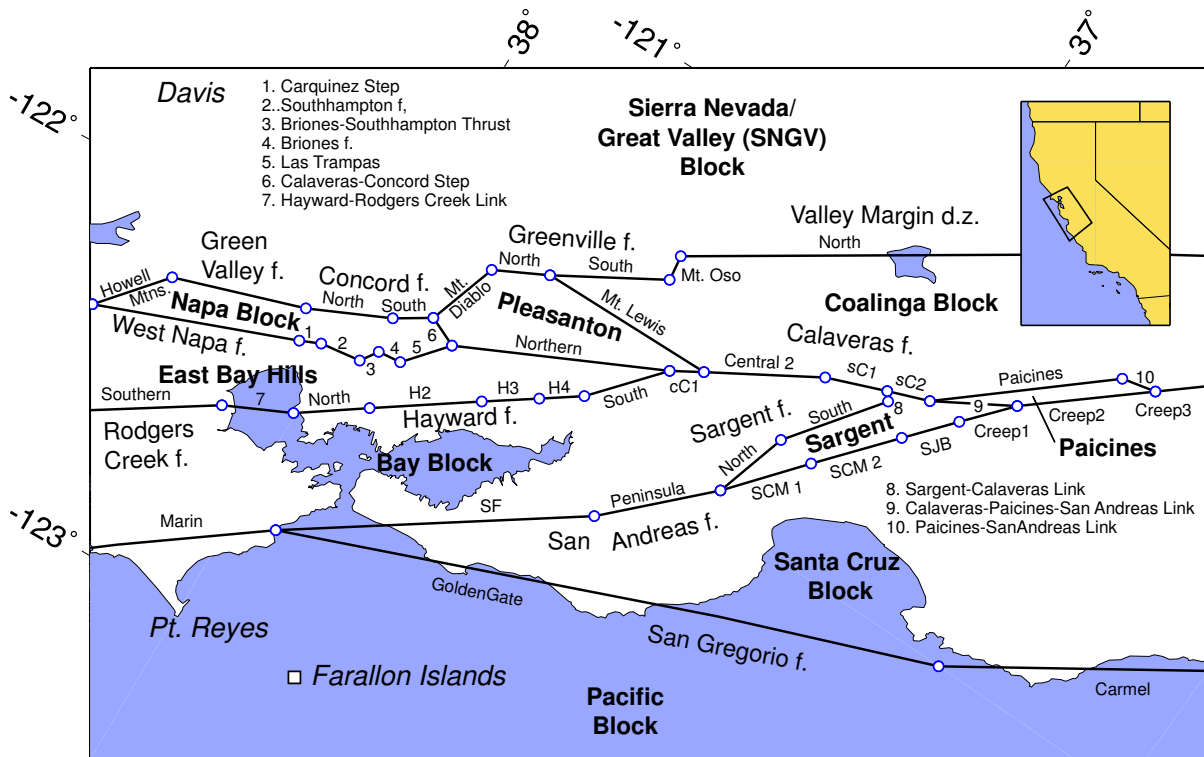


Figure 3.4. Model fault segments in the Bay Area. Note that not all segments are used in all model variations. Block names in large, bold text. Fault names in larger plain text and names of sub-segments of those faults in smaller text. Place names in italics. Abbreviations: cC = central Calaveras; sC = southern Calaveras; SF = San Francisco; SCM = Santa Cruz Mountains; SJB = San Juan Bautista; f. = fault. See also Table 3.2.

Area, provide new constraints on the details of fault geometry [Jeff Unruh, pers. comm., 2004]. We define faults in our model using a combination of several data types: 1) Mapped surface traces of faults; 2) Relocated microseismicity; 3) Topographic lineaments; and 4) Interpreted geologic cross sections.

We have explored dozens of variations on model geometry including a wide range of complexities. Our goals are to determine the simplest model that explains the data and test competing model geometries to determine if they are consistent with the geodetic data. Figure 3.4 and Table 3.2 show model fault segments presented in this manuscript and Table 3.3 describes the variations we discuss. We include models that range in complexity from intentionally oversimplified (such as “TwoPlate”) to those that are likely beyond the resolving power of our data (“Complex”).

Table 3.2. Definition of model geometry. Fault systems are listed from west to east, with individual fault segments listed from north to south. Columns 2 - 5 show longitude (Lon) and latitude (Lat) of starting and ending points of each segment. LD = Locking depth, based on D_{95} . LD of zero indicates only block motion across a segment with no strain accumulation. Such faults are either known to be creeping (central San Andreas) or are short connecting segments with unknown geometry. Creep column indicates the *a priori* constraint and 1σ bounds placed on the shallow slip rate (uniform rate from the surface to the locking depth). If no rate is given, we assume the fault is locked above LD and do not solve for shallow slip on that segment. Last column indicates model geometries in which the segment appears: S = Simple; P= Preferred; C=Complex.

Name	Lon _{start} °E	Lat _{start} °N	Lon _{end} °E	Lat _{end} °N	L.D. km	Creep $mm \cdot yr^{-1}$	Models
SanGregorio_GoldenGate	-122.673	37.905	-122.000	36.501	13	–	SPC
SanGregorio_CarmelSouth	-122.000	36.501	-121.375	35.750	14	–	SPC
SanAndreas_Mendocino	-124.241	40.264	-123.690	38.999	15	–	SPC
SanAndreas_Marin	-123.690	38.999	-122.673	37.905	15	–	SPC
SanAndreas_SF	-122.673	37.905	-122.174	37.324	12	–	SPC
SanAndreas_Peninsula	-122.174	37.324	-121.926	37.120	14	–	SPC
SanAndreas_SantaCruzMountains1	-121.926	37.120	-121.729	36.985	15	–	SPC
SanAndreas_SantaCruzMountains2	-121.729	36.985	-121.533	36.850	15	^a	SPC
SanAndreas_SanJuanBautista	-121.533	36.850	-121.409	36.765	10	14.0 ± 2.0	SPC
SanAndreas_Creep1	-121.409	36.765	-121.286	36.679	0	–	SPC
SanAndreas_Creep2	-121.286	36.679	-121.042	36.448	0	–	SPC
SanAndreas_Creep3	-121.042	36.448	-120.614	36.052	0	–	SPC
SanAndreas_ParkfieldTransition	-120.614	36.052	-120.359	35.814	10	–	SPC
RodgersCreek_North	-123.551	39.756	-122.979	38.810	10	–	SPC
RodgersCreek_South	-122.979	38.810	-122.450	38.147	10	–	SPC
HaywardRodgersCreekStepover	-122.450	38.147	-122.368	38.004	0	–	SPC
Hayward_North	-122.368	38.004	-122.247	37.867	10	4.6 ± 0.5	SPC
Hayward_2	-122.247	37.867	-122.070	37.666	12	3.6 ± 0.5	SPC
Hayward_3	-122.070	37.666	-121.980	37.563	11	5.2 ± 0.3	SPC
Hayward_4	-121.980	37.563	-121.909	37.482	11	4.4 ± 0.5	SPC
Hayward_South	-121.909	37.482	-121.725	37.355	10	–	SPC
WestNapa	-122.389	38.501	-122.188	38.074	11	–	SPC
Calaveras_CarquinezStepover	-122.188	38.074	-122.164	38.030	11	–	PC
SouthHampton	-122.164	38.030	-122.149	37.939	12	–	PC
BrionesSouthHamptonThrust	-122.149	37.939	-122.102	37.914	12	–	PC
Briones	-122.102	37.914	-122.095	37.862	12	–	PC
LasTrampas	-122.095	37.862	-121.982	37.785	12	–	PC
Calaveras_Northern	-121.982	37.785	-121.725	37.355	12	3.0 ± 0.8	SPC
Calaveras_Central1	-121.725	37.355	-121.677	37.290	9	9.4 ± 2.0	SPC
Calaveras_Central2	-121.677	37.290	-121.510	37.062	9	14.0 ± 0.2^b	SPC
Calaveras_Southern1	-121.510	37.062	-121.449	36.933	9	10.6 ± 2.0	SPC
Calaveras_Southern2	-121.449	36.933	-121.407	36.843	9	10.6 ± 2.0	SPC
GreenValley_HowellMtns	-122.389	38.501	-122.215	38.380	0	–	SPC
GreenValley	-122.215	38.380	-122.102	38.098	11	4.4 ± 0.4	SPC
Concord_North	-122.102	38.098	-122.003	37.925	16	3.6 ± 0.3	SPC
Concord_South	-122.003	37.925	-121.944	37.851	16	2.7 ± 0.3	SPC
Calaveras_ConcordStep	-121.944	37.851	-121.944	37.851	15	–	SPC
MtDiabloThrust	-121.944	37.851	-121.749	37.797	17	–	SPC
Greenville_North	-121.749	37.797	-121.678	37.684	18	–	SPC
Greenville_South	-121.678	37.684	-121.516	37.460	18	–	PC
MtOsoAnticline	-121.516	37.460	-121.445	37.467	18	–	PC
ValleyMargin_North	-121.445	37.467	-120.398	36.202	18	–	PC
ValleyMargin_South	-120.398	36.202	-119.385	34.929	18	–	PC
Sargent_North	-121.926	37.120	-121.720	37.069	12	–	C
Sargent_South	-121.720	37.069	-121.471	36.919	10	2.9 ± 0.7	C
SargentClosure	-121.471	36.919	-121.449	36.933	0	–	C
MtLewisTrend	-121.678	37.684	-121.677	37.290	9	–	SC ^c
CalaverasSanAndreasPaicinesConnector	-121.407	36.843	-121.286	36.679	0	–	C
Paicines_North	-121.407	36.843	-121.064	36.523	9	6.0 ± 2.0	SPC
Paicines_South	-121.064	36.523	-121.042	36.448	0	–	SPC
ECSZ	-119.420	39.000	-116.249	33.804	15	–	SPC

Table 3.3. Model name abbreviation key, listed in order of increasing complexity. The second section of the table shows abbreviations for variations on the 5 main models.

<i>TwoPlate</i>	Pure block offset between Pacific and North America. Excludes all GPS data in California and near plate boundaries. Included for comparison with previous global studies.
<i>Simple</i>	Includes the block offset, strain accumulation, and shallow creep on the major Bay Area faults as well as an ECSZ along the east edge of the Sierra Nevada range. Slip transfers from the Calaveras to the Greenville fault via the Mt. Lewis trend. The Calaveras connects to the Concord/Green Valley system eastward across a right step.
<i>Preferred</i>	Similar to the Simple model but slip on the Greenville fault connects to a fault running along the west edge of the Great Valley (“Valley Margin deformation zone”), and no Mt. Lewis trend is included. Calaveras connects to both the West Napa fault to the west and the Concord fault to the east. Preferred is our reference for comparison between the models and the basis for exploration of locking depths or geometric variations.
<i>Complex</i>	Includes all the faults in the Preferred model, along with more complex connections between the Calaveras and San Andreas faults, a Sargent fault, and a Mt. Lewis trend. This model is probably overly complex given our data resolution.
<i>Calaveras West</i>	Forces all slip on the northern Calaveras to transfer in a left-stepping sense onto the West Napa fault.
<i>Calaveras East</i>	Forces all slip on the northern Calaveras to transfer across a right step to the Concord fault.
<i>LD= D₉₅ + 1</i>	Models where we explore locking depth variations. Locking depths start out equal to D_{95} , and then we shift them uniformly up or down by the given amount. Note: In our sign convention, +1 makes the locking depth deeper by 1 km, while -1 is closer to the surface.
<i>LD=13</i>	Sets the locking depth of all faults in the model equal to a uniform value (in this case, 13 km).
<i>MtLewis=2</i>	Imposes an <i>a priori</i> constraint on the slip rate of a single segment (in this case, the Mt. Lewis trend is set to $2 \pm 2mm \cdot yr^{-1}$).

Fault Connections

Faults that are connected can transfer slip between one another and potentially rupture together in large earthquakes. Knowing if two faults connect, as well as the location and geometry of that connection, is therefore important in determining the seismic hazard associated with each fault [e.g., *Harris and Day, 1999*]. Such connections are often not mapped, or are mapped with such complexity that we must simplify their geometry. To define the block boundaries, we must make inferences about these connections. While these inferences add non-uniqueness to our models, this feature of block modeling also allows us to test various scenarios of fault connections to see if they are consistent with our observed surface deformation rates.

3.4.5 Surface Creep

A number of faults in the Bay Area exhibit surface creep and aseismic creep at depths shallower than the seismic/aseismic transition [see the comprehensive compilation of *Galehouse and Lienkaemper, 2003*]. Conclusions from detailed geodetic inverse modeling [*Manaker et al., 2003*; *Schmidt et al., 2004*], as well as comparisons between surface creep and geologic slip rates determined from paleoseismology show that the slip rate on the shallow portions of the fault during the interseismic period can be much slower than the deep slip rate [e.g., *Simpson et al., 2001*]. Faults in the Bay Area that creep at the surface can slip as slow as 10% of the deep slip rate or as fast as the full deep slip rate [*Bakun, 2003*; *Prescott et al., 2003*]. To simulate the effects of near-surface aseismic creep, we model shallow slip as a dislocation with uniform slip that runs from the surface to a certain “transition depth” (TD). The TD must be \leq the fault locking depth (LD) because, by definition, the fault slips at a uniform rate below LD. The fault is locked at depths between TD and LD. Because the detailed distribution of creep at depth is not well known on all Bay Area faults, we assume the simplest case where TD=LD (the fault creeps at one uniform rate from the surface to LD, where it transitions to its deep slip rate at all depths below LD). We explore the depth sensitivity of TD in Section 3.6.6.

The shallow dislocation representing aseismic creep is completely independent from the block motion and is permitted to slip at any rate slower or faster than the deep slip rate if the data favor such behavior. We add a new term to Equation 3.1:

$$\mathbf{v}(\mathbf{r}_i) = \boldsymbol{\Omega}_i \times \mathbf{r}_i - \sum_{f=1}^{\#Faults} \left[\mathbf{G}_i^f \cdot \mathbf{s}^f(\boldsymbol{\Omega}_i) - \mathbf{G}_{creep,i}^f \cdot c^f \right] \quad (3.2)$$

where $\mathbf{G}_{creep,i}^f$ is the Green’s function relating slip between the surface and the transition depth on fault f to deformation at station i . Unlike the deep slip rate, \mathbf{s} , that is a function of the block rotation, $\boldsymbol{\Omega}$, the shallow creep rate, c , is a new model parameter that must be estimated. For segments where *Galehouse and Lienkaemper* [2003] observe a surface creep magnitude less than $1 \text{ mm} \cdot \text{yr}^{-1}$, we do not solve for a shallow dislocation and keep the fault completely locked above its locking depth. We only consider strike-slip motion on shallow dislocations, so c is a scalar.

BÄVÜ includes more than 60 stations within 15 km of the Hayward fault (Fig. 3.5), so we solve for 4 different shallow dislocations along strike. However, it is not possible to reliably

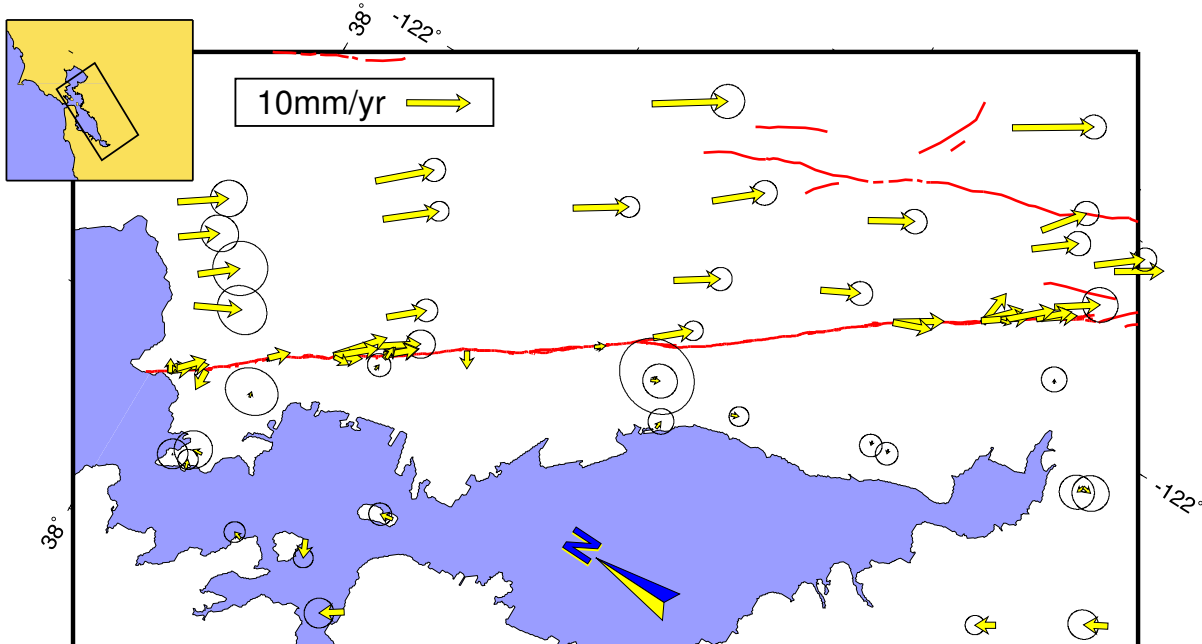


Figure 3.5. Map of deformation near the Hayward fault. See caption to Fig. 3.1. Here, stations adjacent to the Hayward fault are plotted without their error ellipses for clarity. The magnitude of the error ellipses are typically the size of the largest error ellipses on the map.

constrain the surface creep rate for some Bay Area faults with GPS data alone because the stations are not typically located within a few kilometers of the fault. We therefore include the surface slip rates summarized in *Galehouse and Lienkaemper [2003]* as *a priori* constraints for the shallow slip rates with *a priori* uncertainties equal to the published uncertainties that include a random walk component. These uncertainties are sufficiently large such that the creep rate is determined largely by GPS data where stations are close enough to a fault to resolve shallow slip. Where data are absent, the *a priori* constraint stabilizes the inversion. Where segments span multiple observed surface creep rates that differ by values greater than their one-sigma confidence interval, we combine these values as weighted averages to determine a single constraint.

3.5 Results

We evaluated over 100 different variations on fault geometry to determine the models most consistent with the geodetic data and mapped faults. We report only a small subset of these models, highlighting the key parameters that affect model fit. Changes in model geometry (including fault connections, location, orientation, and locking depth) can affect the inferred fault slip rates greater than indicated by the formally propagated uncertainties from the inverse problem, which are typically $< 1.5 \text{ mm} \cdot \text{yr}^{-1}$ at the 95% confidence level. For the range of

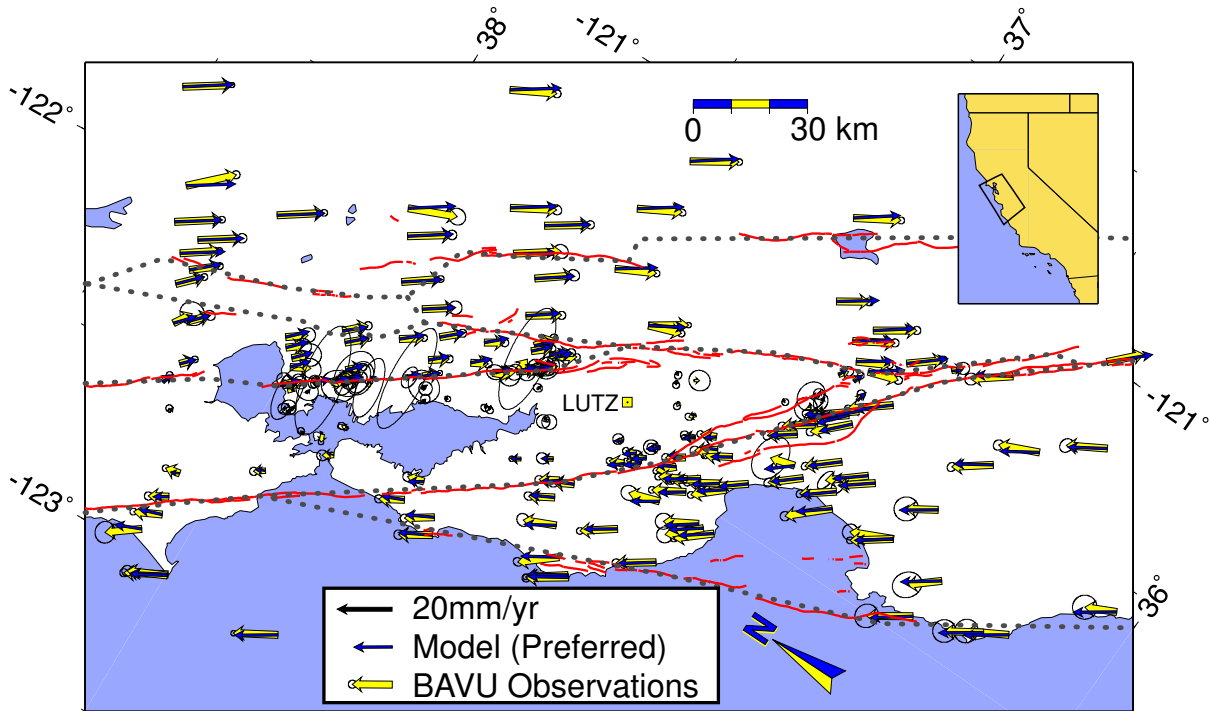


Figure 3.6. Observations (wider vectors with error ellipses) compared with model results (narrow, darker vectors) for our Preferred model. Dotted grey lines on top of mapped fault traces are model geometry.

reasonable geometries we test, the slip rates on almost all faults are within $\pm 3 \text{ mm} \cdot \text{yr}^{-1}$ of the Preferred model, which we consider to be representative of the actual confidence interval of our slip rate estimates. For quantitative comparisons, we restrict our analyses to the formal uncertainties but note that this variation should be considered when interpreting our results.

To evaluate the effectiveness of the block model, we compare the input GPS velocities to model estimates calculated from the best-fitting parameters. Figure 3.3 and 3.6 show observed and modeled GPS velocities for our Preferred model at the scale of all California and the Bay Area, respectively. Overall, the model predictions agree quite well with the observations and we capture many of the details of deformation across the Bay Area. Examining the “residuals,” or the difference between the data and model allows a more detailed comparison of the systematic differences between observations and predictions for several model variations (Fig. 3.7).

We quantify the goodness of fit in terms of the χ^2 and χ^2/DOF statistics:

$$\chi^2 = \sum_{c=1}^{\#data} \left(\frac{v_c^{model} - v_c^{data}}{\sigma_c} \right)^2 \quad (3.3)$$

$$\chi^2/DOF = \frac{\chi^2}{\#data - \#model \text{ parameters}} \quad (3.4)$$

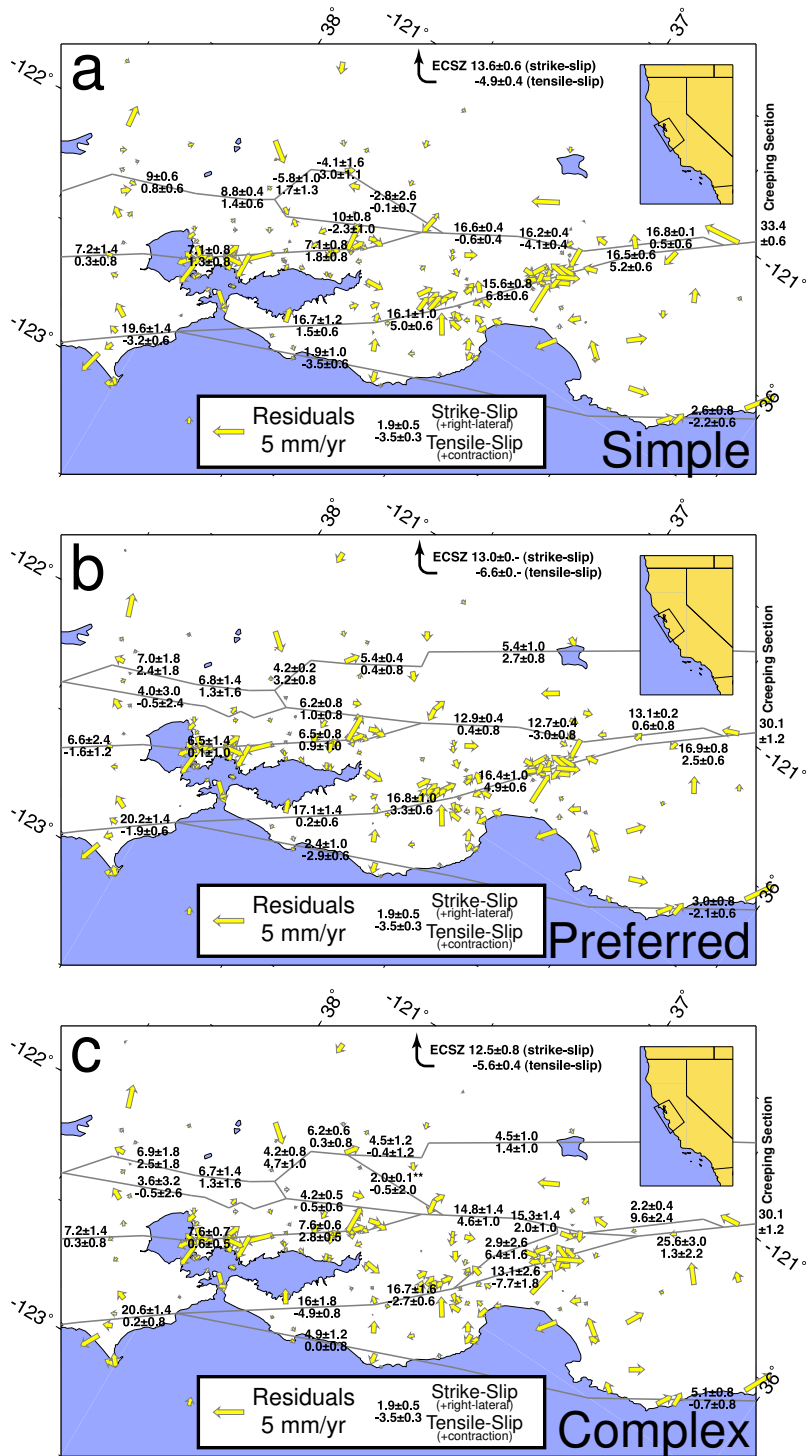


Figure 3.7. Difference between observed GPS velocities and model calculations for three different model scenarios. Numbers indicate strike-slip and tensile-slip rates and 95% (2σ) uncertainties for select fault segments. Positive strike-slip indicates right-lateral slip. Positive tensile-slip indicates contraction while negative tensile-slip indicates extension.

where v_c^{model} and v_c^{data} are the predicted observed velocity components, and σ_c is the 1σ uncertainty for each component of the input GPS velocities. The number of degrees of freedom (DOF) is defined by: $\#data$, the number of GPS components used as input data (east and north component for each station, as well as any *a priori* constraints) and $\#modelparameters$, the number of model parameters that we solve for in the inversion (pole of rotation latitude and longitude, rotation rate, and shallow creep rate for creeping segments). These statistics indicate how well the model fit the data within their uncertainty bounds. Lower values of χ^2 indicate a better fit to the data. χ^2 can be calculated for a single data component or summed over subsets of the model, including both horizontal components at a single station or the entire model. Increasing the number of model parameters inevitably leads to better fits and lower total χ^2 . Dividing by the number of degrees of freedom (DOF) helps us compare models where we solve for a different number of free parameters, but χ^2/DOF ignores all correlations between parameters. Because these correlations change as model geometry changes, caution should be exercised in making strictly quantitative comparisons of models using χ^2/DOF alone. Nonetheless, the statistics do provide a basis for qualitative comparisons. For uncorrelated parameters, a χ^2/DOF of 1 indicates that, on average, all the predicted velocities are consistent with the 1σ standard deviation of the input data. In Table 3.4, we present misfit statistics for the models we discuss. We typically obtain χ^2/DOF of 3-4, which is partly the result of the χ^2 statistic’s strong sensitivity to outliers. Because of these outliers, we emphasize the spatial distribution of the contribution to χ^2 when comparing models.

In the following sections, we look in detail at the model results at a range of scales from global motions to the details of fault connections and stepovers.

3.5.1 Global Plate Motion

To verify that our block model provides valid constraints on the total relative plate motion, we compare them with previously published results in Table 3.5. Our estimates of relative rotation axes incorporate the effect of elastic strain accumulation while the previous studies of block motion typically exclude data from near plate boundaries. With the exception of NUVEL-1A and *DeMets and Dixon* [1999], each study shown is based on geodetic measurements using VLBI and/or GPS. In general, the geodetic measurements show a relative pole of rotation between the Pacific and North American plates that is further to the northeast and faster than the average rate for the last 3 Ma determined from geologic data [NUVEL-1A, *DeMets et al.*, 1994]. Variations in the estimated rotation axes from each study stem not only from the different quality data sets available to each author at the time of publication, but also the stations they use to define each rigid plate. To verify the quality of the BÄVÜ global velocities, we use our block modeling code and the identical subset of stations from *Steblov et al.* [2003]. Our results agree almost identically to their published results, though our propagated uncertainties are slightly smaller. In our model called “TwoPlate,” we include all 21 North American and 6 Pacific sites from BÄVÜ that are further than 100 km from a plate boundary. The pole of rotation from TwoPlate is 1.7° east, 1.3° north, and 0.5% slower than the *Steblov et al.* [2003] pole, but the change is not significant at the 95% confidence level. The estimated pole from our “Preferred” model is about 0.9° east, 1.1° north, and 0.9% slower than the *Steblov et al.*

Table 3.4. Misfit statistics for different models. Note that TwoPlate excludes all data within 100 km of the plate boundary.

Model	χ^2	DOF	χ^2/DOF
TWOPLATE	138.9	45	3.09
SIMPLE	2053.8	520	3.95
PREFERRED	1880.0	517	3.64
COMPLEX	1704.8	510	3.34
Variations on models			
CalaverasWest	1932.5	520	3.72
CalaverasEast	1910.7	520	3.67
Preferred, Thrust	1887.9	517	3.65
Preferred, Unclamped	1871.1	514	3.64
Preferred, LD= $D_{95} - 8$	1911.9	517	3.70
Preferred, LD= $D_{95} - 5$	1795.5	517	3.47
Preferred, LD= $D_{95} + 5$	2053.9	517	3.97
Preferred, LD=5	1923.0	517	3.72
Preferred, LD=8	1805.9	517	3.49
Preferred, LD=13	1875.0	517	3.63
Preferred, LD=18	2047.1	517	3.96
Preferred, TD=5	1997.9	517	3.86
Preferred, TD= $D_{95}/2$	1986.5	517	3.84
Preferred, WG03	3675.7	539	6.82

[2003] pole. Globally, our data set and block modeling produce reasonable estimates of block motion.

Locally, the slight changes in the NA-PA rotation axis are insignificant. Table 3.6 shows the rate at the Farallon Islands station, FARB, predicted from the NA-PA rotation axis. The station is located on the Pacific plate about 36 km west of the San Andreas fault and its velocity is sometimes used as a proxy for the total relative motion between the Pacific and North American or SNGV plates [e.g., Table 4 of *Prescott et al.*, 2001]. The long term rate of block offset is higher than the current observed velocity at FARB. Strain accumulation along Bay Area faults “slows down” FARB by about $3 \text{ mm} \cdot \text{yr}^{-1}$. As such, the observed rate of FARB is not representative of pure Pacific plate motion and should not be directly compared with studies that ignore elastic strain accumulation.

3.5.2 Sierra Nevada / Great Valley Block

Focusing in on California, the Sierra Nevada/Great Valley (SNGV) block is a rigid block that lies at the eastern margin of the Bay Area. Often referred to as a microplate, the relative motion of the SNGV is not as well constrained as larger plates because of the limited size of the block and relatively sparse data. By including stations from throughout northern and southern California along with strain accumulation near the block boundaries, our block model provides an improved constraint on the total PA-SNGV motion that must be accommodated by Bay Area faults. Table 3.5 shows our estimates of the relative motion between PA-SNGV and NA-SNGV compared with previous studies.

In general, the NA-SNGV pole tends to lie southwest of the Bay Area in the Pacific Ocean, as far as 90° from the NA-PA pole. The relative motion expected from these two poles differs in a manner consistent with geologic observations: the relative motion vector from NA-PA in the Bay Area is oriented within a few degrees of the strike of the San Andreas system promoting nearly pure transform faulting, while the NA-SNGV motion would require a substantial amount of opening along such faults relative to the strike-slip component – a feature that manifests itself as extension on the ECSZ and in the Basin and Range further to the east. The NA-SNGV poles from previous studies vary by $> 50^\circ$ in both longitude and latitude, and our results show a similarly broad range due to slight variations in fault geometry and locking depth. These estimates seem to lie along a great circle roughly perpendicular to the average fault strike in the San Andreas fault system and are related to station geometry. The ideal station coverage for determining rotation axes covers a very broad area in all directions. The SNGV and other Bay Area blocks are elongate parallel to the San Andreas system and very narrow perpendicular to it. The orientation of elongated error ellipses for these poles is related to the elongated shape of the blocks.

The PA-SNGV pole is well constrained and located just west of Lake Superior, $\sim 20^\circ$ from the NA-PA pole. Unlike NA-SNGV, formal uncertainties for this pole location are $< 3\sigma$, and the best-fit estimates vary by only $\pm 6^\circ$ for a wide range of model geometries. The pole for PA-SNGV is more tightly constrained and is much less affected by the tradeoff between pole position and rotation rate than the NA-SNGV pole.

3.5.3 Poles of Rotation of Bay Area Blocks

Focusing in on the Bay Area itself, we can examine rotation axes of smaller blocks bounded by Bay Area faults. Figure 3.8 shows the pole of rotation of each block relative to North America. There is a systematic progression of the poles from west to east. In our Preferred model, the poles essentially transition between the NA-SNGV and NA-PA poles. The Santa Cruz block, located adjacent to the Pacific plate, rotates about a pole located near the NA-PA pole. On the other side of the Bay Area, the Coalinga block, located adjacent to the SNGV block, rotates about a pole located very close to the NA-SNGV pole. These blocks near the margins of the Bay Area move very similarly to the larger blocks that bound the region. Blocks within the Bay Area have rotation poles relative to North America in between these poles, with blocks toward the eastern side of the Bay Area tending to move more like NA-SNGV and blocks on the western side moving more like NA-PA. This pattern holds for variations in locking depth and slight variations in geometry on the Preferred model. For the Complex model, the poles of Bay Area blocks are still distributed between the NA-PA and NA-SNGV poles, but the east-west progression breaks down slightly as many of the smaller blocks rotate about poles very close to the blocks themselves. These rotations would result in gradients in slip rate along strike. With the station geometry of BÄVÜ, there is a strong trade-off between the rotation rate and distance of the poles of rotation from the Bay Area.

The limited extent of the blocks allows these different rotation axes to produce nearly identical relative motions in the Bay Area, resulting in the elongated error ellipses for these poles.

3.5.4 Slip Rates on Bay Area Faults

One of the most useful products that geodesy provides to seismic hazard estimates is constraints on the deep slip rates of faults. As described in Section 3.4.2, our block model uses GPS observations of surface deformation to calculate the best fitting deep slip rate from given block/fault geometries and locking depths. Here we present a general discussion about the effect of variations in locking depth on estimated slip rates (also see Section 3.6.6), and we present slip rates using our preferred locking depths.

Locking Depth

Frey Mueller et al. [1999] described the strong trade-off between assumed locking depth and calculated slip rate in dislocation models of the San Andreas system in northern California, making it challenging to uniquely determine the slip rate on a given fault. As a result, several methods including bootstrap resampling [*Murray et al.*, 2001] and Bayesian statistics [*Segall*, 2002] have been used to place statistical bounds on the range of most-likely slip rates given this tradeoff. Without additional physical constraints, such methods remain purely statistical descriptions of the uncertainty and do not help resolve the non-uniqueness problem. *Segall* [2002] advocates integrating prior information about the slip rates from geologic studies and

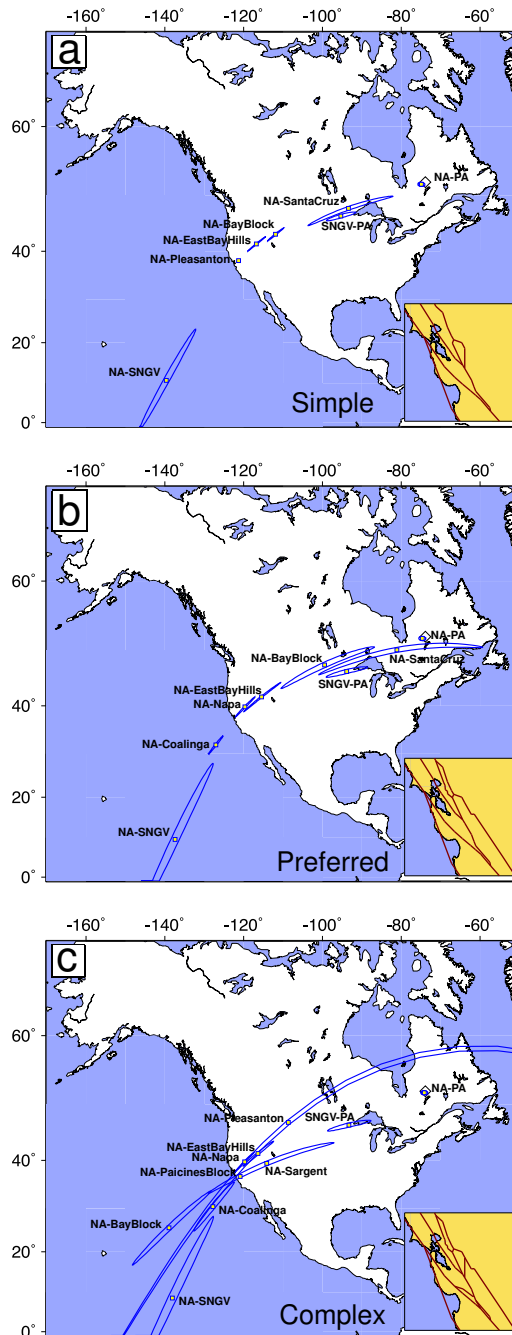


Figure 3.8. Calculated poles of rotation and 95% confidence limits for blocks in the Bay Area. Other than the Pacific-SNGV pole, all poles are relative to North America (NA). The diamond near Hudson Bay indicates the PA-NA pole for TwoPlate, which excludes data near plate boundaries.

earthquake parameters. Because one of our goals is to estimate these rates geodetically, we take an alternate approach.

The maximum depth of seismicity and surface heat flow give insight into the depth of the seismic/aseismic transition. Using this depth as a proxy for the geodetic locking depth helps reduce the ambiguity in determining slip rates. Earthquakes rarely occur below 20 km depth in the Bay Area, and the specific depth where faults become seismically quiet varies spatially throughout the region. Many geodetic studies use seismicity to define the locking depth in their models, but they sometimes neglect variations within the fault system. Here we document temporal and spatial variation in the depth of seismicity throughout the Bay Area in order to accurately determine the seismic/aseismic transition depths.

This transition is commonly quantified by the depth at which 95% of catalog seismicity occurs above and 5% occurs below, or D_{95} . *Williams* [2003] suggests that D_{95} accurately reflects the deepest extent of rupture in large earthquakes and presents the calculated values of D_{95} for Bay Area fault segments derived from high quality Northern California Seismic Network (NCSN) catalog locations from 1980-1998. We perform a similar analysis on the high precision catalog of *Waldhauser and Ellsworth* [2002]. This catalog utilizes relative relocations that have vertical precision of less than about a hundred meters. We divide the Bay Area into a data-driven grid using the quadtree algorithm with a minimum grid cell size of 0.2 degrees [*Townend and Zoback*, 2001]. Figure 3.9 shows the depth of maximum seismicity for the entire duration of the catalog (1984-2001) and a movie in the electronic supplement shows the time evolution of D_{95} . In both illustrations, grid cells are only filled with a color if there are more than 60 events during the time period indicated in the lower left. This number of events seems to produce consistent and stable values for D_{95} [*Magistrale*, 2002].

We do not utilize the D_{95} value as the locking depth for two fault segments. The Marin segment of the San Andreas fault has essentially no seismicity, so we cannot calculate D_{95} . The grid cell south and the grid cell west of it both have locking depths close to 12 km. However, using a locking depth of 15 km provides a better fit to the geodetic data.

D_{95} on the Greenville fault is very deep in the north near Mt. Diablo (18 km), but gets much shallower in grid cells to the south (other than the Geysers, these 3 grid cells have the shallowest seismicity in the Bay Area with values of 8-9 km). A much better fit is achieved to the data if the 18 km locking depth is extended further south along all of the segments, including the fault along the margin of the Great Valley. Heat flow data are sparse in this region, but available data near the Ortigalita fault range from $65 - 85 mW m^{-2}$ [*Lachenbruch and Sass*, 1980], values more consistent with a locking depth of 8-12 km, based on the relationships established by *Williams* [1996]. The model preference for a deeper locking depth results in deformation over a broader region surrounding the single block boundary in our model, which could be indicative of a broader deformation zone in this region.

Slip Rates

Deep slip rates determined by our block model are reported in Table 3.7. The total vector sum of relative motion accommodated by Bay Area faults in the Preferred model is 37.9 ± 0.6

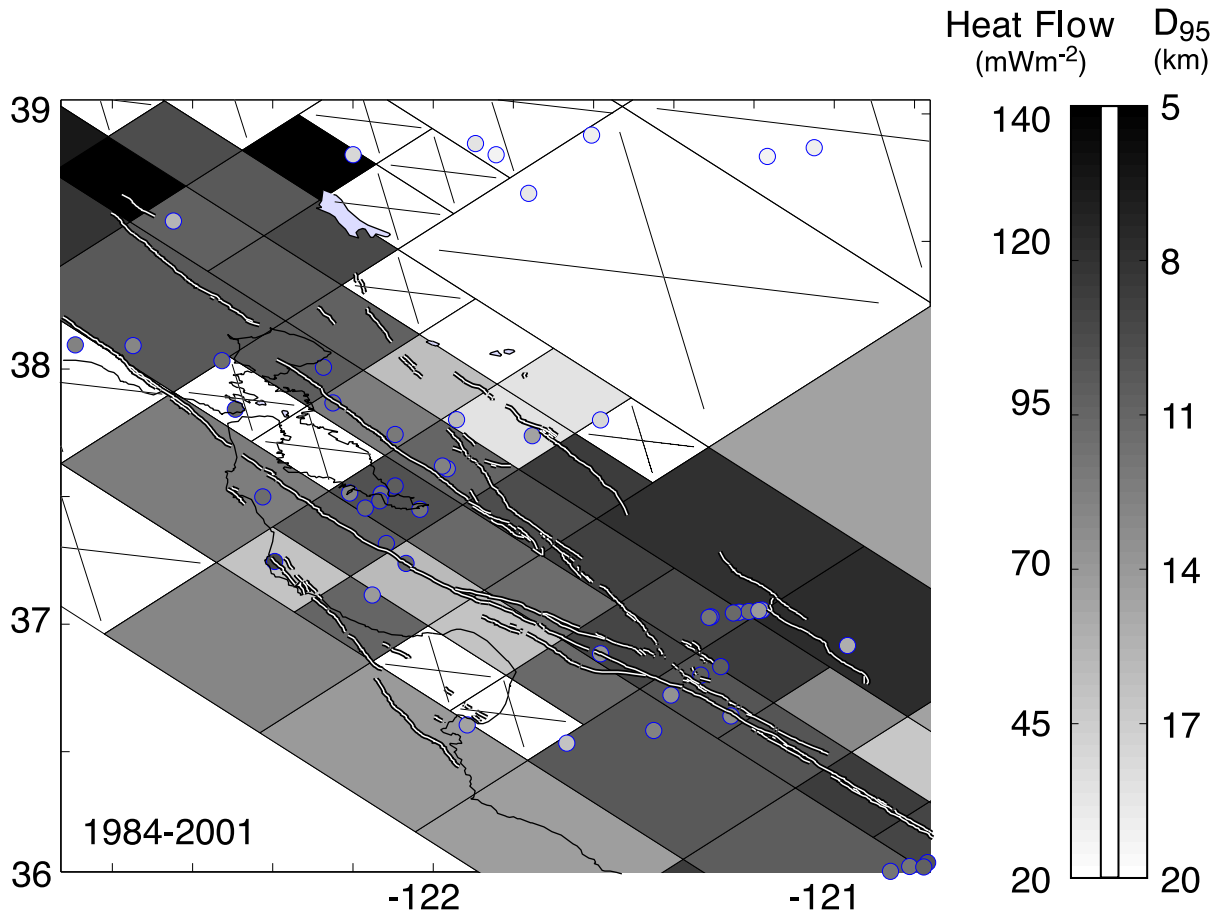


Figure 3.9. D_{95} , the depth at which 95% of the seismicity in a certain area is above and 5% is below, indicated by shading of rectangular grid cells. Earthquakes from 1984-2001 using the relative relocation catalog of *Waldhauser and Ellsworth* [2002]. Shaded circles are borehole heat flow measurements from the USGS California Heat Flow database [<http://quake.wr.usgs.gov/heatflow/>]. The two data sets are plotted using similar color schemes so that shallow D_{95} depths and high heat flows both appear in the same color. While the data sets are often well correlated, the relationship depends on rock type and may not be linear as implied by the shared color scheme [see *Magistrale*, 2002]. D_{95} not estimated for grid cells with < 60 events (cells with X's).

$mm \cdot yr^{-1}$ oriented at $N30.4^\circ W \pm 0.8^\circ$ in the central North Bay and at $N34.2^\circ W \pm 0.8^\circ$ in the central South Bay (Rate varies by 1-2 $mm \cdot yr^{-1}$ from east to west across the Bay Area, while azimuth varies by up to 8° from north to south). The simple sum of all strike-slip rates across the entire fault system for our Preferred model is 37.8 ± 4.5 and 37.7 ± 1.5 $mm \cdot yr^{-1}$ in the northern and southern Bay Area, respectively. We report slip rate uncertainties at the 95% confidence level (2σ). The total best-fit slip rate ranges from 31.5-39.3 $mm \cdot yr^{-1}$ for the different fault geometries and locking depths we have explored. The Simple model consistently produces the lowest total slip rate. Within the Preferred model, the total slip is a strong function of assumed locking depth. The total best-fit slip rate ranges from 34.6-39.3 $mm \cdot yr^{-1}$ as we vary the locking depth over a range of 13 km. Some models show a total slip rate 1-2 $mm \cdot yr^{-1}$ faster in the northern Bay Area than a profile taken in the south, but this difference is smallest in the Preferred model. These values are slightly lower than the total PA-SNGV motion in the Bay Area because some of the motion in the model is accommodated by tensile-slip on the faults.

We highlight the slip rates of a few key fault segments. Our model provides a robust estimate of slip on the San Gregorio fault. Because this fault is partly offshore in the Bay Area it is very difficult to estimate a rate using independent dislocations and onshore data. Our block model includes global stations to help constrain the motion of the Pacific block relative to the Bay Area. The resulting slip rate on the San Gregorio fault from our Preferred model is 2.4 ± 0.5 $mm \cdot yr^{-1}$ near the Golden Gate, with a slightly higher rate off of Monterey Bay.

We include the West Napa fault in some models, as it may be the northern continuation of the Calaveras fault along a series of westward steps [J. Unruh, pers. comm., 2004]. We find that its slip rate ranges from 3.4 - 7.4 $mm \cdot yr^{-1}$ across all models, with most models estimating slip rates near the lower end of this range. Models where 100% of the slip on the northern Calaveras fault transfers to the West Napa fault produce the higher slip rates. In our Preferred model it slips at 4.0 ± 3.0 $mm \cdot yr^{-1}$. This is the highest formal uncertainty for any deep slip rate in the inversion. In models where the West Napa fault and the Green Valley fault are both allowed to carry some of the Calaveras slip, the slip rates of the two faults sum to 9.5-11.0 $mm \cdot yr^{-1}$, depending on model geometry and locking depth.

Models where we include a fault along the western margin of the Great Valley produce systematically better fits to the data than those that exclude this fault. This fault follows the eastern front of the Coast Range, passing along the Ortigalita fault. We find a strike-slip rate of 5.4 ± 1.0 $mm \cdot yr^{-1}$ in our Preferred model, and the rate typically varies between 4-6 $mm \cdot yr^{-1}$.

3.5.5 Shallow Creep

Table 3.9 shows the best-fit slip rates along dislocations that intersect the surface (surface creep) in our Preferred model. These rates typically vary by < 0.5 $mm \cdot yr^{-1}$ between most model geometries. Because data coverage is sparse in some areas, the formal uncertainties in creep rates are larger than for the deep slip rates. The uncertainties are smallest on the Hayward fault (1.2-1.4 $mm \cdot yr^{-1}$) and largest on the southern Calaveras (> 6 $mm \cdot yr^{-1}$).

Figure 3.10 shows a comparison of the best-fit slip rates from the model with observations

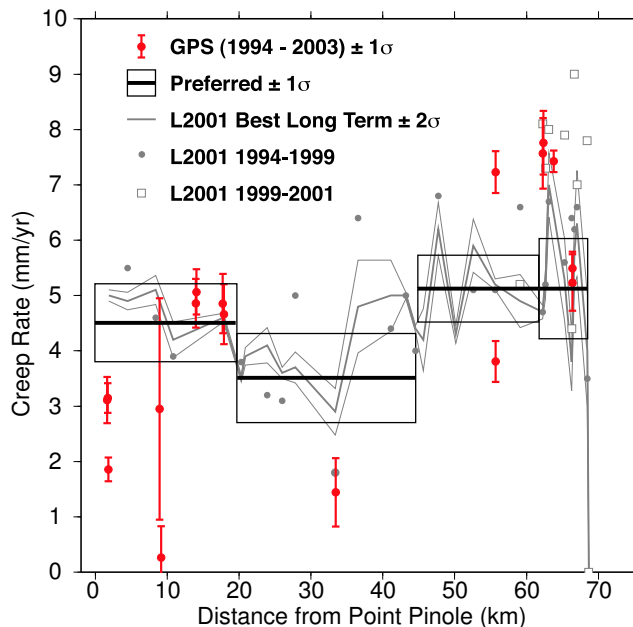


Figure 3.10. Comparison between best-fit shallow slip rate from model and observations of surface creep rate, shown as a function of distance along strike of the Hayward fault. Model results and propagated uncertainties for four shallow dislocations are shown as the horizontal lines with boxes. GPS observations (circles with error bars) are calculated from BÄVÜ. Triangulation data from different time periods (dots, open squares) as well as the best long term average (medium line) and associated error bounds (thin lines) from *Lienkaemper et al.* [2001]. GPS surveys occupy the same survey benchmarks as the triangulation surveys, but span different times. Each GPS observation spans a slightly different time span within the range of 1994-2003.

along the Hayward fault where we have the most near-fault data. While influenced by the *a priori* creep rate constraints which are based on the *Lienkaemper et al.* [2001] data set, the results differ by $< 1 \text{ mm} \cdot \text{yr}^{-1}$ when no constraints are applied and the data are allowed to control the shallow slip rate completely.

In all cases except two, the best-fitting shallow slip rate is less than the best-fitting deep slip rate. Forcing the creep rate on the southern Calaveras fault to be equal to the deep slip rate increases the χ^2/DOF by an insignificant 0.4%, as there is little data coverage in this region. For the San Andreas fault south of San Juan Bautista (Segment SanAndreas-SJB), the calculated shallow slip rate of $\sim 20.3 \text{ mm} \cdot \text{yr}^{-1}$ exceeds the deep strike-slip rate of $\sim 16.4 \text{ mm} \cdot \text{yr}^{-1}$. The higher slip rate is favored in models without *a priori* constraints and produces a 4% reduction in misfit compared to a model where the shallow and deep segments are required to slip at the same rate. While surface creep rates near San Juan Bautista accelerated following the 1989 Loma Prieta earthquake to rates $> 20 \text{ mm} \cdot \text{yr}^{-1}$ [*Behr et al.*, 1997], creepmeter data during the time-span of the BÄVÜ data show a sur-

face creep rate of 12-13 $mm \cdot yr^{-1}$ from 1993-2003 (instruments XSJ2, XHR2; data from <http://quake.wr.usgs.gov/research/deformation/monitoring/data.html>).

Even though no surface creep is observed north of Nyland Ranch [about 1.4 km north of San Juan Bautista, *Galehouse and Lienkaemper, 2003*], we find that the GPS data favor extending shallow creep about 15 km north of San Juan Bautista with a constant rate of $9.0 \pm 2.0 mm \cdot yr^{-1}$. This rate is lower than sections further south, consistent with a relatively smooth transition between creeping and locked behavior. While allowing shallow slip to extend 15 km north of San Juan Bautista (as we do in our Preferred model) reduces the total misfit, there are still very high residuals in this region in all model variations. *Johanson and Bürgmann [2004]* show that slip in this area is spatially complex.

3.6 Discussion

3.6.1 Comparing the Models

Figure 3.11 shows the residuals for the three main model geometries we discuss. The shading in Figure 3.11a show the spatial distribution of the contribution to the total χ^2 misfit. Larger values (darker colors) indicate that the model is doing a particularly poor job of fitting the data in a certain area. The fit in the central Bay Area is overall quite good. There are a few stations that show up as strong outliers, such as the station in the upper-left corner of the map (CAML). The area around the epicenter of the 1989 Loma Prieta earthquake in the Santa Cruz Mountains has a consistent pattern in the residual velocities and a high total misfit. The orientation of the residuals is most systematic northeast of the fault where the data could be fit by a higher right-lateral slip rate and $< 1 mm \cdot yr^{-1}$ of fault perpendicular motion on this section of the San Andreas fault. Such an observation might indicate that accelerated postseismic deformation along the fault persists at rates of $\sim 1 mm \cdot yr^{-1}$ more than a decade after the 1989 earthquake. The block model cannot fit a localized area of accelerated deep slip because it must make slip along the entire San Andreas compatible with one block rotation. Stations near San Juan Bautista, also along the San Andreas fault, are fit poorly, though the orientations of residual velocities are not entirely systematic. Together, the two areas along the San Andreas fault in the southern Bay Area and a few strong outliers dominate the χ^2 statistics. Models that improve the fit of those regions may have lower total χ^2 even if they result in a worse fit throughout the rest of the model.

The shading in Figs. 3.11b-c and 3.12 show where the weighted residuals (χ^2) for each model differ from the Preferred model. We calculate χ^2 for the two components of each GPS velocity in each model and then subtract this from χ^2 in the preferred model. Note how changes to the geometry of the model in one location can alter the predicted velocity throughout the model.

The Simple model (Fig. 3.11b) fits Bay Area GPS data within the uncertainty about as well as the Preferred model. However, the model does a poor job fitting sites east of the Calaveras and San Andreas faults in the southern Bay Area. Figure 3.3b shows that the fit to sites on

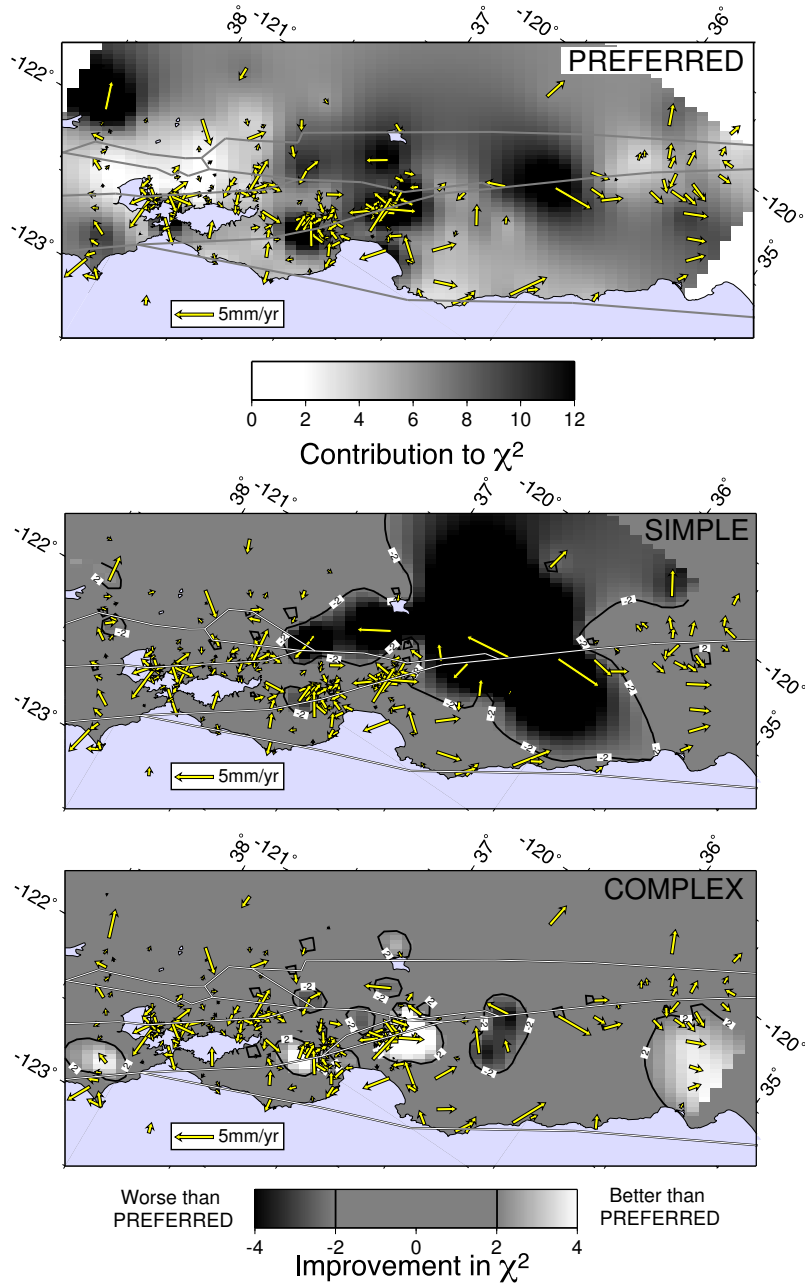


Figure 3.11. Residual velocity (difference between data and model) for three different model geometries. Shading in top panel shows relative contribution to the χ^2 misfit statistic of each station in our Preferred model. Dark colors indicate that the model does a poor job of fitting the data within its error bounds. Bottom two panels use a color scale that highlights differences between the given model and the Preferred model. Values of $|\chi^2| \leq 1$ for each data parameter indicate that the residual velocity is the same magnitude as the 1σ uncertainty. Contour lines at ± 2 .

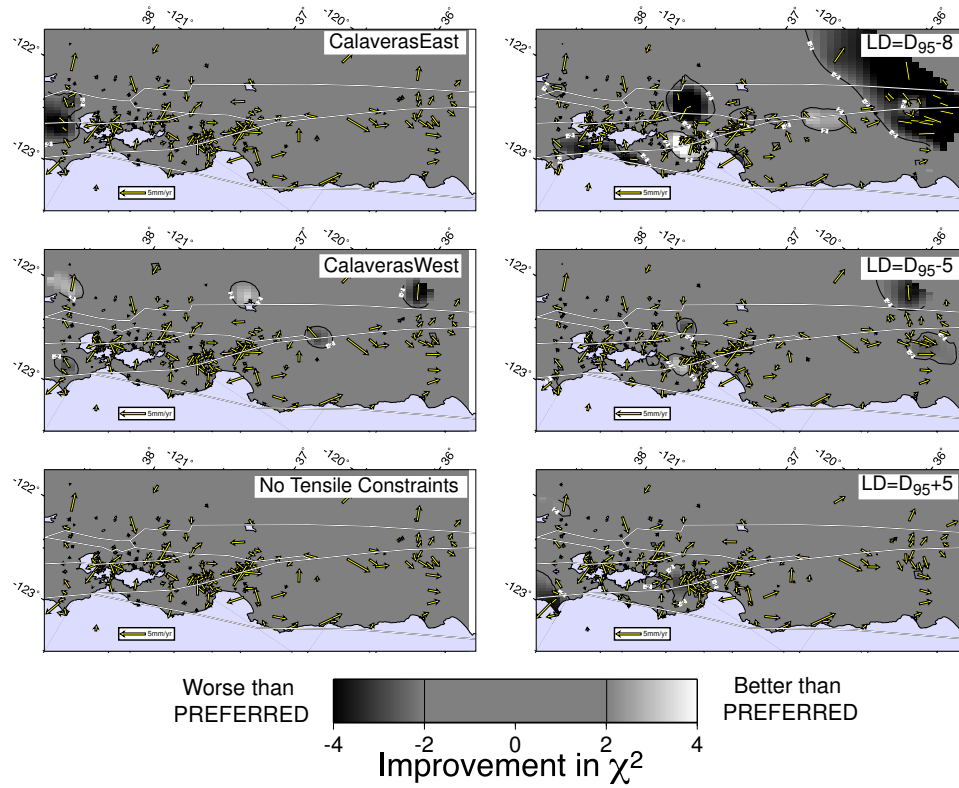


Figure 3.12. Residual velocity (difference between data and model) for multiple model variations. See caption to Fig. 3.11 for explanation.

the SNGV block is also poorer in the Simple model, with a systematic rotation of the predicted velocities to the east (clockwise) of the data. The slip rate on the Mt. Lewis Trend and Greenville faults is left lateral for the Simple model, which is the opposite sense to the required interpretation from earthquake focal mechanisms in the region [e.g., *Kilb and Rubin, 2002*]. The systematic misfit of GPS data in northern California and the opposite sense of slip are the motivation for including a “Valley Margin deformation zone” in our Preferred model. *Unruh and Sawyer [1998]* suggest that the Greenville fault connects with the Ortigalita fault, a Holocene-active fault with both vertical and strike-slip components that parallels the San Andreas fault system along the eastern margin of the Coast Range [*Bryant and Cluett, 2000*]. We extend a vertical fault through the trace of the Ortigalita fault, connecting to the San Andreas at the Carrizo Plain in the south and to the Greenville fault in the north. Geologic and geophysical evidence supports the existence a major fault structure in this vicinity along the eastern front of the Coast Range [e.g., *Wong and Ely, 1983; Wentworth and Zoback, 1989, 1990; Fuis and Mooney, 1990*]. However, that specific structure may not be the active feature bounding the Bay Area and the Great Valley today. Seismicity, including the 1983 Coalinga event [*Wong and Ely, 1983*] suggest that a broad zone of faults may actually be accommodating the total relative motion across the Coast Range, and not a single discrete structure. Because the GPS data are sparse in this region, we are not able to differentiate between a single fault structure and a zone of faults along the eastern Coast Range, nor are we sensitive to the dip of the structure or structures. If deformation at this boundary is distributed over a broad zone, the measured slip rate along any individual structure in the field (such as the Ortigalita fault) would be smaller than the aggregate rate across the whole range calculated in our models for the Valley Margin deformation zone fault.

The Complex model (Fig. 3.11c) provides strong improvement to the model fit in some areas, particularly the areas most poorly fit in the preferred model near Loma Prieta and San Juan Bautista. These improvements are substantial and result in an 8% reduction in total χ^2/DOF even though there are some areas where the fit is slightly poorer in the Complex model than the Preferred model. The Complex model has three blocks (Pleasanton, Sargent, and Paicines) added to the Preferred model’s 8 blocks. The Paicines block only has a single GPS station on it and is therefore poorly constrained by the data. Improved fit to data around San Juan Bautista accounts for the greatest reduction in misfit – probably because we add two additional blocks (Sargent and Paicines) in this area. The inferred slip rates in this region might not represent the unique motion of independent blocks, but rather the exploitation of additional degrees of freedom in the model. Unlike southern California, there is minimal geologic evidence for blocks rotating about poles within the boundaries of the blocks themselves [e.g., *Jackson, 2002*]. Even though this model has the lowest misfit, the sparse data coverage on these blocks and the known complexity of slip in this area suggest that the Complex model may not be the most accurate block model representation of the fault system in the southern Bay Area.

3.6.2 Dipping faults

All fault segments in our model are vertical, and in this section we discuss the technical and conceptual limitations to using dipping faults in a block model based on dislocation theory. We describe the challenge of determining how faults connect from mapped fault traces that

do not intersect in Section 3.4.4. This problem is amplified in 3-D, as we define a network of interconnecting faults along the 3-D boundaries of the block. Besides the structural geology problem of defining fault geometry, the mathematical implementation of dipping faults for dislocation models is better suited to environments where thrust geometry is well determined and the fault dip is relatively constant. In the “backslip” implementation of our block model, we assume that faults have a constant dip along their entire extent. For faults like the Las Trampas blind thrust that dips towards the Hayward fault, the two faults should intersect at depth in the real world [see *Unruh et al.*, 2002]. The numerical implementation of our model, however, effectively treats the system as two dislocations extending to infinite depth. While there are alternate physical interpretations of the mathematical formulation of our model that involve a the elastic limit of a viscoelastic lower crust [*Meade and Hager*, 2004], there are limitations when using of models based on deep dislocations in complex structural environments.

For vertical faults throughout all our models, we allow for the faults to open or the blocks to converge as a proxy for dip-slip faulting. This “tensile-slip” component (Table 3.8) accurately represents the total block motion, but the symmetric strain accumulation about a vertical fault is not a perfect analog for dipping faults. The differences between dip-slip and tensile-slip are pronounced for vertical deformation, but the differences are minor when only modeling horizontal components of GPS velocity.

Because thrust faulting may be important locally in the eastern Bay Area, we explore a variation on the Preferred model that includes dipping Mount Diablo and Mount Oso thrust faults (“Preferred, Thrust”). For the area where the structural environment is most complex to the northwest of the Calaveras fault, we use only vertical faults even though there is geologic evidence for dipping blind thrust faults [*Unruh et al.*, 2002]. Using dipping faults for these segments causes a substantial increase in χ^2 and reduces the slip rate on the Hayward fault by $\sim 1.5 \text{ mm} \cdot \text{yr}^{-1}$. The effect on the Hayward occurs because the bottom edge of the locked thrust faults is virtually collocated with the bottom edge of the creeping Hayward fault. The inversion is therefore not able to reliably distinguish between slip on the two faults. The χ^2/DOF for “Preferred, Thrust” is just 0.2% higher than the Preferred model and all slip rates are within $0.2 \text{ mm} \cdot \text{yr}^{-1}$ of the Preferred model.

With our block model, we provide geodetic constraints of active thrust faulting on the Mount Diablo fault system. All of our model geometries produce convergence across the Mount Diablo fault. Variations on the Simple and Complex models that include a dipping Mount Diablo fault find it has a reverse-slip of 2.7 and $5.7 \text{ mm} \cdot \text{yr}^{-1}$, respectively. In the “Preferred, Thrust” model, we find $3.9 \pm 0.5 \text{ mm} \cdot \text{yr}^{-1}$ of reverse-slip along with $4.2 \pm 0.5 \text{ mm} \cdot \text{yr}^{-1}$ of strike-slip across the fault. The reverse component is within the $1.3\text{-}7.0 \text{ mm} \cdot \text{yr}^{-1}$ range determined from restorations of geologic cross sections [*Unruh and Sawyer*, 1997]. The ratio between strike-slip and horizontal shortening components depends entirely on fault strike, but the total magnitude of the slip vector does not. The dip-slip magnitude is particularly sensitive to fault dip because horizontal shortening is projected onto the dipping fault. We use a dip of $38^\circ N$ for the Mount Diablo thrust, based on the $30\text{--}45^\circ$ range in *Working Group on Northern California Earthquake Probabilities* [2003]. Because of the Mount Diablo thrust system’s role of transferring slip from the Greenville fault to the Concord/Green Valley system in our model, it must carry several $\text{mm} \cdot \text{yr}^{-1}$ of slip consistent with block motion. In addition to any shortening, a substantial

portion of this slip must be strike-slip deformation because the thrust system’s average strike is not perfectly perpendicular to the relative block motion that it must accommodate.

3.6.3 Convergence in the Coast Range

Perfect transform faulting can occur when the rotation axes for a sequence of blocks are located at the same point but have different rates. Faulting will only be pure strike-slip if all of the block boundaries are parallel to the small circle path of the relative motion vector and parallel to one another. The situation in the Bay Area meets neither of these conditions perfectly – the rotation axes of Bay Area blocks follow a systematic progression between the NA-PA and NA-SNGV blocks, and the faults in the system are rarely parallel to one another. The Bay Area system could therefore allow a certain amount of fault-perpendicular motion. Abundant folds and thrust faults roughly parallel to the San Andreas system suggest that pure strike-slip motion on the major Bay Area faults does not accommodate all of the plate boundary motion. We use our block model to constrain the magnitude and location of any fault-perpendicular convergence.

Savage et al. [1998] use trilateration measurements collected over nearly 20 years to determine the regional strain field in the Bay Area. They find that the Bay Area as a whole undergoes an insignificant amount of areal dilatation. They identify localized zones where contraction would give rise to thrust faulting such as the region around the 1989 Loma Prieta rupture.

In contrast to the trilateration work, some authors suggest that Bay Area GPS data require a small component of fault-normal contraction between the SNGV block and the Bay Area. *Prescott et al.* [2001] analyze a profile between Point Reyes and Davis and find $\sim 3.8 \pm 1.5 \text{ mm} \cdot \text{yr}^{-1}$ of shortening over a 25-km-wide zone localized at the margin of the Great Valley. For a similar time span and data covering a larger range of latitudes in the Bay Area, *Murray and Segall* [2001] find $\sim 2.4 \pm 0.4 \text{ mm} \cdot \text{yr}^{-1}$ of contraction accommodated over a similarly narrow (<15km) zone. *Freytmueller et al.* [1999] present data from further north and conclude that shortening must be less than $1 - 3 \text{ mm} \cdot \text{yr}^{-1}$. *Pollitz and Nyst* [2004] fit regional GPS data with a viscoelastic model and find $3 \text{ mm} \cdot \text{yr}^{-1}$ of shortening perpendicular to the PA-SNGV relative plate velocity. *Savage et al.* [2004] prefer an interpretation where there is uniform contraction across the entire Coast Range. The U.S.G.S. collected additional campaign GPS observations since the publication of those papers and the reduced scatter in the data allow more reliable constraints on the magnitude of convergence and the area over which it is accommodated. Here we discuss those new results along with observations further south in the Bay Area.

Several of the previous observations of convergence in the Coast Range were based on the presentation and interpretations of profiles across the plate boundary, such as we show for BÄVÜ in Fig. 3.13 [e.g., Fig. 2 of *Murray and Segall*, 2001; Fig. 5 of *Prescott et al.*, 2001; Fig. 4 of *Savage et al.*, 2004]. These plots show the two horizontal components of GPS velocity projected onto a coordinate system with axes parallel and perpendicular to an “average” plate boundary orientation (usually parallel to the PA-NA relative motion and not PA-SNGV). The shape of the profile is highly dependent on the choice of the orientation used to define this average. Because the deformation field is projected onto a single orientation, pure strike-slip

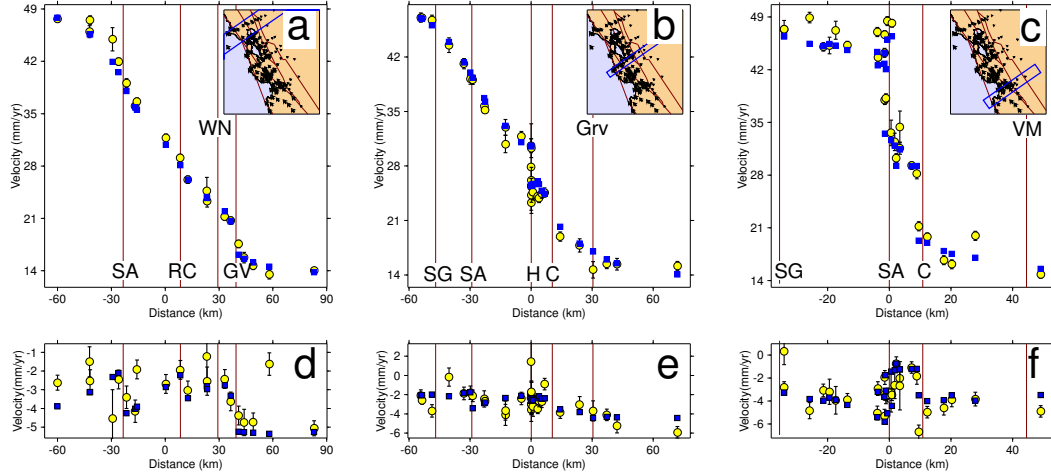


Figure 3.13. Profiles of GPS velocities along profiles perpendicular to the San Andreas fault system. Top panels show the component of the velocity parallel to N33.85W, the approximate strike of the San Andreas fault in the Bay Area. Bottom panels show component of velocity perpendicular to N33.85W. Circles are observations with 1σ uncertainties. Squares are model fit from our Preferred model. For each profile, we include velocities within the box shown in the inset map.

motion on faults with a range of orientations can yield an apparent "fault normal contraction" signal. Figure 3.14 shows GPS data from the North Bay profile perpendicular to the San Andreas fault (N33.85W, Fig. 3.14a) and the azimuth of maximum shear strain from *Savage et al.* [2004] (N29.4W, Fig. 3.14b). When accounting for the formal uncertainties, both profiles are statistically permissive of a scenario with no net convergence. The systematic pattern in both plots, however, implies that the variations are not random scatter. In the first profile, there is an abrupt step in the data at the Green Valley fault, suggesting $\sim 2 \text{ mm} \cdot \text{yr}^{-1}$ of contraction between the Pacific and SNGV accommodated near that structure. In the latter example, there is no net plate-boundary normal motion between the Pacific and SNGV blocks (the data have nearly the same value on both ends of the profile). Within the Bay Area, the systematic triangular shape in Fig. 3.14b suggests localized contraction across the Green Valley fault balanced by a broader zone of extension of equal magnitude west of the Rodgers Creek fault. These two different projections of the same data yield different conclusions about the magnitude and location of convergence in the Bay Area – even though the profile orientation differs by only 4.5° . This comparison should emphasize the hazard of representing spatially complex 2-D velocity data in an essentially 1-D illustration. Evidence for convergence cannot come from these "plate-boundary perpendicular" profiles.

More precise and rigorous measurements of the convergence across individual Bay Area faults comes from comparing the vector representing the relative motion between blocks and the orientation of individual faults accommodating that motion. Faults that are perfectly parallel to the relative motion vector will have pure strike-slip motion. *Argus and Gordon* [2001] present a detailed comparison of mapped fault strikes with predicted relative velocities

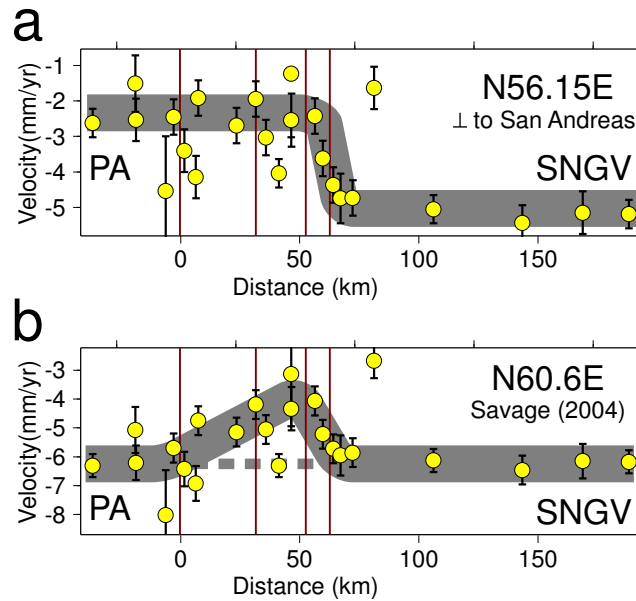


Figure 3.14. Effect of profile orientation on conclusions about convergence. Top panel here is the same as the bottom panel of Fig. 3.13a showing the profile-perpendicular component of velocities from the northern Bay Area along a profile at N56.15E, perpendicular to the strike of the San Andreas fault. Bottom panel shows profile-perpendicular velocities projected onto a slightly different orientation, N60.6E [the orientation of maximum extension from *Savage et al.*, 2004]. The orientation perpendicular to PA-SNGV motion at this latitude from our Preferred model is N59.6E. Thick grey bands show possible interpretations of the data. Dashed line in bottom panel is horizontal for reference. Even though profiles differ by only 4.5 degrees, the apparent convergence between the Pacific and SNGV blocks changes dramatically. Figure inspired by comments of Jim Savage, 2004.

between the Pacific and SNGV blocks and we present a similar analysis here. Figure 3.15 shows the orientation of PA-SNGV and PA-NA relative motion in central California derived from the rotation axes in our Preferred model. Note how the relative motion of the blocks is close to parallel at the southern end of the SNGV block and becomes less and less parallel further to the north. If the Bay Area is influenced in any way by the relative motion between PA-NA, this interaction would be more easily identifiable in the northern part of California where the PA-NA relative motion differs most from the PA-SNGV motion. Lacking geodetic data within the Bay Area, *Argus and Gordon* [2001] use a comparison between geologic slip rate estimates on Bay Area faults and their geodetic estimate of PA-SNGV relative motion to estimate the magnitude of fault normal convergence. With our block model, we are able to calculate the relative motion vector for individual blocks within the Bay Area directly. The yellow vectors in Fig. 3.15 show the orientation and magnitude of relative motion that is accommodated by faults in our Preferred model. For the vectors, we hold the eastern side of each fault fixed. They show that relative motion is, in general, nearly parallel to local fault strike. Resolving these vectors onto the local fault orientation indicates how much convergence must be accommodated. These results are reported as “tensile-slip rates” in Table 3.8. The bend in the San Andreas fault at the the Santa Cruz Mountains shows as much as $4.9 \pm 0.6 \text{ mm} \cdot \text{yr}^{-1}$ of contraction perpendicular to the segment (likely accommodated by a number of thrust faults alongside the San Andreas fault). In general, motions east of the Bay are slightly clockwise of the faults, indicating convergence across the block boundaries, which is balanced by a slight extensional component west of the Bay. The magnitude of convergence increases from $0.1 \pm 1.0 \text{ mm} \cdot \text{yr}^{-1}$ along the northern Hayward fault to $1.1 \pm 1.0 \text{ mm} \cdot \text{yr}^{-1}$ on the southernmost creeping segment of the Hayward fault (Hayward.3). The segment connecting the Hayward and Calaveras faults that roughly parallels the seismicity beneath Mission Peak (Hayward_South) has $3.0 \pm 1.0 \text{ mm} \cdot \text{yr}^{-1}$ of convergence. Along the eastern margin of the Coast Range, the Valley Margin deformation zone converges by $2.7 \pm 0.8 \text{ mm} \cdot \text{yr}^{-1}$. The Concord/Green Valley system requires a similar magnitude of convergence, but is located so close to the West Napa fault that the elastic model would probably not be able to distinguish between deep tensile-slip on the two faults. We therefore treat the Concord/Green Valley and West Napa fault systems together and find $1.9 \pm 3.0 \text{ mm} \cdot \text{yr}^{-1}$ of convergence. The San Gregorio fault and Marin segment of the San Andreas fault both show extension, with 2.9 ± 0.6 and $1.9 \pm 0.6 \text{ mm} \cdot \text{yr}^{-1}$, respectively. It is not possible to determine if this motion is accommodated onshore or offshore because of the sparse data west of these faults. Either way, this slight extension is required to satisfy the total PA-SNGV relative motion. We therefore agree with the assertion by *Savage et al.* [2004] that there is minimal net convergence across the Bay Area.

While thrust faulting parallel to the major faults is likely to accommodate much of the “convergence” implied by the relative motion vectors of some faults in the system, we note that it is possible for strike-slip faults to carry all of the relative motion if they are oriented correctly. This caveat is analogous to the discussion of profile orientation in the previous paragraph. When calculating the magnitude of fault-normal displacements, it is essential to know the orientation of the structure that will be accommodating that motion.

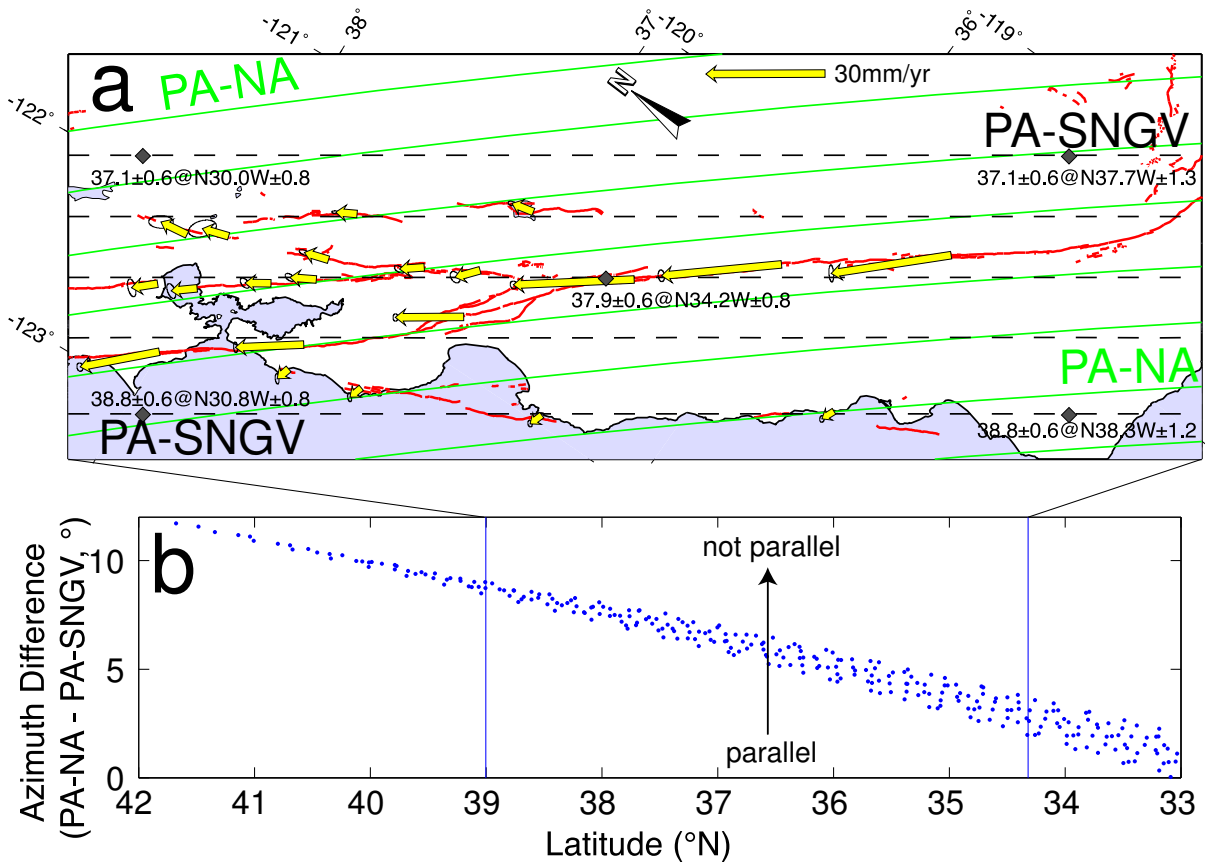


Figure 3.15. a) Calculated orientation of relative motion for PA-NA (light colored, solid curves) and PA-SNGV (black, dashed horizontal lines) based on rotation axes from our Preferred model. Map projected about the PA-SNGV pole so that fault segments and velocities parallel to the PA-SNGV relative motion show up as horizontal. Velocity vectors with error ellipses are the relative motion vector accommodated by each fault at the given location, assuming that the northeastern side of the fault (top of figure) is held fixed. Vectors parallel to fault indicate pure strike-slip motion. Because the eastern block is fixed on these dominantly right-lateral faults, vectors with azimuths clockwise of their respective fault segment indicate convergence and vectors trending counterclockwise represent divergence. In general, note that faults nearer to the top of the figure tend to show more convergence while those near the bottom of the page show a slight divergence. Filled diamonds with labels are PA-SNGV rate in $\text{mm} \cdot \text{yr}^{-1}$ and azimuth at select locations. b) Difference in azimuth between the PA-NA and PA-SNGV relative motion vectors for points on a regular grid spaced throughout the map above. The two differ in azimuth by only 2° at the south end of the map and almost 8° at the north end. Note that this graph extends further north and south beyond the Great Valley to accentuate the trend of the line and show that the two relative velocities become parallel just south of the Great Valley. The parallel motions would theoretically allow pure transform faulting to accommodate all of the relative motion across southern California if the Great Valley extended south to a latitude of 33°N .

A Note about Block Modeling

The fault-normal slip rates from some previously published block models are sometimes of larger magnitude than geologically inferred slip rates [e.g., *McClusky et al.*, 2001; *Meade et al.*, 2002]. From our own modeling, we find this is especially true when faults are separated by horizontal distance less than a few locking depths and there is limited GPS data on the blocks. The inversion assigns high fault-normal slip rates of opposite signs to pairs of faults that are located close to one another. In such cases, the total fault-normal slip satisfies the far-field constraints well because the large convergence on one fault is balanced by an equally large extension on a neighboring fault. *Meade and Hager* [2004] refer to this phenomenon as “checkerboarding.” We found through trial and error that constraining the inversion to minimize the fault-perpendicular component on a very small number of segments reduces these slip rate oscillations throughout the entire model. We add an *a priori* constraint to the fault perpendicular slip rate on three segments whose strike is within 2.5° of the orientation of the PA-SNGV relative motion (northernmost Calaveras, northern Greenville, and northern Concord). We use a value of $0 \pm 3 \text{ mm} \cdot \text{yr}^{-1}$ for this constraint. These 1σ error bounds should allow convergence up to the total rate implied by previous geodetic studies for the entire Bay Area to occur on these three segments if the data actually require it. We apply an identical constraint to the Paicines fault because of its extremely close proximity to the much larger San Andreas fault. All other segments in the model are unconstrained. Adding these constraints increases the total χ^2 by 0.5%, but improves the χ^2/DOF because the constraints reduce the number of degrees of freedom. The constrained model does not cause a statistically significant change in any of the model estimates. Figure 3.12 shows the difference between our Preferred model (with the constraint) and an identical geometry without the constraint (“Preferred, Unclamped”). The blank map indicates that the two produce an almost identical residual velocity field and that there are no localized degradations to the model fit. We feel that the model with these loose constraints produces physically reasonable slip rates without compromising the model fit or changing the qualitative interpretation of the results.

3.6.4 Implications for fault system development

What does the systematic progression of poles of rotation from west to east shown in Fig. 3.8 tell us about the evolution and behavior of the Bay Area faults? There are two possibilities: 1) The rotation axes reflect the existing geometry of the faults. Blocks merely move in a manner that is kinematically and mechanically favorable, given the orientation of pre-existing weaknesses in the area. Or, 2) Active faults are oriented at an optimal angle to the far-field motion of the plates that drive them (to produce pure strike-slip faulting, for example) [*Wesnowsky*, 1999]. Faults that are less optimally oriented might be abandoned over time. Distinguishing the relative contributions of these two end-member processes is beyond the scope of this work, but we can discuss the latter option that fault orientation reflects the orientation of present-day plate motion. Some faults in the Bay Area such as the San Andreas are oriented parallel with present day PA-NA motion, despite the fact that the plate boundary that should exert a controlling influence on the Bay Area is between the Pacific and SNGV blocks [e.g., *Argus and Gordon*, 2001, ; *W. Lettis*, pers. comm., 2004]. Such an observation might imply

that the orientation of these faults could be inherited from a time when the SNGV block moved more closely with North America. Figure 3.15a shows the geometry of the San Andreas fault system compared with small circle traces parallel to the relative motion of the PA-NA and PA-SNGV. Faults that accommodate pure strike-slip motion between the PA-SNGV show up as horizontal lines in this map projection. Few, if any, of the faults in the Bay Area are horizontal over much of their extent. Most notably, almost the entire San Andreas fault is rotated counter-clockwise by $\sim 5^\circ$ from the ideal PA-SNGV motion (with the Santa Cruz Mountains segment rotated $> 20^\circ$ away). It is, in fact, roughly parallel with the predicted PA-NA motion from our Preferred model. The central Calaveras, central Greenville, Concord, and Ortigalita faults have strikes approximately parallel to PA-SNGV motion. Other fault segments, such as the southern Calaveras, the Green Valley, and San Gregorio faults strike as much as 10° clockwise of the present PA-SNGV motion. With the exception of the San Gregorio fault, faults striking parallel to or clockwise of PA-SNGV motion are east of the Bay. The general disagreement between fault strike and total plate-boundary motion suggests that present-day plate motion cannot explain the orientation of active faults in the Bay Area. *Wakabayashi* [1999] shows a general progression where the oldest active faults in the Bay Area initiated in the west while the youngest faults in the Bay Area are to the east (though he emphasizes that there are abundant exceptions to this trend, especially for faults that appear to have been abandoned and are currently inactive that show a much more complex age distribution). We focus here on the active faults because those are the ones that are relevant for rotation axes derived from active deformation measurements. Figure 3.16 explores the relationship between the orientation of plate motion in the past and the timing of initiation for individual fault segments. We calculate the PA-SNGV motion by subtracting the Basin and Range motion [reference point ‘A’, *Wernicke and Snow*, 1998] from PA-NA motion [*Atwater and Stock*, 1998]. The exact timing of initiation for many of the faults is not constrained reliably enough to make any definitive conclusions from this figure. However, the plate reconstructions emphasize that the relative motion between PA-SNGV has rotated by $> 30^\circ$ during the lifetime of many Bay Area faults, and that this range encompasses most of the range of fault strikes observed in the Bay Area. In light of these dramatic changes in plate motion in the past, it is probably unwise to make conclusions about fault system development from our present-day GPS-derived rotation axes.

3.6.5 Fault Connections

Calaveras-Paicines-San Andreas

Maps of Holocene faults show the Paicines fault running parallel to the San Andreas for about 50 km [*Jennings*, 1994]. These maps show no Holocene connection between the San Andreas and Calaveras/Paicines system. Attempts to exclude the Paicines fault from our models provide very bad fits to the station between the San Andreas and Paicines faults, and the Paicines fault is known to creep at the surface [*Sauber*, 1989; *Galehouse and Lienkaemper*, 2003]. In our Simple and Preferred models, we include the Paicines and connect it to the San Andreas near the southern end of its mapped Holocene trace (segment 10 of Fig. 3.4). In our Complex model, we add a segment extending the southern Calaveras fault to intersect the San Andreas fault (segment 9 of Fig. 3.4). This new segment bounds an independent block between

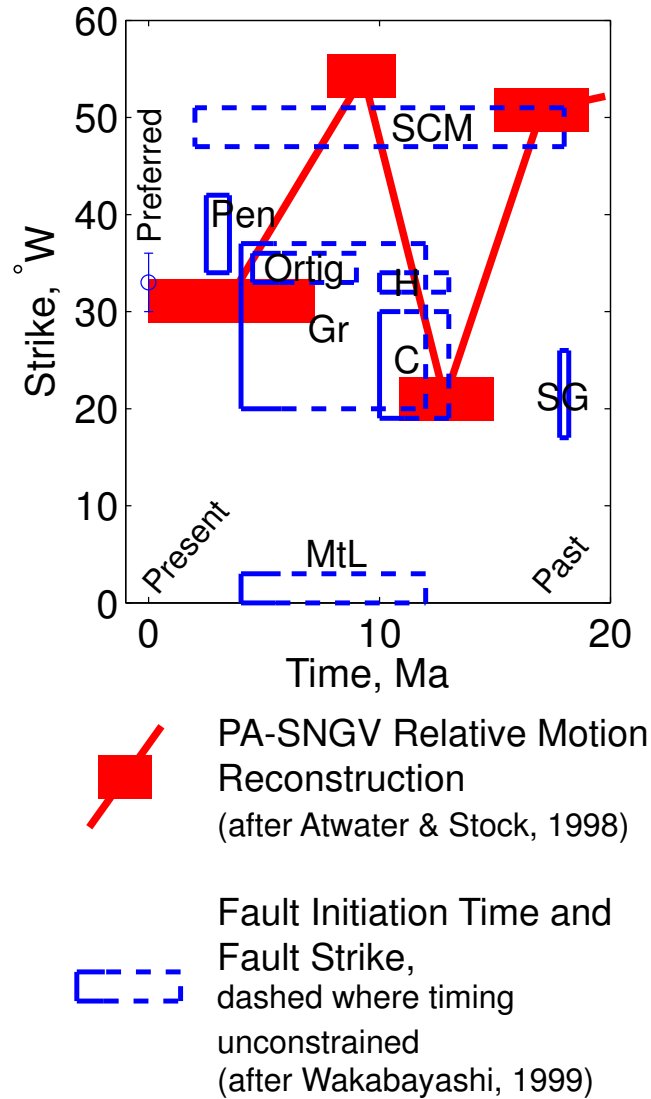


Figure 3.16. Comparison of the present-day strike of Bay Area faults (open rectangles) with the orientation of relative motion between the Pacific and SNGV blocks (filled rectangles and line connecting them). Fault abbreviations: C, Calaveras; Gr, Greenville; H, Hayward; MtL, Mt, Lewis; Ortig, Ortigalita; Pen, Peninsula segment of the San Andreas; SCM, Santa Cruz Mountains segment of the San Andreas; SG, San Gregorio. Fault initiation times come from *Wakabayashi* [1999], and are dashed where loosely constrained. For example, the San Gregorio fault's initiation is well constrained, but the Mt. Lewis fault could have initiated as early as 12 Ma (dashed right edge of box) and must have initiated by 5 Ma (solid left edge of box). Height of open box represents range of fault strikes for the given fault. Relative motion is reconstructed in the geologic past by *Atwater and Stock* [1998] (PA-NA) and *Wernicke and Snow* [1998] (SNGV-NA). They report average rates over the given time interval indicated by the width of the solid bars. The height is arbitrary because no uncertainty is reported. Circle with error bars at present day shows relative motion calculated from our Preferred model.

the San Andreas, Calaveras, and Paicines faults and allows more slip to be transferred from the Calaveras/Paicines system to the San Andreas fault. This connection is typically included in models that exclude the Paicines fault [e.g., *Matsu'ura et al.*, 1986], but our Complex model shows that both this connection and the Paicines fault improve the fit to data. The strike-slip rates in the Complex model are $25.6 \pm 3.0 \text{ mm} \cdot \text{yr}^{-1}$ and $2.2 \pm 0.4 \text{ mm} \cdot \text{yr}^{-1}$ on the San Andreas and Paicines faults, respectively.

Northern Calaveras

The northern termination of the mapped Calaveras fault is an area where there is still significant debate about which faults are connected to each other and where slip on the Calaveras gets transferred after the mapped Calaveras fault terminates. *Galehouse and Lienkaemper* [2003] argue that nearly identical surface creep rates on the two systems implies that the Calaveras connects eastward to the Concord-Green Valley fault via a mechanically favorable releasing step. Others [*Unruh and Lettis*, 1998; *Unruh et al.*, 2002] argue that fold and fault geometry in the East Bay Hills requires that the Calaveras steps westward with a restraining geometry, connecting to the West Napa fault and eventually transferring slip to the Rodgers Creek fault somewhere north of San Pablo Bay. Determining how slip is distributed between faults in the northern East Bay has important implications for the seismic hazard in these growing suburban areas. Using our block model, we focus on this junction and test a wide range of model geometries.

Overall, there is no significant difference between models where the Calaveras steps east versus west, though there are some scenarios where the east-stepping model produces a slightly smaller model misfit. Here we describe the effects of the two models “CalaverasWest” and “CalaverasEast,” which are both based on the Preferred model.

Forcing the Calaveras to transfer all slip to the west (CalaverasWest) decreases the distance between the Calaveras and Hayward/Rodgers Creek systems. The deformation gradient in the GPS data near these two fault systems limits the combined slip that can be accommodated by deep locked faults. When the two fault systems are close together, there is a tradeoff where more slip on the Calaveras/West Napa system requires less slip on the Hayward/Rodgers Creek system. Slip on the Hayward fault in the CalaverasWest model is $5.2 \text{ mm} \cdot \text{yr}^{-1}$, well below the $\sim 9 \text{ mm} \cdot \text{yr}^{-1}$ geologic slip rate estimated from offset stream channels. The total misfit and χ^2/DOF of the CalaverasWest model is higher than the CalaverasEast and Preferred models, though not substantially higher. Compared to the Preferred model, the χ^2/DOF is 2.0% higher, but CalaverasWest affects the fit to stations as far away as Parkfield (Fig. 3.12).

CalaverasEast produces a higher slip rate on the Hayward fault of about $7.5 \text{ mm} \cdot \text{yr}^{-1}$, but also allows for $10.0 \text{ mm} \cdot \text{yr}^{-1}$ on the Green Valley fault because the Green Valley fault carries slip from both the northern Calaveras fault and the Valley Margin deformation zone. The χ^2/DOF of the CalaverasEast model is 0.8% higher than the Preferred model and only affects the fit to GPS data in the northern Bay Area near where the model geometry differs.

Our Preferred model allows Calaveras slip to transfer both east and west. In it, slip rates are about half-way between the two scenarios CalaverasWest and CalaverasEast. Other model

geometries that include the Mount Lewis trend, exclude the Valley Margin deformation zone, or use slightly different fault geometries have similar results.

Despite the fact that there are a number of GPS stations in the area of interest, it may never be possible to distinguish between these different scenarios using geodetic data alone. The West Napa and Green Valley faults are located < 10 km apart, roughly the same as the geodetic locking depth. It is difficult to distinguish between two elastic dislocations buried about 15 km below the surface and spaced only 10 km apart. The added constraint from block offset could help distinguish between the two faults, especially as the details of shallow creep on the Green Valley fault are determined more precisely.

Beyond fault connections

While fault connections provide a likely explanation for the variation in slip rate along strike, there are other reasonable explanations that involve additional complexity. Variations in creep rate during transient slip events are common [e.g., *Linde et al.*, 1996] and probably not artifacts of the observations. The modeled slip rate on our segments therefore represents an average over space and time. Similarly, observations of different slip rates on adjacent fault segments could be indicative of deformation that is accommodated by inelastic processes or more complex 3-D kinematics that are not considered in our block model. Both of these explanations would likely produce complex deformation patterns that could not be detected with our GPS data set alone, but would require denser spatial coverage from techniques such as InSAR.

3.6.6 Locking Depth

The transition between creeping and locked behavior may not occur exactly at D_{95} , but we would expect the relative values of D_{95} to reflect the relative depth of this transition. To allow for the uncertainty in the absolute depth of the geodetic transition, we run the model multiple times and shift the locking depths uniformly up and down over a range of average depths. For example, D_{95} for the northern Hayward fault is 12 km and D_{95} for the Concord fault is 16 km. In our model runs, the locking depth of the Hayward fault is always 4 km shallower than the Concord fault, but we evaluate locking depths over the range of 3 - 17 km for the Hayward fault. This uniform vertical shift also allows for the uncertainty in the exact depth of D_{95} because we derive D_{95} from an earthquake catalog where earthquakes are all located precisely relative to one another, but their exact location in space is not known as accurately.

We show model misfit as a function of locking depth in Figure 3.17. The best fit comes when the locking depths are about 5 km shallower than D_{95} for each segment. In model runs where faults are assigned a uniform locking depth, we find similar results. A 8 km uniform locking depth provides the best geodetic fit, even though it is also about 5 km shallower than the average 13 km D_{95} for the entire Bay Area. Locking depths based on D_{95} produce insignificantly better model fit than the best-fitting uniform locking depth, but we prefer them because they are consistent with data outside the model.

Neither the uniform locking depth or deviations from D_{95} represent the absolute best sta-

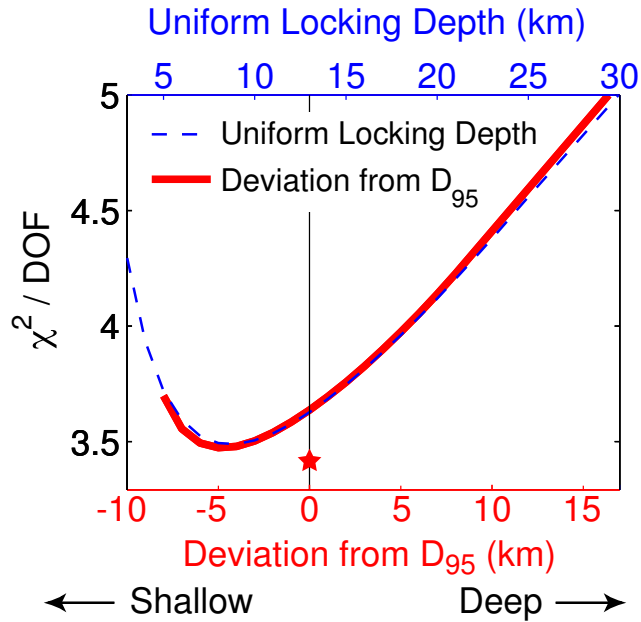


Figure 3.17. Model misfit v. locking depth for the preferred geometry. Uniform locking depth (thin dashed curve, top axis) assigns all dislocations the same locking depth. Deviation from D_{95} (thick solid curve, bottom axis) assumes that locking depths deviate by the amount indicated on the x-axis deeper or shallower than D_{95} for their specific location. Negative values on the x-axis are shallower than D_{95} . For faults with surface creep, the locking depth represents the transition between the deep slip rate and the shallow creep rate. The two curves are almost identical. Solid curve does not extend shallower than -8 because the shallowest locking depths would intersect the surface. Small star at $x=0$ shows misfit for a model assuming locking depths of D_{95} everywhere except the Santa Cruz Mountains segment of the San Andreas fault where we arbitrarily assign a very shallow locking depth of 5 km. This model gives better fit than uniform locking depth or deviations from D_{95} , highlighting the fact that the greatest misfit to GPS data occurs near that segment.

tistical fit to the data. Both approaches shift all locking depths uniformly up or down. Since some of the largest differences between observed and model GPS velocities occur near the San Andreas fault in the southern Bay Area, Fig. 3.17 is dominated by the preference for shallow slip in that area. For example, fixing the locking depth of the Santa Cruz Mountains segment of the San Andreas fault to 5 km and keeping all other locking depths at D_{95} produces a better model fit than shifting the entire model shallower by 5 km (star, Fig. 3.17). While simultaneously inverting for both locking depth and slip rate would avoid such sensitivity, *Prescott et al.* [2001] found that such joint inversions produce poorer constraints on the slip rate and result in less geologically reasonable slip distributions.

Shallow Creep Transition Depth

Our treatment of shallow aseismic creep is probably oversimplified compared to faults in nature. Distributed slip models of the Calaveras and Hayward faults show a general pattern of high aseismic slip rates near the surface with locked patches (very low aseismic slip rates) extending from a few kilometers depth to the seismic/aseismic transition (LD) [*Manaker et al.*, 2003; *Schmidt et al.*, 2004]. While the spatial resolution of our GPS data is not high enough to constrain the fine details of the aseismic slip distribution, we can explore the general distribution of slip within three depth intervals along creeping faults: 1) a shallow dislocation representing aseismic creep from the surface to some depth, TD; 2) a locked patch between the depths of TD and LD; and 3) a deep dislocation below LD. In the models considered thus far, we assumed that TD=LD, resulting in only two depth intervals along the fault (1 and 3 from above). Here we evaluate a variation on the Preferred model where TD is a fixed depth of 5 km on all creeping faults, representing shallow creep restricted to the upper 5 km (Model “Preferred, TD=5”). The χ^2/DOF is 6% higher in “Preferred, TD=5” compared to the Preferred model. Slip rates for TD=5 are almost all within the 95% confidence limits of the Preferred model, but there are some notable differences. The shallower TD produces less slip at intermediate depths, so slip rates on the remaining dislocations must be higher to yield the same surface deformation. The resulting shallow slip rate is universally faster than for cases where TD=LD. For the Hayward fault where the data constrain the shallow creep very well, the increase is $< 0.2 \text{ mm} \cdot \text{yr}^{-1}$. For creeping segments of the San Andreas and Calaveras faults, the shallower TD produces slip rates 1-2 $\text{mm} \cdot \text{yr}^{-1}$ faster than when TD=LD. By assuming TD=5, the deep strike-slip rate on the central Calaveras fault increases from 12.9 to 15.0 $\text{mm} \cdot \text{yr}^{-1}$ and the slip on the Hayward fault increases from 6.5 to 6.9 $\text{mm} \cdot \text{yr}^{-1}$. These slip increases are balanced by a decrease of slip on several of the other Bay Area faults such that the total slip across the entire Bay Area differs by less than 0.3 $\text{mm} \cdot \text{yr}^{-1}$ as TD varies. The San Gregorio and Greenville faults both have decreased slip rates (drops of 0.6 and 1.2 $\text{mm} \cdot \text{yr}^{-1}$, respectively). We find similar results in a model where the shallow creep transition is exactly half-way between D_{95} and the surface (Model “Preferred, TD= $D_{95}/2$ ”).

This relative insensitivity to the shallow creep transition depth is similar to the findings of *Thatcher et al.* [1997] who describe a geodetic inversion of slip during the 1906 earthquake. Aseismic creep and coseismic slip are modeled using identical dislocations – they differ only in the time scale over which they occur. *Thatcher et al.* [1997] find that varying the depth extent of dislocations from 5-20 km causes $<20\%$ difference in the calculated slip on those elements.

They also emphasize that even though the calculated slip is uniform along the entire dislocation, the inversion is more sensitive to the slip rate in the shallow portions of the fault that are closer to the surface geodetic data.

We employ the assumption that $TD=LD$ in our Preferred model because it produces the lowest χ^2/DOF . The improved fit may be due to the fact that slip rates between TD and LD are not exactly zero for the natural faults and that TD is likely to vary widely among the faults considered. By exploring a range of TD, we find that the shallow creep rates in our Preferred model are a lower bound, and the deep slip rates may vary from the Preferred model by $1 - 2 \text{ mm} \cdot \text{yr}^{-1}$ for more complex distributions of shallow slip.

3.6.7 Comparison With Long Term Slip Rates

Numerous geologic investigations have determined long term average slip rates for Bay Area faults during portions of the Holocene. Such studies provide essential input into earthquake hazard assessment and an comprehensive summary of previous work has been compiled for this purpose [Chapter 3 of *Working Group on Northern California Earthquake Probabilities*, 2003, “WG03”]. In general, the geodetically observed slip rates agree well with the values from WG03 (Table 3.7). Slight differences could reflect a combination of errors in each of the data sets or a real difference in the behavior of faults during the last decade compared to the last several thousand years. Both the Greenville fault and the Green Valley/Concord fault system have slip rates higher than preferred bounds from WG03. More recent paleoseismological work by *Sawyer and Unruh* [2002] constrains the slip rate on the Greenville fault to $4.1 \pm 1.8 \text{ mm} \cdot \text{yr}^{-1}$. Our Preferred model is $1.3 \text{ mm} \cdot \text{yr}^{-1}$ higher, but now within the error bounds. The northern San Gregorio fault and Marin segment of the San Andreas fault both have slip rates lower than the preferred bounds. The Hayward fault, Calaveras fault, and San Andreas fault from the Peninsula south all have slip rates within the bounds described by the working group, but slightly lower than the most probable value. WG03 does not explicitly consider the effects of the West Napa fault as a possible extension of the Calaveras fault, while we find a slip rate of $\sim 3.5 \text{ mm} \cdot \text{yr}^{-1}$. We find a strike-slip rate for the Valley Margin deformation zone of $5.4 \pm 1.0 \text{ mm} \cdot \text{yr}^{-1}$ in our Preferred model. WG03 does not estimate a slip rate for this region, but geologic investigations by *Anderson and Piety* [2001] show that the northern Ortigalita fault carries $0.5\text{-}2.5 \text{ mm} \cdot \text{yr}^{-1}$ of slip. The slip rate across the entire eastern Coast Range must be at least as high as the rate for this single structure.

To test if the preferred WG03 fault parameters (long-term slip, fault width, and shallow locking ratio, R) are compatible with the BÄVÜ geodetic data, we apply these parameters as *a priori* constraints on our preferred model geometry. Running the inversion with these constraints produces very poor model fit (χ^2/DOF of 29.8). Where geodetic data are sparse, the inversion relies very strongly on the *a priori* slip rates. On the San Gregorio fault, WG03 uses a high slip rate ($7 \pm 3 \text{ mm} \cdot \text{yr}^{-1}$) on the northern section and a lower rate ($3 \pm 2 \text{ mm} \cdot \text{yr}^{-1}$) further south. Since the weight of the *a priori* constraints overwhelms the sparse data in the area, the inversion fits this slip gradient by imposing an internal rotation of the Santa Cruz block. The rotation requires almost $20 \text{ mm} \cdot \text{yr}^{-1}$ of deep fault-normal slip on the San Gregorio fault, which must then be balanced by nearly equal and opposite displacements on other Bay

Area faults in order to satisfy the regional block motion that have minimal total convergence across the Bay Area. We can avoid this highly unrealistic scenario by removing the slip rate constraints on both segments and allowing the geodetic data alone to dictate the slip rate. That model (“Preferred, WG03”) has χ^2/DOF of 9.6 and slip rates of 5.8 and 7.0 $mm \cdot yr^{-1}$ on the northern and southern segments, respectively. The misfit from our best WG03-based model is more than twice that of our Preferred model.

3.7 Conclusions

The interseismic velocities at over 200 Bay Area stations make BÄVÜ the most comprehensive picture of crustal deformation in the region compiled to date. We show that the block modeling approach enables us to interpret these velocities at an unprecedented range of spatial scales.

We constrain the motion of blocks in the Bay Area relative to adjacent global plates (North America and Pacific), as well as the SNGV microplate. Individual blocks within the Bay Area do not move about identical poles of rotation of any of these major blocks as a “perfect transform” system, but instead have poles at intermediate locations. The poles transition systematically from west to east (Fig. 3.8). This systematic pattern may have implications for the development of the fault system, though we show that the present-day relative plate motions cannot explain the configuration of most Bay Area faults.

Looking at the Bay Area region itself, we focus on quantifying the slip rates of individual faults. We use precise relocations of earthquakes to determine the maximum depth of seismicity as a proxy for the local seismic/aseismic transition. We find slip rates that are typically within the uncertainty of geologic estimates (Table 3.7). We also document substantial slip on segments that have not been emphasized in previous studies. Models that include up to 4 $mm \cdot yr^{-1}$ of strike-slip on the West Napa fault north of San Pablo Bay provide almost identical model fit to those that exclude this fault. In our Preferred model, we favor this geometry because it is consistent with geologic evidence showing that the some slip from the Calaveras fault is transferred westward, eventually connecting to the West Napa fault system. Adding a fault along the eastern margin of the Coast Range in our Preferred model produces lower misfit and a geologically reasonable slip sense (right-lateral) on the Greenville – a notable improvement over models that exclude this “Valley Margin” deformation zone. This fault, running parallel to the San Andreas through central California carries $\sim 5 mm \cdot yr^{-1}$ of right-lateral slip and 3 $mm \cdot yr^{-1}$ of fault-normal convergence. Poor data coverage near the model fault segment prevent us from determining if the deformation is accommodated by a single structure or a broad zone with many structures as might be implied by the distribution of moderate thrust earthquakes within the Diablo and Coast Ranges. We find that a similar magnitude of convergence is preferred along the entire eastern front of the Coast Range, but that an equal and opposite extension is observed west of the Bay in our models. Our block modeling approach provides some of the first strong geodetic constraints on the slip rates of several other faults because we include global GPS data from the Pacific plate and the physical constraint of coherent block motion. These faults include the San Gregorio fault ($2.4 \pm 0.5 mm \cdot yr^{-1}$ right-lateral slip rate) and the Mount

Diablo thrust ($3.9 \pm 0.5 \text{ mm} \cdot \text{yr}^{-1}$ reverse slip and an almost equal magnitude of right-lateral strike-slip). Overall, we find that the slip rates we determine fit GPS data substantially better than the slip rates defined in WG03.

Locally, block modeling allows us to test the connectivity of faults. Faults that are connected can transfer slip, so these connections have implications for slip rates and seismic hazard assessment. We show that shallow creep on Paicines fault is important, but that deep slip is best modeled when the Calaveras fault is directly connected to both the Paicines and San Andreas faults. East of the Bay, we explore the possibility that the northern Calaveras fault transfers its slip east to the Concord/Green Valley fault, west to the West Napa fault system, or a combination of the two. The data slightly favor the eastern step over the western step alone, but we prefer models where both connections are included because they most closely reproduce the geologically inferred slip rate on the Green Valley fault and the lowest total model misfit.

In block modeling, three-dimensional fault geometry and connectivity have a very strong impact on the interpretation of surface deformation. While we systematically explored an extremely wide range of model geometries in this work, we look forward to further geologic constraints on fault geometry in 3-D to improve the reliability of block models. The ability to iteratively explore these different block geometries and test their consistency with geodetic data make the block modeling approach an excellent tool for understanding fault kinematics in the Bay Area.

Table 3.5. Vectors representing axes of relative rotation from various studies.

Reference	Lon °E	Lat °N	Rate °Myr ⁻¹	σ_1^a °	σ_2^a °	θ^a °	σ_{rate}^b °Myr ⁻¹
<i>North America - Pacific – Other Studies</i>							
NUVEL-1A ^c	-78.2	48.7	0.749	1.3	1.2	-61	0.012
<i>DeMets and Dixon</i> [1999] Geologic	-76.1	50.0	0.777	0.8	0.6	65	0.007
<i>Larson et al.</i> [1997]	-84.3	49.6	0.83	2.0	1.0	94	0.02
<i>Bennett et al.</i> [1999]	-78.5	49.9	0.78				
<i>DeMets and Dixon</i> [1999] GPS	-73.7	51.5	0.765	2.0	1.0	-85	0.016
<i>Kogan et al.</i> [2000]	-78.7	50.5	0.74				
<i>Murray and Segall</i> [2001]	-78.2	48.7	0.774				+0.007 -0.043
<i>Miller et al.</i> [2001]	-77.7	50.9	0.78				
<i>Beavan et al.</i> [2002]	-75.0	50.3	0.773	0.4	0.2	94	0.005
<i>Sella et al.</i> [2002]	-72.1	50.4	0.755	0.6	0.4	-79	0.004
<i>Gonzalez-Garcia et al.</i> [2003]	-77.0	49.9	0.766	0.25	0.17	94	0.007
<i>Kreemer et al.</i> [2003]	-77.8	50.8	0.77				
<i>Steblov et al.</i> [2003] (Preferred)	-75.6	50.8	0.777	0.6	0.4	109	0.007
<i>Steblov et al.</i> [2003] 2	-75.1	50.1	0.780	0.6	0.4	109	0.007
<i>North America - Pacific – This Study</i>							
TWOPLATE (Global Sites Only)	-73.9	52.1	0.773	0.5	0.2	94	0.003
SIMPLE	-74.88	51.79	0.770	0.4	0.1	95	0.003
PREFERRED	-74.65	51.85	0.770	0.4	0.1	95	0.003
COMPLEX	-74.16	51.89	0.771	0.4	0.1	95	0.003
CalaverasEast	-74.69	51.85	0.770	0.4	0.1	95	0.003
CalaverasWest	-74.59	51.76	0.770	0.4	0.1	95	0.003
Preferred, Thrust	-74.65	51.84	0.770	0.4	0.1	95	0.003
Preferred, Unclamped	-74.65	51.85	0.771	0.4	0.1	95	0.003
Preferred, LD= $D_{95} - 8$	-76.28	51.80	0.761	0.3	0.1	91	0.003
Preferred, LD= $D_{95} - 5$	-75.61	51.80	0.764	0.3	0.1	93	0.003
Preferred, LD= $D_{95} + 5$	-73.98	51.86	0.776	0.4	0.1	97	0.003
Preferred, TD=5	-74.70	51.86	0.770	0.4	0.1	95	0.003

Table 3.5. (continued) Vectors representing axes of relative rotation from various studies

Reference	Lon $^{\circ}E$	Lat $^{\circ}N$	Rate $^{\circ}Myr^{-1}$	σ_1^a $^{\circ}$	σ_2^a $^{\circ}$	θ^a $^{\circ}$	σ_{rate}^b $^{\circ}Myr^{-1}$
<i>Sierra Nevada/Great Valley - North America</i> – Other Studies							
<i>Argus and Gordon</i> [1991]	-128	32	0.61	6	1	51	0.15
<i>Hearn and Humphreys</i> [1998]	-154.4	-13	0.13				
<i>Dixon et al.</i> [2000]	-138.6	19.1	0.243	30.7	2.1	34	0.218
<i>Murray and Segall</i> [2001]	-90.1	53.9	0.208	~ 180			$^{+280}$ $^{-113}$
<i>Sierra Nevada/Great Valley - North America</i> – This Study							
SIMPLE	-139.61	10.71	0.242	5.2	2.9	28	0.040
PREFERRED	-137.41	9.54	0.231	7.6	3.6	25	0.054
COMPLEX	-138.11	8.51	0.224	8.2	3.9	25	0.054
CalaverasEast	-142.47	-0.01	0.176	12.0	5.6	25	0.044
CalaverasWest	-130.65	24.05	0.435	1.7	1.1	30	0.053
Preferred, Thrust	-137.65	9.24	0.228	7.8	3.7	25	0.054
Preferred, Unclamped	-137.52	8.54	0.226	8.1	3.7	24	0.054
Preferred, LD= $D_{95} - 8$	-174.17	-46.17	0.129	21.7	18.3	39	0.006
Preferred, LD= $D_{95} - 5$	-156.03	-25.06	0.133	20.7	12.4	28	0.019
Preferred, LD= $D_{95} + 5$	-129.42	24.32	0.450	2.1	1.2	26	0.067
Preferred, TD=5	-135.60	13.44	0.259	5.9	2.9	25	0.056
<i>Sierra Nevada/Great Valley - Pacific</i> – Other Studies							
<i>Dixon et al.</i> [2000]	-94.6	46.7	0.930	6.5	0.7	78	0.227
<i>Sierra Nevada/Great Valley - Pacific</i> – This Study							
SIMPLE	-95.32	46.50	0.896	1.5	0.3	74	0.044
PREFERRED	-93.86	46.36	0.890	2.2	0.4	76	0.059
COMPLEX	-93.28	46.54	0.882	2.2	0.4	76	0.060
CalaverasEast	-91.43	46.91	0.829	2.4	0.3	78	0.055
CalaverasWest	-99.85	45.36	1.099	1.2	0.3	70	0.053
Preferred, Thrust	-93.78	46.39	0.887	2.2	0.4	76	0.059
Preferred, Unclamped	-93.67	46.29	0.885	2.2	0.4	77	0.060
Preferred, LD= $D_{95} - 8$	-87.18	47.26	0.688	2.9	0.3	82	0.048
Preferred, LD= $D_{95} - 5$	-89.14	47.06	0.744	2.7	0.3	80	0.052
Preferred, LD= $D_{95} + 5$	-99.35	45.29	1.120	1.5	0.4	72	0.066
Preferred, TD=5	-94.92	46.24	0.922	2.0	0.4	75	0.059

Table 3.6. Predicted magnitude of velocity at the Farallon Islands (station FARB) in a fixed North American reference frame. Note that FARB is “slowed” down by $\sim 3 \text{ mm}\cdot\text{yr}^{-1}$ compared to the total rigid plate motion because of elastic strain along Bay Area faults. FARB is far enough from creeping fault segments to be relatively insensitive to their effect. Studies that ignore strain accumulation are not able to reliably predict the velocity at FARB.

Reference	Rate <i>mmyr</i> ⁻¹	Azimuth ^o NW
BAVU <i>observed</i>	47.7 ± 0.8	37.0 ± 1.0
NUVEL-1A	46.5	33.5
SIMPLE	48.0	38.4
PREFERRED	48.0	38.5
COMPLEX	48.2	38.5
<i>Variations on models</i>		
CalaverasWest	48.0	38.4
CalaverasEast	48.0	38.3
Preferred, Thrust	48.0	38.5
Preferred, Unclamped	48.0	38.5
Preferred, LD= $D_{95} - 8$	48.2	38.8
Preferred, LD= $D_{95} - 5$	48.2	38.7
Preferred, LD= $D_{95} + 5$	47.7	38.0
Preferred, TD=5	47.9	38.5
Preferred, TD= $D_{95}/2$	47.9	38.5
Preferred, WG03	49.6	38.5
<i>Contributions to Preferred model</i>		
Long-term Block Offset	50.7	38.8
Strain Accumulation	-2.9	47.0
Shallow Creep	0.2	80.1
Sum	48.0	38.5

Table 3.7. Comparison of strike-slip rates for geologic estimates (WG03) and this study. Fault system names from top row: SG, San Gregorio; SA, San Andreas; RC, Rodgers Creek; H, Hayward; C, Calaveras; GV, Green Valley; Gr, Greenville. Fault segments from second row: N, North; C, Central; S, South; Mr, Marin; SF, San Francisco; SCM, Santa Cruz Mountains; RC, Rodgers Creek; H, Hayward; WN, West Napa; Cn, Concord; Gr, Greenville. Total for the northern section includes the sum of SA-Mrn + RC + WN + GV. Southern total is sum of SG-S + SA-SCM + C-C + Gr. We show 95% confidence bounds ($\pm 2\sigma$) for the three main models. Bounds for other models are similar in magnitude.

Model	SG			SA			RC/H			C			GV/Gr			Total	
	N	S		Mr	SF	SCM	RC	H	WN	N	C	S	GV	Cn	Gr	N	S
WG03	7	3	3	24	17	17	9	9	9	6	15	15	5	4	2	38	37
SIMPLE	1.9	2.6	2.6	19.6	16.7	15.6	7.2	7.1	0.0	10.0	17.1	16.2	9.0	8.8	-4.1	35.8	31.2
±	1.0	0.8	1.4	1.2	0.8	0.8	1.4	0.8	0.0	1.6	2.6	0.2	0.6	0.4	1.6	2.1	3.3
PREFERRED	2.4	3.0	3.0	20.2	17.1	16.4	6.6	6.5	4.0	6.2	12.9	12.7	7.0	6.7	5.4	37.8	37.7
±	1.0	0.8	1.4	1.4	1.0	1.0	2.4	1.4	3.0	0.8	0.6	0.4	1.8	1.4	0.6	4.5	1.5
COMPLEX	4.9	5.1	5.1	20.6	16.0	13.0	7.8	7.6	3.6	4.2	12.4	20.6	6.9	6.5	6.2	38.9	36.7
±	1.2	0.8	1.4	1.8	1.8	3.8	2.4	1.4	3.2	1.0	1.8	2.2	1.8	1.4	0.6	4.6	4.3
Variations on models																	
CalaverasWest	2.4	3.0	3.0	20.3	17.1	16.1	5.2	5.2	7.4	7.0	12.3	12.0	5.3	5.3	5.3	38.2	36.7
CalaverasEast	2.6	3.1	3.1	19.9	16.7	16.2	7.6	7.5	0.0	5.8	13.2	13.0	10.6	10.6	5.3	38.1	37.8
Preferred, Thrust	2.4	3.0	3.0	20.1	17.1	16.4	6.6	6.6	4.1	6.4	13.1	12.9	6.9	6.5	5.2	37.7	37.7
Preferred, Unclamped	2.5	3.1	3.1	20.1	17.0	16.4	7.0	6.9	2.4	5.7	13.2	12.9	8.3	7.1	5.1	37.8	37.8
Preferred, LD= $D_{95} - 8$	2.5	3.0	3.0	17.5	14.5	13.7	6.5	6.5	3.6	6.7	13.2	12.8	7.3	7.0	4.7	34.9	34.6
Preferred, LD= $D_{95} - 5$	2.4	2.9	2.9	18.5	15.6	14.7	6.5	6.5	3.7	7.0	13.5	13.1	7.2	6.8	4.6	35.9	35.7
Preferred, LD= $D_{95} + 5$	2.5	3.1	3.1	21.1	17.8	17.5	6.9	6.8	5.1	5.0	12.3	12.3	6.2	5.9	6.4	39.3	39.3
Preferred, LD=5	2.7	3.2	3.2	16.9	13.8	12.9	7.5	7.5	3.4	6.8	14.2	13.8	6.7	6.4	3.9	34.5	34.2
Preferred, LD=8	2.5	3.1	3.1	18.2	15.2	14.3	6.8	6.8	4.2	7.3	14.0	13.6	6.4	6.0	4.1	35.6	35.5
Preferred, LD=13	2.6	3.1	3.1	20.1	16.9	16.1	6.3	6.3	5.1	7.0	13.4	13.1	6.1	5.8	4.8	37.6	37.4
Preferred, LD=18	2.8	3.3	3.3	21.2	17.7	17.3	6.5	6.4	6.1	6.1	12.8	12.7	5.5	5.2	5.7	39.3	39.1
Preferred, TD=5	1.8	2.3	2.3	19.6	17.3	16.6	6.9	6.9	4.9	7.9	15.0	14.7	6.7	6.4	4.2	38.1	38.1
Preferred, TD= $D_{95}/2$	1.8	2.3	2.3	19.5	17.2	16.5	7.1	7.1	4.5	7.7	15.0	14.7	6.8	6.5	4.1	37.9	37.9
Preferred, WG03	5.7	7.0	7.0	23.8	16.5	16.3	9.2	9.2	1.6	5.1	14.0	14.4	4.2	3.2	3.2	38.8	40.5

Table 3.8. Comparison of tensile-slip rates for calculated from models. Note that positive “tensile-slip” represents contraction and negative values represent extension. See caption of Table 3.7 for abbreviations.

Model	SG			SA			RC/H			C			GV/Gr		
	N	S	Mr	SF	SCM	RC	H	WN	N	C	S	GV	Cn	Gr	
SIMPLE	-3.5	-2.2	-3.2	1.5	6.8	0.3	1.3	0.0	-2.3	4.0	-4.5	0.8	1.4	3.0	
±	0.6	0.6	0.6	0.6	0.6	0.8	0.8	0.0	2.0	2.4	0.4	0.6	0.6	2.2	
PREFERRED	-2.9	-2.1	-1.9	0.2	4.9	-1.6	0.1	-0.5	1.0	1.1	-3.0	2.4	1.2	-0.4	
±	0.6	0.6	0.6	0.6	0.6	1.2	1.0	2.4	0.8	0.8	0.8	1.8	1.8	0.6	
COMPLEX	0.0	-0.7	0.2	-4.9	-8.9	-3.3	0.6	-0.5	0.5	4.5	4.7	2.5	1.2	0.3	
±	0.8	0.8	0.8	0.8	2.0	1.2	1.0	2.6	1.2	2.2	1.8	1.8	1.8	0.8	
Variations on models															
CalaverasWest	-3.2	-1.8	-2.3	1.3	6.3	-2.4	-1.0	3.6	0.7	0.1	-3.3	-0.4	0.8	0.1	
CalaverasEast	-2.5	-2.0	-2.3	-0.5	4.4	3.2	2.5	0.0	0.4	1.0	-3.2	-1.2	1.5	-0.3	
Preferred, Thrust	-2.9	-2.1	-1.9	0.2	4.9	-1.6	0.0	-0.5	1.0	1.1	-3.1	2.4	1.2	-0.3	
Preferred, Unclamped	-2.7	-2.1	-2.0	-0.3	4.5	-1.5	1.1	-2.8	-2.0	0.1	-3.6	4.7	4.7	1.4	
Preferred, LD= $D_{95} - 8$	-2.3	-2.0	0.4	1.3	5.1	-0.4	-0.1	-2.4	0.4	-0.3	-3.7	1.5	1.2	-0.2	
Preferred, LD= $D_{95} - 5$	-2.7	-2.1	0.2	1.4	5.4	-0.8	-0.2	-3.1	0.6	-0.0	-3.7	2.6	1.2	-0.3	
Preferred, LD= $D_{95} + 5$	-3.1	-2.0	-5.8	-2.0	3.8	-1.6	1.0	3.0	1.6	2.7	-2.1	2.3	1.1	-0.3	
Preferred, LD=5	-2.2	-1.8	0.6	1.4	5.0	-0.5	-0.3	-3.1	0.3	-0.7	-4.2	2.0	1.1	-0.2	
Preferred, LD=8	-2.5	-1.9	0.4	1.5	5.3	-0.6	-0.3	-3.9	0.4	-0.4	-4.0	2.9	1.1	-0.2	
Preferred, LD=13	-2.7	-1.8	-1.1	0.7	5.1	-1.0	-0.0	-1.8	0.7	0.5	-3.4	2.6	1.1	-0.3	
Preferred, LD=18	-2.8	-1.6	-4.2	-1.2	4.1	-1.4	0.6	1.4	1.3	1.9	-2.7	2.3	0.9	-0.3	
Preferred, TD=5	-2.4	-2.0	-1.2	0.1	4.7	-1.9	-0.3	-0.3	1.0	0.8	-3.7	2.0	1.1	-0.4	
Preferred, TD= $D_{95}/2$	-2.3	-2.0	-1.3	0.1	4.8	-1.8	-0.2	-0.4	1.0	0.8	-3.7	2.1	1.1	-0.4	
Preferred, WG03	-6.6	-4.2	0.7	0.8	1.4	-0.2	1.2	-1.7	8.1	6.8	-0.8	5.4	3.5	-2.6	

Table 3.9. Shallow strike-slip (“creep”) rates from model. Fault system names from top row: SA, San Andreas; H, Hayward; C, Calaveras; GV, Green Valley. Fault segments from second row: SCM, Santa Cruz Mountains; SJB, San Juan Bautista; Pk, Parkfield; H1-H4, 4 segments from North - South; N, North; Ctl, Central; S1-S2, Southern 1 - 2; nCn, northern Concord; sCn, southern Concord.

Model	SA			H				C				GV		
	SCM	SJB	Pk	H1	H2	H3	H4	N	Ctl	S1	S2	nCn	sCn	GV
SIMPLE	9.1	20.6	14.1	4.6	3.9	5.1	4.9	1.5	5.4	14.0	7.8	3.7	3.5	2.7
±	2.0	3.0	4.4	1.4	1.4	1.2	1.6	1.8	6.4	0.8	3.6	1.4	1.2	1.2
PREFERRED	9.0	20.3	13.5	4.5	3.7	5.2	5.2	2.0	8.9	14.0	8.4	3.7	3.5	2.6
±	2.0	3.0	4.2	1.4	1.4	1.2	1.6	1.6	6.2	0.8	3.4	1.4	1.2	1.2
COMPLEX	7.5	20.4	14.3	4.6	3.9	5.3	5.3	1.7	8.9	14.1	6.2	3.8	3.5	2.6
±	2.0	2.8	4.2	1.2	1.4	1.0	1.4	1.8	6.0	0.8	3.4	1.4	1.0	1.0
Variations on models														
CalaverasWest	9.3	20.6	14.0	4.4	3.7	5.2	5.2	2.0	8.9	14.0	8.5	3.8	3.4	2.6
CalaverasEast	9.0	20.3	13.6	4.7	3.8	5.2	5.1	2.2	8.5	14.0	8.4	3.5	3.5	2.7
Preferred, Thrust	9.0	20.3	13.5	4.6	3.7	5.2	5.2	1.8	8.9	14.0	8.3	3.8	3.5	2.6
Preferred, Unclamped	8.9	20.3	13.6	4.6	3.9	5.2	5.3	1.6	8.4	14.0	8.4	3.7	3.5	2.6
Preferred, LD= $D_{95} - 8$	8.9	22.3	-2.3	4.5	3.9	5.2	4.9	1.6	8.6	14.0	6.2	3.9	3.5	2.6
Preferred, LD= $D_{95} - 5$	8.9	20.9	10.0	4.6	3.8	5.2	5.0	1.6	7.7	14.0	7.6	3.8	3.5	2.6
Preferred, LD= $D_{95} + 5$	9.3	20.0	14.7	4.5	3.8	5.3	5.5	2.2	10.3	14.0	8.6	3.7	3.4	2.6
Preferred, LD=5	7.9	21.7	9.9	4.5	3.8	5.2	5.0	1.4	7.7	14.0	7.9	3.9	3.5	2.6
Preferred, LD=8	8.2	21.0	12.4	4.6	3.8	5.2	5.1	1.6	8.2	14.0	8.3	3.9	3.5	2.6
Preferred, LD=13	8.6	20.4	14.0	4.6	3.8	5.2	5.3	2.0	9.4	14.0	8.6	3.8	3.5	2.6
Preferred, LD=18	9.1	20.1	14.7	4.5	3.9	5.3	5.5	2.2	10.7	14.0	8.7	3.8	3.5	2.6
Preferred, TD=5	9.9	22.8	16.5	4.6	3.9	5.3	5.2	2.3	10.2	14.1	8.8	4.0	3.6	2.7
Preferred, TD= $D_{95}/2$	9.9	22.5	16.6	4.6	3.9	5.3	5.2	2.2	10.6	14.1	9.1	4.0	3.5	2.7
Preferred, WG03	7.3	21.3	14.3	5.1	4.0	5.2	6.5	4.0	13.8	12.3	8.3	3.2	4.5	3.7

Chapter 4

No frictional heat along the San Gabriel fault, California: Evidence from fission-track thermochronology

4.1 ABSTRACT

Large earthquakes generate frictional heat, and the magnitude of heating is related to the slip magnitude, the applied effective normal stress, and the frictional strength of the fault. We looked for evidence of this heating in apatite fission-track age and track-length distributions of samples from adjacent to and within the San Gabriel fault zone in southern California. The fault is thought to be an abandoned major trace of the San Andreas fault system active from 13 to 4 Ma and has since been exhumed from depths of 2–5 km. At our sample locality, as much as 40 km of total slip is thought to have accumulated along a localized ultracataclasite layer just 1–8 cm thick. We see no evidence of a localized thermal anomaly in either fission-track ages or track lengthseven in samples within just 2 cm of the ultracataclasite. Because of the absence of any measurable impact on fission tracks, we have been able to use forward modeling of heat generation, heat transport, and fission-track annealing to constrain the frictional properties of the fault. We find that either there has never been an earthquake with > 4 m of slip at this locality or the average apparent coefficient of friction must have been < 0.4 .

4.2 Introduction

Faults live and die by their frictional properties. Friction determines how and when a fault slips, how faults interact with each other, and influences fault geometry. Frictional strength affects heat production and stresses in the rocks around faults. Despite the fundamental role of friction in controlling fault behavior, different techniques for determining fault strength in nature have produced radically different estimates of the coefficient of friction, and many of these estimates conflict with values determined in the laboratory. The first constraints on the frictional strength of large faults in nature came from measurements of surface heat flow [*Brune et al.*, 1969; *Lachenbruch and Sass*, 1980]. During fault slip, a significant amount of frictional heat should be generated, resulting in measurably high heat flow adjacent to the fault after a few million years of fault activity. The fact that no heat-flow anomaly has been observed in surface measurements suggests that the coefficient of friction for major natural faults is 0.1–0.2, a factor of 3 to 7 times lower than measurements from laboratory experiments [*Byerlee*, 1978]. Studies of heat flow assume that conduction is the sole mechanism of heat transport, but strong evidence for fluid circulation at seismogenic depths [e.g., *O’Neil and Hanks*, 1980] indicates that advective heat transport could dramatically change estimates of fault strength. Even though *Lachenbruch and Sass* [1980] presented strong arguments against the role of fluids, they conceded that heat-flow data alone cannot rule out contamination of the signal by advective heat transport. We therefore seek independent constraints on the frictional heating of faults.

In this study, we use fission-track thermochronology and first-order models of frictional heating to constrain the amount of heat generated by individual fault-slip events and over geologic time periods. We collect samples from transects perpendicular to an exhumed fault and use evidence of complete or partial annealing of fission tracks to infer the magnitude of transient temperature pulses from repeated large earthquakes.

4.2.1 Frictional Heating

Heat is generated virtually instantaneously during an earthquake, causing a transient and localized temperature increase. The amount of heat generated per unit area (Q) is related to the amount of work done by friction:

$$Q = e\tau_{app}D \quad (4.1)$$

where D is the amount of slip, τ_{app} is the average shear stress during slip, and e is a coefficient representing the proportion of total work that is converted into heat rather than seismic energy or grain-size reduction. *McGarr* [1999] presented calculations of seismic efficiency that are in agreement with laboratory experiments [*Lockner and Okubo*, 1983], which indicate that e is probably between 0.90 and 0.99. We have adopted a value of 0.90 for our calculations. We used the relationship $\tau_{app} = \mu_{app}\sigma_n$, where μ_{app} is the average apparent coefficient of friction and σ_n is the normal stress. In our forward model, we assumed values for μ_{app} and determined the normal stress from the weight of the overburden ($\sigma_n = \sigma_v$). The apparent coefficient of friction includes the effects of pore pressure and the relative compressibility of the fault zone materials [*Harris*, 1998]. Higher pore pressures will result in lower values of μ_{app} , thus making

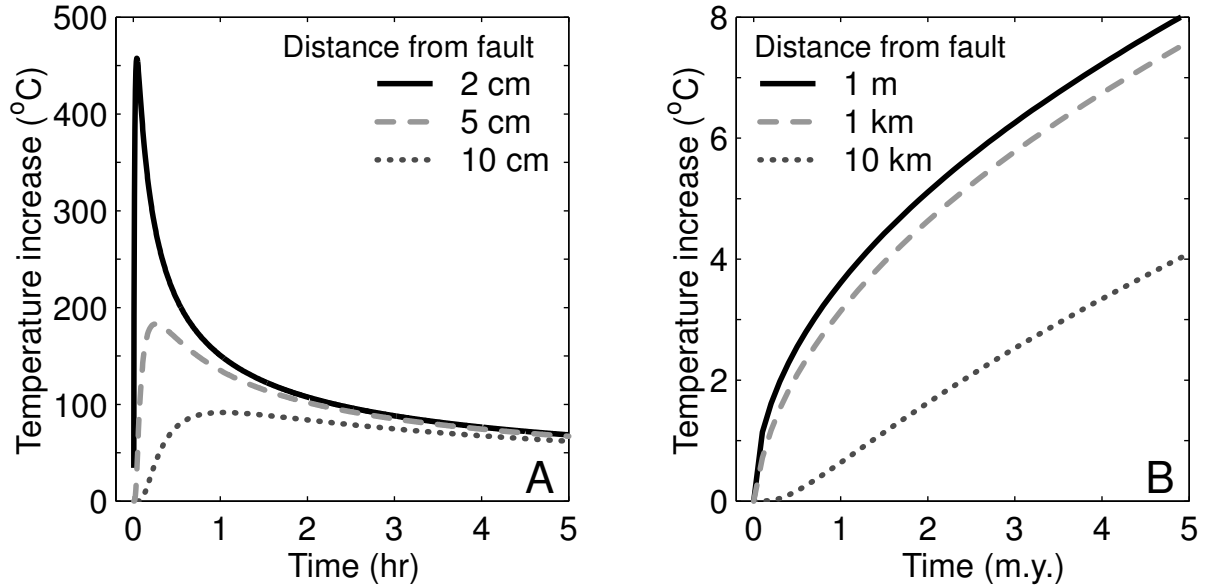


Figure 4.1. Typical temperature vs. time histories calculated for different distances away from a fault for (A) transient frictional heating from a single earthquake with 4 m slip and (B) cumulative heating from a geologic slip rate of $4.4 \text{ mm}\cdot\text{y}^{-1}$. Note extremely different scales of x- and y-axes. Parameters used: depth = 2.3 km, apparent coefficient of friction = 0.35.

the fault appear weaker. We calculated the temperature v. time histories shown in Figure 4.1 by approximating heating events as instantaneous plane sources of heat [Lachenbruch, 1986] and using simple analytical solutions for one-dimensional conductive heat flow [Carslaw and Jaeger, 1959]. For a single earthquake, the most significant temperature increases are confined to within ~ 10 cm of the fault surface, and temperatures return to within a few degrees of their preearthquake levels within a few days (Fig. 4.1A).

As earthquakes recur, more heat is generated before residual heat from previous events can escape to the surface, eventually leading to temperature increases of several degrees within a few tens of kilometers of the fault (Fig. 4.1B). Note that the heating signature of the long-term buildup covers a much broader area and persists for millions of years longer than the localized and transient spike shown in Figure 4.1A. Existing studies of frictional heat from surface heat flow are only able to investigate the broad anomaly from the cumulative buildup of heat [e.g., Lachenbruch and Sass, 1980].

4.2.2 Thermochronology and Frictional Heat

There have been several attempts to use thermochronology to demonstrate thermal anomalies around natural faults [e.g., Scholz *et al.*, 1979; Xu and Kamp, 2000; Batt *et al.*, 2000; Camacho *et al.*, 2001]. Like studies of surface heat flow, these efforts focus on observing the broad anomalies that are produced by the accumulation of heat over millions of years. In ad-

dition to concerns over advective heat transport on these time scales, observing frictional heat with thermochronology requires that profiles tens of kilometers long have minimal differential uplift. Further, Figure 4.1B shows that slip rates of $< 5 \text{ mmyr}^{-1}$ may not cause temperature increases large enough ($\sim 20 \text{ }^\circ\text{C}$) to be resolved by thermochronology.

Fission-track thermochronology can record thermal events lasting from minutes to millions of years and could therefore resolve the quick heat pulses from single earthquakes in addition to the long-term accumulation of heat. Exposure to high temperatures causes fission tracks to heal and shorten, i.e., to anneal. Large thermal events can cause the tracks to disappear entirely, resetting the apparent age of the sample. Thus, frictional heating should cause fission-track lengths to be shorter or ages to appear younger adjacent to a fault. *Green et al.* [1986] performed laboratory experiments showing that fission-track ages in apatite can be completely reset by heating events as short as 20 min if the temperature exceeds $\sim 400 \text{ }^\circ\text{C}$, and exposures to more moderate temperatures ($> 80\text{--}100 \text{ }^\circ\text{C}$) over geologic time can also cause resetting.

To resolve transient heat pulses from individual earthquakes, we can compare samples within a few centimeters to samples tens of meters from the fault. These samples have undergone nearly identical long-term thermal histories (including any cumulative buildup of frictional heat), but samples close to the fault also might have been subject to transient frictional heating. As illustrated in Figure 4.1A, temperatures hot enough to reset fission tracks will only be reached within $\sim 0.1 \text{ m}$ of the fault and will persist for less than 1 h.

Fission tracks can only image frictional heating in a reasonably narrow depth range, a Goldilocks zone. Fission tracks are not present at depths where the ambient temperature is hot enough to continuously anneal damage to the crystal lattice ($\sim 120 \text{ }^\circ\text{C}$ in apatite), corresponding to depths $\sim 3.5 \text{ km}$ near the present-day San Andreas fault. If the depth is too shallow, shear stresses may be too low, so that even large earthquakes will not generate enough frictional heat to raise temperatures enough to anneal tracks. The depth range of the Goldilocks zone depends on geothermal gradient, normal stress, and the apparent coefficient of friction of the fault. Considering these factors, the approximate depth range in which apatite fission-track thermochronology can record frictional heat from individual earthquakes corresponds to depths of $\sim 2.0\text{--}3.5 \text{ km}$, under the conditions of a $30 \text{ }^\circ\text{C}\cdot\text{km}^{-1}$ geothermal gradient.

4.3 San Gabriel Fault Zone

The San Gabriel fault is thought to be an ancient and abandoned trace of the San Andreas fault system that accommodated $\sim 40 \text{ km}$ of plate-boundary motion from 13 Ma to 4 Ma [*Powell*, 1993]. Since that time, uplift and erosion have exposed features that were originally 2–5 km deep while the fault was slipping [*Chester et al.*, 1993; *Blythe et al.*, 2000].

4.3.1 Site Description

The specific site we examined in this study (Fig. 4.2) is located along Little Tujunga Road near Pacoima Canyon [*Oakeshott*, 1958; *Anderson et al.*, 1983; *Evans and Chester*, 1995]. At

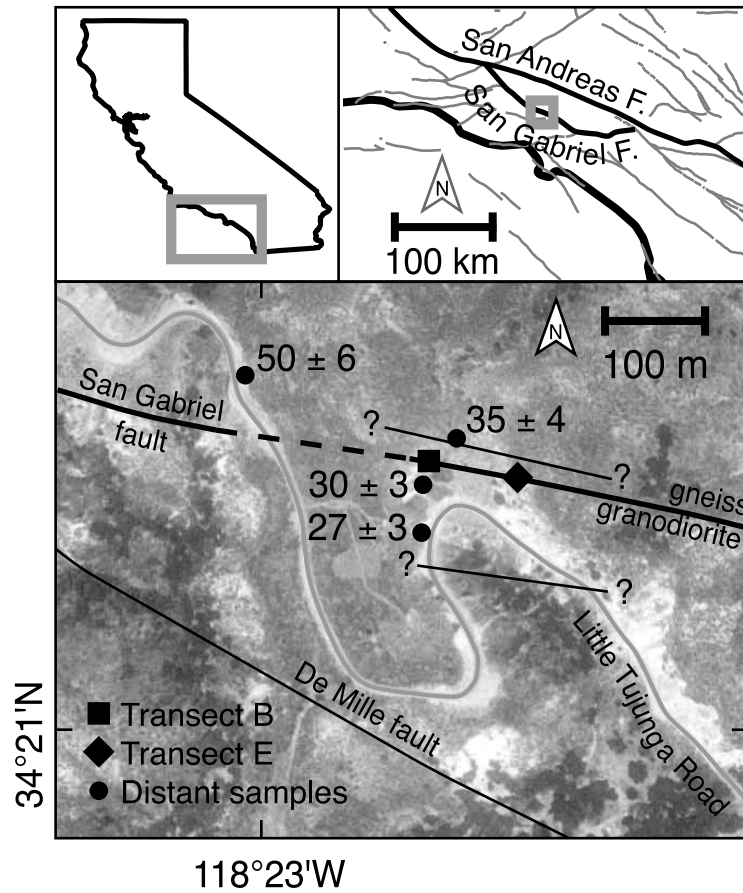


Figure 4.2. Location of samples along San Gabriel fault in southern California, an ancient and abandoned trace of San Andreas fault system. Samples far from fault show apatite fission-track ages and 1 σ uncertainty. Ages along transects B and E are shown in Figure 4.3

this site, the San Gabriel fault consists of a 1–8-cm-wide ultracataclasite zone that juxtaposes the Mendenhall gneiss to the north with the Josephine granodiorite to the south. Because of this extremely narrow fault zone, our heat-transport models can approximate the fault as a planar source of heat. [Evans and Chester, 1995] showed that fluids were not present in appreciable amounts at this locality while the fault was active.

4.3.2 Samples

We collected samples along two transects perpendicular to the fault (B and E, Fig. 4.2) that are ~75 m apart along strike of the fault. The samples closest to the slip surface are as narrow as 2 cm in the direction perpendicular to the fault. As the temperature vs. time curves in Figure 4.1A illustrate, we require such spatial resolution to observe the extremely localized effects of transient frictional heating. The most distant samples are from ~70 m away from the fault. Because this distance is comparable to the distance between the transects, we use the same samples far from the fault as the endpoints of both transects.

4.4 Fission-track Results and Analysis

We plot the fission-track age of samples along our transects in Figure 4.3 (see also Fig. DR1 and Table 4.1 which contain additional information about fission-track procedures). Far from the fault, the apparent age on the granodiorite side (30 ± 3 Ma) differs from the gneiss side (50 ± 6 Ma), indicating that the two sides underwent slightly different thermal histories (likely owing to vertical offset along the fault) or that the chemistry of the apatite crystals is sufficiently different that they anneal at slightly different rates [Donelick *et al.*, 1999]. Although there is some variability in ages adjacent to the fault, none of the samples is reset to the 13–4 Ma time of fault slip.

For both transects on the gneiss side of the fault, fission-track ages are youngest in samples closest to the fault, a feature qualitatively consistent with a frictional-heating signature. Quantitatively, however, none of these ages coincide with the timing of San Gabriel fault activity, implying that either the ages were partially reset by frictional heating or this thermal signature predates the fault. We evaluate these two possibilities by examining the lengths of the fission tracks. Our forward modeling shows that heat pulses that partially reset fission-track ages always cause existing tracks to shorten, resulting in a lower mean track length. Our data have the opposite feature: The mean track length close to the fault (12.5 mm for both transects) is slightly longer than the mean for samples far from the fault (12.2 mm), not significantly different at the 95% confidence level (Table 4.2 and Fig. 4.4). Therefore, frictional heating did not raise the temperature enough to cause a measurable decrease in track lengths and thus cannot explain the apparent reduction in ages near the fault.

We utilize the observation that there is no localized reduction in age or track length to constrain the magnitude of frictional heat that affected this locality. By using the fission-track annealing equations of Laslett *et al.* [1987], we compute the maximum temperature increase

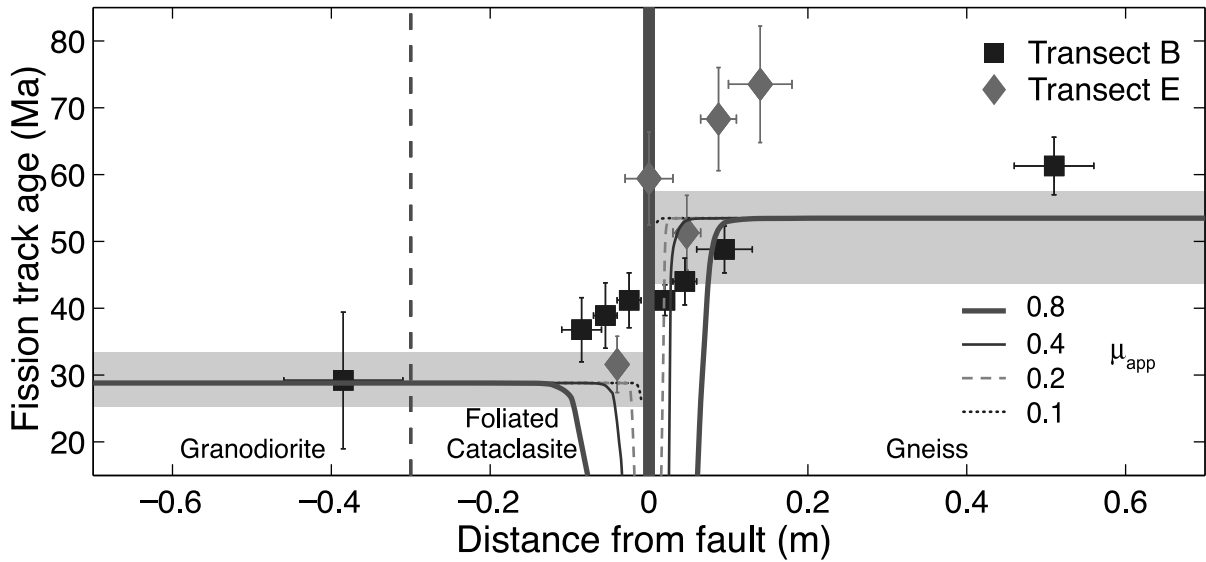


Figure 4.3. Apatite fission-track age as a function of distance from San Gabriel fault. Symbols show data from two transects with x-axis error bars indicating width of samples and y-axis error bars showing 1σ uncertainty in age. Shaded gray area shows 1σ uncertainty range for samples 10–70 m from fault (Fig. 4.1B). Curves are theoretical calculations for expected age of samples exposed to frictional heat from a single 4 m slip event at 2.3 km depth and a range of apparent coefficients of friction (μ_{app}). Foliated cataclasite zone is present along Transect B only

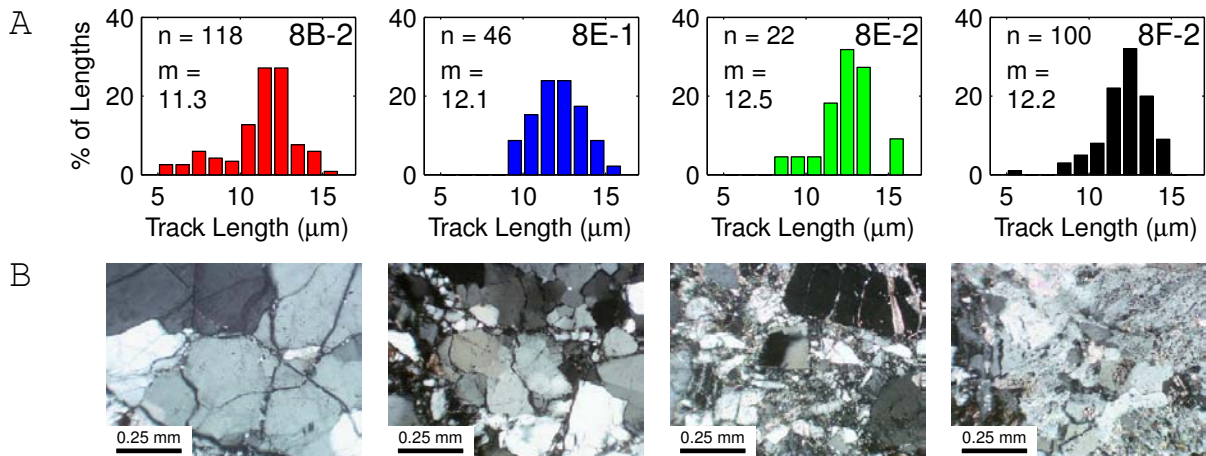


Figure 4.4. (A) Fission-track length distributions for select samples; 8B-2 and 8F-2 are samples far from fault whereas 8E-1 and 8E-2 are from within 2–4 cm of fault. (B) Photomicrographs of thin sections of corresponding samples. Scale bars are 0.25 mm.

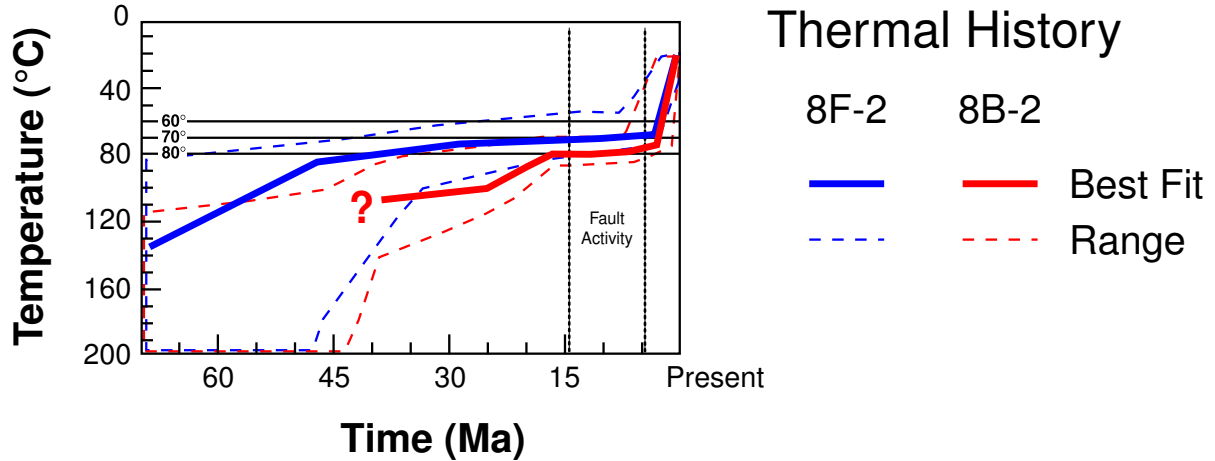


Figure 4.5. Forward modeling of thermal history of samples 8b-2 and 8f-2 (far from fault, granodiorite side and gneiss side, respectively) using AFTSolve [Ketcham *et al.*, 2000] and annealing algorithm of Laslett *et al.* [1987]. The thick curves shows best fit after Monte Carlo simulations with 100,000 runs, whereas the dashed lines outline the range of acceptable fits. Modeling shows that our sample locality was at an ambient temperature between 70 and 80 °C while the fault was active.

the samples close to the fault could have undergone without causing a measurable change in fission-track age or track-length distribution. We find that the temperature in these samples could never have exceeded ~380 °C for > 20 min while the fault was active. The amount of annealing for a given heating event depends nearly linearly on the duration of the event and exponentially on its temperature. For example, it takes 20 min to completely anneal tracks in apatite at 400 °C, but it will take nearly 40 yr to accomplish the same annealing at 200 °C.

If there are multiple earthquakes on the same fault, the largest earthquake will cause the most annealing because it will have the largest temperature increase but similar duration of heating. Multiple earthquakes of identical size have the effect of increasing only the duration, and thousands of earthquakes are needed before there is a measurable difference between a single earthquake and multiple earthquakes of equal slip. A plate-boundary fault with as much as 40 km of total slip may have had tens of thousands of large earthquakes of similar magnitude. Because we have no information about the total number of earthquakes on this strand of the San Gabriel fault or their relative size, we have focused our analysis on the effect of the single largest earthquake.

Our estimates of the approximate depth of the samples during fault activity (13–4 Ma) rely on traditional modeling of fission-track length distributions to determine exhumation history [e.g., Ketcham *et al.*, 2000]. We have found that the ambient temperature at this locality was 70–80 °C while the fault was active (Fig. 4.5; see footnote 1); the gneiss side was consistently ~5 °C cooler than the granodiorite side. If a geothermal gradient of 30 °C·km⁻¹ and a 10 °C surface temperature are assumed [Williams *et al.*, 2001], then these ambient temperatures

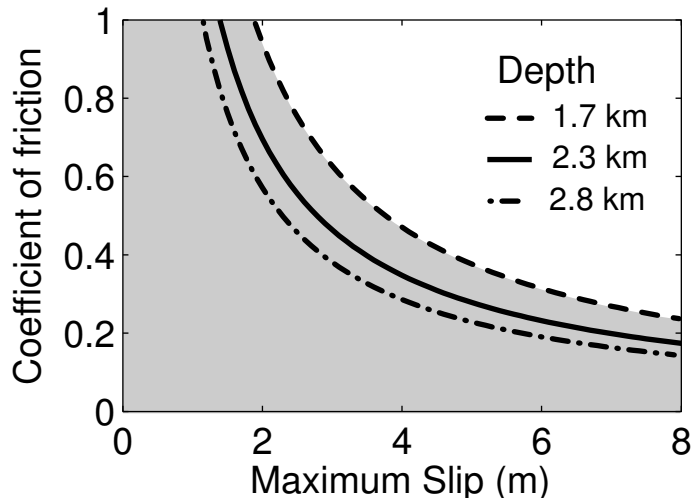


Figure 4.6. Constraints on maximum value of apparent coefficient of friction (μ_{app}) at our sample locality for different assumptions about largest-magnitude slip event and paleodepth of samples. Uncertainty in estimates of the ambient temperature and geothermal gradient while the fault was active contribute to uncertainty in estimates of the paleodepth. The range of depths shown here corresponds to estimates of ambient temperatures between 70–80 °C and geothermal gradients of 25–35 °C·km⁻¹. We have shaded the region below the curves to emphasize that the curves represent upper bounds on the coefficient of friction.

correspond to ~2.0–2.3 km depth (with < 350 m of vertical offset across the fault during its entire history).

4.5 Constraining Fault Strength

We constructed a forward model integrating heat generation by fault-slip events, heat flow, and fission-track annealing. By using our model, we can provide constraints on the frictional strength of the fault at this locality. The solid lines in Figure 4.3 show our calculations of fission-track age along the transect for a model slip event with 4 m of slip at 2.3 km depth. Apparent coefficients of friction of > 0.4 would result in reset ages in the samples closest to the fault, but we do not observe any such reset.

Equation 4.1 shows that it is not possible to use estimates of heat generation to uniquely constrain the coefficient of friction (μ_{app}) without assuming a slip distance (D), or vice versa. We must therefore assume a reasonable slip magnitude appropriate for a major plate-boundary fault, remembering that the largest event will dominate the thermal history. Additional uncertainty stems from our estimates of the paleodepth of the transect because the overburden affects the amount of normal stress on the fault. Paleodepth estimates rely on both our estimate of paleotemperature and geothermal gradient at the time the fault was active both of which have

associated uncertainties. Figure 4.6 shows how different slip magnitudes and paleodepths affect our constraints on the apparent coefficient of friction. We plot a range of depths appropriate for paleotemperatures between 70–80 °C and geothermal gradients ranging from 25–35 °C·km⁻¹, with the most likely paleodepth being between 1.7–2.8 km.

4.6 Conclusions

At one locality along the exhumed San Gabriel fault, we see no evidence in fission-track thermochronology for a localized thermal anomaly from transient frictional heating caused by individual earthquakes. The absence of measurable changes in fission tracks allows us to conclude that the temperature near the fault never exceeded 380 °C for > 20 min while the fault was active. Given the best estimated depth of the section during fault activity from 13 to 4 Ma, this thermal constraint suggests that either no single earthquake ever exceeded 4 m of slip on a frictionally strong fault (≥ 0.6) or that the apparent coefficient of friction on the fault is < 0.4 .

Table 4.1. Apatite Fission Track Analyses - San Gabriel Fault

Sample	Distance from fault (m)	# Grains	Standard track density ($\times 10^{-6} \text{ cm}^{-2}$)	Fossil track density ($\times 10^{-6} \text{ cm}^{-2}$)	Induced track density ($\times 10^{-6} \text{ cm}^{-2}$)	χ^2 prob. %	Central age (Ma)	Mean track length (μm)	Std dev. (μm)
8b-1	-0.09	20	1.76 (2866)	12.21 (82)	95.48 (641)	13	36.1 \pm 4.8	12.5 \pm 0.3 (14*)	1.18
8b-2	-67	25	1.79 (2911)	9.82 (77)	102.93 (807)	98	27.3 \pm 3.4	11.3 \pm 0.2 (118*)	2.08
8b-4	0.50	33	2.24 (3586)	26.1 (293)	152.2 (1705)	95	61.3 \pm 4.3	12.9 \pm 0.3 (15)	1.04
8b-5	-9.0	20	1.85 (2999)	12.2 (67)	117.1 (642)	92	30.8 \pm 4.1	12.0 \pm 0.9 (8)	2.44
8b-6	-0.39	9	1.85 (2999)	3.5 (9)	35.5 (91)	96	29.2 \pm 10.2	11.1 \pm 0.5 (20*)	2.03
8b-7	0.02	40	2.28 (3641)	34.5 (221)	304.7 (1950)	99	41.2 \pm 3.2	12.5 \pm 0.2 (20)	0.67
8b-8	0.05	27	2.28 (3641)	25.4 (215)	209.6 (1777)	85	44.0 \pm 3.5	12.6 \pm 0.4 (13)	1.28
8b-9	0.10	29	2.31 (3696)	29.5 (271)	222.4 (2044)	92	48.8 \pm 3.5		
8b-e	-0.06	20	2.08 (3325)	12.6 (75)	107.4 (639)	77	38.9 \pm 4.9	10.6 \pm 0.4 (6*)	0.96
8b-f	-0.03	20	2.06 (3294)	21.3 (152)	166.2 (1188)	38	41.2 \pm 4.1		
8e-1	-0.04	20	1.91 (3087)	11.4 (67)	109.5 (645)	94	31.6 \pm 4.2	12.1 \pm 0.2 (46*)	1.48
8e-2	0.05	20	2.31 (3696)	16.4 (105)	117.7 (753)	80	51.3 \pm 5.6	12.5 \pm 0.4 (22)	1.68
8e-3	0.09	20	2.34 (3752)	16.7 (102)	90.9 (556)	99	68.3 \pm 7.7		
8e-4	0.14	17	2.34 (3752)	12.7 (98)	64.6 (471)	92	73.5 \pm 8.7		
8e-gouge	0	12	2.15 (3441)	19.7 (97)	112.8 (556)	63	59.4 \pm 7.0		
8f-1	12.3	20	2.38 (3807)	16.4 (105)	170.3 (1090)	78	36.6 \pm 3.9	12.7 \pm 0.2 (26)	1.18
8f-2	70	20	2.38 (3807)	10.2 (65)	76.3 (488)	98	50.5 \pm 6.9	12.2 \pm 0.2 (100)	1.60

See following page for table explanation.

Explanation of Table 4.1

Distances shown are from the center of the ultracataclasite layer to the midpoint of the sample. Negative distances from the fault indicate samples on the granodiorite (south) side of the fault, while positive distances indicate samples from the gneiss (north) side. Samples were processed by d'Alessio and Donelick Analytical: standard magnetic and heavy liquid mineral separation processes were used. All samples were analyzed by Blythe. Apatites were mounted in epoxy. Sample surfaces were ground and polished. Apatite mounts were etched in 7% HNO₃ at 18°C for 22s. An “external detector” [e.g., *Naeser*, 1979], consisting of low-U (<5 ppb) Brazil Ruby muscovite, was used for each sample. Samples were irradiated in the Cornell University Triga nuclear reactor. Following irradiation, the muscovites were etched in 48% HF at 18°C for 30 min. Tracks were counted using a 100X dry lens and 1250X total magnification in crystals with well-etched, clearly visible tracks and sharp polishing scratches. A Kinitex stage and software written by *Dumitru* [1993] were used for analyses. Parentheses show number of tracks counted. Standard and induced track densities were determined on external detectors (geometry factor = 0.5), and fossil track densities were determined on internal mineral surfaces. Ages were calculated using $\zeta = 320 \pm 9$ for dosimeter glass SRM 962a [e.g., *Hurford and Green*, 1983]. All ages are central ages, with the conventional method [*Green*, 1981] used to determine errors on sample ages. The chi-square test estimated the probability that individual grain ages for each sample belong to a single population with Poissonian distribution [*Galbraith*, 1981]. * lengths were measured by Blythe on grains exposed to Cf-252 by Donelick Analytical.

Table 4.2. Measured track lengths for all samples

Sample	Track Length Bins (μm)																Mean Length (#)	S.D.
	4-5	5-6	6-7	7-8	8-9	9-10	10-11	11-12	12-13	13-14	14-15	15-16						
8b-1						3	1	5	4							12.54 \pm 0.32 (14)	1.18	
8b-2		3	3	7	5	4	4	15	32	32	9	7	1			11.31 \pm 0.19 (118)	2.08	
8b-4						1	2	6	4	2						12.89 \pm 0.27 (15)	1.04	
8b-5					1	1	0	3	0	1	1	1	1			11.98 \pm 0.86 (8)	2.44	
8b-6				2	2	2	2	6	3	1	1	1	1			11.1 \pm 0.45 (20)	2.03	
8b-7								5	10	5						12.49 \pm 0.15 (20)	0.67	
8b-8								2	1	6	2	2				12.61 \pm 0.36 (13)	1.28	
8b-e							1	3	2							10.6 \pm 0.39 (6)	0.96	
8e-1							4	7	11	11	8	4	1			12.11 \pm 0.22 (46)	1.48	
8e-2					1	1	1	1	4	7	6	0	2			12.48 \pm 0.36 (22)	1.68	
8f-1								3	4	7	8	3	1			12.74 \pm 0.23 (26)	1.18	
8f-2	1	0	0	0	3	5	8	22	32	20	9					12.18 \pm 0.16 (100)	1.60	

Chapter 5

Constraining the exhumation and burial history of the SAFOD Pilot Hole with apatite fission track and (U-Th)/He thermochronometry

5.1 ABSTRACT

The San Andreas Fault Observatory at Depth (SAFOD) Pilot Hole traverses the upper 2 km of a site 1.8 km west of the San Andreas fault (SAF) near Parkfield, California. To evaluate the burial and exhumation history of the site in relation to the kinematics and mechanics of the SAF, we present 15 apatite fission-track (FT) and 5 (U-Th)/He analyses from Pilot Hole samples. Sample ages decrease with depth: FT and (U-Th)/He ages range from ~ 60 and ~ 31 Ma, respectively, in the upper 800 m of the hole to ~ 3 and 1 Ma at the base of the hole (2.2 km depth, 93°C). Thermal modeling of the distribution of FT lengths indicates three events in the last 80 Ma: 1) cooling and exhumation of $> 60^\circ\text{C}$ that culminated at ~ 30 Ma; 2) reheating of $\sim 50^\circ\text{C}$ from ~ 30 to 8-4 Ma, probably as the result of basin subsidence and burial by 1-1.5 km of sediments; and 3) cooling of $\sim 30^\circ\text{C}$ and estimated Coast Range exhumation of ~ 1 km since 8-4 Ma.

5.2 Introduction

The San Andreas Fault Observatory at Depth (SAFOD) provides a unique opportunity to study one of the world's major active faults by acquiring measurements and samples from seismogenic depths. Here, we present a study of the low-temperature thermal history of the samples from the SAFOD Pilot Hole to gain insight into the long-term fault kinematics (block uplift and exhumation) and mechanics (frictional heating) of the San Andreas fault (SAF) near Parkfield. Since heat flow observations are fundamental in constraining the frictional strength of the fault, it is crucial to understand how the long-term thermal evolution affects present thermal observations. We use a combination of apatite fission track (FT) and (U-Th)/He thermochronometry on samples recovered from the Pilot Hole drilled during the summer of 2002 to determine the thermal history of the SAFOD site and interpret it in the context of the geologic history of the region.

5.3 SAFOD setting

The SAFOD site is located in the Coast Ranges of central California, 1.8 km southwest of the San Andreas fault (SAF) near Parkfield (Figure 5.1). The geology is complex surrounding the active fault. In the Pilot Hole, 768 m of Tertiary-age sediments overlie Salinian granodiorites of ~ 110 Ma age [Kistler and Champion, 1986] which were transported northward alongside the SAF from their original emplacement as part of the southern Sierra Nevada batholith. Previous low-temperature dating studies of surface Salinian samples from throughout central California [Figure 5.1A; Naeser and Ross, 1976; Bürgmann *et al.*, 1994a] indicate a relatively heterogeneous cooling history. Most places have cooled by $< 100^\circ\text{C}$ in the last 30 Myr, and thus have been exhumed by less than 2-3 km since the initiation of the SAF.

5.4 Samples and Thermochronometry Results

During June and July 2002, borehole cuttings were collected from the Pilot Hole, which extended to a depth of 2160 m. The SAFOD team extracted 20 samples for our analyses, at downhole intervals of approximately 100 m. Here we present 15 apatite FT analyses and 5 (U-Th)/He analyses of these samples (Figure 5.2; Tables 5.1, 5.2, and 5.3) and an additional FT sample from a nearby granitic outcrop (BARN on Figure 5.1B).

Fission tracks are linear zones of damage in the crystal lattice that form as the result of the spontaneous fission of ^{238}U . At high temperatures, the crystal lattice “anneals” and the tracks shorten. At moderate geologic cooling rates, the closure temperature for FT annealing in F-rich apatites is $\sim 110^\circ\text{C}$ [Green *et al.*, 1986]. Annealing, however, occurs at slower rates at lower temperatures also, and therefore a range of temperatures from ~ 110 to 60°C is referred to as the partial annealing zone (PAZ) [Gleadow and Fitzgerald, 1987]. The length distribution of fission tracks in individual samples can be used to reconstruct the thermal history of the

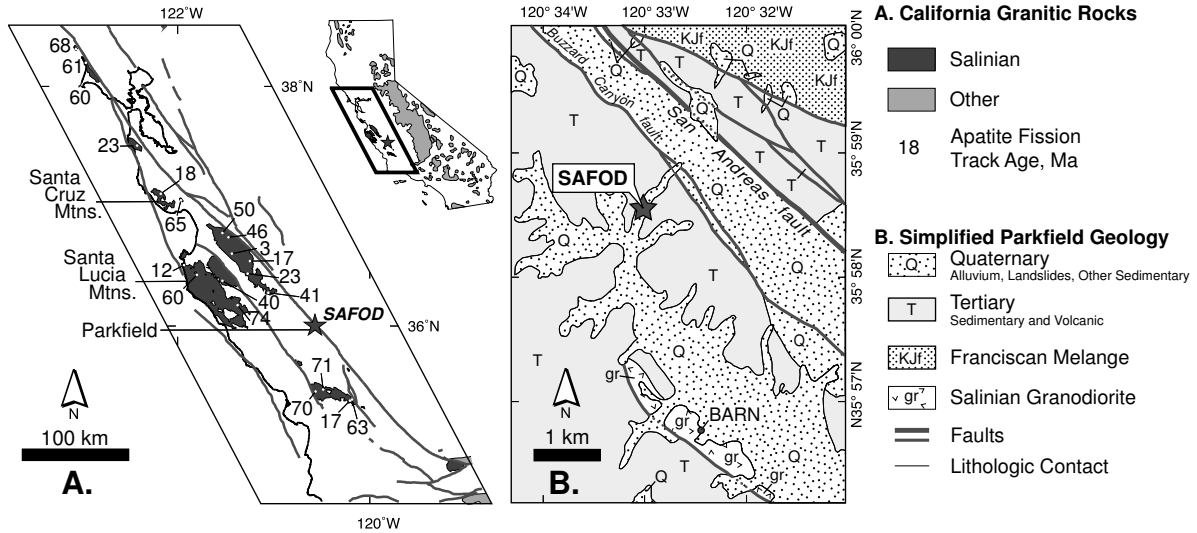


Figure 5.1. Location maps for study: A. Simplified tectonic map of central California, showing the locations of granitic terrains and major faults. Fission track ages from *Naeser and Ross* [1976] and *Bürgmann et al.* [1994a]. B. Simplified geologic map for the SAFOD site near Parkfield, CA, after Rymer, pers. comm., based on *Dibblee* [1971].

sample through the PAZ [*Gleadow et al.*, 1986]: long tracks indicate a short residence time and short tracks a long residence time within the PAZ.

A nearby surface sample (BARN) from the Salinian bedrock yielded an apatite FT age of 60.2 ± 6.0 Ma. This 60 Ma age can be interpreted to indicate that the sample has not been buried or exhumed >2.5 -3 km since that time, if the present-day geotherm of $\sim 35^\circ\text{C}/\text{km}$ is assumed.

In the Pilot Hole, samples from the shallow Tertiary-age sediments have apatite FT ages of 49.2 ± 5.8 , 28.0 ± 3.0 , and 59.6 ± 4.9 Ma. These ages probably reflect the ages of their source rocks. The apatite FT ages in the underlying Salinian granodiorites generally decrease with depth from 54.3 ± 4.8 Ma at a depth of 914 m to ages of 3.0 ± 0.8 and 3.8 ± 0.7 Ma from the two deepest samples (from 2103 and 2160 m, respectively; temperatures of $\sim 93^\circ\text{C}$).

(U-Th)/He thermochronometry, which is based on the release of He during the decay of U and Th, has a closure temperature of $70 - 75^\circ\text{C}$ in apatite [*Farley*, 2000]. The (U-Th)/He system in apatite has a partial retention zone (PRZ) which ranges from ~ 85 to 45°C [*Wolf et al.*, 1998]. Five samples from the Pilot Hole were analyzed in Ken Farley's laboratory at Caltech with two replicates obtained from each sample. The shallowest sample was from the top of the granodiorite (depth of 792 m) and yielded replicate ages of 32 and 19 Ma. The two deepest samples (at current temperatures of $\sim 93^\circ\text{C}$) yielded He ages of ~ 1.7 and 1 Ma. These two non-zero sample ages immediately signal a somewhat complicated thermal history for the Pilot Hole, as 93°C is substantially hotter than the helium closure temperature (for Pilot Hole samples that have mean crystal radii of $60 \pm 10 \mu\text{m}$, we expect closure temperatures of $\sim 66^\circ$ for a $10^\circ\text{C}/\text{Myr}$ cooling rate; *Farley*, 2000). In a study of Otway Basin borehole samples, *House*

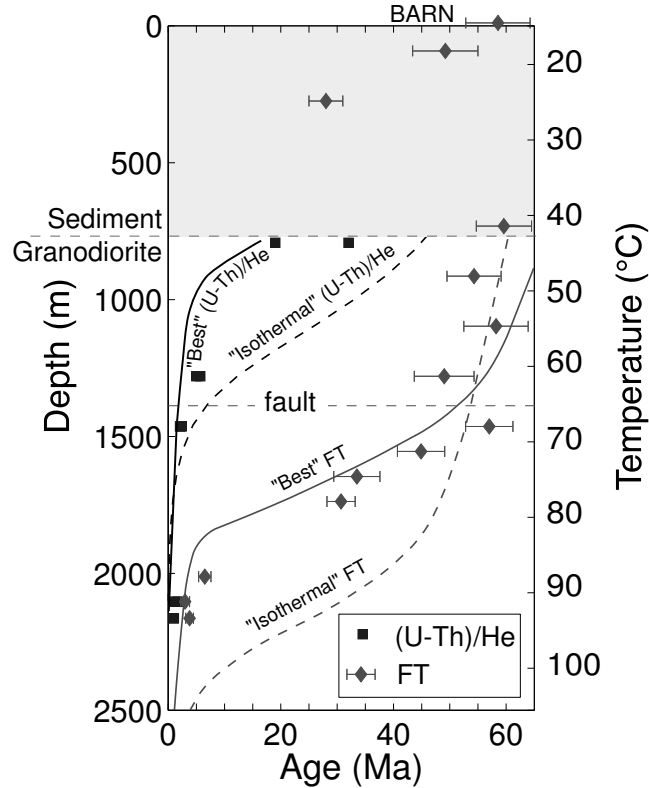


Figure 5.2. Apatite fission track and (U-Th)/He ages plotted with respect to depth and temperature. The location of the granite/sediment contact is shown as is the location of a fault of unknown importance. Dashed lines show predicted ages for the samples if they had resided at their present-day temperature for the last 60 Myr. Solid curves show ages predicted from the best fit thermal history derived from track lengths (Figure 5.3) and assuming no change in the local geothermal gradient (Table 5.4).

et al. [1999] obtained similarly young (U-Th)/He ages at ambient temperatures of $> 80^{\circ}\text{C}$. They attribute these ages to complexities in the long-term thermal history, and possibly helium diffusivities of the borehole apatite crystals that differ slightly from laboratory values.

5.5 Apatite Fission Track Length Analysis and Thermal Model

The kinetics of FT annealing and He loss depend strongly on temperature and have been well characterized in the laboratory [e.g., *Laslett et al.*, 1987; *Wolf et al.*, 1998]. We use the FT length distributions to constrain the past thermal history of the site. Three of the samples yielded a sufficient number of track lengths for thermal modeling. Two of these samples, CU4800 and CU5100, were granitic rocks from depths of 1463 and 1554 m and current temperatures of ~ 70 and 72°C , respectively. The third, CU300, was a near-surface sample from the Tertiary

sedimentary sequence. The single crystal FT ages from this sample indicate the presence of more than one population of ages, most likely from two or more source terranes, making it inappropriate for thermal modeling.

We model the FT length distributions of samples CU4800 and CU5100 to derive time-temperature histories experienced by those samples (Figure 5.3; methodology briefly explained in caption). The two models are consistent with each other and with the known geologic record, however, they are poorly constrained at temperatures outside the PAZ and a wide range of solutions (lighter gray lines, Figure 5.3) fit the observed data. The solutions with the best statistical fit to the observed FT analyses (solid black lines) indicate three distinct phases: The earliest phase is one of slow cooling from ~ 80 until ~ 31 Ma. During this phase, both samples cooled fully through the PAZ, reaching temperatures of 40 - 50°C. The second phase is a reheating of 48 - 58°C that occurred between 31 and 8 - 4 Ma. During the final phase, beginning between 8 and 4 Ma, samples cooled 30 - 47°C to their present-day temperatures.

If we adopt the simplifying assumption that the geothermal gradient of the site did not change, we can use forward modeling to predict both FT and (U-Th)/He ages as a function of depth. This test allows us to verify that the thermal history derived in an inverse sense from two samples using FT alone (Figure 5.3), is consistent with the entire suite of data. For reference, the dashed curves in Figure 5.2 (“Isothermal”) show theoretical age profiles for the hypothetical case that samples remained at present-day downhole temperatures for the last 60 Myr. The observed ages are consistently younger than the isothermal curve, implying that the borehole was exposed to temperatures hotter than the present-day. The solid curves in Figure 5.2 (“Best Fit”) show the expected FT and (U-Th)/He ages for samples that experienced the thermal history shown in Figure 5.3 (also Table 5.4). Heating of 48°C between 31 and 8 Ma does an excellent job of fitting the age-depth data, corresponding to ~ 1.3 km of burial. Overall, ages in the borehole are predicted quite well by our best fit thermal history.

5.6 Interpretation

The initial phase of cooling from ~ 80 to 30 Ma is consistent with regional cooling ages of the Salinian block plutons [e.g., *Mattinson, 1978; Naeser and Ross, 1976*]. This long period of cooling may well be attributable to multiple causes such as cooling and exhumation of granitic intrusions and Laramide cooling as the result of flat-slab subduction [*Dumitru, 1989*]. Granitic rocks near the Salinian/sediment contact are weathered and this contact is interpreted to be a paleosurface exposed during part of the Tertiary [M. Rymer, pers. comm., 2004]. Our best-fit thermal history has samples at the contact cooling to a temperature of less than 30°C and is consistent with this geologic interpretation.

The reheating phase indicated by the thermal models from ~ 30 to 8 Ma is consistent with the onset of SAF movement, and burial of the site by 1 - 1.5 km of Tertiary sediment. Heat flow in the Coast Range may have evolved significantly over time related to the transition from subduction to transform faulting [*ten Brink et al., 1999*], but we cannot detect changes in the geothermal gradient with our current data. It is possible that some component of this heating could be from frictional heat generation on the SAF, however, the existing mantle of nearly 800

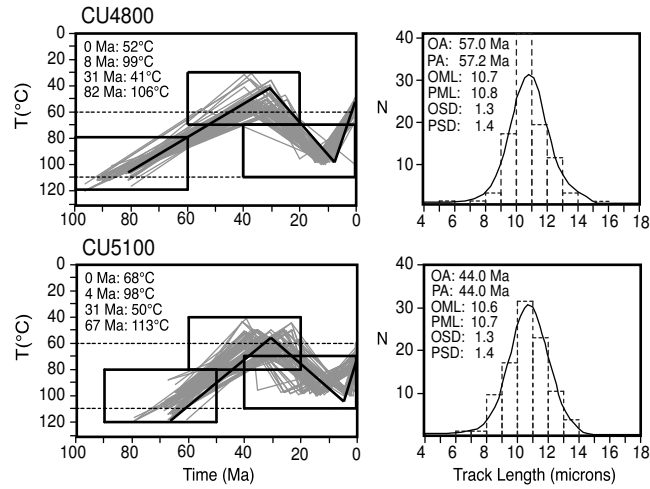


Figure 5.3. Modeled thermal histories for samples CU4800 and CU5100 are shown on the left-hand side. These were obtained using the modeling program MonteTrax [Gallagher, 1995] on measured FT age and length distributions for each sample. The thermal models were obtained using forward modeling (4 time temperature boundaries were specified) and a genetic algorithm approach (20 iterations of 100 solutions). A starting mean track length of $14.5 \mu\text{m}$, a high-F apatite composition (Durango), and the annealing model of Laslett *et al.* [1987] were assumed. The dashed horizontal lines on each model represent the boundaries of the apatite PAZ. The black boxes are the specified input ranges of time and temperature. The lightly shaded lines are possible thermal histories that produced statistically acceptable fits to the observed data. The black line is the best fit solution and the ages and temperatures of its inflection points are in the upper left corners. Shown on the right-hand side are the measured track length distributions (histograms) and the modeled track length distribution (solid curves) for the best fit thermal history solution. OA - observed age, PA predicted age, OML observed mean length, PML predicted mean length, OSD observed standard deviation, PSD predicted standard deviation.

m of overlying late Cenozoic sediments suggests that sediment burial, seen throughout central California at this time [e.g., *Blake et al.*, 1978; *Crouch et al.*, 1984], was the dominant source of heating.

The final phase of cooling seen in the thermal models, beginning between 8 and 4 Ma, is probably the result of ~ 0.8 - 1.3 km of exhumation, assuming the present-day geotherm of $\sim 35^\circ\text{C}/\text{km}$. This event is consistent with the timing of Coast Ranges uplift seen in nearby ranges [*Page et al.*, 1998]. Exhumation began at ~ 4 Ma in the Santa Cruz Mountains [*Bürgmann et al.*, 1994a, apatite FT] and ~ 4 Ma in the Santa Lucia Mountains [*Ducea et al.*, 2003, (U-Th)/He)]. This uplift can be attributed to the increased convergence rate along the Pacific-North American plate boundary indicated at ~ 8 Ma by the reconstructions of *Atwater and Stock* [1998]. Locally, *Sims* [1993] shows that the SAF achieved a geometry similar to its present-day configuration in Parkfield at ~ 5 Ma and its slip rate accelerated from 10 mm/yr to 33 mm/yr. Active convergence and uplift in the region is continuing today, as evidenced by nearby seismically active thrust faults (e.g., 1984 Coalinga and 2003 San Simeon earthquakes).

The exhumation rate in the final phase of cooling for the best fitting model is 0.1-0.2 mm/yr, removing $\sim 1\text{km}$ of sedimentary cover since cooling began between 8 and 4 Ma. With such a low rate of exhumation, we would not expect significant disturbances in the geotherm at depth caused by uplift – allowing extrapolation of the present-day geotherm to the target depth of the main SAFOD hole.

5.7 Conclusions

The thermal history indicated by the Pilot Hole samples is consistent with the general geologic history of the central San Andreas fault. This includes evidence for 1) a phase of gradual exhumation of the Salinian intrusives in the late Cretaceous and early Tertiary; 2) reburial by 1-1.5 km during the early phases of SAF transform faulting in the mid-Tertiary; and 3) exhumation related to regional Coast Ranges uplift in the late Cenozoic. What is remarkable is that given the complex tectonic history of these rocks, including lateral transport of 160 km over the last 5 Ma [*Sims*, 1993], only ~ 1 km of vertical motion (up and down) occurred during the last 60 Ma.

5.8 Appendix: Fission Track Analysis Procedure

Samples were processed by Donelick Analytical: standard magnetic and heavy liquid mineral separation processes were used. All samples were analyzed by Blythe. Apatites were mounted in epoxy. Sample surfaces were ground and polished. Apatite mounts were etched in 7% HNO_3 at 18°C for 22s. An “external detector” [e.g., *Naeser*, 1979], consisting of low-U ($< 5\text{ppb}$) Brazil Ruby muscovite, was used for each sample. Samples were irradiated in the Oregon State University Triga nuclear reactor. Following irradiation, the muscovites were etched in 48% HF at 18°C for 30 min. Tracks were counted using a 100X dry lens and 1250X total magnification

Table 5.1. SAFOD Pilot Hole Summary of Observations.

¹ S - sediment, G - Granodiorite.

² number in brackets is the standard deviation, number in parentheses is the total number of lengths measured.

Sample	Lithology ¹	Depth (m)	Temp. (°C)	Fission Track Central Age $\pm 1\sigma$ (Ma)	Track Length Distribution ² (μm)	Helium Ages (Ma)
BARN	G	0	15	60.2 \pm 6.0	13.3 \pm 0.23 [1.35] (34)	
CU300	S	91	18	49.2 \pm 5.8	11.50 \pm 0.15 [1.39] (84)	
CU900	S	274	26	28.0 \pm 3.0		
CU2400	S	732	42	59.6 \pm 4.9		
CU2600	G	792	44			31.95, 18.91
CU3000	G	914	48	54.3 \pm 4.8		
CU3600	G	1097	55	58.2 \pm 5.7		
CU4200	G	1280	62	49.0 \pm 5.3		7.61, 6.60
CU4800	G	1463	68	57.0 \pm 4.2	10.73 \pm 0.13 [1.30] (102)	3.11, 2.68
CU5100	G	1554	72	44.9 \pm 4.2	10.61 \pm 0.13 [1.33] (102)	
CU5400	G	1646	76	35.8 \pm 4.1		
CU5700	G	1737	79	30.7 \pm 2.5		
CU6000	G	1920	82	8.5 \pm 1.2		
CU6600	G	2012	89	6.5 \pm 1.1		
CU6900	G	2103	92	3.0 \pm 0.8	10.78 \pm 0.68 [2.05] (9)	2.01, 1.53
CU7100	G	2164	94	3.8 \pm 0.7		1.01, 0.94

in crystals with well-etched, clearly visible tracks and sharp polishing scratches. A Kinitex stage and software written by *Dumitru* [1993] were used for analyses. Parentheses show number of tracks counted. Standard and induced track densities were determined on external detectors (geometry factor = 0.5), and fossil track densities were determined on internal mineral surfaces. Ages were calculated using zeta 359 ± 10 for dosimeter CN5 [e.g., *Hurford and Green*, 1983]. All ages are central ages, with the conventional method [*Green*, 1981] used to determine errors on sample ages. The chi-square test estimated the probability that individual grain ages for each sample belong to a single population with Poissonian distribution [*Galbraith*, 1981]. The data were reduced with software provided by I. *Dunkl* [2002].

Table 5.2. Apatite Fission Track Analyses - SAFOD Pilot Hole

Sample	Depth from fault (m)	# Grains	Standard track density ($\times 10^{-6} \text{ cm}^{-2}$)	Fossil track density ($\times 10^{-6} \text{ cm}^{-2}$)	Induced track density ($\times 10^{-6} \text{ cm}^{-2}$)	χ^2 prob. %	Central age (Ma)	Mean track length (μm)	Std dev. (μm)
BARN	0	20	1.48 (2845)	31.68 (294)	141.27 (1311)	5	60.2 \pm 6.0	13.3 \pm 0.23 (34)	1.35
CU300	91	24	1.26 (2431)	42.58 (402)	190.68 (1800)	Fail	49.2 \pm 5.8	11.50 \pm 0.15 (84)	1.39
CU900	274	20	1.55 (2993)	25.39 (195)	260.03 (1997)	21	28.0 \pm 3.0		
CU2400	732	20	1.41 (2707)	38.93 (355)	164.58 (1501)	90	59.6 \pm 4.9		
CU3000	914	20	1.55 (2993)	46.79 (283)	239.42 (1448)	33	54.3 \pm 4.8		
CU3600	1097	20	1.41 (2845)	40.81 (198)	176.86 (858)	73	58.2 \pm 5.7		
CU4200	1280	13	1.51 (2907)	41.07 (385)	226.19 (2341)	89	49.0 \pm 5.3		
CU4800	1463	20	1.34 (2569)	118.11 (737)	496.31 (3097)	20	57.0 \pm 4.2	10.73 \pm 0.13 (102)	1.30
CU5100	1554	20	1.51 (2907)	100.26 (347)	609.64 (760)	Fail	44.9 \pm 4.2	10.61 \pm 0.13 (102)	1.33
CU5400	1646	12	1.34 (2569)	58.38 (275)	403.15 (1899)	Fail	35.8 \pm 4.1		
CU5700	1737	20	1.55 (2983)	63.83 (337)	576.52 (3044)	51	30.7 \pm 2.5		
CU6000	1920	20	1.51 (2821)	4.53 (58)	140.70 (1801)	93	8.5 \pm 1.2		
CU6600	2012	20	1.55 (2983)	3.54 (43)	151.32 (1840)	83	6.5 \pm 1.1		
CU6900	2103	12	1.26 (2431)	2.43 (15)	183.2 (1130)	72	3.0 \pm 0.8	10.78 \pm 0.68 (9)	2.05
CU7100	2164	21	1.48 (2707)	3.40 (37)	237.41 (2583)	40	3.8 \pm 0.7		

Table 5.3. Fission Track Length Analysis Details

Sample	bins (microns)																Mean length (μm)	S.D. (μm)	Total #
	5-6	6-7	7-8	8-9	9-10	10-11	11-12	12-13	13-14	14-15	15-16	16-17							
BARN	-	-	-	-	-	-	6	10	9	4	4	1	13.30 \pm 0.23	1.35	34				
CU300	-	-	1	3	5	19	30	14	7	5	-	-	11.50 \pm 0.15	1.39	84				
CU4800	1	0	1	3	18	43	20	12	3	0	1	-	10.73 \pm 0.13	1.30	102				
CU5100	-	1	1	10	18	33	24	11	4	-	-	-	10.61 \pm 0.13	1.33	102				
CU6900	-	-	1	1	1	2	1	2	1	-	-	-	10.78 \pm 0.68	2.05	9				

Table 5.4. Summary and comparison of thermal histories determined for the SAFOD Pilot Hole.

D1 - D4 are dates in *Myr* before present. T1-T4 are the temperature of the sample at that time. D4 represents the present-day and T4 is the observed or predicted downhole temperature. Because the two samples with enough fission tracks to model thermal histories yield similar but not identical thermal histories (Figure 3), this table clarifies the precise thermal history we define as the “Best fit” (Solid curves in Figure 2). The downhole temperatures observed in the SAFOD pilot hole by *Williams et al.* [2004] are shown for reference at 4 points in the borehole. The thermal histories shown in Figure 3 are reproduced in the second set of rows. In addition to the constraints indicated by the rectangles in Figure 3, note that we constrain the present-day temperature to $\pm 20^\circ C$ of its observed value. The last set of rows is the “Best fit” thermal history we use in Figure 2. Between each date in this table, we assume either linear heating or cooling. The four thermal histories are presented for reference, but show redundant information; given one of the thermal histories at a known depth, we calculate the other thermal histories by assuming a constant geothermal gradient over time. We use a geothermal gradient of $37^\circ C km^{-1}$, consistent with the temperature logs from the SAFOD Pilot Hole [*Williams et al.*, 2004], and a surface temperature of $16^\circ C$. The best fit thermal history for fission track uses the annealing relationships defined by *Laslett et al.* [1987]. For (U-Th)/He, we use the numerical method outlined in *Wolf et al.* [1998] and apatite diffusivities similar to the Durango composition from *Wolf et al.* [1996] ($\log_{10} D_o/a^2 = 7.8 s^{-1}$, $E_a = 36.3 kcal/mol$).

Description	Depth m	D1 Ma	T1 °C	D2 Ma	T2 °C	D3 Ma	T3 °C	D4 Ma	T4 °C
<i>Observed Downhole Temperature Log</i>									
Salinian-Sediment Contact	768	-	-	-	-	-	-	0	46
Sample CU4800	1463	-	-	-	-	-	-	0	69
Sample CU5100	1554	-	-	-	-	-	-	0	72
Bottom of Hole	2160	-	-	-	-	-	-	0	93
<i>Derived from Fission Track Length Modeling in an “Inverse” Sense; Figure 3</i>									
Sample CU4800	1463	82	106	31	41	8	99	0	52
Sample CU5100	1554	67	113	31	50	8	98	0	68
<i>Used to Forward Model “Best Fit” Curves in Figure 2</i>									
Salinian-Sediment Contact	768	75	90	31	27	8	75	0	45
Sample CU4800	1463	75	115	31	52	8	100	0	70
Sample CU5100	1554	75	118	31	55	8	103	0	73
Bottom of Hole	2160	75	138	31	75	8	123	0	94

Chapter 6

Frictional heterogeneity and heat flow

6.1 ABSTRACT

The magnitude of frictionally generated heat varies as a function of the frictional strength of a fault. The heterogeneity of natural faults suggests that realistic models of frictional heat generation should consider variations in frictional strength. Here we use numerical models to explore the effects of faults with spatially and temporally heterogeneous frictional strength on the spatial distribution of surface heat flow. Lateral variations of friction along strike combined with the lateral displacement of the blocks by a strike-slip fault requires a non-linear solution to heat flow equations and can produce heat flow patterns that are asymmetric across the fault and along-strike. This asymmetry has implications for conclusions about fault strength drawn from existing heat flow measurements. We explore a range of slip rate-asperity size combinations to determine the limit in which a heterogeneous fault is indistinguishable from a fault with uniform frictional properties.

6.2 Introduction

The frictional strength of large faults controls the amount of frictional heat generated during slip. While there is currently much debate on which factors most strongly control fault friction, it is unlikely that faults will have uniform friction throughout. Heterogeneity in gouge zone structure, composition, hydrologic properties, as well as the magnitude and timing of fault slip

events will all lead to heterogeneous frictional properties that will in turn produce a complex spatial distribution of frictional heat generation.

Our understanding of fault friction began in the laboratory where sliding experiments show that the coefficient of friction (μ) for faults is greater than 0.6 for almost all geologic materials [Byerlee, 1978]. However, these experiments may be neglecting crucial processes that control friction at the scale of large faults in nature. Evidence from surface heat flow [Brune *et al.*, 1969; Lachenbruch and Sass, 1980], thermochronology [Xu and Kamp, 2000; d'Alessio *et al.*, 2003], and the orientation of the maximum principal stress [Mount and Suppe, 1987; Hardebeck and Hauksson, 1999; Provost and Houston, 2001] all suggest that the coefficient of friction of natural faults could be 0.2 or lower (a “weak fault”). While such studies are intriguing, similar types of data also have been used to argue that natural faults have frictional properties quite similar to laboratory measurements [Scholz *et al.*, 1979; Camacho *et al.*, 2001; Scholz, 2000; Castillo and Hickman, 2000]. These conflicting results and the ongoing debate about fault strength highlight the fact that fault friction is a complex property that may depend on many factors.

Researchers have proposed a number of physical mechanisms that could explain the apparent weakness of natural faults, and all of the mechanisms would likely lead to heterogeneous frictional properties. These mechanisms fall into two general categories: 1) permanent (structural or lithologic features of the fault) and 2) dynamic (resulting from events related to the rupture process of large earthquakes). Serpentine gouge [Moore *et al.*, 1996, 2004] and kaolinite clay [Allen, 1968; Moore and Lockner, 2004] are frictionally weak under certain pressure and temperature conditions. Heterogeneous distributions of these minerals within the fault core would create non-uniform friction, and gouge composition is known to vary along fault strike [e.g., Anderson *et al.*, 1983]. Several weakening mechanisms suggest that elevated pore pressures in the fault zone could drastically alter the apparent coefficient of friction of natural faults. Rice [1992] hypothesized that a constant source of deep fluids causes consistently elevated pore pressures while other authors have shown that earthquake-induced thermal expansion of pore fluids could reduce the effective normal stress within the fault zone [Lachenbruch, 1980; Mase and Smith, 1987; Sibson, 1992]. Fluid pressures depend on the permeability structure of the fault, which varies with lithology on opposite sides of the San Andreas fault [Lachenbruch and Sass, 1980] and along strike within the core of exhumed fault zones [Evans and Chester, 1995]. A class of dynamic weakening mechanisms have been proposed where seismic wave propagation reduces the normal stress on the fault during an earthquake. Interface separation during slip due to vibrations between the fault blocks depends on the roughness of the fault [Brune *et al.*, 1993]. Acoustic fluidization of fault zone materials depends upon the width of the gouge zone [Melosh, 1996]. A wrinkle-like slip pulse related to rheologic differences between the two fault blocks is fundamentally tied to lithologic contrasts, which vary along large faults [Andrews and Ben-Zion, 1997]. Faults slipping aseismically (i.e., creep and slow/silent earthquakes) cannot be weakened dynamically because their slip rates are too low to generate dynamic effects. All of the factors that control dynamic weakness would be non-uniform along faults, including the relative contribution of earthquake slip compared to aseismic creep.

Both the absolute frictional strength of natural faults and the mechanisms controlling this strength are hotly debated within the community. Since frictional sliding generates heat, thermal measurements around faults remain the most direct way to infer the friction of natural

faults. Models that describe the generation and transport of heat in fault zones are therefore essential to solving this puzzle. In this work, we present a new formulation of the heat flow problem that considers the effects of heterogeneous frictional strength along faults. We show that discrete heat sources representing frictional asperities alter the predicted distribution of surface heat flow compared to the existing models that assume homogeneous faults. We then present an example application of our model for the creeping section of the San Andreas fault to demonstrate how the predicted heat flow pattern from a heterogeneous fault can affect the inferred frictional strength.

6.3 Existing formulations of frictional heat

Previous theoretical work exploring frictional heat tends to be grouped into one of two main categories: 1) the rupture process and generation of frictional heat; and 2) the flow of frictional heat over long time and length scales, either conductively or advectively.

6.3.1 Rupture Process

Quantifying total frictional heat generation involves complex feedbacks between heat generation, fluid pressure, effective normal stress, melting, seismic wave generation, and frictional stability. *McKenzie and Brune* [1972] begin with the simplest case of frictional sliding along an infinite fault between two homogeneous blocks. In this theoretical case, they show that near-fault temperatures can vastly exceed the melting temperature of rock – at which point their assumptions break down. Citing the absence of frictional melt along most fault systems, *Lachenbruch* [1980] presents a summary of how frictionally generated heat could pressurize fluids within a fault gouge zone and reduce the effective normal stress, thus altering frictional heat generation rates – results echoed by *Mase and Smith* [1987]. *Blanpied et al.* [1998] discuss an alternative feedback where frictional stability and strength increases with increasing temperature. These foundational works are complemented by the abundant theories attempting to explain the frictional strength of natural faults in the context of heat flow measurements discussed in the Introduction [see also Section 3.4 of *Scholz*, 2002]. To encompass all of these effects without regard to their detail or origin, the concept of an “apparent coefficient of friction” (μ_{app}) is frequently employed [*Harris*, 1998]. This quantity represents an average frictional strength over the time scale of heat generation. For earthquakes which persist for only a few seconds, this average is acceptable for heat flow analysis that involves time scales of days to millions of years. Another important factor is the relative amount of energy dissipated by frictional heat compared to seismic wave generation or the creation of new surface area (grain crushing). Measurements in the laboratory [*Lockner and Okubo*, 1983] and inferences from seismic waves [*McGarr*, 1999] show that > 90% of all energy released during fault slip is converted to frictional heat.

6.3.2 Transport of Frictional Heat

As noted in Section 4.2 and *d’Alessio et al.* [2003], the time and length scale of heat flow covers a very wide range. *Lachenbruch* [1986] lay the framework for estimates of the localized effects of frictional heating in the days to months following an earthquake. These formulations were verified in laboratory work [*Lockner and Okubo*, 1983; *Blanpied et al.*, 1998], but there were few ways to directly test these heat flow models outside the laboratory until the development and advancement of thermochronology [*Bustin*, 1983; *d’Alessio et al.*, 2003]. Longer-time-scale thermal features near faults were well explored through surface heat flow. *Henye* [1968] developed the main theoretical groundwork for the large-scale diffusion of heat near fault zones, work followed by the published summary of *Brune et al.* [1969] and the comprehensive treatment by *Lachenbruch and Sass* [1980]. To determine the temperature field, they integrate the solution of a horizontal line source over a range of depths [Appendix A of *Lachenbruch and Sass*, 1980]. The line source is infinitely long, resulting in infinitely long fault planes with homogeneous parameters along strike. These models assume all heat flow is conductive, but there is debate over the role of fluid flow in advective heat transport around faults [*O’Neil and Hanks*, 1980; *Williams and Narasimhan*, 1989; *Saffer et al.*, 2003; *Fulton et al.*, 2004]. The recent studies suggest that heat flow near the San Andreas is consistent with conductive models, so we only consider conductive heat flow in this work. Even though more complicated numerical models have been formulated to include a viscous lower crust [e.g., *Thatcher and England*, 1998; *Leloup et al.*, 1999; *Rolandone and Jaupart*, 2002], these models still restrict themselves to an infinite fault plane. While reasonable for many cases, this assumption does have its limitations. In the following sections, we introduce analytic solutions and numerical models of conductive heat flow about a finite fault.

6.4 Heat Flow Distribution about a finite fault

In the Appendix (Section 6.9), we present a simple derivation for the spatial and temporal distribution of temperature surrounding a rectangular fault patch in three dimensions. The fault patch is analogous to a high-friction asperity surrounded along strike by frictionless sections. We focus in this work on the case of a vertical strike-slip fault. Following *Lachenbruch and Sass* [1980], we allow for heat generation to be constant or vary linearly with depth. While we assume constant heat generation along strike of each rectangular element, complex 3-D distributions of frictional asperities can be constructed as a series of these rectangular patches. We calculate surface heat flow by multiplying the temperature gradient in the top kilometer of crust by the thermal conductivity of the medium.

Figure 6.1 shows the distribution of surface heat flow for a single frictional asperity of various sizes. Overall, the map view of heat flow magnitude (Fig. 6.1a) is similar to the infinite case near the midpoint of the surface trace of the asperity, but, as might be expected for a finite fault, heat flow diminishes radially from the fault tips. Fig. 6.1a shows our “reference model” case of a 170 km frictional asperity (see Table 6.1 for parameters used). We show the end member case of a very strong fault ($\mu_{app} = 0.8$), but that result can be linearly scaled to represent faults with lower coefficients of friction. Profiles perpendicular to the fault patch (Fig.

Table 6.1. Values for reference model. See Table 6.2 for explanation of variables. Note that for our heating rate, we use a “strong fault” with a coefficient of friction of 0.8 and 100% of earthquake/slip energy converted into heat. This is an extreme case.

Variable	Value	Units
C_p	800	$J/(kg \cdot K)$
Q_0	0	J
$\frac{dQ}{dz}$	734	kJ/km
	$= \tau * v_{slip} = 21.6 \text{MPa/km} \cdot 3.4 \text{cm/yr}$	
asperity length	170	km
t	10	myr
z_{top}	0	km
z_{bottom}	15.0	km
κ	$1.3 \cdot 10^6$	m^2/s
ρ	2750	kg/m^3

6.1a) are similar to the infinitely long fault of *Lachenbruch and Sass* [1980], though peak heat flow values on profiles near the fault termination are lower than those at the fault midpoint. The peak heat flow always occurs at the midpoint of the fault trace, but the magnitude at the midpoint decreases as the size of patches decreases.

The profile along fault strike (Fig. 6.1e) shows that heat flow drops proportionally to $\text{erf}[y/(fault\ length/2)]$. Heat flow remains near its maximum value along much of the heat-generating fault surface. However, near the two ends of the fault, heat flow falls off fairly rapidly, with the values at the two ends equal to about half the maximum value. For cases near steady-state, the coefficient of proportionality depends strongly on the depth-extent of fault heating and less so on the thermal diffusivity. For this case, the heat flow distribution is symmetric along strike and across the fault such that profiles perpendicular to the fault at equal distances from the midpoint are identical (i.e., profiles at $y = \pm 85 \text{km}$ both look like 6.1d), as are two profiles parallel to the y-axis and equally spaced away from the fault on opposite sides.

Figure 6.2 shows the temporal evolution of the along-strike heat flow profile. Much like the case for the infinite fault of *Lachenbruch and Sass* [1980], the system evolves towards steady-state, with locations closest to the fault reaching steady-state sooner. The exact timing of these curves depends on the depth extent of the heat generating fault and the thermal properties of the medium. Even though the magnitude of steady-state heat flow for the fault tip is about half the peak at the fault midpoint, the shape of the temporal evolution is very similar. The slight differences between the two are most pronounced for greater distances from the fault. Note that for the maximum age of the San Andreas fault system of $\sim 28 \text{Ma}$ [*Atwater and Stock*, 1998], points 40 km from the fault only reach about 70% of their steady-state value, though the heat flow at these distances is always a small fraction of the peak heat flow at the fault plane.

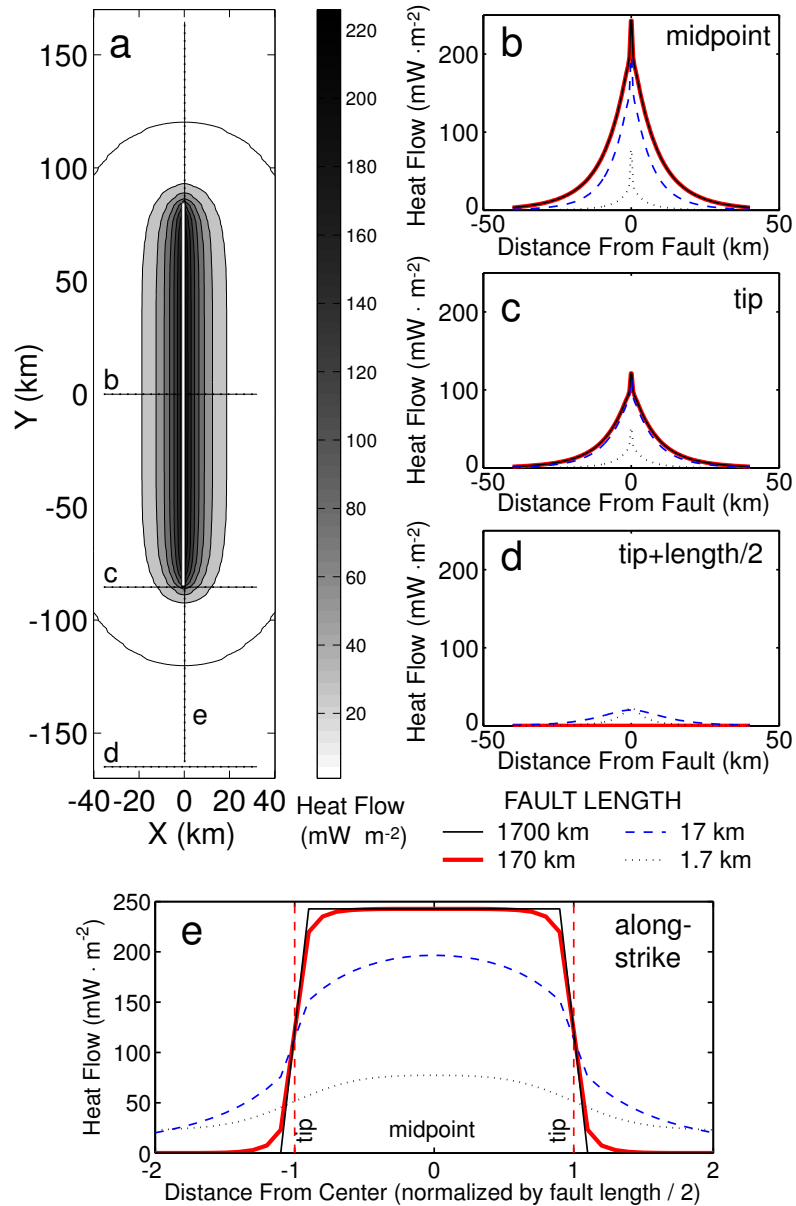


Figure 6.1. Predicted surface heat flow for a single, vertical, rectangular fault patch of various sizes. a) Representative map-view of a 170 km long-fault patch. Approximate location of profiles from panels b-e are shown as dotted lines. b-d) Heat flow profiles taken perpendicular to the fault patch at its midpoint (b), tip (c), and one half the length of the fault trace beyond the tip (d). While the y-position of these profiles varies, the width of the profile in the x-direction (perpendicular to fault) remains constant profiles along the fault. e) Heat flow profile along the strike of the fault patch, normalized by the length of the fault patch so that all profiles are shown with unit length. The absolute distance where elevated heat flow extends is roughly constant, but extends several fault lengths beyond the patch when the trace length of the patch is small relative to the depth of the heat generating surface (15 km, in this case).

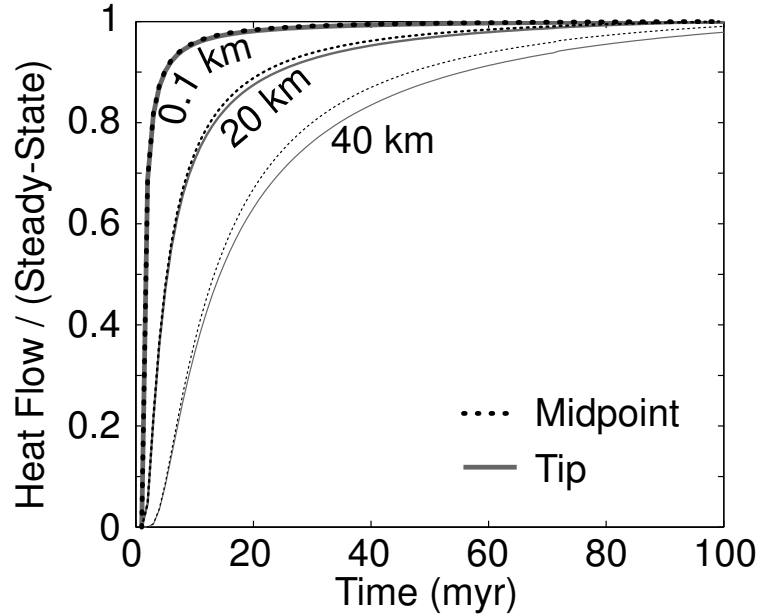


Figure 6.2. Temporal Evolution of heat flow on a finite fault patch 170 km long shown normalized by their steady-state values. (as in Fig. 6.1a). Solid lines are for fault midpoint (Fig. 6.1b). Dotted lines are for fault tips (Fig. 6.1c). Distances indicate distance away from the fault along the fault perpendicular profile. Note that there is very little difference between the shape of the profiles at the tip and midpoint.

6.5 Lateral Transport

The models of frictional heat transport that we have discussed thus far neglect a key component of faulting: relative motion. As a fault slips, it not only displaces the geologic units in the crustal blocks surrounding it, but it also transports all of the thermal energy contained within the blocks. If the fault slip rate is fast compared to the rate of conduction, then this effect could be very important. For a fault with frictional asperities, block offset can move hot material away from a heat generating asperity and juxtapose hot areas with an area that has not experienced heat generation. When these two surfaces are in contact, the direction of the thermal gradient near the fault changes direction such that flow is directed from the hot block into the cold block across the fault (instead of radially away from the fault). This effect can completely alter the spatial and temporal distribution of heat flow. For an infinite strike-slip fault with uniform heat generation along strike, block offset does not affect the calculation of surface heat flow because the entire length of the fault is heated. Here we include heat transport by block offset and discuss the distribution of surface heat flow for a fault with heterogeneous friction.

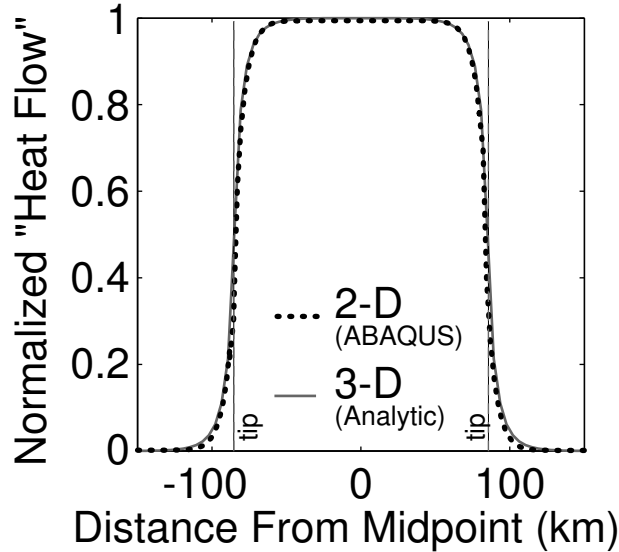


Figure 6.3. Comparison between shape of along-strike heat flow profile for 3-D analytic solution and 2-D numerical solution from ABAQUS software package. Both capture the error function decay of the profile about the fault tip, though the 2-D approach slightly underestimates the amount of heat flow beyond the fault tip.

6.5.1 Method

To model vertical heat flow in a system where crustal blocks and heat sources move laterally, we solve a fully coupled thermal-displacement system in three dimensions. The problem cannot be solved analytically, so we use the commercially available ABAQUS finite element package using over 50,000 thermal brick elements in each model run. These model runs take 1-2 weeks on a 900 MHz Sun Fire v480. During initial tests, we found that fully 3-D models produce qualitatively similar results to substantially less computationally intense 2-D model runs. We use temperature within the 2-D space as a proxy for heat flow in the 3-D case. Figure 6.3 shows a comparison between the 3-D version calculated in our analytic model for a stationary frictional asperity compared with a 2-D run from ABAQUS with the amplitude scaled to match the peak heat flow. We find a similar correspondence between 2-D and 3-D numerical models that include block offset. We therefore use the computationally easier 2-D calculations for the duration of this discussion, with the caveat that we hope to verify these results with 3-D runs in the future.

6.5.2 A Single Asperity

In Fig. 6.4 (also Movie 1 in the electronic supplement), we show the distribution of heat flow after 10 myr for a single frictional asperity on a fault with block offset. Here, the asperity is fixed to the western block while the eastern block moves past at $3.4 \text{ cm}\cdot\text{yr}^{-1}$ in a right-lateral

sense (long-term offset rate of the San Andreas fault). We discuss alternate transport scenarios in Section 6.6. After the first model time step of 0.1 myr, the results are indistinguishable from an asperity in a stationary half space. As time passes, fault offset becomes important. We focus first on the thermal history of the eastern block. Cooler material on the “leading edge” (northeast of asperity) is now juxtaposed with the heat source. This cool section of the block has a lower heat flow because it has been far away from the heat source in the geologic past. As we show for the simple stationary case in Fig. 6.2, the shorter amount of time a block is exposed to heat, the lower its heat flow. At the trailing edge of the heat source (southeast), material that has been exposed to heating is progressively moved away from that heat and coming in contact with cooler material. In the absence of additional heat input in this region, the only control on heat flow is the thermal gradient which draws heat exclusively from the recently heated east side to the cooler west side. The view in the reference frame of the western block is slightly different. Since the heat source in this example is fixed to the western block, the crust adjacent to the frictional asperity is exposed to heat during the entire time. While portions of the western block near the leading edge in the north are constantly exposed to cooler eastern rocks, by the time these sections of the eastern block reach the trailing edge, they have been constantly heated for the entire time it takes to travel the length of the asperity. The different history of heating and contact with cool blocks gives rise to a strong asymmetry in the heat flow pattern along strike. Near the trailing edge of the frictional asperity, heat flow is most similar to the stationary case because the “pre-heated” material in contact with the heat source is most similar to the case where the two sides were always in contact. The peak heat flow occurs near the southern end of the asperity ($y = -75$) where the heat flow pattern is most symmetric across the fault. The heat flow at the midpoint is 8% lower than for a stationary case and is uniformly lower throughout the model because heat is spread over a larger area when the blocks move.

The resulting heating distribution is asymmetric along strike (compare Figs. 6.4b-e) and on opposite sides of the fault (6.4f). Note that even though the heating rate is identical, as in the stationary case, the peak heat flow in this moving case is lower than for the stationary case at most locations.

6.5.3 Dependence on Slip Rate

The stationary fault represents one end-member of heating along finite faults that produces a symmetric profile, and asymmetry will arise for any non-zero fault offset rate. The opposite end-member would be a fault moving infinitely fast such that it is effectively a constant-temperature boundary condition. For typical fault slip rates, this “icy conveyor belt” scenario is never achieved, but the two end members clearly illustrate an importance of slip rate in defining the precise distribution of heat flow about a finite frictional asperity. Figure 6.5 shows the map view heat flow distribution for variations on the reference case that involve a range of slip rates. In reality, the heating rate depends on the slip rate of the fault. A slower slip rate should yield a more symmetric heat flow distribution with a lower peak heat flow. For our model illustrations, however, we vary only the slip rate but keep the heating rate constant to isolate the effect of slip rate. For the fast case ($6.8 \text{ cm} \cdot \text{yr}^{-1}$), the peak and midpoint heat flow are 13% and 24% lower

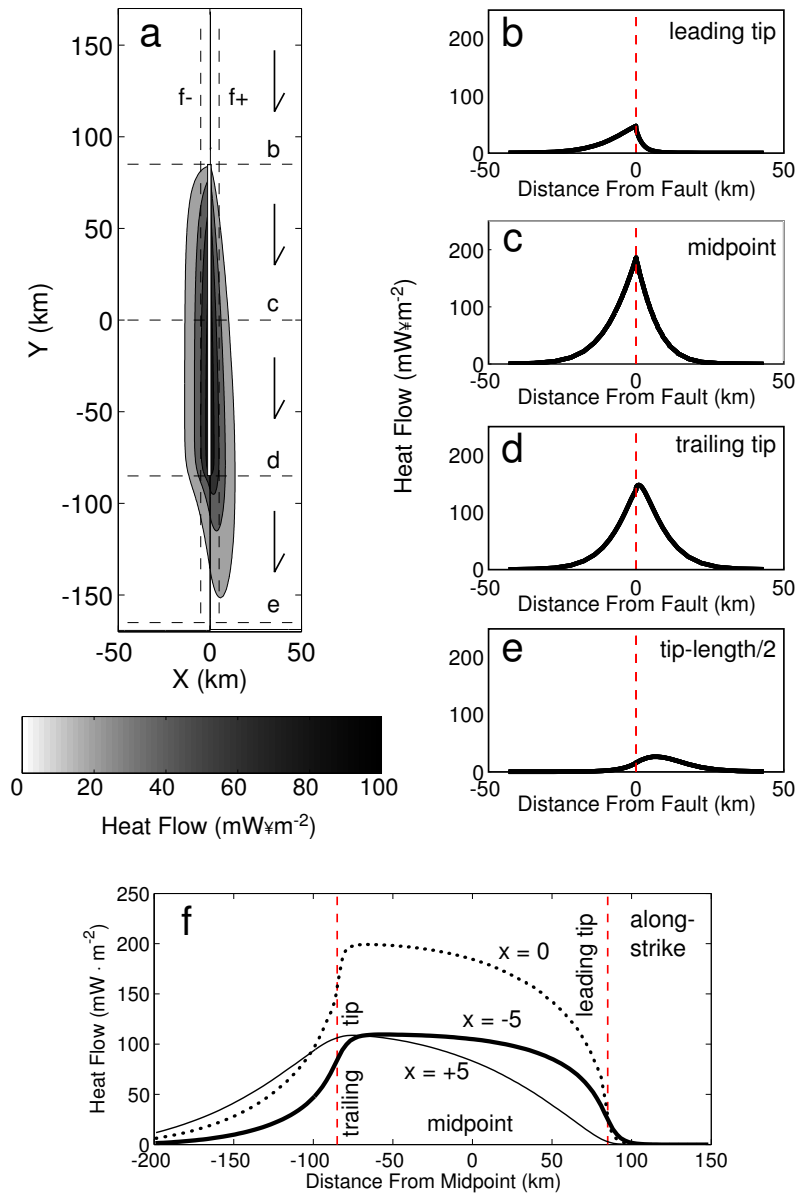


Figure 6.4. Heat flow distribution for a single frictional heat generating asperity in a model that include block offset.

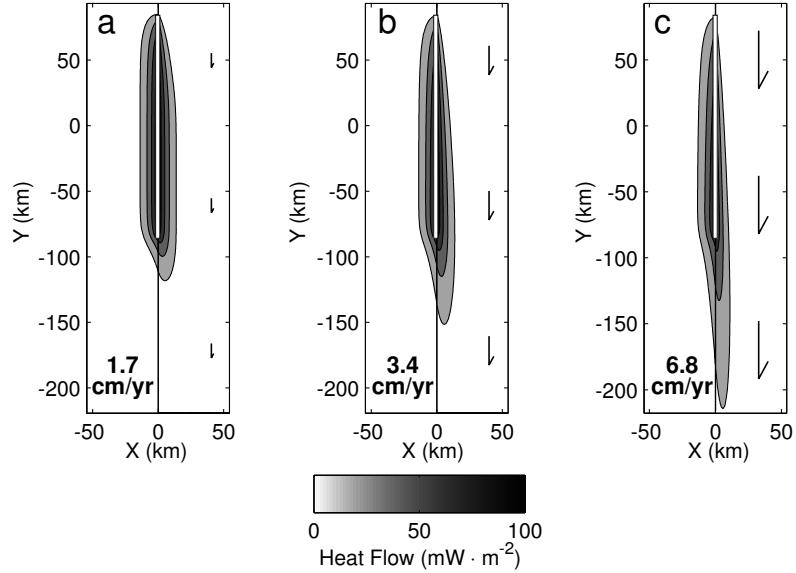


Figure 6.5. Surface heat flow distribution for a single frictional heat generating asperity in models that include different rates of block offset: a) $1.7 \text{ cm}\cdot\text{yr}^{-1}$; b) $3.4 \text{ cm}\cdot\text{yr}^{-1}$, representative of the San Andreas fault since 5 Ma [*Sims*, 1993]; and c) $6.8 \text{ cm}\cdot\text{yr}^{-1}$. A solid line marks the location of the heat generating surface ($-85 \text{ km} < y < 85 \text{ km}$), which remains fixed to the stationary western block while the eastern block moves right-laterally. Slower slip rates are most similar to a stationary asperity (Fig. 6.1) and faster slip rates cause greater asymmetry and a lower peak heat flow.

than for the stationary fault, respectively. Changes of this magnitude would have a noticeable impact on heat flow data for natural faults.

6.5.4 Multiple Asperities and the Infinite Limit

In reality, there may be a suite of frictional asperities across a range of scales. The ability to resolve these asperities depends on their size and the spatial resolution of observations. We calculate the heat flow distribution for three scenarios with a different number of asperities (Fig. 6.6). Each model has the same slip rate, same shear stress resisting slip, and similar total area of high friction asperities (50-66% of the total along-strike distance of 170 km). The spatial pattern of heat flow along the fault plane itself is quite complex and differs dramatically between the three different examples, but at about 20 km away from the fault plane, the distributions are nearly identical. The distance away from the fault at which the asperities become indistinguishable depends most strongly on the depth extent of faulting.

In the early time steps of model runs with multiple asperities, the individual heat generating patches produce miniature versions of a single isolated asperity – each one slightly asymmetric in the same pattern as Fig. 6.4a. Because these asperities are smaller and spaced close together,

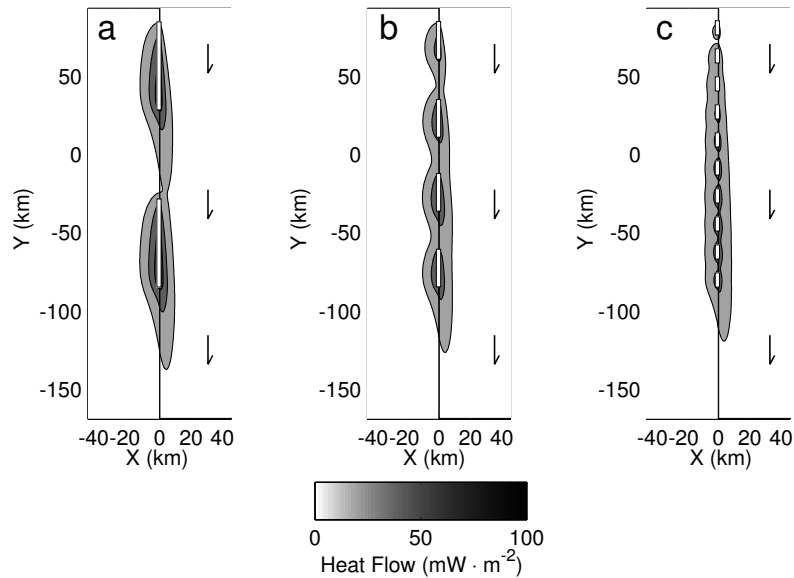


Figure 6.6. Heat flow distribution for multiple frictional heat generating asperities in models that include block offset.

a section of fault that was “left behind” by the trailing edge of one asperity quickly encounters the leading edge of another asperity. Unlike the case of an isolated asperity where the leading edge of the heat generating patch is always in contact with unheated (“cold”) blocks of crust, the leading edge of a patch in the multiple asperity scenario might encounter a patch of fault that was recently in contact with another asperity and has only been away from a heat generating asperity for a relatively short period of time. If the asperities are closer together than the depth-extent of faulting, then even when a section of crust is not in direct contact with a heat generating asperity, it will still be close enough for a substantial amount of heat to conduct to it from the nearby heating patches. The shorter distance between asperities therefore reduces the amount of time for sections of the fault to cool between being in contact with frictional asperities and increases the amount of heat the block is exposed to conductively during those intervening times. As the asperities get smaller and smaller, we approach the limiting case of an infinite, homogeneous fault – much like integrating a series of closely spaced point-sources of heat to represent a continuous heat source. While the asperities in Fig. 6.6 are all confined to a 170 km long zone, real faults likely have high friction asperities distributed continuously. Heterogeneity is most important when these asperities are large compared to the depth extent of heat generation.

6.5.5 Frictional Asperities and Interpretations of Heat Flow

The three scenarios pictured in Fig. 6.6 all have less total heat generation than the single asperity case because they span the same distance along strike of the fault (170 km) but have low friction gaps in between. This difference is an aspect of our chosen model geometry that

includes these gaps. While it is a direct result of our initial assumptions, we feel that such a model geometry may be a more accurate representation of heat generation surfaces at depth on natural faults. Models of infinite, homogeneous faults assume that the entire surface area of a fault is generating heat, when in fact much of the heat could be generated on a few high friction asperities. The area of these asperities relative to the total area of the fault surface is another factor that can be lumped into the “apparent” coefficient of friction inferred when assuming homogeneous fault heating models, but one must consider this factor when interpreting μ_{app} in terms of frictional properties during sliding. For example, if one third of fault area is frictionally strong and the other two thirds are weak or frictionless, an aggregate μ_{app} of 0.25 could indicate that the sliding friction of the strong asperities is 0.75 – in accordance with Byerlee’s law and we must explain how the rest of the fault surface behaves frictionless. However, if this same μ_{app} is interpreted assuming a uniform friction along the entire fault surface, none of the rocks obey Byerlee’s law and we must come up with a mechanism that produces a uniform coefficient of friction of 0.25.

6.6 The Creeping San Andreas Fault

We have shown that frictional asperities tens of kilometers long can have a notable impact on the distribution of frictional heat resulting in lower peak heat flow and asymmetry both across the fault and along strike. One possible example of such a frictional heterogeneity along a natural fault is the creeping section of the San Andreas fault in California. Unique frictional properties give rise to creeping behavior, and the creeping section is not subject to potential dynamic weakening because of the slow slip velocities. Based on suggestions by *Brune* [2002], we explore possible implications of this frictional heterogeneity on the heat flow pattern and compare predictions with available observations.

The creeping section of the San Andreas fault is a 160-170 km long portion of the fault located in central California between San Juan Bautista and Parkfield (Fig. 6.7). This section rarely experiences large earthquakes – in stark contrast to sections of the fault to the north (1906 San Francisco rupture extent) and to the south (1857 Fort Tejon rupture extent) that have produced repeated large earthquakes. Instead, nearly all of the slip is accommodated by relatively steady, aseismic creep. Creep reflects frictionally stable or velocity strengthening sliding [e.g., *Scholz*, 1998]. The fact that the creeping section exhibits this behavior while adjacent sections slip in large earthquakes implies that the frictional properties of this section of the fault are quite different than their surroundings. Frictional stability is not the same as frictional strength, so the heterogeneity in creep behavior does not necessarily indicate that the creeping section is anomalously strong or weak. *Brown* [1998] investigate this relationship in the laboratory and find that stable sliding produces heat at a consistently higher rate than earthquake-producing stick-slip behavior. Alternately, *Provost and Houston* [2001] suggest that the creeping section is weak and displays different mechanical behavior than the San Andreas fault system further to the north [*Provost and Houston*, 2003] and south [*Hardebeck and Hauksson*, 1999]. For our model exploration, we assume that creep does correspond to anomalous frictional strength and we explore both possible extremes of a strong and weak creeping section.

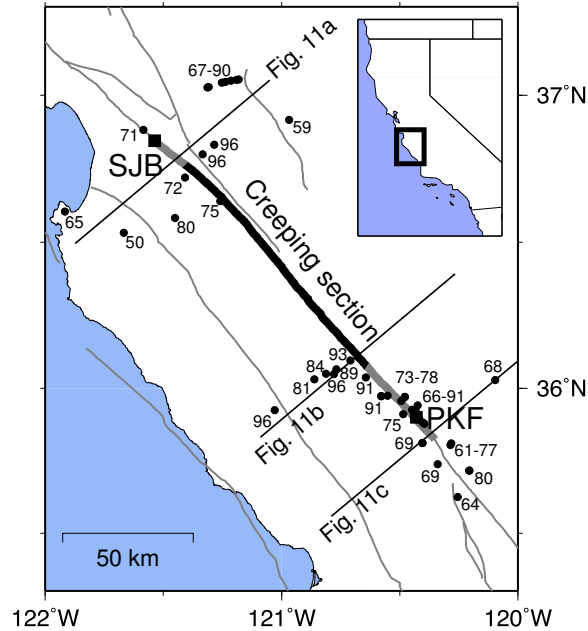


Figure 6.7. Creeping Section of the San Andreas fault. Labeled symbols are existing heat flow measurements in $mW \cdot m^{-2}$ from *Lachenbruch and Sass* [1980] and *Williams et al.* [2004]. Thick black line indicates where the SAF is thought to be freely slipping, thick grey lines are transition zones between creeping and locked behavior. Thin lines are all active faults. SJB, San Juan Bautista; PKF, Parkfield.

The exact mechanism causing creeping behavior is still debated. Dynamic weakness – weakness resulting from events during the rupture of large earthquakes – cannot affect the creeping section because it does not experience large earthquakes. Its frictional properties, therefore, must be explained by a permanent weakness (unique structure or lithology). *Allen* [1968] originally suggested that the frictional properties of serpentinite may promote creep, and recent laboratory investigations show that serpentine minerals do undergo stable sliding under certain conditions of temperature, pressure, and fluid content [*Moore et al.*, 1996, 2004]. Field investigations near the drill site for the San Andreas Fault Observatory at Depth (SAFOD) reveal that the 10 m wide core of the creeping fault consists entirely of serpentinite in at least one locality [M. Rymer, pers. comm., 2002]. Serpentinite could therefore be the cause of fault creep.

If bodies with unique lithology control fault creep, the creeping section of the fault will have migrated over time because lithologic units are displaced as the fault accumulates offset. The active trace of the San Andreas fault in central California initiated about 4-6 Ma and has accumulated approximately 160 km of cumulative offset [*Sims*, 1993]. The striking coincidence between the length of the creeping section and the total amount of cumulative offset (~ 160 km) supports the idea that the creep may be related to a migrating lithologic boundary. Figure 6.8 shows two possibilities for this genetic relationship, “displacement” and “dragging.” In the displacement model (A), the creeping segment has always been the same length, but is displaced

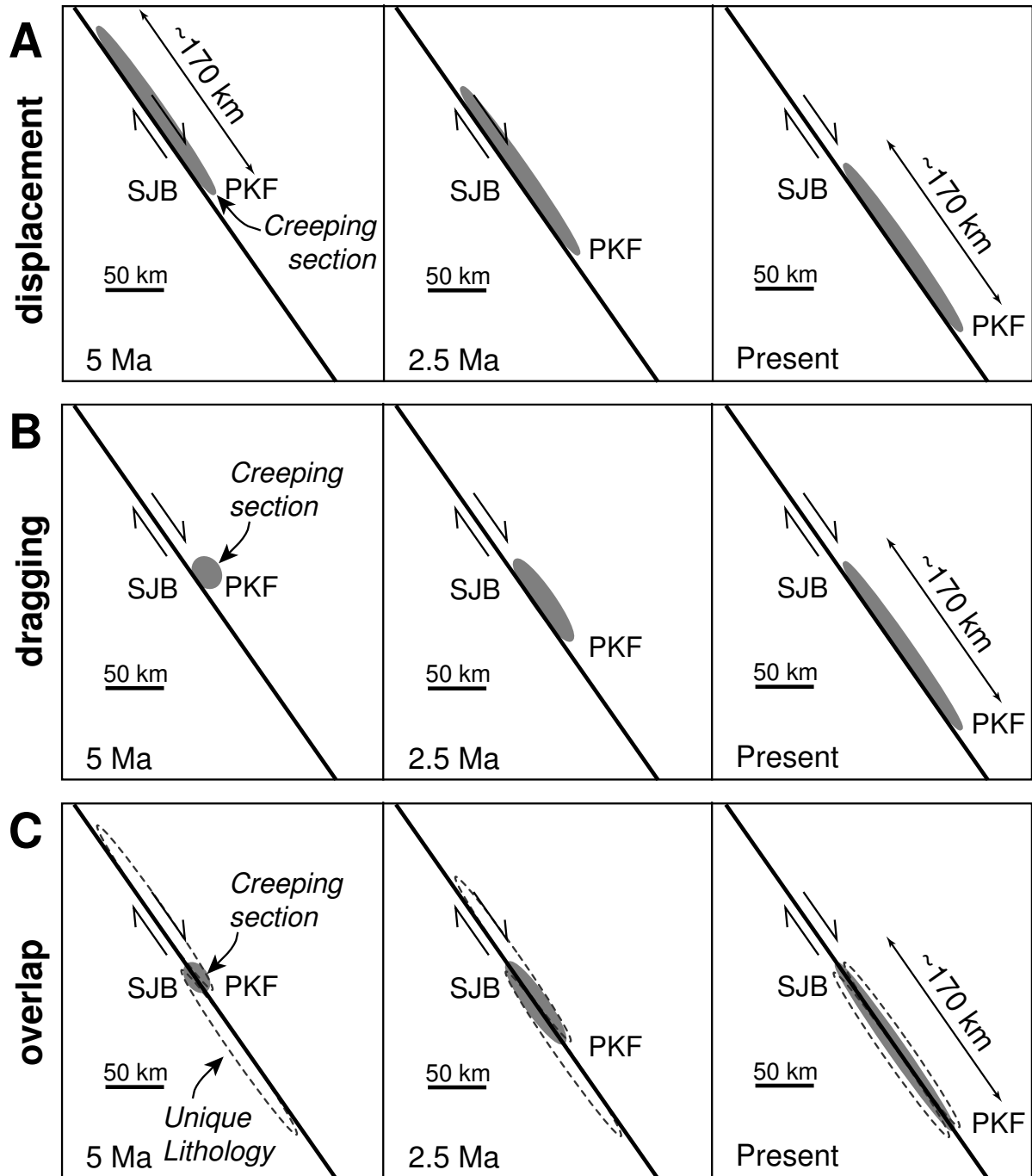


Figure 6.8. Different models for how the length and position of the creeping section could have evolved over time.

as the fault slips. Our models from Section 6.5 are examples of this scenario. In the dragging model (B), the creeping section is related to a localized lithologic unit when faulting initiates, but that material is dragged along within the fault zone causing the creeping segment to grow with time. A third scenario related to the “overlap” of two unique lithologies produces an identical evolution as the dragging model.

We consider two extreme cases of frictional heterogeneity along fault strike: A) the creeping section is frictionless ($\mu = 0$) while the fault further north and south is stronger ($\mu = 0.4$); and B) the opposite scenario where the creeping section is relatively strong ($\mu = 0.4$) and the surrounding fault is weak ($\mu = 0$). A weak creeping section (A) would correspond to a lithologic or structural feature of the creeping section that is permanently weaker than the surrounding fault, while a relatively strong creeping section (B) could be explained physically if dynamic processes weaken the fault to the north and south while the aseismic creeping section remains unaffected by dynamic weakening. We explore both frictional scenarios with the creeping section geometries defined by both the dragging and displacement histories of Fig. 6.8. We assume the creeping section is fixed to the Pacific plate while the North American plate travels southeastward. For the alternate case, the model solution would simply be rotated 180° , resulting in the same sense of asymmetry but a slightly different pattern.

Figure 6.9 shows the calculated distribution of surface heat flow for all four model runs. Note that all models result in a strongly asymmetric distribution of heat flow across the fault. For an observer standing on top of a strong frictional asperity of a fault with a right-lateral sense of slip, the highest heat flow will always be on his or her left side when looking straight ahead. Along strike (Fig. 6.10), the displacement models have the most extreme values and cover the broadest area at the trailing edge of the asperity (south end when heat source fixed to west side of right-lateral fault). The distribution from the dragging model (Fig. 6.9c-d) is asymmetric from one side of the fault to the other, but would look the same when rotated by 180° . Dragging from north to south would therefore be identical to the opposite case, so a snapshot in time of heat flow would not allow us to determine where the dragged unit originated.

6.7 Comparisons with Observations

6.7.1 Comparing Predictions to Observations

Figure 6.11 shows a comparison between predictions based upon our numerical model and the available data. For the models in Fig. 6.9, the average duration a section of a block is exposed to heating can be quite short and averages less than three myr. The magnitude of the predicted frictional heat anomaly is therefore lower than the values predicted from an infinite fault at steady state [e.g., *Lachenbruch and Sass, 1980*]. The lack of a heat flow anomaly of the magnitude predicted for the steady state, infinite fault case is not sufficient evidence that the creeping section is weak.

As *Lachenbruch and Sass [1980]* noted, heat flow is not a strong function of distance away from the fault. The observations do, however, show distinct asymmetry across the fault –

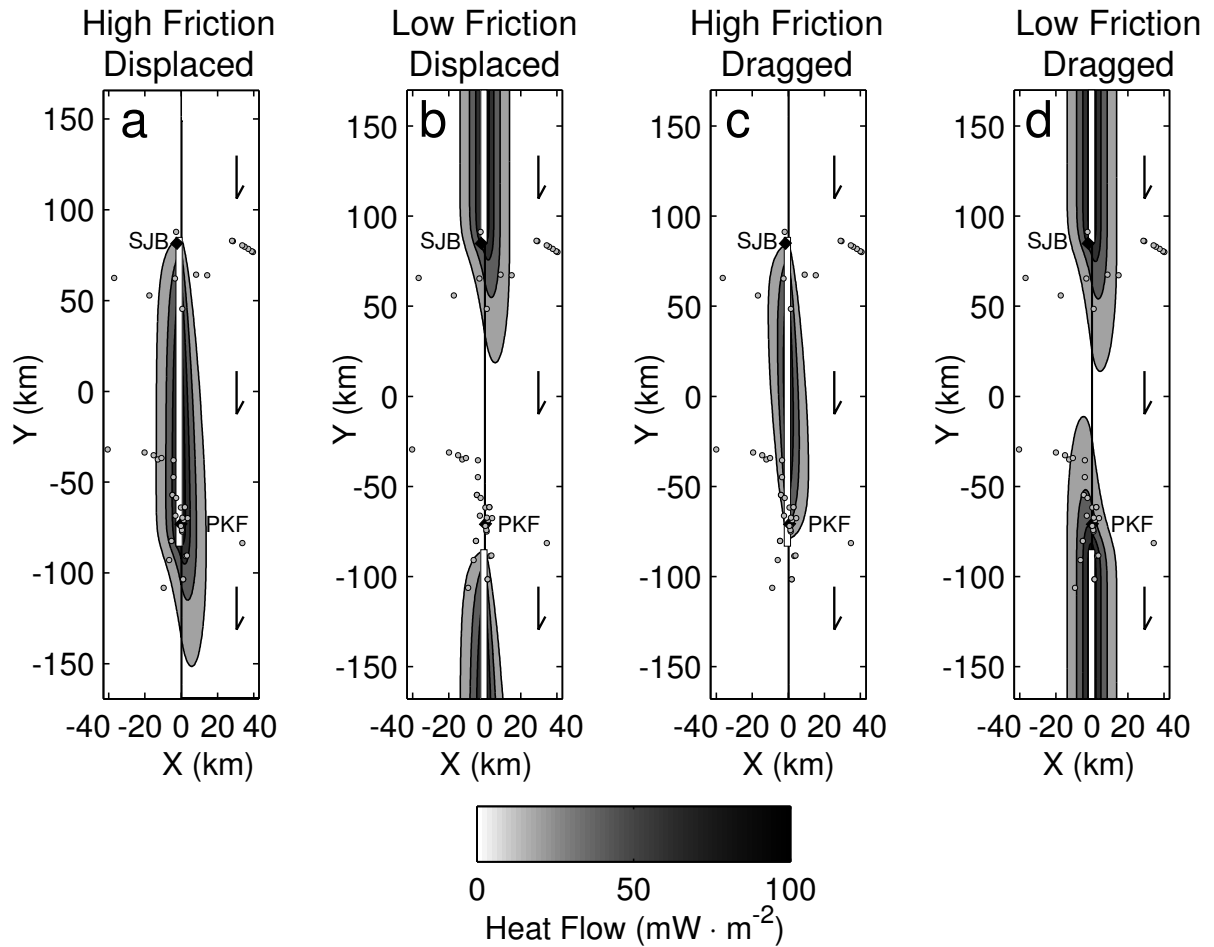


Figure 6.9. Predicted heat flow for the model creeping section of the San Andreas fault after 5 myr of fault activity. Sections of fault along $x=0$ are either strong (thick line) or weak (thin line). Creeping section ($-85 < y < 85$) has coefficient of friction μ_c ; surrounding fault, μ_s . a) “Displacement” geometry with strong creeping section ($\mu_c = 0$, $\mu_s = 0.4$); b) “Displacement” geometry with weak creeping section ($\mu_c = 0.4$, $\mu_s = 0$); c) “Dragging” geometry with strong creeping section ($\mu_c = 0.4$, $\mu_s = 0$); d) “Dragging” geometry with weak creeping section ($\mu_c = 0$, $\mu_s = 0.4$). Dots indicate locations of heat flow observations from Fig. 6.7. SJB = San Juan Bautista; PKF = Parkfield.

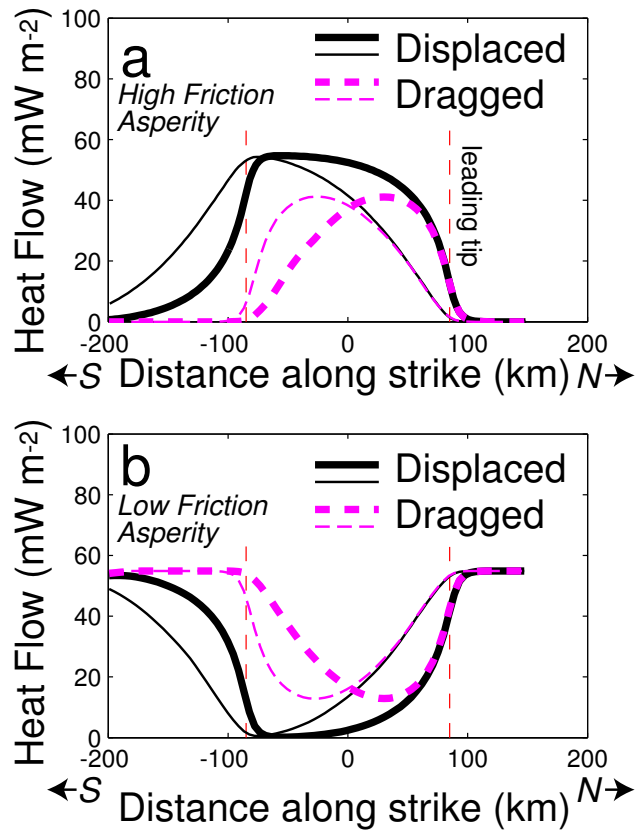


Figure 6.10. Models of frictional asperities on the creeping section as a function of distance along fault strike. Thick lines for a profile parallel to fault and 5 km east; thin lines for 5 km west. Solid lines for a creeping section that evolves by “Displacement”; dashed for “Dragging.” Top panel (a) shows results for a frictionally strong creeping section surrounded by frictionless fault sections to the north and south; bottom panel (b) for a weak creeping section. Note the asymmetry of the profiles.

especially near San Juan Bautista (Fig. 6.11a) where heat flow data span both sides. Data are totally absent from the northeast side of the fault in Fig. 6.11b, but heat flow on the southwest side is uniformly higher than the average heat flow in the Coast Range. For a right lateral fault, this sense of asymmetry is most consistent with a weak creeping section (thin lines of Fig. 6.11; Fig. 6.9b,d). These models also produce very broad heat flow anomalies in the creeping section, but the magnitude of the heat flow should be much lower than in surrounding areas. While a weak creeping section surrounded by a stronger San Andreas fault is consistent with the qualitative findings of [Provost and Houston, 2001], this scenario produces heat flow anomalies to the north and south. *Lachenbruch and Sass* [1980] show that such anomalies are not present in the data. The observed asymmetry would be best fit by a strong creeping section with left-lateral offset inconsistent with the San Andreas fault.

Overall, we do not find that a single strong frictional heterogeneity along the entire length of the creeping section can explain the asymmetry. While *ad hoc* placement of multiple asperities could fit the data substantially better, the sparse heat flow observations in the area prevent us from testing any such models. New measurements from PBO heat flows proposed by R. Harris will provide valuable measurements at distances of 5-30 km east and west of the fault. Coverage on both sides of the fault is essential to capture any asymmetry. Measurements from < 1-3 times the depth extent of heat generation will be most useful. Since the seismogenic zone is about 14 km deep near Parkfield [Murray *et al.*, 2001], observations from > 40 km are considered “background” values (which are essential, but can be sparse). The ideal maximum spacing between segments along strike would be a similar value, though the proposed PBO installations will leave gaps >75 km in the central creeping section. This central area would not yield much important information if the creeping section itself acts as a homogeneous asperity, but two additional profiles would be essential for constraining any individual asperities within the creeping section. The lack of any known variations in creep behavior along strike in the creeping section (with the exception of transition regions at the north and south) argue against any obvious first-order frictional heterogeneity. However, spatial resolution of geodetic observations of the creeping section remain sparse, and recent observations of transient aseismic slip within the region may provide further insight into any such features.

There are other physical processes related to the geologic history that we have neglected that may have an important impact on the surface heat flow in this region. As noted by *Lachenbruch and Sass* [1980], the heat flow throughout the Coast Range is higher than the surrounding areas. This “Coast Range anomaly” is much broader than the anomalies we predict for frictional heat and have been attributed to deep viscous heating [e.g., *Thatcher and England*, 1998] or hot asthenospheric intrusion into a “slab window” as the Farallon plate disappears beneath California [e.g., *ten Brink et al.*, 1999; *Guzofski and Furlong*, 2002]. Our modeling neglects both these processes and therefore is not able to match the broadly elevated background heat flow in the region. Frictional heat generation on closely spaced fault segments can also produce broader heat flow anomalies. *Williams et al.* [2004] show the effect of the San Gregorio fault on heat flow profiles, but this fault is so far away that it produces an essentially isolated heat flow anomaly. The Calaveras and San Andreas faults intersect near San Juan Bautista at the northern end of Fig. 6.7. We have completely neglected heat generation along the Calaveras fault, which is also known to creep, as well as other active faults throughout the Coast Range (such as those that produced the 1983 Coalinga and 2003 San Simeon earthquakes, the Ortigalita fault, etc.).

The formulation for finite faults that we present in this work are a better representation of this complex geometry than the the infinitely long faults modeled by *Williams et al.* [2004] for the San Gregorio fault. Along with complex geometry, individual traces of the fault become active and inactive over time as fault systems migrate at a range of scales. This migration will lead to broader heat flow with lower peak magnitudes. With better geologic constraints on the development and evolution of individual fault traces in the area, we can use models the spatially and temporally complex heat generation along finite faults. Other geologic events such as volcanism and exhumation can perturb regional heat flow. *Blythe et al.* [2004] show that at least one location near Parkfield along the San Andreas fault was relatively unaffected by such events since ~ 60 Ma, but Miocene volcanism related to the migration of triple junctions at the formation of the young San Andreas fault undoubtedly affected the heat flow locally throughout the Coast Range. In this study, we focus on frictional heat generation since 5 Ma, long after this volcanism subsided in Parkfield [*Sims*, 1993].

6.8 Conclusions

Localized high friction asperities will produce localized heating. If these asperities are tied to the crustal block on one side of the fault, they will migrate over time producing a strongly asymmetric heat flow pattern whose magnitude is smaller than for a stationary asperity would be. This effect is a strong function of slip rate, asperity size, and the temporal history of the heat source. Heat flow tends to be symmetric trailing edges of asperities, and the asymmetry is most pronounced near the leading edges and beyond the trailing edges of the heat sources. A single profile across a fault would therefore not capture the full complexity of the heat flow signal, nor would the peak heat flow be as large as as has been predicted by models of infinitely long, uniform faults. Recognizing zones of heterogeneous high friction is best accomplished with a dense distribution of stations within 1-3 times the depth extent of the heat source. Heat flow near the San Andreas fault shows heat flow patterns that are asymmetric across the fault and along strike. Treating the creeping section of the San Andreas fault as a single migrating asperity predicts frictional heat flow anomalies that are lower magnitude than those from an infinite fault model. They reproduce the observed sense of asymmetry of heat flow in the region for an exceptionally weak creeping section, but this would require the rest of the San Andreas fault to be strong. Overall, the effect of heterogeneous frictional strength on the magnitude and spatial pattern of surface heat flow is important and should be considered when interpreting these observations in terms of fault strength and frictional processes.

6.9 Appendix

Here we present the detailed derivation of instantaneous heat generation along a rectangular heat source in a homogeneous half space. The derivation involves simply integrating a point source over a rectangle. In the form presented here, the heat source must lie parallel to the y-z plane, but simple coordinate system rotations about the z axis could allow for the solution of arbitrarily oriented vertical heat sources. Dipping heat sources require slightly more complex treatment because the half-space derivation utilizes the concept of “image sources” to account for the presence of a free surface at $z = 0$. A simple coordinate transform would not properly transform the image source of a dipping fault.

6.9.1 Point Source

We begin with the conduction equation:

$$\frac{d^2T}{dx^2} + \frac{d^2T}{dy^2} + \frac{d^2T}{dz^2} = \frac{1}{\kappa} \frac{dT}{dt} \quad (6.1)$$

A solution to this homogeneous differential equation is:

$$T = t^{-\frac{3}{2}} e^{-\frac{R^2}{4\kappa t}} \quad (6.2)$$

Where R^2 is the distance between the observation point and the heating source ($R^2 = (x^2 + y^2 + z^2)$). We can show that this equation satisfies the differential equation by simply taking the appropriate derivatives. (Note that $\frac{dT}{dx}$, $\frac{dT}{dy}$, and $\frac{dT}{dz}$ are identical in form – simply replace y or z for x in the equations below).

$$\frac{dT}{dx} = t^{-\frac{5}{2}} \left(-\frac{x}{2\kappa} \right) \cdot e^{-\frac{R^2}{4\kappa t}} \quad (6.3a)$$

$$\frac{d^2T}{dx^2} = \frac{1}{2\kappa} t^{-\frac{5}{2}} \left(\frac{x^2}{2\kappa t} - 1 \right) \cdot e^{-\frac{R^2}{4\kappa t}} \quad (6.3b)$$

$$\frac{dT}{dt} = \left(-\frac{3}{2} t^{-\frac{7}{2}} + \frac{1}{4\kappa} R^2 t^{-\frac{5}{2}} \right) \cdot e^{-\frac{R^2}{4\kappa t}} \quad (6.3c)$$

Following in the footsteps of *Carslaw and Jaeger* [1959, p. 50], we note that this particular solution corresponds physically to the instantaneous release of heat from a point source located at the origin into an infinite medium at time zero. We know this because as time goes to zero, the temperature everywhere except the origin is also zero. At time zero at the origin, however, there is an infinite temperature. The magnitude of the heating event is $8\rho * C_p * (\pi\kappa)^{\frac{3}{2}}$. This magnitude comes from integrating the Temperature over space from $-\infty$ to ∞ to determine the total amount of heat in the system. The amount of heat is the same no matter which time you evaluate the integral.

6.9.2 Rectangular Source

A fault, however, is not well represented by a point source, and can be more closely approximated by one or more rectangular sources of heat. The temperature due to an instantaneous heating event from a rectangular source of heat comes from integrating a more general form of the point source solution shown above over the area of the fault. We define a coordinate system with the surface of the earth at $z=0$ and a vertical strike-slip fault lying in the y - z plane. The magnitude of heating will be a linear function of z within the element and constant at all y positions. This linear dependence is designed to mirror the approximately linear increase in shear stress with depth.

We integrate the temperature at an observation point (x, y, z) due to an instantaneous point source at (x_1, y_1, z_1) at time t_o with depth-dependent strength $(\frac{dQ}{dz}z_1 + Q_o)$:

$$T(x, y, z, t) = \int \int \left(\frac{dQ}{dz} z_1 + Q_o \right) (t - t_o)^{-\frac{3}{2}} e^{\left[-\frac{(x-x_1)^2 + (y-y_1)^2 + z_1^2}{4\kappa(t-t_o)} \right]} dy_1 dz_1 \quad (6.4)$$

Rewriting the exponential in terms of products and pulling out the terms that are constant in y and z :

$$T(x, y, z, t) = (t - t_o)^{-\frac{3}{2}} e^{\left[-\frac{(x-x_1)^2}{4\kappa(t-t_o)} \right]} \int e^{\left[-\frac{(y-y_1)^2}{4\kappa(t-t_o)} \right]} dy_1 \int \left(\frac{dQ}{dz} z_1 + Q_o \right) e^{\left[-\frac{(z-z_1)^2}{4\kappa(t-t_o)} \right]} dz_1 \quad (6.5)$$

To make things easier to follow, we make a few substitutions:

$$b = \frac{1}{4\kappa(t - t_o)} \quad (6.6a)$$

$$timeDependence = (t - t_o)^{-\frac{3}{2}} \quad (6.6b)$$

$$xDependence = e^{[-b(x-x_1)^2]} \quad (6.6c)$$

$$yDependence = \int e^{[-b(y-y_1)^2]} dy_1 \quad (6.6d)$$

$$zDependence = \int \left(\frac{dQ}{dz} z_1 + Q_o \right) e^{[-b(z-z_1)^2]} dz_1 \quad (6.6e)$$

Leaving us with:

$$T(x, y, z, t) = timeDependence \times xDependence \times yDependence \times zDependence \quad (6.7)$$

We note that the integral in $yDependence$ is essentially the definition of the error function and we substitute in:

$$yDependence = \sqrt{\frac{\pi}{4b}} erf[-\sqrt{b}(y - y_1)] \Big|_{y_{left}}^{y_{right}} \quad (6.8)$$

There is a bit of slop allowable in the negative signs because \sqrt{b} can be either positive or negative.

Integrating by parts and using the same definition of the error function, we find that:

$$z\text{Dependence} = \left[Q_0 \left\{ \sqrt{\frac{\pi}{4b}} \operatorname{erf}[-\sqrt{b}(z - z_1)] \right\} + \frac{dQ}{dz} \left\{ -\frac{e^{(-b(z-z_1)^2)}}{2b} + z \sqrt{\frac{\pi}{4b}} \operatorname{erf}[-\sqrt{b}(z - z_1)] \right\} \right] \Bigg|_{z_{top}}^{z_{bottom}} \quad (6.9)$$

We now have the final solution for an instantaneous rectangular source of heat observed at a single point. We simply plug in 6.6b, 6.6c, 6.8, and 6.9 to 6.7.

The solution as posed thus far is for a rectangle in an infinite body. To generate slip in a half space, we simply apply the concept of an “image source”. Using the functional form of Eqn. 6.7, we simply subtract the magnitude of an image heat source reflected across the x-y plane. Thus at $z = 0$, the two terms cancel one another and the temperature is zero everywhere as expected for a free surface.:

$$T_{halfspace}(x, y, z, t) = T(x, y, z, t) - T(x, y, -z, t) \quad (6.10)$$

Continuous Heat Source

Note that 6.6c, 6.8, and 6.9 all have a dependence on t through the substituted variable b . As such, integrating the instantaneous solution over time to give a continuous source of heat generation is best accomplished numerically.

Table 6.2. Variables and meanings

Variable	Meaning	Typical units (SI)
C_p	Heat Capacity	$J/(kg \cdot K)$
Q	Heat	Joules (J or $kg \cdot m^2/s^2$)
Q_o	Heat Generation at zero depth	Joules (J or $kg \cdot m^2/s^2$)
R	Radial distance ($R^2 = x^2 + y^2 + z^2$)	meters (m)
t	Time	seconds (s)
t_0	Time of instantaneous heat generation	seconds (s)
T	Temperature	Kelvin (K)
v_{slip}	Fault slip rate (assuming one side stationary)	m/s
x, y, z	Position of observation point along axes	meters (m)
x_1	Distance from y-z plane of heat source	meters (m)
y_1, z_1	Position along heat source	meters (m)
y_{left}, y_{right}	Distance along strike of the heat source	meters (m)
z_{bottom}, z_{top}	Depth extent of the heat source	meters (m)
κ	Thermal diffusivity	m^2/s
ρ	Density	kg/m^3

Bibliography

- Allen, C. R., The tectonic environments of seismically active and inactive areas along the San Andreas fault systems, in *Proceedings of Conference of Geological Problems of San Andreas Fault System*, edited by W. R. Dickenson and A. Grantz, Stanford University Publishing, Stanford, CA, 1968.
- Altamimi, Z., P. Sillard, and C. Boucher, ITRF2000: A new release of the international terrestrial reference frame for earth science applications, *J. Geophys. Res.*, *107*(B10), doi:10.1029/2001JB000561, 2002.
- Anders, M. H., and D. V. Wiltschko, Microfracturing, paleostress and the growth of faults, *J. Struc. Geol.*, *16*(6), 795–815, 1994.
- Anderson, J. L., R. H. Osborne, and D. F. Palmer, Cataclastic rocks of the San Gabriel fault; an expression of deformation at deeper crustal levels in the San Andreas fault zone, *Tectonophys.*, *98*(3-4), 209–251, 1983.
- Anderson, L. W., and L. A. Piety, Geologic seismic source characterization of the San Luis-O'Neill area, eastern Diablo Range, California, *Seismotectonic Report 2001-2*, Bureau of Reclamation, 2001.
- Andrews, D. J., and Y. Ben-Zion, Wrinkle-like slip pulse on a fault between different materials, *J. Geophys. Res.*, *102*(B1), 553–571, 1997.
- Argus, D. F., and R. G. Gordon, Current Sierra-Nevada North America motion from Very Long Base-Line Interferometry - implications for the kinematics of the western United States, *Geology*, *19*(11), 1085–1088, 1991.
- Argus, D. F., and R. G. Gordon, Present tectonic motion across the Coast Ranges and San Andreas fault system in central California, *Geol. Soc. Amer. Bull.*, *113*(12), 1580–1592, 2001.
- Arnadottir, T., and P. Segall, The 1989 Loma Prieta earthquake imaged from inversion of geodetic data, *J. Geophys. Res.*, *99*(B11), 21,835–21,855, 1994.
- Arnadottir, T., and P. Segall, The 1989 Loma Prieta earthquake imaged from inversion of geodetic data - reply, *J. Geophys. Res.*, *101*(B9), 20,137–20,140, 1996.
- Atwater, T., and J. Stock, Pacific-North America plate tectonics of the Neogene southwestern United States: An update, *Int. Geol. Rev.*, *40*(5), 375–402, 1998.

- Aydin, A., and R. A. Schulz, Effect of mechanical interaction on the development of strike-slip faults with echelon patterns, *J. Struc. Geol.*, *12*(1), 123–129, 1990.
- Bakun, W. H., The seismogenic scaling factor, r , *U. S. Geol. Survey Open File Rep.*, *03-214*, B1–B9, 2003.
- Batt, G. E., J. Braun, B. P. Kohn, and I. McDougall, Thermochronological analysis of the dynamics of the Southern Alps, New Zealand, *Geol. Soc. Amer. Bull.*, *112*(2), 250–266, 2000.
- Bayasgalan, A., J. Jackson, J.-F. Ritz, and S. Carretier, Field examples of strike-slip fault terminations in Mongolia and their tectonic significance, *Tectonics*, *18*(3), 394–411, 1999.
- Beavan, J., P. Tregoning, M. Bevis, T. Kato, and C. Meertens, Motion and rigidity of the Pacific plate and implications for plate boundary deformation, *J. Geophys. Res.*, *107*(B10), doi:10.1029/2001JB000282, 2002.
- Behr, J., R. Bilham, P. Bodin, K. Breckenridge, and S. A.G, Increased surface creep rates on the San Andreas fault southeast of the Loma Prieta mainshock, in *Loma Prieta, California, earthquake of October 17, 1989: Aftershocks and postseismic effects*, edited by P. Reasonberg, U.S. Geological Survey Professional Paper 1550, pp. D179–D192, 1997.
- Bennett, R. A., W. Rodi, and R. E. Reilinger, Global positioning system constraints on fault slip rates in southern California and northern Baja, Mexico, *J. Geophys. Res.*, *101*(B10), 21,943–21,960, 1996.
- Bennett, R. A., J. L. Davis, and B. P. Wernicke, Present-day pattern of Cordilleran deformation in the western United States, *Geology*, *27*(4), 371–374, 1999.
- Bennett, R. A., B. P. Wernicke, N. A. Niemi, A. M. Friedrich, and J. L. Davis, Contemporary strain rates in the northern Basin and Range province from GPS data, *Tectonics*, *22*(2), 1008, doi:10.1029/2001TC001355, 2003.
- Bergbauer, S., and S. J. Martel, Formation of joints in cooling plutons, *J. Struc. Geol.*, *21*, 821–835, 1999.
- Blake, M. C., R. H. Campbell, T. W. Dibblee, D. G. Howell, T. H. Nilsen, W. R. Normark, J. C. Vedder, and E. A. Silver, Neogene basin formation in relation to plate-tectonic evolution of San Andreas fault system, California, *Amer. Assoc. Petrol. Geol. Bull.*, *62*(3), 344–372, 1978.
- Blanpied, M. L., D. A. Lockner, and J. D. Byerlee, Fault slip of granite at hydrothermal conditions, *J. Geophys. Res.*, *100*(B7), 1995.
- Blanpied, M. L., T. E. Tullis, and J. D. Weeks, Effects of slip, slip rate, and shear heating on the friction of granite, *J. Geophys. Res.*, *103*(B1), 489–511, 1998.
- Blythe, A. E., D. W. Burbank, K. A. Farley, and E. J. Fielding, Structural and topographic evolution of the central Transverse Ranges, California, from apatite fission-track, (U-Th)/He and Digital Elevation Model analysis, *Basin Res.*, *12*(2), 97–114, 2000.

- Blythe, A. E., M. A. d'Alessio, and R. Bürgmann, Constraining the exhumation and burial history of the SAFOD pilot hole with apatite fission track and (U-Th)/He thermochronometry, *Geophys. Res. Lett.*, *31*(L15S16), doi:10.1029/2003GL019407, 2004.
- Brace, W. F., and E. G. Bombalakis, A note on brittle crack growth in compression, *J. Geophys. Res.*, *68*, 3709–3713, 1963.
- Brown, S. R., Frictional heating on faults: Stable sliding versus stick slip, *J. Geophys. Res.*, *103*(B4), 7413–7420, 1998.
- Brune, J. N., Heat flow on the creeping section of the San Andreas fault: A localized transient perspective, *EOS, Trans. Amer. Geophys. Union*, *83*(47), Abstract S21A-0979, 2002.
- Brune, J. N., T. L. Henyey, and R. F. Roy, Heat flow, stress, and rate of slip along the San Andreas fault, California, *J. Geophys. Res.*, *74*(15), 3821–3827, 1969.
- Brune, J. N., S. Brown, and P. Johnson, Rupture mechanism and interface separation in foam rubber models of earthquakes: A possible solution to the heat flow paradox and the paradox of large overthrusts., *Tectonophys.*, *218*, 59–67, 1993.
- Bryant, W., and S. Cluett, Fault number 52b, Ortigalita fault zone, Los Banos Valley section, in *Quaternary fault and fold database of the United States, ver 1.0*, U.S. Geological Survey Open File report 03-417, <http://qfaults.cr.usgs.gov>, 2000.
- Bürgmann, R., R. Arrowsmith, T. Dumitru, and R. Mclaughlin, Rise and fall of the southern Santa Cruz mountains, California, from fission tracks, geomorphology, and geodesy, *J. Geophys. Res.*, *99*(B10), 20,181–20,202, 1994a.
- Bürgmann, R., D. D. Pollard, and S. J. Martel, Slip distributions on faults: Effects of stress gradients, inelastic deformation, heterogeneous host-rock stiffness, and fault interaction, *J. Struc. Geol.*, *16*(12), 1675–1690, 1994b.
- Bürgmann, R., P. Segall, M. Lisowski, and J. Svarc, Postseismic strain following the 1989 Loma Prieta earthquake from GPS and leveling measurements, *J. Geophys. Res.*, *102*(B3), 4933–4955, 1997.
- Bürgmann, R., D. Schmidt, R. M. Nadeau, M. A. d'Alessio, E. Fielding, T. V. McEvelly, and M. H. Murray, Earthquake potential along the northern Hayward fault, California, *Science*, *289*(18 August 2000), 1178–1182, 2000.
- Bustin, R. M., Heating during thrust faulting in the Rocky Mountains - friction or fiction, *Tectonophys.*, *95*(3-4), 309–328, 1983.
- Byerlee, J. D., Friction of rocks, *Pure Appl. Geophys.*, *116*(4), 615–626, 1978.
- Camacho, A., I. McDougall, R. Armstrong, and J. Braun, Evidence for shear heating, Musgrave block, central Australia, *J. Struc. Geol.*, *23*(6-7), 1007–1013, 2001.
- Carslaw, H. S., and J. C. Jaeger, *Conduction of heat in solids*, Oxford University Press, Oxford, 1959.

- Castillo, D., and S. H. Hickman, Systematic near-field stress rotations adjacent to the Carrizo Plain segment of the San Andreas fault, in *Proceedings of the 3rd conference on tectonic problems of the San Andreas fault system*, vol. XXI, edited by G. Bokelmann and R. Kovach, Stanford University Publications, Stanford, CA, 2000.
- Chester, F. M., and J. M. Logan, Composite planar fabric of gouge from the Punchbowl fault, California, *J. Struc. Geol.*, *9*, 621–634, 1987.
- Chester, F. M., J. P. Evans, and R. L. Biegel, Internal structure and wearing mechanisms of the San Andreas fault, *J. Geophys. Res.*, *98*, 771–786, 1993.
- Cowie, P. A., and C. H. Scholz, Physical explanation for the displacement-length relationship of faults using a post-yield fracture mechanics model, *J. Struc. Geol.*, *14*(10), 1133–1148, 1992.
- Cox, A., and R. B. Hart, *Plate tectonics: How it works*, Blackwell Scientific Publications, Palo Alto, California, 1986.
- Crouch, J. K., S. B. Bachman, and J. T. Shay, Post-Miocene compressional tectonics along the California margin, in *Tectonics and sedimentation along the California margin, Pacific section, Society of Economic Paleontology and Mineralogy*, vol. 38, edited by J. K. Crouch and S. B. Bachman, pp. 37–54, 1984.
- Crouch, S. L., and A. M. Starfield, *Boundary element methods in solid mechanics*, Allen and Unwin, London, 1983.
- d'Alessio, M. A., and S. J. Martel, Development of strike-slip faults from dikes, Sequoia National Park, California, *J. Struc. Geol.*, *in press*, 2004a.
- d'Alessio, M. A., and S. J. Martel, Fault terminations and barriers to fault growth, *J. Struc. Geol.*, *26*(10), 1885–1896, 2004b.
- d'Alessio, M. A., A. E. Blythe, and R. Bürgmann, No frictional heat along the San Gabriel fault, California: Evidence from fission-track thermochronology, *Geology*, *31*(6), 541–544, 2003.
- DeMets, C., and T. H. Dixon, New kinematic models for Pacific-North America motion from 3 Ma to present, I: Evidence for steady motion and biases in the NUVEL-1A model, *Geophys. Res. Lett.*, *26*(13), 1921–1924, 1999.
- DeMets, C., R. G. Gordon, D. F. Argus, and S. Stein, Effect of recent revisions to the geomagnetic reversal time-scale on estimates of current plate motions, *Geophys. Res. Lett.*, *21*(20), 2191–2194, 1994.
- Dibblee, T. W., Geologic maps of seventeen 15-minute quadrangles (1:62,500) along the San Andreas fault in the vicinity of King City, Coalinga, Panoche Valley, and Paso Robles, California, *U. S. Geol. Survey Open File Rep.*, *71*(87), 1971.
- Dixon, T. H., M. Miller, F. Farina, H. Z. Wang, and D. Johnson, Present-day motion of the Sierra Nevada block and some tectonic implications for the Basin and Range province, North American Cordillera, *Tectonics*, *19*(1), 1–24, 2000.

- Donelick, R., R. Ketcham, and W. Carlson, Variability of apatite fission-track annealing kinetics: II. Crystallographic orientation effects, *Amer. Mineral.*, *84*, 1224–1234, 1999.
- Ducea, M., M. A. House, and S. Kidder, Late Cenozoic denudation and uplift rates in the Santa Lucia mountains, California, *Geology*, *31*(2), 139–142, 2003.
- Dumitru, T., A new computer-automated microscope stage system for fission-track analysis, *Nuc. Tracks and Radiation Meas.*, *21*, 575–580, 1993.
- Dumitru, T. A., Constraints on uplift in the franciscan subduction complex from apatite fission-track analysis, *Tectonics*, *8*(2), 197–220, 1989.
- Dunkl, I., Trackkey: A windows program for calculation and graphical presentation of fission track data, *Comput. Geosci.*, *28*, 3–12, 2002.
- Evans, J. P., and F. M. Chester, Fluid-rock interaction in faults of the San Andreas system; inferences from San Gabriel fault rock geochemistry and microstructures, *J. Geophys. Res.*, *100*(7), 13,007–13,020, 1995.
- Farley, K. A., Helium diffusion from apatite: General behavior as illustrated by Durango fluorapatite, *J. Geophys. Res.*, *106*(B2), 2903–2914, 2000.
- Freymueller, J. T., M. H. Murray, P. Segall, and D. Castillo, Kinematics of the Pacific-North America plate boundary zone, northern California, *J. Geophys. Res.*, *104*(B4), 7419–7441, 1999.
- Fuis, G. S., and W. D. Mooney, Lithospheric structure and tectonics from seismic refraction and other data, in *The San Andreas fault system, California*, edited by R. E. Wallace, U.S. Geological Survey Professional Paper 1515, pp. 207–236, 1990.
- Fulton, P. M., D. M. Saffer, R. N. Harris, and B. A. Bekins, Re-evaluation of heat flow data near Parkfield, CA: Evidence for a weak San Andreas fault, *Geophys. Res. Lett.*, *31*(L15S15), doi: 10.1029/2003GL019,378, 2004.
- Galbraith, R., On statistical-models for fission-track counts, *J. Int. Assoc. Math.*, *13*, 471–478, 1981.
- Galehouse, J. S., and J. J. Lienkaemper, Inferences drawn from two decades of alignment array measurements of creep on faults in the San Francisco Bay Region, *Bull. Seism. Soc. Amer.*, *93*(6), 2415–2433, 2003.
- Gallagher, K., Evolving temperature histories from apatite fission-track data, *Earth Planet. Sci. Lett.*, *136*, 421–435, 1995.
- Gilbert, L. E., C. H. Scholz, and J. Beavan, Strain localization along the San Andreas fault - consequences for loading mechanisms, *J. Geophys. Res.*, *99*(B12), 23,975–23,984, 1994.
- Gleadow, A. J. W., and P. G. Fitzgerald, Uplift history and structure of the Transantarctic mountains - new evidence from fission-track dating of basement apatites in the Dry Valleys area, southern Victoria Land, *Earth Planet. Sci. Lett.*, *82*(1-2), 1–14, 1987.

- Gleadow, A. J. W., I. R. Duddy, P. F. Green, and J. F. Lovering, Confined fission-track lengths in apatite - a diagnostic-tool for thermal history analysis, *Contr. Mineral. Petrol.*, *94*(4), 405–415, 1986.
- Gonzalez-Garcia, J. J., L. Prawirodirdjo, Y. Bock, and D. Agnew, Guadalupe Island, Mexico as a new constraint for Pacific plate motion, *Geophys. Res. Lett.*, *30*(16), doi:10.1029/2003GL017,732, 2003.
- Granier, T., Origin, damping, and pattern of development of faults in Granite, *Tectonics*, *4*(7), 721–737, 1985.
- Green, P. F., A new look at statistics in fission-track dating, *Nuc. Tracks and Radiation Meas.*, *5*, 77–86, 1981.
- Green, P. F., I. R. Duddy, A. J. W. Gleadow, P. R. Tingate, and G. M. Laslett, Thermal annealing of fission tracks in apatite; 1, a qualitative description, *Chem. Geol. (Isot. Geosci. Sec.)*, *59*(4), 237–253, 1986.
- Gupta, A., and C. H. Scholz, A model of normal fault interaction based on observations and theory., *J. Struc. Geol.*, *22*, 865–879, 2000.
- Guzofski, C. A., and K. P. Furlong, Migration of the mendocino triple junction and ephemeral crustal deformation: Implications for California Coast Range heat flow, *Geophys. Res. Lett.*, *29*(1, 1012), doi:10.1029/2001GL013,614, 2002.
- Hardebeck, J., and E. Hauksson, Role of fluids in faulting inferred from stress field signatures, *Science*, *285*, 236–239, 1999.
- Harris, R. A., Introduction to special section: Stress triggers, stress shadows, and implications for seismic hazard, *J. Geophys. Res.*, *103*(B10), 24,347–24,358, 1998.
- Harris, R. A., and S. M. Day, Dynamic 3d simulations of earthquakes on en echelon faults, *Geophys. Res. Lett.*, *26*, 2089–2092, 1999.
- Hearn, E. H., and E. D. Humphreys, Kinematics of the southern Walker Lane belt and motion of the Sierra Nevada block, California, *J. Geophys. Res.*, *103*(B11), 27,033–27,049, 1998.
- Heney, T. L., Heat flow near major strike-slip faults in central and southern California, Ph.d., California Institute of Technology, 1968.
- Herring, T. A., GLOBK, global Kalman filter VLBI and GPS analysis program, 2002.
- House, M. A., K. A. Farley, and B. P. Kohn, An empirical test of helium diffusion in apatite: Borehole data from the Otway basin, Australia, *Earth Planet. Sci. Lett.*, *170*, 463–474, 1999.
- Hurford, A., and P. Green, The zeta-age calibration of fission-track dating, *Isotope Geosci.*, *1*, 285–317, 1983.
- Jackson, J., Faulting, flow, and the strength of the continental lithosphere, *Int. Geol. Rev.*, *44*(1), 39–61, 2002.

- Jennings, C., *Fault activity map of California and adjacent areas*, California Division of Mines and Geology, GDM 6, scale 1:750,000, 1994.
- Johanson, I. A., and R. Bürgmann, Complexity at the junction of the Calaveras and San Andreas faults, *J. Geophys. Res.*, *in preparation*, 2004.
- Kanamori, H., and E. E. Brodsky, The physics of earthquakes, *Phys. Today*, *54*(6), 34–40, 2001.
- Kenner, S. J., and P. Segall, Postseismic deformation following the 1906 San Francisco earthquake, *J. Geophys. Res.*, *105*(B6), 13,195–13,209, 2000.
- Ketcham, R. A., R. A. Donelick, and M. B. Donelick, AFTSolve: A program for multi-kinetic modeling of apatite fission-track data, *Geol. Mat. Res.*, *2*(1), 1–32, 2000.
- Kilb, D., and A. M. Rubin, Implications of diverse fault orientations imaged in relocated aftershocks of the Mount Lewis, M-L 5.7, California, earthquake, *J. Geophys. Res.*, *107*(B11), doi:10.1029/2001JB000149, 2002.
- King, G., Speculations on the geometry of the initiation and termination processes of earthquake rupture and its relation to morphology and geological structure, *Pure Appl. Geophys.*, *124*, 567–584, 1986.
- King, R. W., and Y. Bock, Documentation for the GAMIT GPS analysis software, v.10.0, , Massachusetts Institute of Technology, Scripps Institute of Oceanography, 2002.
- Kistler, R. W., and D. E. Champion, Rb-Sr whole-rock and mineral ages, K-Ar, $^{40}\text{Ar}/^{39}\text{Ar}$, and U-Pb mineral ages, and Strontium, lead, Neodymium, and Oxygen isotopic compositions for Granitic rocks from the Salinian composite terrane, *U. S. Geol. Survey Open File Rep.*, *01-453*, 1–84, 1986.
- Kogan, M. G., G. M. Steblov, R. W. King, T. A. Herring, D. I. Frolov, S. G. Egorov, V. Y. Levin, A. Lerner-Lam, and A. Jones, Geodetic constraints on the rigidity and relative motion of Eurasia and North America, *Geophys. Res. Lett.*, *27*(14), 2041–2044, 2000.
- Kreemer, C., W. E. Holt, and A. J. Haines, An integrated global model of present-day plate motions and plate boundary deformation, *Geophys. J. Int.*, *154*(1), 8–34, 2003.
- Lachenbruch, A. H., Frictional heating, fluid pressure, and the resistance to fault motion, *J. Geophys. Res.*, *85*(B11), 6097–6112, 1980.
- Lachenbruch, A. H., Simple models for the estimation and measurement of frictional heating by an earthquake, *U. S. Geol. Survey Open File Rep.*, *86-508*, 1–13, 1986.
- Lachenbruch, A. H., and J. H. Sass, Heat flow and energetics of the San Andreas fault zone, *J. Geophys. Res.*, *85*(B11), 6185–6222, 1980.
- Larson, K. M., J. T. Freymueller, and S. Philipson, Global plate velocities from the Global Positioning System, *J. Geophys. Res.*, *102*(B5), 9961–9981, 1997.
- Laslett, G. M., P. F. Green, I. R. Duddy, and A. J. W. Gleadow, Thermal annealing of fission tracks in apatite, *Chem. Geol.*, *65*(1), 1–13, 1987.

- Lawn, B., and T. Wilshaw, *Fracture of brittle solids*, Cambridge University Press, Cambridge, 1975.
- Leloup, P. H., Y. Ricard, J. Battaglia, and R. Lacassin, Shear heating in continental strike-slip shear zones: Model and field examples, *Geophys. J. Int.*, *136*(1), 19–40, 1999.
- Lienkaemper, J., J. Galehouse, and R. Simpson, Creep response of the Hayward fault to stress changes caused by the Loma Prieta earthquake, *Science*, *276*, 2014–2016, 1997.
- Lienkaemper, J. J., J. S. Galehouse, and R. W. Simpson, Long-term monitoring of creep rate along the Hayward fault and evidence for a lasting creep response to 1989 Loma Prieta earthquake, *Geophys. Res. Lett.*, *28*(11), 2265–2268, 2001.
- Linde, A. T., M. T. Gladwin, M. J. S. Johnston, R. L. Gwyther, and R. G. Bilham, A slow earthquake sequence on the San Andreas fault, *Nature*, *383*(6595), 65–68, 1996.
- Little, T. A., Brittle deformation adjacent to the Awatere strike-slip fault in New Zealand: Faulting patterns, scaling relationships, and displacement partitioning, *Geol. Soc. Amer. Bull.*, *107*(11), 1255–1271, 1995.
- Liu, J., K. Sieh, and E. Hauksson, A structural interpretation of the aftershock “cloud” of the 1992 Mw 7.3 Landers earthquake, *Bull. Seism. Soc. Amer.*, *93*, 1333–1344, 2003.
- Lockner, D. A., and P. G. Okubo, Measurements of frictional heating in Granite, *J. Geophys. Res.*, *88*(B5), 4313–4320, 1983.
- Lockwood, J. P., and P. A. Lydon, *Geologic map of the Mount Abbot quadrangle, California*, U.S. Geological Survey Quadrangle Map GQ-1155, scale 1:62,500, 1975.
- Magistrale, H., Relative contributions of crustal temperature and composition to controlling the depth of earthquakes in southern California, *Geophys. Res. Lett.*, *29*(10), 2002.
- Malservisi, R., C. Gans, and K. P. Furlong, Numerical modeling of strike-slip creeping faults and implications for the Hayward fault, California, *Tectonophysics*, *361*(1-2), 121–137, 2003.
- Manaker, D. M., R. Bürgmann, W. H. Prescott, and J. Langbein, Distribution of interseismic slip rates and the potential for significant earthquakes on the Calaveras fault, central California, *J. Geophys. Res.*, *108*(B6), doi:10.1029/2002JB001,749, 2003.
- Martel, S. J., Formation of compound strike-slip fault zones, Mount Abbot quadrangle, California, *J. Struc. Geol.*, *12*, 869–882, 1990.
- Martel, S. J., Effects of cohesive zones on small faults and implications for secondary fracturing and trace geometry, *J. Struc. Geol.*, *19*(6), 835–847, 1997.
- Martel, S. J., and D. D. Pollard, Mechanics of slip and fracture along small faults and simple strike-slip fault zones in Granitic rock, *J. Geophys. Res.*, *94*(B7), 9417–9428, 1989.
- Martel, S. J., D. D. Pollard, and P. Segall, Development of simple fault zones in granitic rock, Mount Abbot quadrangle, Sierra Nevada, California, *Geol. Soc. Amer. Bull.*, *100*, 1451–1465, 1988.

- Mase, C. W., and L. Smith, Effects of frictional heating on the thermal, hydrologic, and mechanical response of a fault, *J. Geophys. Res.*, *92*(B7), 6249–6272, 1987.
- Matsu'ura, M., D. D. Jackson, and A. Cheng, Dislocation model for aseismic crustal deformation at Hollister, California, *J. Geophys. Res.*, *91*(B12), 2661–2674, 1986.
- Mattinson, J. M., Age, origin, and thermal histories of some plutonic rocks from the Salinian block of California, *Contr. Mineral. Petrol.*, *67*, 233–245, 1978.
- McCaffrey, R., Crustal block rotations and plate coupling, in *Plate boundary zones, AGU Geodynamics Series*, vol. 30, edited by S. Stein and J. T. Freymueller, pp. 101–122, 2002.
- McClusky, S. C., S. C. Bjornstad, B. H. Hager, R. W. King, B. J. Meade, M. M. Miller, F. C. Monastero, and B. J. Souter, Present day kinematics of the Eastern California Shear Zone from a geodetically constrained block model, *Geophys. Res. Lett.*, *28*(17), 3369–3372, 2001.
- McGarr, A. F., On relating apparent stress to the stress causing earthquake fault slip, *J. Geophys. Res.*, *104*(B2), 3003–3011, 1999.
- McKenzie, D., and J. N. Brune, Melting on fault planes during large earthquakes, *Geophys. J. Royal Astron. Soc.*, *29*, 65–78, 1972.
- Meade, B. J., and B. H. Hager, Block models of crustal motion in southern California constrained by GPS measurements, *J. Geophys. Res.*, *in review*, 2004.
- Meade, B. J., B. H. Hager, S. McClusky, R. E. Reilinger, S. Ergintav, O. Lenk, A. Barka, and H. Ozener, Estimates of seismic potential in the Marmara Sea region from block models of secular deformation constrained by Global Positioning System measurements, *Bull. Seism. Soc. Amer.*, *92*, 208–215, 2002.
- Melosh, H. J., Dynamical weakening of faults by acoustic fluidization, *Nature*, *379*(6566), 601–606, 1996.
- Miller, M. M., D. J. Johnson, C. M. Rubin, H. Dragert, K. Wang, A. Qamar, and C. Goldfinger, GPS-determination of along-strike variation in Cascadia margin kinematics: Implications for relative plate motion, subduction zone coupling, and permanent deformation, *Tectonics*, *20*(2), 161–176, 2001.
- Moore, D. E., and D. A. Lockner, Crystallographic controls on the frictional behavior of dry and water-saturated sheet structure minerals, *J. Geophys. Res.*, *109*(B3), 2004.
- Moore, D. E., D. A. Lockner, R. Summers, M. Shengli, and J. Byerlee, Strength of chrysotile-serpentinite gouge under hydrothermal conditions: Can it explain a weak San Andreas fault?, *Geology*, *24*(11), 1041–1044, 1996.
- Moore, D. E., D. A. Lockner, H. Tanaka, and K. Iwata, The coefficient of friction of chrysotile gouge at seismogenic depths, *Int. Geol. Rev.*, *46*(5), 385–398, 2004.
- Moore, J., Geology of the Mount Pinchot quadrangle, *U. S. Geol. Survey Bull.*, *1130*, 1963.

- Moore, J., *Geologic map of the Marion Peak quadrangle, Sierra Nevada, California*, U.S. Geological Survey Quadrangle Map GQ-1399, scale 1:62,500, 1978.
- Moore, J., and T. Sisson, *Geologic map of the Triple Divide Peak quadrangle, Tulare County, California*, U.S. Geological Survey Quadrangle Map GQ-1636, scale 1:62,500, 1987.
- Mount, V. S., and J. Suppe, State of stress near the San Andreas fault, *Geology*, 15(12), 1143–1146, 1987.
- Murray, J. R., P. Segall, P. Cervelli, W. Prescott, and J. Svarc, Inversion of GPS data for spatially variable slip-rate on the San Andreas fault near Parkfield, CA, *Geophys. Res. Lett.*, 28(2), 359–362, 2001.
- Murray, M. H., and P. Segall, Modeling broadscale deformation in northern California and Nevada from plate motions and elastic strain accumulation, *Geophys. Res. Lett.*, 28(22), 4315–4318, 2001.
- Naeser, C., Fission track dating and geological annealing of fission tracks, in *Lectures in isotope geology*, edited by E. Jaeger and J. C. Hunziker, pp. 154–169, Springer-Verlag, New York, 1979.
- Naeser, C. W., and D. C. Ross, Fission-track ages of sphene and apatite of Granitic rocks of Salinian block, Coast Ranges, California, *J. Res. U.S. Geol. Survey*, 4(4), 415–420, 1976.
- Oakeshott, G. B., Geology and mineral deposits of San Fernando quadrangle, Los Angeles county, California, *California Division of Mines Bulletin*, 172, 1958.
- Okada, Y., Surface deformation due to shear and tensile faults in a half-space, *Bull. Seism. Soc. Amer.*, 75(4), 1135–1154, 1985.
- Olson, J., and D. D. Pollard, Inferring paleostresses from natural fracture patterns: A new method, *Geology*, 17, 345–348, 1989.
- O’Neil, J. R., and T. C. Hanks, Geochemical evidence for water-rock interaction along the San Andreas and Garlock faults of California, *J. Geophys. Res.*, 85(B11), 6286–6292, 1980.
- Pachell, M. A., and J. P. Evans, Growth, linkage, and termination processes of a 10-km-long strike-slip fault in jointed granite: The Gemini fault zone, Sierra Nevada, California, *J. Struct. Geol.*, 24, 1903–1924, 2002.
- Page, B. M., G. A. Thompson, and R. G. Coleman, Late Cenozoic tectonics of the central and southern Coast Ranges of California, *Geol. Soc. Amer. Bull.*, 110(7), 846–876, 1998.
- Pollard, D. D., and A. Aydin, Progress in understanding jointing over the past century, *Geol. Soc. Amer. Bull.*, 100, 1181–1204, 1988.
- Pollard, D. D., and P. Segall, Theoretical displacements and stresses near fractures in rocks: With applications to faults, joints, veins, dikes, and solution surfaces, in *Fracture mechanics of rocks*, edited by B. Atkinson, pp. 277–349, Academic, San Diego, CA, 1987.

- Pollitz, F. F., and M. C. J. Nyst, A physical model for strain accumulation in the San Francisco Bay Region, *Geophys. J. Int.*, *in review*, 2004.
- Powell, R. E., Balanced palinspastic reconstruction of pre-late Cenozoic paleogeology, southern California; geologic and kinematic constraints on evolution of the San Andreas fault system, in *Memoir - Geological Society of America*, edited by R. E. Powell, R. J. I. Weldon, and J. C. Matti, pp. 1–106, Geological Society of America, Boulder, CO, 1993.
- Prescott, W., D. Manaker, R. W. Simpson, and W. Ellsworth, R-factors inferred from geodetic modeling, *U. S. Geol. Survey Open File Rep.*, *03-214*, C1–C9, 2003.
- Prescott, W. H., J. C. Savage, J. L. Svarc, and D. Manaker, Deformation across the Pacific-North America plate boundary near San Francisco, California, *J. Geophys. Res.*, *106*(B4), 6673–6682, 2001.
- Provost, A.-S., and H. Houston, Orientation of the stress field surrounding the creeping section of the San Andreas fault: Evidence for a narrow mechanically-weak fault zone, *J. Geophys. Res.*, *106*(B6), 11,373–11,386, 2001.
- Provost, A.-S., and H. Houston, Stress orientations in northern and central California: Evidence for the evolution of frictional strength along the San Andreas plate boundary system, *J. Geophys. Res.*, *108*(B3), doi:10.1029/2001JB001,123, 2003.
- Reid, H. F., The mechanics of the earthquake, in *The California earthquake of April 18, 1906: Report of the State Investigation Commission*, vol. 2, Carnegie Institute of Washington, Washington, D.C., 1910.
- Rice, J. R., Fault stress states, pore pressure distributions, and the weakness of the San Andreas fault, in *Fault mechanics and transport properties of rocks*, edited by T.-F. Wong and B. Evans, pp. 475–503, Academic, San Diego, CA, 1992.
- Roering, J. J., M. L. Cooke, and D. D. Pollard, Why blind thrust faults do not propagate to the earth's surface: Numerical modeling of coseismic deformation associated with thrust-related anticlines, *J. Geophys. Res.*, *102*(B6), 11,901–11,912, 1997.
- Rolandone, F., and C. Jaupart, The distribution of slip rate and ductile deformation in a strike-slip shear zone, *Geophys. J. Int.*, *148*, 179–192, 2002.
- Saffer, D. M., B. A. Bekins, and S. Hickman, Topographically driven groundwater flow and the San Andreas heat flow paradox revisited, *J. Geophys. Res.*, *108*(B5), doi:10.1029/2002JB001,849., 2003.
- Sauber, J., Geodetic measurement of deformation east of the San Andreas fault in central California, in *Slow deformation and transmission of stress in the Earth, Geophysical monograph*, vol. 49, edited by S. C. Cohen and P. Vanicek, pp. 71–86, American Geophysical Union, 1989.
- Savage, J. C., Equivalent strike-slip earthquake cycles in half-space and lithosphere-asthenosphere Earth models, *J. Geophys. Res.*, *95*(B4), 4873–4879, 1990.
- Savage, J. C., Viscoelastic-coupling model for the earthquake cycle driven from below, *J. Geophys. Res.*, *105*(B11), 25,525–25,532, 2000.

- Savage, J. C., R. W. Simpson, and M. H. Murray, Strain accumulation rates in the San Francisco Bay Area, 1972-1989, *J. Geophys. Res.*, *103*(B8), 18,039–18,051, 1998.
- Savage, J. C., J. L. Svarc, and W. H. Prescott, Geodetic estimates of fault slip rates in the San Francisco Bay Area, *J. Geophys. Res.*, *104*(B3), 4995–5002, 1999.
- Savage, J. C., W. Gan, W. H. Prescott, and J. L. Svarc, Strain accumulation across the Coast Ranges at the latitude of San Francisco, 1994-2000, *J. Geophys. Res.*, *109*(B3), doi:10.1029/2003JB002,612, 2004.
- Sawyer, T. L., and J. R. Unruh, Holocene slip rate constraints for the northern Greenville fault, eastern San Francisco Bay Area, California: Implications for the Mt. Diablo restraining stepover model, *EOS, Trans. Amer. Geophys. Union*, *83*(47), Abstract T62F-03, 2002.
- Schmidt, D. A., R. Bürgmann, R. M. Nadeau, and M. A. d'Alessio, Distribution of aseismic slip-rate on the Hayward fault inferred from seismic and geodetic data, *J. Geophys. Res.*, *in review*, 2004.
- Scholz, C. H., Earthquakes and friction laws, *Nature*, *391*(1), 37–42, 1998.
- Scholz, C. H., Evidence for a strong San Andreas fault, *Geology*, *28*(2), 163–166, 2000.
- Scholz, C. H., *The mechanics of earthquakes and faulting*, Cambridge University Press, Cambridge, 2002.
- Scholz, C. H., J. Beavan, and T. C. Hanks, Metamorphism, argon depletion, heat flow and stress on the Alpine fault, in *Proceedings of conference VIII: Analysis of actual fault zones in bedrock*, vol. 79-1239, pp. 534–586, U.S. Geol. Survey Open File Rep., Menlo Park, CA, 1979.
- Scholz, C. H., N. H. Dawers, J.-Z. Yu, M. H. Anders, and P. A. Cowie, Fault growth and fault scaling laws: Preliminary results, *J. Geophys. Res.*, *98*(B12), 21,951–21,961, 1993.
- Schultz, R. A., Understanding the process of faulting: Selected challenges and opportunities at the edge of the 21st century, *J. Struc. Geol.*, *21*, 985–993, 1999.
- Segall, P., Integrating geologic and geodetic estimates of slip rate on the San Andreas fault system, *Int. Geol. Rev.*, *44*(1), 62–82, 2002.
- Segall, P., and R. Harris, Earthquake deformation cycle on the San Andreas fault near Parkfield, California, *J. Geophys. Res.*, *92*(B10), 10,511–10,525, 1987.
- Segall, P., and D. D. Pollard, Mechanics of discontinuous faults, *J. Geophys. Res.*, *85*(B8), 4337–4350, 1980.
- Segall, P., and D. D. Pollard, Nucleation and growth of strike slip faults in Granite, *J. Geophys. Res.*, *88*(B1), 555–568, 1983.
- Segall, P., E. H. McKee, S. J. Martel, and B. D. Turrin, Late Cretaceous age of fractures in the Sierra Nevada batholith, California, *Geology*, *18*(12), 1248–1251, 1990.

- Segall, P., R. Bürgmann, and M. V. Matthews, Time dependent triggered afterslip following the 1989 Loma Prieta earthquake, *J. Geophys. Res.*, *105*, 5615–5634, 2000.
- Sella, G. F., T. H. Dixon, and A. L. Mao, REVEL: A model for recent plate velocities from space geodesy, *J. Geophys. Res.*, *107*(B4), doi:10.1029/2000JB000,033, 2002.
- Shen, Z.-K., et al., Southern California Earthquake Center Crustal Motion Map Version 3.0, <http://epicenter.usc.edu/cmm3/>, 2003.
- Sibson, R. H., Fault zone models, heat flow, and the depth distribution of earthquakes in the continental crust of the United States, *Bull. Seism. Soc. Amer.*, *68*, 1421–1448, 1982.
- Sibson, R. H., Implications of fault-valve behavior for rupture nucleation and recurrence, *Tectonophysics*, *211*(1-4), 283–293, 1992.
- Sibson, R. H., A brittle failure mode plot defining conditions for high-flux flow, *Econ. Geol.*, *95*, 41–47, 2000.
- Simpson, R. W., J. J. Lienkaemper, and J. S. Galehouse, Variations in creep rate along the Hayward fault, California, interpreted as changes in depth of creep, *Geophys. Res. Lett.*, *28*(11), 2269–2272, 2001.
- Sims, J. D., Chronology of displacement on the San Andreas fault in central California: Evidence from reversed positions of exotic rock bodies near Parkfield, CA, in *Memoir - Geological Society of America*, edited by R. E. Powell, R. J. I. Weldon, and J. C. Matti, pp. 231–256, Geological Society of America, Boulder, CO, 1993.
- Steblov, G. M., M. G. Kogan, R. W. King, C. H. Scholz, R. Bürgmann, and D. I. Frolov, Imprint of the North American plate in Siberia revealed by GPS, *Geophys. Res. Lett.*, *30*(18), doi:10.1029/2003GL017,805, 2003.
- Storti, F., F. Rossetti, and F. Salvini, Structural architecture and displacement accommodation mechanisms at the termination of the priestley fault, northern Victoria Land, Antarctica, *Tectonophysics*, *341*, 141–161, 2001.
- ten Brink, U. S., N. Shimizu, and P. C. Molzer, Plate deformation at depth under northern California: Slab gap or stretched slab?, *Tectonics*, *18*(6), 1084–1098, 1999.
- Thatcher, W., Strain accumulation on northern San Andreas fault zone since 1906, *J. Geophys. Res.*, *80*(35), 4873–4880, 1975.
- Thatcher, W., and P. C. England, Ductile shear zones beneath strike-slip faults: Implications for the thermomechanics of the San Andreas fault zone, *J. Geophys. Res.*, *103*(B1), 891–905, 1998.
- Thatcher, W., G. Marshall, and M. Lisowski, Resolution of fault slip along the 470-km-long rupture of the great 1906 San Francisco earthquake and its implications, *J. Geophys. Res.*, *102*(B3), 5353–5367, 1997.

- Thatcher, W., G. R. Foulger, B. R. Julian, J. Svarc, E. Quilty, and G. W. Bawden, Present-day deformation across the Basin and Range province, western United States, *Science*, *283*, 1714–1718, 1999.
- Townend, J., and M. D. Zoback, Focal mechanism stress inversions in southern California and the strength of the San Andreas fault, in *Proceedings of the Conference on Tectonic Problems of the San Andreas Fault System*, vol. 30, pp. 268–276, Stanford University Publication, Geological Sciences, 2001.
- Tse, S. T., and J. R. Rice, Crustal instability in relation to the depth variation of frictional slip properties, *J. Geophys. Res.*, *91*(B9), 9452–9472, 1986.
- Unruh, J. R., and W. R. Lettis, Kinematics of transpressional deformation in the eastern San Francisco Bay region, California, *Geology*, *26*, 19–22, 1998.
- Unruh, J. R., and T. L. Sawyer, Assessment of blind seismogenic sources, Livermore Valley, eastern San Francisco Bay Region: Final technical report submitted to the U.S. Geological Survey, National Earthquake Hazards Reduction Program, award no. 1434-95-g-2611, 1997.
- Unruh, J. R., and T. L. Sawyer, Paleoseismic investigation of the northern Greenville fault, eastern San Francisco Bay Area, California: Final technical report submitted to the U.S. Geological Survey, National Earthquake Hazards Reduction Program award no. 1434-hq-97-gr-03146, , 1998.
- Unruh, J. R., K. I. Kelson, D. Manaker, and A. Barron, Critical evaluation of the northern termination of the Calaveras fault, eastern San Francisco Bay Area, California, *Report 1430*, William Lettis and Associates, 2002.
- Vermilye, J. M., and C. H. Scholz, The process zone: A microstructural view of fault growth, *J. Geophys. Res.*, *103*(B6), 12,223–12,237, 1998.
- Wakabayashi, J., Distribution of displacement on and evolution of a young transform system: The northern San Andreas fault system, California, *J. Geophys. Res.*, *18*(B6), 1245–1274, 1999.
- Waldhauser, F., and W. L. Ellsworth, Fault structure and mechanics of the Hayward fault, California, from double-difference earthquake locations, *J. Geophys. Res.*, *107*(B3), doi:10.129/2000JB000,084, 2002.
- Weertman, J., *Dislocation based fracture mechanics*, World Scientific, Singapore, 1996.
- Wentworth, C. M., and M. D. Zoback, The style of late Cenozoic deformation at the eastern-front of the California Coast Ranges, *Tectonics*, *8*(2), 237–246, 1989.
- Wentworth, C. M., and M. D. Zoback, The style of the late Cenozoic deformation at the eastern-front of the California Coast Ranges - reply, *Tectonics*, *9*(5), 1267–1268, 1990.
- Wernicke, B., and J. K. Snow, Cenozoic tectonism in the central Basin and Range: Motion of the Sierran-Great Valley block, *Int. Geol. Rev.*, *40*(5), 403–410, 1998.

- Wesnousky, S. G., Crustal deformation processes and the stability of the Gutenberg-Richter relationship, *Bull. Seism. Soc. Amer.*, *89*(4), 1131–1137, 1999.
- Wilkins, S. J., and M. R. Gross, Normal fault growth in layered rocks at Split Mountain, Utah: Influence of mechanical stratigraphy on dip linkage, fault restriction, and fault scaling, *J. Struc. Geol.*, *24*, 1431–1429, 2002.
- Willemse, E. J. M., and D. D. Pollard, Normal fault growth: Evolution of tipline shapes and slip distribution, in *Aspects of tectonic faulting*, edited by F. Lehner and J. Urai, pp. 193–226, SpringerVerlag, Berlin, 1994.
- Williams, C. F., Temperature and the seismic/aseismic transition: Observations from the 1992 Landers earthquake, *Geophys. Res. Lett.*, *23*(16), 2029–2032, 1996.
- Williams, C. F., Implications of the depth of seismicity for the rupture extent of future earthquakes in the San Francisco Bay Area, *U. S. Geol. Survey Open File Rep.*, *03-214*, A1–A16, 2003.
- Williams, C. F., and T. N. Narasimhan, Hydrogeologic constraints on heat-flow along the San Andreas fault - a testing of hypotheses, *Earth Planet. Sci. Lett.*, *92*(2), 131–143, 1989.
- Williams, C. F., L. Beyer, F. Grubb, and S. P. Galanis, Jr., Heat flow and seismotectonics of the western Transverse Ranges [abs.], *Amer. Assoc. Petrol. Geolog. Bull.*, *85*, 1150, 2001.
- Williams, C. F., F. Grubb, and S. P. Galanis, Heat flow in the SAFOD pilot hole and implications for the strength of the San Andreas fault, *Geophys. Res. Lett.*, *31*(L15S14), doi:10.1029/2003GL019,352, 2004.
- Wolf, R. A., K. A. Farley, and L. T. Silver, Helium diffusion and low-temperature thermochronometry of apatite, *Geochem. et Cosmochem. Acta*, *60*(21), 4231–4240, 1996.
- Wolf, R. A., K. A. Farley, and D. M. Kass, Modeling of the temperature sensitivity of the apatite (U-Th)/He thermochronometer, *Chem. Geol.*, *148*(1-2), 105–114, 1998.
- Wong, I. G., and R. W. Ely, Historical seismicity and tectonics of the Coast Ranges-Sierra block boundary: Implications to the 1983 Coalinga earthquakes, in *The 1983 Coalinga, California earthquakes*, edited by J. Bennet and R. Sherburne, California Division of Mines and Geology Special Publication 66, pp. 89–104, 1983.
- Working Group on Northern California Earthquake Probabilities, Earthquake probabilities in the San Francisco Bay region: 2002 to 2031, *U.S. Geol. Surv. Open File Rep.*, *03-214*, 2003.
- Xu, G., and P. J. J. Kamp, Tectonics and denudation adjacent to the Xianshuihe fault, eastern Tibetan plateau: Constraints from fission track thermochronology, *J. Geophys. Res.*, *105*(B8), 19,231–19,251, 2000.
- Yu, E., and P. Segall, Slip in the 1868 Hayward earthquake from the analysis of historical triangulation data, *J. Geophys. Res.*, *101*(B7), 16,101–16,118, 1996.